Morton Effect Induced Instability in Mid-Span Rotor–Hydrodynamic Bearing Systems

Zenglin Guo

Dissertation submitted to the Faculty of the
Virginia Polytechnic Institute and State University
In partial fulfillment of the requirement for the degree of
Doctor of Philosophy
In
Mechanical Engineering

R. Gordon Kirk
Mary E. Kasarda
John C. Nicholas
Brian Vick
Robert L. West

May 20, 2011
Blacksburg, Virginia

Keywords: Morton Effect, rotor, bearing, instability, mid-span

Morton Effect Induced Instability in Mid-Span Rotor–Hydrodynamic Bearing Systems

Zenglin Guo

ABSTRACT

The Morton Effect in the rotor - bearing systems may lead to an unstable operation. Up to the present, most of the established research efforts have been focused on the overhung rotor systems. In this dissertation, a systematic study on the Morton Effect induced instability in mid-span rotor systems is presented.

First, the mechanism study is conducted. The simplified rotor models with isotropic linear bearing supports are adopted for the derivation of analytical expressions. The threshold speeds of instability in simple forms are obtained for the systems with the thermal imbalance acting concurrent with or perpendicular to the direction of the response displacement. For a perspective view of the system stability, a stability map for the damped rigid mid-span rotors with the thermal imbalance having arbitrary phase difference has been generated. It shows that the stable operating regions of the system are bounded by two curves of threshold of instability. The results show that the Morton Effect induced instability thresholds are actually affected by both the magnitude and relative phase of the thermal imbalance. The mechanism of the Morton Effect induced thermal instability of mid-span rotors supported by linear isotropic bearings can be explained through the fact that the Morton Effect introduces either negative stiffness or negative cross-coupled stiffness.

Next, the steady-state response performance under the influence of the Morton Effect is discussed. The results show that the Morton Effect has a comprehensive impact on both the amplitude and phase lag of the steady-state unbalance response. It may shift both curves in a manner dependent on the relative magnitude and direction of the thermal imbalance.

Then, the mid-span rotors supported by the hydrodynamic journal bearings are analyzed. The models to calculate the thermal bending of the shaft and the temperature distribution across the journal surface are established. The calculations of the temperature difference and its equivalent thermal imbalance are conducted and discussed with the comparison to the analytical results. It shows that the thermal imbalance may increase to the level of the mechanical imbalance and its influence on the system stability should be then included. The suggested thermal bending model also explains that the mid-span rotors are less liable to be influenced by the Morton Effect than are the overhung configurations, because of the restraining effect between the two supports. The simulation results of a symmetric mid-span rotor - hydrodynamic journal bearing system show that the inclusion of the Morton Effect may lead to an unstable operation of the system. Considering the existence of the oil film self-induced vibration due to the dynamic characteristics of fluid film bearings, the Morton Effect may make a further negative impact on the instabilities of the rotor system under some working conditions.

Finally, the predictive solution method for the general mid-span rotors is discussed. The computer code, VT-MAP, is developed for the predictions of the Morton Effect induced instability of rotor systems in either mid-span and overhung configurations.

Dedicated to

My wife, Yihua Yang

and

My children, Huachen Guo and David Guo

ACKNOWLEDGEMENTS

I am heartily thankful to my advisor, Dr. R. Gordon Kirk, for his continuous encouragement, guidance and support during the completion of my dissertation and the entire studies for the degree. I am also very grateful to Dr. Mary E. Kasarda, Dr. John C. Nicholas, Dr. Brian Vick, Dr. Robert L. West and Dr. Daniel J. Inman in my advisory and examination committees, for their prompt advisory comments during each phase of the project. This dissertation would not have been possible without the encouragement and guidance of my advisor and other professors in my committees.

I would like to express my sincere appreciation to the Virginia Tech Rotor Dynamics Lab Industrial Affiliates Group for their support and interest in this research project.

In addition, I am very thankful to the faculty and staff in the Mechanical Engineering Department. I am indebted to James Archual, Ben Poe, Cathy Hill, Melissa Williams, and many others, for their support and help in a number of different respects. I am also grateful to all of my colleagues in the rotor lab to support me in any respect during my studies for the degree.

Finally, I offer my sincere regards and blessings to all of my family members. Especially, I owe my deepest gratitude to my wife, Yihua Yang, for her precious and continuous support during the completion of the project.

TABLE OF CONTENTS

LIST OF FIGURES

LIST OF TABLES

NOMENCLATURE

A_i	dimensionless coefficients of fourth-order polynomial equations ($i=0$-4)
A_t	thermal imbalance mass ratio, $A_t = \frac{\alpha_t}{m_d}$
A_x	amplitude of journal in x-coordinate (L)
A_y	amplitude of journal in y-coordinate (L)
a_i	coefficients of fourth-order polynomial equations (i=0-4)
B	length of bearing (L)
C, C_i	constant of integration ($i=1$-6)
C_b	radial clearance of bearing (L)
C_{ij}	dimensionless damping coefficients of hydrodynamic bearing ($i, j=x, y$)
c_b	damping coefficient of isotropic support (Mt^{-1})
c_{ij}	damping coefficients of hydrodynamic bearing ($i, j=x, y$) (Mt^{-1})
c_l	specific heat capacity of lubricant ($L^2t^{-2}T^{-1}$)
D	diameter of bearing (L)
E	Young's modulus ($ML^{-1}t^{-2}$)
$\dot{E}_{visc}$	energy generation rate by viscous friction (ML^2t^{-3})
$\dot{E}_{lub}$	net energy out flux by the flow of lubricant (ML^2t^{-3})

$\dot{E}_J$	energy out flux through journal by heat transfer (ML^2t^{-3})
$\dot{E}_B$	energy out flux through bearing housing by heat transfer (ML^2t^{-3})
e	eccentric distance of journal center (L)
e_m	eccentric distance of mechanical imbalance mass (L)
f	fraction factor of energy out flux through the journal
H	heat transfer coefficient ($Mt^{-3}T^{-1}$)
h	fluid film thickness of bearing / height of cross section of beam (L)
h_a	height of cross section of journal on left-hand side (L)
h_b	height of cross section of journal on right-hand side (L)
I	area of moment inertia (L^4)
J	Jacobian matrix
J_{25}	element of Jacobian matrix at the 2nd row and the 5th column (t^{-2})
J_{27}	element of Jacobian matrix at the 2nd row and the 7th column (t^{-2})
J_{45}	element of Jacobian matrix at the 4th row and the 5th column (t^{-2})
J_{47}	element of Jacobian matrix at the 4th row and the 7th column (t^{-2})
K_{ij}	stiffness coefficients of hydrodynamic bearing ($i, j=x, y$) (Mt^{-2})
k	stiffness of shaft (half value for symmetrical rotor model) (Mt^{-2})
k_b	stiffness of isotropic support (Mt^{-2})
L	length of rotor or beam (L)
L_a	length of beam within the LHS bearing (L)
L_b	length of beam within the RHS bearing (L)
L_d	distance between the left end of the bearing on the LHS and the center-of-gravity of equivalent disk mass (L)

M	bending moment (ML^2t^{-2})
M_a	equivalent thermal-induced bending moment due to LHS bearing (ML^2t^{-2})
M_b	equivalent thermal-induced bending moment due to RHS bearing (ML^2t^{-2})
M_{eq}	equivalent thermal-induced bending moment (ML^2t^{-2})
m_d	mass of disk (half value for symmetrical rotor model) (M)
m_j	mass of journal (M)
N	speed of rotation in revolutions per minute (RPM) (t^{-1})
O_b	center of bearing
O_d	center of disk
O_j	center of journal
O_{jo}	static equilibrium of journal
O_m	center of mechanical imbalance mass
T	temperature (T)
ΔT	temperature difference between hot spot and cold spot (T)
ΔT_a	temperature difference across beam within LHS bearing (T)
T_{amb}	ambient temperature (T)
ΔT_b	temperature difference across beam within RHS bearing (T)
T_o	lubricant supply temperature (T)
T_1	temperature on the top surface of beam (T)
T_{1a}	temperature on the top surface of journal within LHS bearing (T)
T_{1b}	temperature on the top surface of journal within RHS bearing (T)
T_2	temperature on the bottom surface of beam (T)
T_{2a}	temperature on the bottom surface of journal within LHS bearing (T)

T_{2b}	temperature on the bottom surface of journal within RHS bearing (T)
t	time (t)
U	total imbalance (ML)
U_m	mechanical imbalance (half value for symmetrical rotor model) (ML)
U_t	thermal imbalance (half value for symmetrical rotor model) (ML)
U_{to}	characteristic thermal imbalance (ML)
u_s	system damping (Mt^{-1})
v	deflection of beam (L)
v_1	deflection of beam within LHS bearing (L)
v_2	deflection of beam beyond bearings (L)
v_3	deflection of beam within RHS bearing (L)
W	load of bearing (MLt^{-2})
W_{rotor}	weight of rotor (MLt^{-2})
X, Y, Z	fixed coordinate system with origin at bearing center
x, y, z	Cartesian coordinate system
x_d	displacement of disk in x-coordinate (L)
x_j	displacement of journal in x-coordinate (L)
y_d	displacement of disk in y-coordinate (L)
y_j	displacement of journal in y-coordinate (L)
z	complex displacement (L)
z_d	complex displacement of disk (L)
z_{do}	magnitude of displacement of disk (L)
$\bar{z}_{do}$	complex magnitude of displacement of disk

z_j complex displacement of journal (L)

z_{jo} magnitude of displacement of journal (L)

$\overline{z}_{jo}$ complex magnitude of displacement of journal (L)

z_o magnitude of complex displacement (L)

α coefficient of thermal expansion (T^{-1})

α_t equivalent coefficient of thermal effect (M)

β thermoviscosity coefficient (T^{-1})

γ phase angle of dynamic center of journal

ε eccentricity ratio of bearing

ε_o static eccentricity ratio of bearing

ζ damping ratio of rigid rotor model, $\zeta=\frac{c_b}{2\sqrt{k_b m_d}}$

θ phase lag

θ_d phase lag of disk

θ_j phase lag of journal

θ_{jo} phase angle of static equilibrium of journal

θ_t phase angle of thermal imbalance

κ curvature of bending (L^{-1})

Λ dimensionless characteristic root, $\Lambda=\frac{\lambda}{\omega_n}$

λ phase angle of hot spot; characteristic root

μ dynamic viscosity of lubricant ($ML^{-1}\ t^{-1}$)

μ_o lubricant supply dynamic viscosity ($ML^{-1}\ t^{-1}$)

ξ circumferential angle used in film thickness expression

ρ radius of curvature (L)

ρ_l density of lubricant (ML^{-3})

τ shear stress $(ML^{-1}\ t^{-2})$

ϕ phase difference between mechanical imbalance and thermal imbalance

φ attitude angle

φ_o static attitude angle

φ_x phase angle of journal in x-coordinate

φ_y phase angle of journal in y-coordinate

ψ phase angle of thermal imbalance relative to response displacement

ψ_b relative clearance of bearing

Ω dimensionless speed of rotation, $\Omega = \dfrac{\omega}{\omega_n}$

ω speed of rotation in radians per second (t^{-1})

ω_n undamped natural frequency in radians per second (t^{-1})

$$\omega_n = \sqrt{\frac{k_b}{m_d}} \text{ (rigid rotor)}; \quad \omega_n = \sqrt{\frac{k}{m_d}} \text{ (elastic rotor)}$$

ω_{thr} threshold speed in radians per second (t^{-1})

ω_{thr1} first threshold speed in radians per second (t^{-1})

ω_{thr2} second threshold speed in radians per second (t^{-1})

ω_{MCOS} maximum continuous operating speed in radians per second (t^{-1})

Dimensions: M = mass, L = length, t = time, T = temperature

1 INTRODUCTION

1.1 History

One of the most important events in the history of rotor dynamics was the famous publication by Jeffcott in 1919 [1]. In his paper, a symmetric elastic rotor with a single disk mass supported on rigid supports was studied and it was suggested that the rotor can operate below, at or above its critical speed. This has become a theoretical foundation for the design of various rotating machines in modern industry. It seemed that there was no barrier for the high-speed rotor design once the critical speed was successfully traversed. However, the later research work by Newkirk in 1925 presented a new threshold speed caused by "oil film whirl", a self-induced vibration due to fluid film bearings [2]. Since then, the instability of rotor-hydrodynamic bearing systems has become a major concern in high-speed rotating machine design [3-9].

There are many factors which can cause the unstable operation of a rotor system. The most typical one is the self-induced vibration due to the dynamic characteristics of fluid film bearings or seals, as mentioned above [3-9]. From the last decade, a new instability phenomenon called the Morton Effect was frequently reported in industry and began to receive attentions of designers and research workers in the field of rotor dynamics, which actually falls into a general category of the rotor thermal bending [10-25].

Rotor thermal bending is a complicated phenomenon which can lead to unstable spiral vibrations [26]. This phenomenon is primarily due to a temperature difference developing across the journal. This temperature difference can either be caused by the journal rubbing against stationary components or by viscous shearing within the lubricant. The former mechanism was first noticed by Newkirk in 1926 [27] and later clearly explained by Dimarogonas in 1973 [28]. This mechanism is called the Newkirk Effect. The latter mechanism has been studied since 1970's and was formally published by Keogh and Morton in 1993 [10] and 1994 [11] and is often referred to as the Morton Effect [25].

In 1975, Morton performed an experiment in a rig on a typical 28 inches (711 mm) diameter shaft running at 1800 RPM. It was found that the significant differential temperatures were measured across the shaft, even for shaft orbits of only a few percent of the radial clearance [24]. A linear relationship between differential temperature and orbit size was identified during these experiments. In 1976, Morton observed spiral vibrations due to this effect on particular designs of industrial gas turbine [24].

In 1978, the phenomenon was investigated by Hesseborn who performed experiments on a bearing test rig [29]. Larsson analyzed the results of this report and concluded that an almost linear relation exists between bearing journal vibration and differential temperature across the journal [17-18].

Morton Effect induced thermal instability can be roughly explained using the model of an overhung rotor supported by hydrodynamic journal bearings (Figure 1.1). When the rotor is excited by the external force such as the mechanical imbalance, the journal center moves (whirl) along its orbit in addition to the rotation. In this process, the temperature difference develops in circumferential direction in the lubricant. Use the hot spot to stand for the high temperature

region and the cold spot for the low temperature region. For simplicity of illustration, assuming that the journal is executing a synchronous orbit around the bearing center, this centered orbit causes one portion of the journal surface to always be at the minimum film thickness, while a diametrically opposite section of the journal surface is always at the maximum film thickness. Lower film thickness areas are generally associated with higher viscous shear stresses which produce higher temperatures. As a result, a hot spot will develop on the journal surface exposed to the minimum film thickness region and a cold spot will be formed on the surface at maximum film thickness. This leads to a temperature gradient developing across the journal. This temperature difference across the journal will produce the thermal bending of the rotor. If this thermal induced bending of shaft is represented by an equivalent thermal imbalance, it can be considered that the thermal bending of rotor may lead to an increase or decrease of equivalent total imbalance acting on the disk mass. The increase of imbalance will raise the response level of the rotor including that of the journal at the bearing locations. If this is the case, the

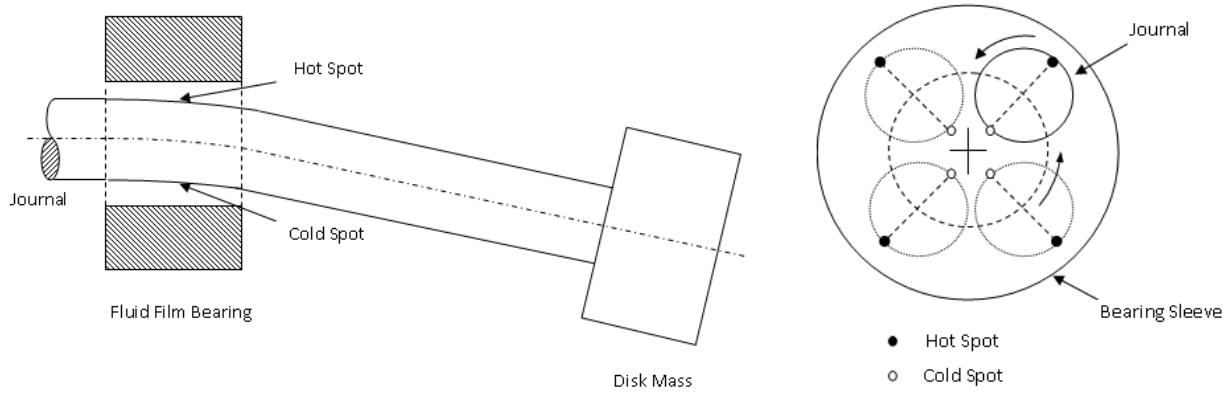

(a) Overhung rotor (b) Whirling orbit of the journal

Figure 1.1 Overhung rotor with Morton Effect involved

temperature difference within the lubricant may increase again, which result in an increasing thermal bending. Consequently, an increasing total imbalance may be initiated. The entire process would exhibit a diverging positive feedback cycle. This may lead to the unstable operation of the rotor system.

Morton Effect induced instability is a complex phenomenon. It took a long time for the research workers to identify it and explain its mechanism [10, 25, and 30].

In reality, the Morton Effect induced thermal instability may not be easily identified at first because the occurrence of such synchronous vibration excursions may be caused by more than one mechanism. For hot machines, the impeller or disk may be forced to move off-center due to non-uniform slip in the centering mechanism or the disk may simply become loose and move eccentric. A hard mechanical rub may also cause local heating and bending of the rotor, resulting in a mechanical imbalance. It may be very difficult to clearly distinguish between a loose impeller and a fluid shear produced imbalance. The two part paper by Faulkner, Strong and Kirk described a field problem for a gas engine turbocharger that first experienced a mechanical looseness excited vibration and then a Morton Effect vibration [14-15].

1.2 Literature Review

Since Morton published his first papers in 1993 and 1994, it has shown a steady increase of interests on this phenomenon in the field of rotor dynamics. According to the statistics by de Jongh, the total amount of publications on the Morton Effect induced instability shows a linear increasing trend since then [25].

Keogh and Morton in their first publications and the succeeding paper [10, 11, 24] firstly investigated this phenomenon and indicated that the thermal shaft bending could be devolved in

a fluid film bearing because of non-uniform viscous shearing in the oil film, Under certain circumstances, this can create similar “spiral vibrations “ as in the Newkirk Effect . The initial model using control theory was set up to calculate the thermal gain defined as the ratio between the local shaft bend and the oil film perturbation orbit.

The paper by de Jongh and Morton [12] described a case study on a gas compressor for an offshore gas lift application. For this compressor, the synchronous vibration problem on the test stand was resolved by reducing the weight of the couplings. However, the true nature of the vibration mechanism was not fully understood at the time of shipment. Further research was carried out on a scaled test rotor of this specific compressor. By measuring the temperature distribution around a rotating bearing journal, the bearing behavior of this compressor rotor was explained.

Faulkner, Strong and Kirk [14-15] described a case history of a radial inflow overhung turbine of a turbocharger, exhibiting synchronous rotor instability after a machine upgrade. The original design was changed in order to increase the capacity and efficiency of the turbocharger, which resulted in a turbine wheel mass increase. The problem of instability was solved finally by changing the bearing geometry.

Larsson [17-18] described a complex stability analysis model by means of control theory. An initial deformed rotor configuration was assumed and was then used as an input in a dynamic model of the rotor system. This dynamic model produced a synchronous orbit which caused a circumferential temperature distribution to develop on portions of the shaft within the bearings. A thermal bend, which depended on the temperature distribution and the rotor thermal characteristics, was subsequently initiated. This thermal bend affected the rotor dynamics and

gave rise to the positive feedback behavior. The stability of the resulting feedback transfer function was then analyzed by using Nyquist plots.

Balbahadur [19-21] presented a predictive model for the overhung rotor systems, which involved Morton Effect induced thermal instability. This model aimed to reduce the complex stability analysis employed by the other publications. The following concept was adopted in this new model: In real machines satisfactory performance is established by using specified vibration or unbalance threshold levels that are given in standards published by various organizations. One method of specifying such levels is to restrict the maximum allowable centrifugal force that acts on the machine. This restriction then limits the allowable imbalance for each speed value. Such a criterion determines whether the rotor will be "stable" or "unstable" during operation, i.e. if the total mechanical and thermal unbalance level exceeds the threshold level given by the allowable imbalance then the rotor will be "unstable." At first, an estimate for the initial mechanical imbalance in the rotor was made. This imbalance was then put into the dynamic rotor model to obtain the synchronous orbit. A fluid film bearing model was then used to establish the temperature distribution which leads to the thermal imbalance. Finally, an unbalance threshold criterion is used to determine the system stability.

Kirk, Guo and Balbahadur [22-23] have made this model programmed with user-friendly interface and applied in relevant industries. This model was reported with a promising success in many case studies for the overhung rotor systems.

A systematic overview on the Morton Effect induced instability has been made by de Jongh [25]. The historical background was described and some vibration diagnoses were presented. Finally, the corrective actions for the Morton Effect induced instability problems were suggested:

- Limit design speed

- Reduce overhung moments
- Change bearing clearance
- Reduce bearing length
- Change bearing type or geometry
- Apply a heat barrier sleeve
- Increase specific bearing loading and eccentricity
- Change shaft material
- Change lubrication oil viscosity
- Increase inlet oil flow for better cooling

1.3 Objective of Research

The motivation of the current study is that most of the above publications concentrated on the overhung rotor systems. Some references even listed the configuration of overhung rotors as one of the characteristics of the Morton Effect induced instability [25]. It was true that most cases reported in the literature occurred in overhung rotor systems. However, from the mechanism of the Morton Effect, it should not be limited to this particular rotor configuration. There were some indications that the similar instability phenomenon also occurred in mid-span rotor configurations, according to Larsson [17-18]. Exploring the possibility of the Morton Effect induced instability in the mid-span rotor – hydrodynamic bearing systems has therefore become the major motivation of the current study. In addition, it is hopeful that this research will be helpful to explain the reason that this instability phenomenon occurs more often in overhung rotors than in mid-span rotors.

Another consideration when this research was initiated is that most of existing publications employed very complicated stability analysis procedure based on the control theory, except for the predictive methods. The latter shown effective in solving many problems but it lacked the rigor of the solutions which included the feedback mechanism. There were no simple forms of formulas or equations for the explanation or analysis of the Morton Effect induced instability.

Based on the above considerations, the objectives of the current study consist of:

(1) The mid-span rotors supported by the hydrodynamic journal bearings will be the major system to be investigated.

(2) The mechanism study of the Morton Effect induced instability will be conducted where basic concepts and equations are expected to be generated for the mid-span rotor systems.

(3) The influence of the Morton Effect on the unbalanced response of the system will also be discussed.

(4) Both analytical solutions and predictive solutions on mid-span rotors supported by hydrodynamic bearings will be conducted and discussed. Considering the existing practice of standard rotor dynamics analysis both in industry and classroom, the latter is still of important practical meaning. The case studies will be conducted to prove the theoretical results.

(5) Program the theoretical model and calculations into VT-MAP (Virginia Tech Morton Analysis Program). The final version of the commercial quality code, VT-MAP, will include the capabilities to analyze multiple rotor configurations and bearing types

1.4 Development of Current Study

As mentioned above, it seems that there lacks relevant formulas or equations to explain and calculate the Morton Effect induced instability, even for the overhung rotors. Hence, as the first

step, the mechanism study will be conducted. For this purpose, the simplified rotor and bearing models with reasonable assumptions will be adopted for the derivation of analytical expressions. The results are expected to explain the mechanism of the Morton Effect induced instability in mid-span rotors. The relevant equations are expected to prove the existence and evaluate the threshold of the Morton Effect induced instability.

Next, the influence of the Morton Effect on the steady-state response of the system will be discussed. The comparisons between the two cases of with and without the Morton Effect will be made.

Then, a more realistic model, the mid-span rotor supported by hydrodynamic journal bearings, will be studied. Compared to the overhung rotor systems, the modeling of the thermal bending of mid-span rotors is more complex. The research effort will then be concentrated on the calculation of the thermal bending of the rotor and differential temperature in the bearing and the resultant thermal imbalance. The system equations for a symmetrical mid-span rotor – hydrodynamic bearing systems will be derived. The stability and the transient response of this system are then calculated and discussed.

Finally, for the purpose of application in industry, the predictive solutions for the mid-span rotor systems will be discussed based on the previous theoretical studies. The corresponding predictive program, VT-MAP, will be developed.

For the ease of reading, there is an arrangement of chapter summary in each chapter except for the first chapter “Introduction’ and the last two chapters, “Conclusions” and “Suggested Future Research”.

2 MECHANISM STUDY OF MORTON EFFECT IN MID-SPAN ROTOR SYSTEMS

2.1 Simplified Model and Approach Method

As discussed in the introductory chapter, the viscous thermal induced instability (Morton Effect) in the rotor-hydrodynamic bearing systems is a complex phenomenon involving the feedback process and the interaction of rotor and bearings. This might partially be a reason that the existing literatures usually employed either the complicated feedback calculations or relatively easy-to-operate predictive calculations. In this chapter, a new approach will be conducted aimed to obtain the analytical solutions of the viscous thermal induced instability in the typical mid-span rotor-bearing systems. This will be used to explain the mechanism hidden behind this complicated phenomenon.

For this purpose, some basic assumptions about rotor and bearings have been made:

(1) A mid-span rotor is assumed to be symmetrical. The symmetrical rotor models are very representative and are widely-used for rotor dynamics analysis and calculations. These rotor models may include rigid rotors and elastic rotors (Jeffcott or extended Jeffcott rotors).

(2) The supports on the two ends of the rotor are assumed to be two identical bearings. In addition, they are also assumed to be of linear and isotropic dynamic characteristics. Both of the support stiffness and damping values are assumed to be positive. In this way, the whirling orbit

of the rotor will be in circular. In practice, the linear isotropic bearing models could be the representatives of either rolling journal bearings or fluid lubricated tilting pad journal bearings, to the some extend.

(3) The whirling speed of rotor is synchronous, i.e. the whirling speed of rotor (journal) is equal to the speed of rotation. The stability analysis and derived results are to be used to predict instabilities when the system is subjected to the forced unbalance excitations.

(4) The dynamic influence on the rotor systems due to the viscous thermal effect in the bearings, or the Morton Effect, will be represented by its equivalent thermal imbalance acting on the disk.

2.2 Undamped Rigid Rotor with Linear Isotropic Supports

First, a simple but illustrative model will be examined. Figure 2.1 shows an undamped symmetrical rigid rotor supported by two identical linear isotropic journal bearings.

It has also been assumed that:

(1) The rotor operates under its critical speed. Hence, there are no phase differences between the mechanical imbalance and the resultant response. More general situations will be discussed in Section 2.3.

(2) For the mid-span rotor-bearing system, it is reasonable to assume that the direction of the thermal imbalance is from the cold spot to the hot spot. The detailed analysis about the direction of the thermal imbalance will be discussed in the following sections. In this specific case, it is specified as that from the maximum clearance to the minimum clearance.

(3) It is obvious that there is also no phase difference between the thermal imbalance or the resultant total imbalances and the displacement response.

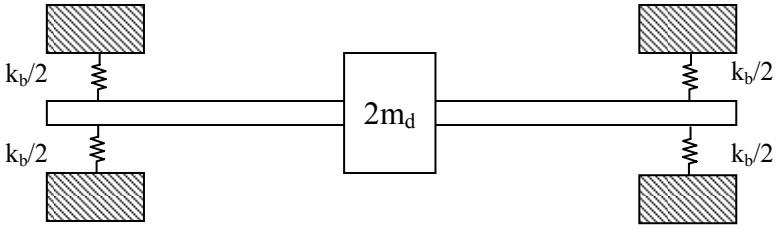

(a) Rotor and bearing model

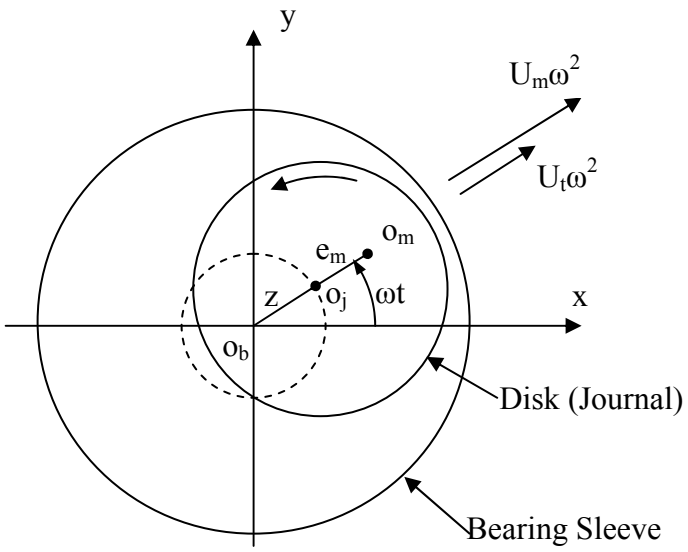

(b) Orbit

Figure 2.1 Undamped rigid rotor with linear isotropic supports

The equations of motion about the journal center O_j (x, y) of this system can be written as

$$\begin{aligned} m_d\ddot{x}+k_b x &= U_m\omega^2\cos\omega t+U_t\omega^2\cos\omega t \\ m_d\ddot{y}+k_b y &= U_m\omega^2\sin\omega t+U_t\omega^2\sin\omega t \end{aligned} \qquad \textbf{(2.1)}$$

where

$U_m = m_d e_m$

$z = x + iy$

$x = z\cos\omega t$

$y = z\sin\omega t$

In addition, an assumption on the magnitude of the thermal imbalance has been made based on the basic understanding of the viscous thermal effect. It is reasonable to deduce that the magnitude of the thermal imbalance is proportional to the displacement of the journal, which is correspondent with the viscous thermal induced temperature difference between hot spot and cold spot. The dependence of the thermal imbalance on the journal displacement may be nonlinear. However, a linear relationship is still a reasonable assumption [10, 11, 17, 18, 24, 25]. Or, it may be regarded as a linearization around the equilibrium for the general nonlinear expression. It is observed that the differential temperature may increase with the increase of operating speed. However, considering this imbalance is also proportional to the viscosity of the lubricant and the latter will decrease with the increase of operating speed, the effect due to the rotation speed of rotor and the viscosity of lubricant can be roughly assumed to be compensated.

From above considerations, the magnitude (half-value) of the thermal imbalance can be assumed as

$$U_t = \alpha_t z \tag{2.2}$$

where α_t is denoted as the equivalent coefficient of thermal effect. α_t is a constant mainly determined by the parameters of structures and materials. Obviously, it has the dimension of mass and is positive. This coefficient can also be translated as an additional unbalanced mass due to the viscous shearing thermal effect.

The equations of motion can be reduced to

$$m_d\ddot{x}+\left(k_b-\alpha_t\omega^2\right)x=m_de_m\omega^2\cos\omega t$$
$$m_d\ddot{y}+\left(k_b-\alpha_t\omega^2\right)y=m_de_m\omega^2\sin\omega t \quad \textbf{(2.3)}$$

If using complex notations

$$m_d\ddot{z}+(k_b-\alpha_t\omega^2)z=m_de_m\omega^2e^{i\omega t} \quad \textbf{(2.4)}$$

The corresponding homogeneous equation is

$$m_d\ddot{z}+(k_b-\alpha_t\omega^2)z=0 \quad \textbf{(2.5)}$$

For stability [31]

$$k_b-\alpha_t\omega^2>0 \quad \textbf{(2.6a)}$$

$$\omega<\omega_{thr}=\sqrt{\frac{k_b}{\alpha_t}} \quad \textbf{(2.6b)}$$

From the above analysis, it can be seen that:

(1) The inclusion of the Morton Effect in this rotor system actually introduces a negative stiffness.

(2) There exists a thermal induced threshold of instability. This has a physical meaning, even that the above is just based on the linear mid-span rotor system model.

(3) The magnitude of threshold speed is proportional to the squared root of ratio between support stiffness k_b and the equivalent thermal coefficient α_t. It is interesting to note that it has a similar simple form as the undamped natural frequency.

(4) Small support stiffness and large equivalent thermal coefficient may lead to the occurrence of low threshold speed of the thermal induced instability.

So it seems that once the equivalent thermal coefficient α_t is known, the thermal induced instability threshold can be calculated. The calculation of the equivalent thermal coefficient will be discussed in Chapter 4.

2.3 Damped Rigid Rotor with Linear Isotropic Supports

Next, the damped rigid rotor model will be considered, which is more general (Figure 2.2). Once the damping is included, the entire behavior of the rotor for all of cases including below, at and above its critical speed can be analyzed. Because of the existence of damping, there is a phase difference between the mechanical imbalance and the response displacement. In addition, the thermal imbalance is still assumed to be in the direction from the cold spot to the hot spot as discussed in Section 2.2, which is concurrent with the direction of the displacement of the journal (line of centers). The thermal imbalance may have effects on both the magnitude and phase of the response displacement. Only the under-damped case will be discussed, which is the most typical in rotor systems.

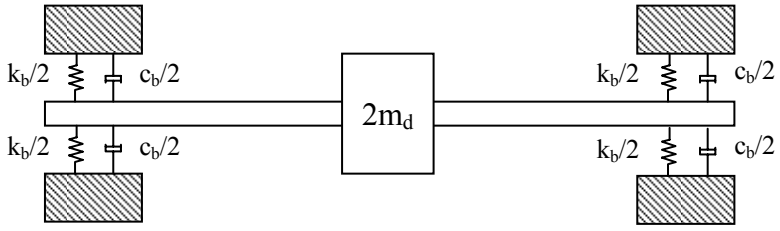

(a) Rotor and bearing model

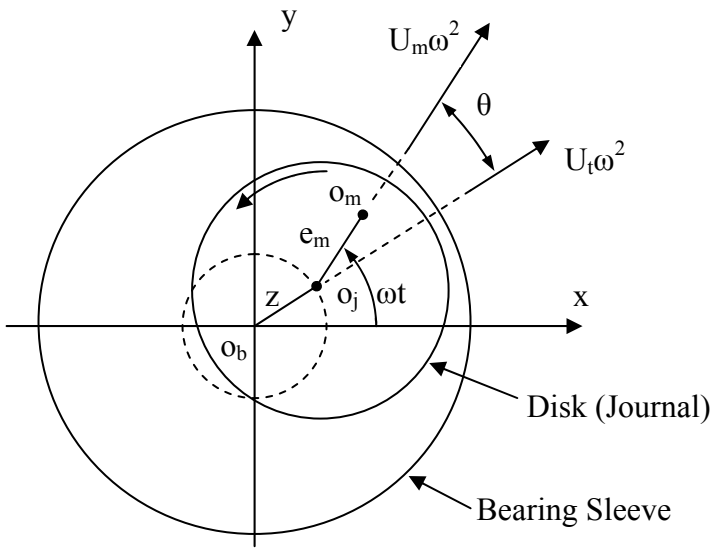

(b) Orbit

Figure 2.2 Damped rigid rotor with linear isotropic supports

The equations of motion about the journal center $O_j(x, y)$ are

$$m_d\ddot{x}+c_b\dot{x}+k_bx=U_m\omega^2\cos\omega t+U_t\omega^2\cos(\omega t-\theta)$$
$$m_d\ddot{y}+c_b\dot{y}+k_by=U_m\omega^2\sin\omega t+U_t\omega^2\sin(\omega t-\theta) \quad \textbf{(2.7a)}$$

Note

$$U_m=m_de_m$$
$$z=x+iy$$
$$x=z\cos(\omega t-\theta)$$
$$y=z\sin(\omega t-\theta)$$

Then

$$m_d\ddot{x}+c_b\dot{x}+k_bx=U_m\omega^2\cos\omega t+\alpha_tz\omega^2\cos(\omega t-\theta)$$
$$m_d\ddot{y}+c_b\dot{y}+k_by=U_m\omega^2\sin\omega t+\alpha_tz\omega^2\sin(\omega t-\theta) \quad \textbf{(2.7b)}$$

The equations of motion can then be reduced as

$$m_d\ddot{z}+c_b\dot{z}+(k_b-\alpha_t\omega^2)z=m_d e_m\omega^2 e^{i\omega t} \quad \textbf{(2.8)}$$

The stability of the system can be analyzed by calculating its homogeneous equation (Equation (2.9)). As stated before, to simplify the derivation, only the typical situation, i.e. under-damped $(0<\zeta<1)$ system, will be discussed

$$m_d\ddot{z}+c_b\dot{z}+(k_b-\alpha_t\omega^2)z=0 \quad \textbf{(2.9a)}$$

or

$$\ddot{z}+2\zeta\omega_n\dot{z}+(\omega_n^2-\frac{\alpha_t}{m_d}\omega^2)z=0 \quad \textbf{(2.9b)}$$

Assume

$$z=z_o e^{\lambda t} \quad \textbf{(2.10)}$$

The characteristic equation can be obtained

$$\lambda^2+2\zeta\omega_n\lambda+(\omega_n^2-\frac{\alpha_t}{m_d}\omega^2)=0 \quad \textbf{(2.11)}$$

The characteristic roots are

$$\lambda_{1,2}=-\zeta\omega_n\pm\sqrt{(\zeta\omega_n)^2-\left(\omega_n^2-\frac{\alpha_t}{m_d}\omega^2\right)} \quad \textbf{(2.12a)}$$

or

$$\lambda_{1,2}=-\zeta\omega_n\pm\omega_n\sqrt{\zeta^2-1+\frac{\alpha_t}{k_b}\omega^2} \quad \textbf{(2.12b)}$$

If only the under-damped system ($0<\zeta<1$) is considered, essentially there are two cases for the stability analysis where the Morton Effect is included:

Case 1: $\zeta^2-1+\frac{\alpha_t}{k_b}\omega^2<0$ or $\omega<\sqrt{(1-\zeta^2)\frac{k_b}{\alpha_t}}$

The characteristic roots will be in the form of

$$\lambda_{1,2}=-\zeta\omega_n \pm i\omega_n\sqrt{1-\zeta^2-\frac{\alpha_t}{k_b}\omega^2} \qquad \textbf{(2.13)}$$

The system is always stable. The operating speed region $0<\omega<\sqrt{(1-\zeta^2)\frac{k_b}{\alpha_t}}$ can be called "oscillatory stable region". The frequency of the oscillation is $\omega_n\sqrt{1-\zeta^2-\frac{\alpha_t}{k_b}\omega^2}$, which is less than the damped natural frequency when the thermal effect is not included

Case 2: $\zeta^2-1+\frac{\alpha_t}{k_b}\omega^2>0$ or $\omega>\sqrt{(1-\zeta^2)\frac{k_b}{\alpha_t}}$

In this case, there is a possibility that one of the characteristic roots is positive. If

$$\omega_n\sqrt{\zeta^2-1+\frac{\alpha_t}{k_b}\omega^2}>\zeta\omega_n \qquad \textbf{(2.14a)}$$

then the system will be unstable. So a threshold speed of instability can be found

$$\omega_{thr}=\sqrt{\frac{k_b}{\alpha_t}} \qquad \textbf{(2.14b)}$$

The system will be stable under this threshold. To distinguish it with the regular stable region, the stable speed region $\sqrt{(1-\zeta^2)\frac{k_b}{\alpha_t}} \le \omega < \omega_{thr} = \sqrt{\frac{k_b}{\alpha_t}}$ can be called "exponential stable region". When the operating speed goes above the threshold as shown in Equation (2.14b), the system will become unstable.

Figure 2.3 illustrates the entire operating speed regions for stability analysis.

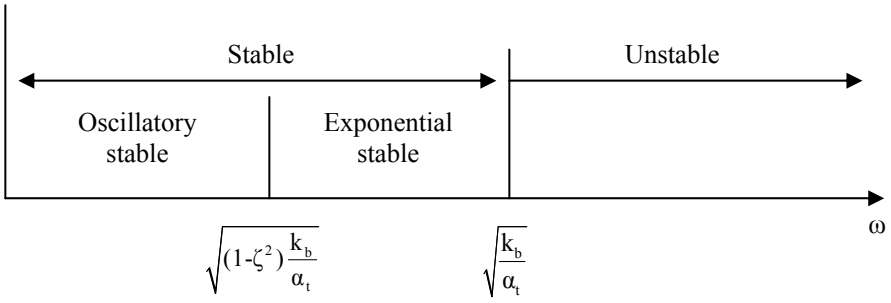

Figure 2.3 Operating speed regions with Morton Effect involved

Figure 2.4 are the transient processes of free response for the disk in a typical rotor (Table 2.1) whose threshold speed is 1581.16 rad/s (15099 RPM), operating in three different regions when the Morton Effect is involved.

Table 2.1 Parameters of illustrative damped rigid rotor

Parameter	Value	Unit
$2m_d$	200	kg
k_b	5E6	N/m
c_b	5E3	N-s/m
α_t	2	kg

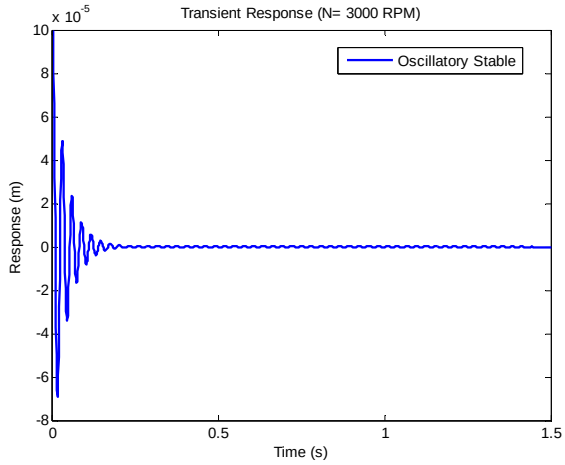

(a) Oscillatory stable (N=3000 RPM)

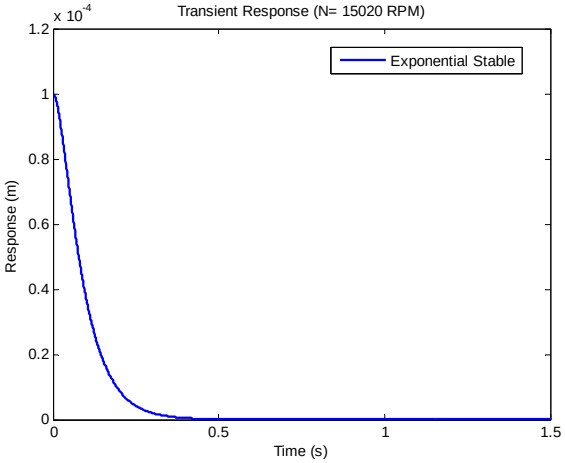

(b) Exponential stable (N=15020 RPM)

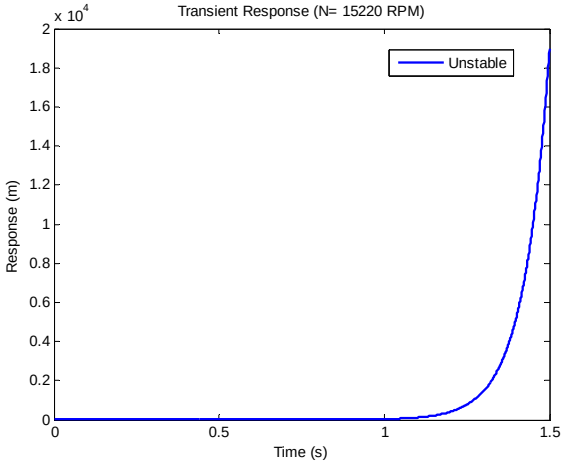

(c) Unstable (N=15220 RPM)

Figure 2.4 Three regions of transient response of disk with Morton Effect involved

Comparing the results shown by Equation (2.6b) and Equation (2.14b), it seems that the inclusion of the damping does not affect the threshold speed of instability due to the thermal effect.

To better express the influence of the thermal effect, introduce a new term, the thermal imbalance mass ratio, defined as $A_t = \frac{\alpha_t}{m_d}$. The ratio of the above threshold speed (Equation (2.14b)) over the undamped natural frequency $\omega_n = \sqrt{\frac{k_b}{m_d}}$ can be written as

$$\frac{\omega_{thr}}{\omega_n} = \frac{1}{\sqrt{A_t}} \tag{2.15}$$

Figure 2.5 shows the curve of the threshold speed ratio versus the thermal imbalance mass ratio. High values of thermal imbalance mass ratios result in low threshold speeds of instability.

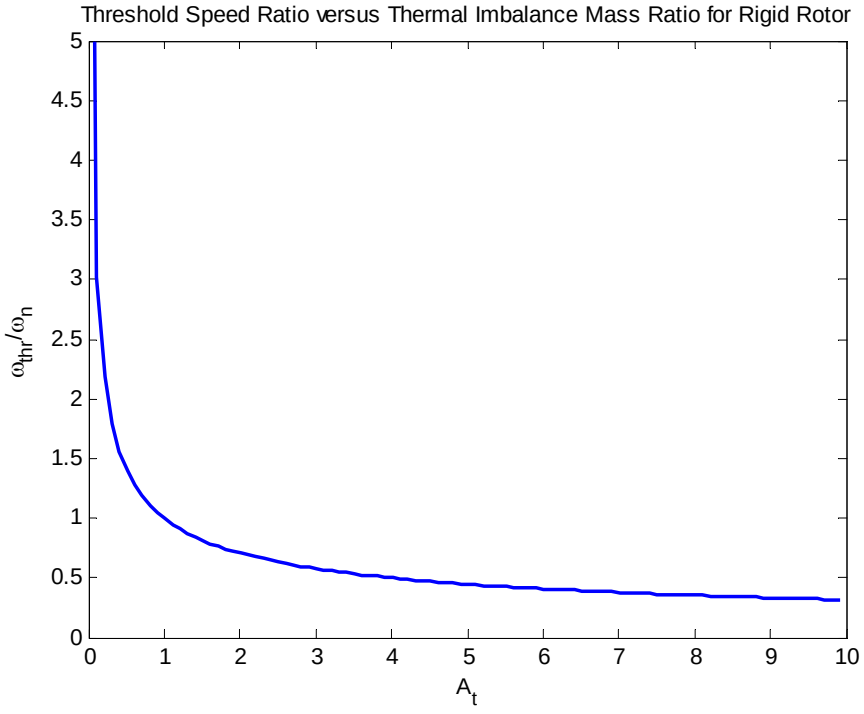

Figure 2.5 Threshold speed ratio versus thermal imbalance mass ratio for rigid rotor

2.4 Extended Jeffcott Rotor with Linear Isotropic Supports

In this section, an elastic rotor with linear isotropic supports, commonly called extended Jeffcott rotor, will be discussed. This system is more realistic and typical in the analysis of rotor dynamics. Figure 2.6 shows the system model and the orbits of the disk and the journal at the bearing position. Some assumptions have been made for this model:

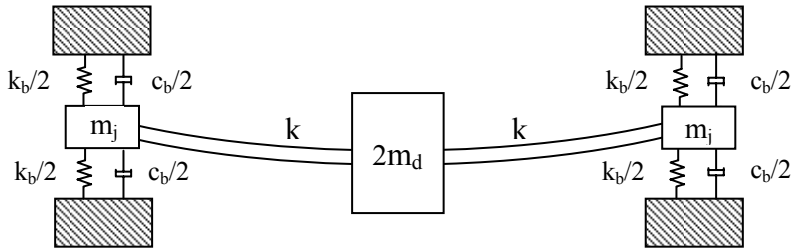

(a) Rotor and bearing model

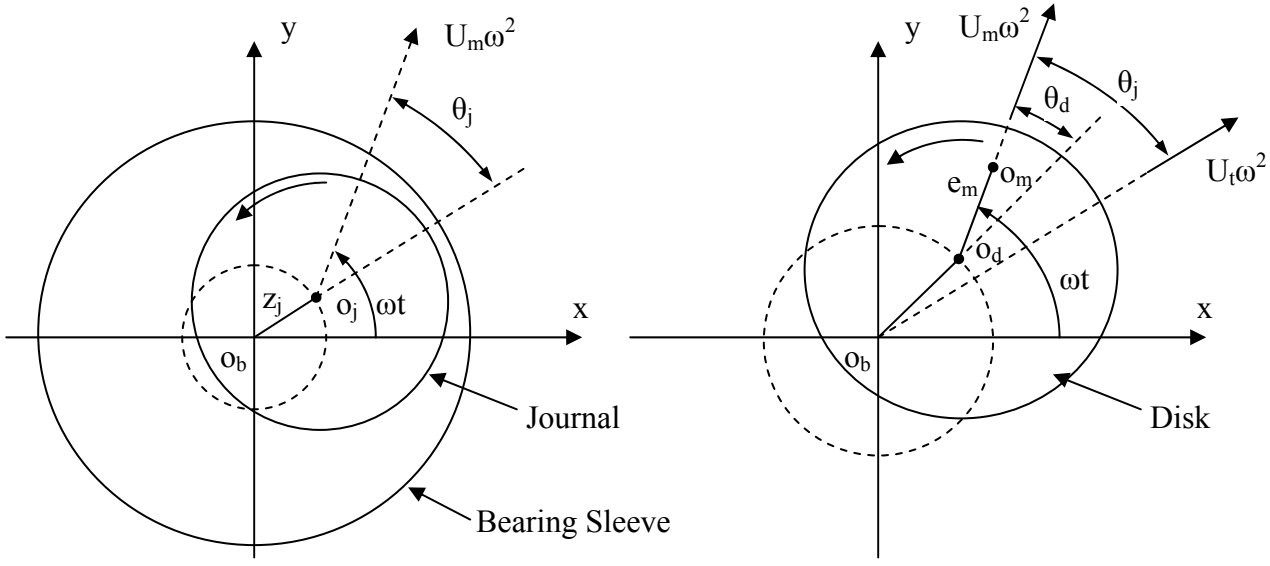

(b) Orbits of journal and disk

Figure 2.6 Extended Jeffcott rotor with linear isotropic supports

(1) The thermal imbalance is still assumed to be in the direction from the cold spot to the hot spot, which coincides with the direction of the displacement of the journal.

(2) The damping of the bearing is still assumed to be small.

The equations of motion are

$$\begin{aligned} &m_d\ddot{x}_d+k(x_d-x_j)=U_m\omega^2\cos\omega t+U_t\omega^2\cos(\omega t-\theta_j)\\ &m_d\ddot{y}_d+k(y_d-y_j)=U_m\omega^2\sin\omega t+U_t\omega^2\sin(\omega t-\theta_j)\\ &m_j\ddot{x}_j+c_b\dot{x}_j+k_bx_j-k(x_d-x_j)=0\\ &m_j\ddot{y}_j+c_b\dot{y}_j+k_by_j-k(y_d-y_j)=0 \end{aligned} \qquad \textbf{(2.16)}$$

Note

$$U_t=\alpha_t z_j$$

$$U_m=m_d e_m$$

$$z_d=x_d+iy_d$$

$$z_j=x_j+iy_j$$

$$x_j=z_j\cos(\omega t-\theta_j)$$

$$y_j=z_j\sin(\omega t-\theta_j)$$

The equations of motion in complex notation are

$$\begin{aligned} &m_d\ddot{z}_d+kz_d-(k+\alpha_t\omega^2)z_j=m_de_m\omega^2e^{i\omega t}\\ &m_j\ddot{z}_j+c_b\dot{z}_j-kz_d+(k+k_b)z_j=0 \end{aligned} \qquad \textbf{(2.17)}$$

The homogeneous equations of the system are

$$\begin{aligned} &m_d\ddot{z}_d+kz_d-(k+\alpha_t\omega^2)z_j=0\\ &m_j\ddot{z}_j+c_b\dot{z}_j-kz_d+(k+k_b)z_j=0 \end{aligned} \qquad \textbf{(2.18)}$$

Assume

$$\begin{aligned} &z_d=\bar{z}_{do}e^{\lambda t}\\ &z_j=\bar{z}_{jo}e^{\lambda t} \end{aligned} \qquad \textbf{(2.19)}$$

Substitute above into Equation (2-18)

$$\begin{bmatrix} m_d\lambda^2+k & -(k+\alpha_t\omega^2) \\ -k & m_j\lambda^2+c_b\lambda+k+k_b \end{bmatrix}\begin{bmatrix} \bar{z}_{do} \\ \bar{z}_{jo} \end{bmatrix}=0 \tag{2.20}$$

The characteristic equation is

$$m_d m_j\lambda^4+m_d c_b\lambda^3+(m_d k+m_d k_b+m_j k)\lambda^2+kc_b\lambda+kk_b-k\alpha_t\omega^2=0 \tag{2.21}$$

For the stability analysis, Routh's stability rules can be applied. There are two possibilities:

Case 1: $kk_b-k\alpha_t\omega^2<0$

Since the coefficients of $\lambda^4, \lambda^3, \lambda^2, \lambda$ are predominately assumed to be positive, the system would be unstable if the constant term is negative, $kk_b-k\alpha_t\omega^2<0$

So, the system would be unstable for

$$\omega>\omega_{thr}=\sqrt{\frac{k_b}{\alpha_t}} \tag{2.22}$$

It is interesting to note that this threshold speed has the same form as in the rigid rotor system and specifically, the support stiffness and the equivalent thermal coefficient determine the stability threshold.

Case 2: $kk_b-k\alpha_t\omega^2>0$

If all coefficients are positive, there is still a possibility that instability occurs. For a fourth-order polynomial equation:

$$a_0\lambda^4+a_1\lambda^3+a_2\lambda^2+a_3\lambda+a_4=0 \tag{2.23}$$

where

$$a_0=m_d m_j$$
$$a_1=m_d c_b$$
$$a_2=m_d k+m_d k_b+m_j k$$
$$a_3=kc_b$$
$$a_4=kk_b-k\alpha_t\omega^2$$

Using the following array

$$\begin{array}{llll} \lambda^4 & a_0 & a_2 & a_4 \\ \lambda^3 & a_1 & a_3 & 0 \\ \lambda^2 & \dfrac{a_1a_2-a_0a_3}{a_1} & a_4 & 0 \\ \lambda^1 & \dfrac{(a_1a_2-a_0a_3)a_3-a_1^2a_4}{a_1a_2-a_0a_3} & 0 & 0 \\ \lambda^0 & a_4 & 0 & 0 \end{array} \qquad \textbf{(2.24)}$$

The stability of system can be determined by looking at the signs of the first column after λ's

$$a_0=m_d m_j>0$$
$$a_1=m_d c_b>0$$
$$\frac{a_1a_2-a_0a_3}{a_1}=\frac{m_d c_b(m_d k+m_d k_b+m_j k)-m_d m_j kc_b}{m_d c_b}=\frac{m_d c_b(m_d k+m_d k_b)}{m_d c_b}>0$$
$$a_4=kk_b-k\alpha_t\omega^4>0 \quad \text{(as assumed)}$$

Hence, the stability will be determined by the sign of $\dfrac{(a_1a_2-a_0a_3)a_3-a_1^2a_4}{a_1a_2-a_0a_3}$. It has been proved that the denominator is positive. So just look at the numerator

$$(a_1a_2-a_0a_3)a_3-a_1^2a_4=m_d c_b(m_d k+m_d k_b)kc_b-m_d^2c_b^2(kk_b-k\alpha_t\omega^2)=m_d^2c_b^2k(k+\alpha_t\omega^2)>0$$

So the system will be always stable if $kk_b-k\alpha_t\omega^2>0$

In conclusion, the stability threshold for the elastic rotor system will be

$$\omega_{thr} = \sqrt{\frac{k_b}{\alpha_t}} \tag{2.25}$$

It seems that the instability threshold is determined by the support stiffness and the equivalent thermal coefficient for both the rigid and elastic rotor systems, under the given assumptions. However, the ratio of the threshold speed over the undamped natural frequency of the rotor with rigid supports $\omega_n = \sqrt{\frac{k}{m_d}}$ is

$$\frac{\omega_{thr}}{\omega_n} = \sqrt{\left(\frac{k_b}{k}\right)\frac{1}{A_t}} \tag{2.26}$$

Figure 2.7 shows the curves of the threshold speed ratios versus the thermal imbalance mass ratios for the extended Jeffcott rotor.

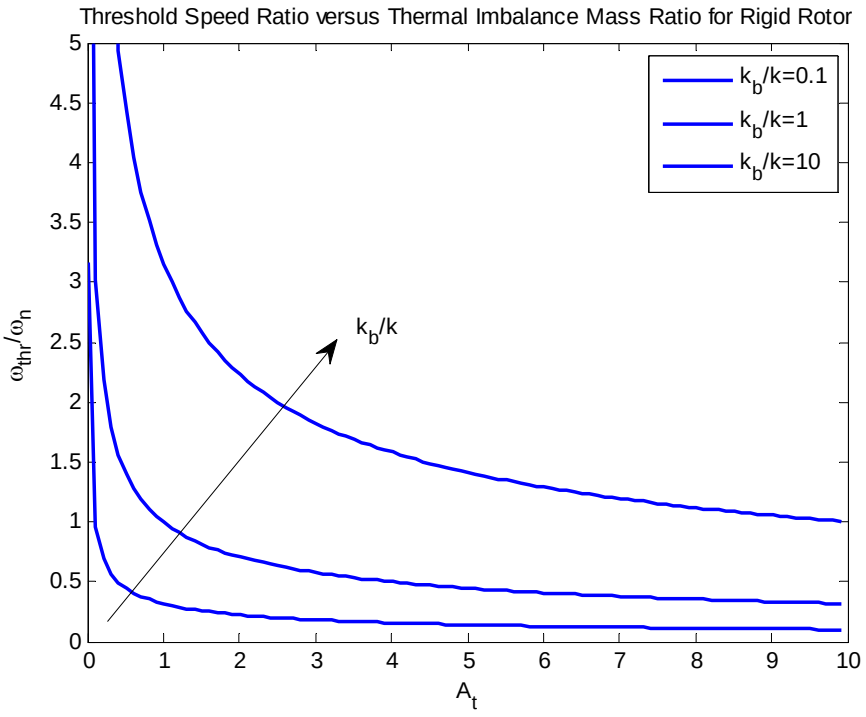

Figure 2.7 Threshold speed ratio versus thermal imbalance mass ratio for Jeffcott rotor

From above analysis, it can be seen that:

(1) It seems that the instability threshold is determined by the support stiffness and the equivalent thermal coefficient for both rigid and elastic rotor systems

(2) The damping seems to have no direct influence on the thermal induced instability threshold for this specific model and corresponding assumptions.

An illustrative calculation has been conducted using the MATHWORKS MATLAB-SIMULINK. Consider an extended Jeffcott rotor system whose parameters are assumed and shown in Table 2.2.

Table 2.2 Parameters of illustrative extended Jeffcott rotor

Parameter	Value	Unit
$2m_d$	100	kg
m_j	10	kg
$2k$	12E6	N/m
k_b	5E6	N/m
c_b	5E3	N-s/m
$2U_m$	0.4	kg-m
A_t	0.1	

Figure 2.8 shows the transient process of unbalanced response for the first 2 seconds below and above this threshold speed, for the system without Morton Effect included. Figure 2.9 is the corresponding transient process for the system with Morton Effect included. The non-Morton Effect rotors are always stable during the entire operating speed range. However, the Morton

Effect involved rotors have a threshold of instability. According to Equation (2.25), this instability threshold is at 1000 rad/s (9549 RPM). The simulation results have proved the existence and the values of this threshold of instability. Figure 2.10 shows the SIMULINK model which is used to simulate both of the two systems.

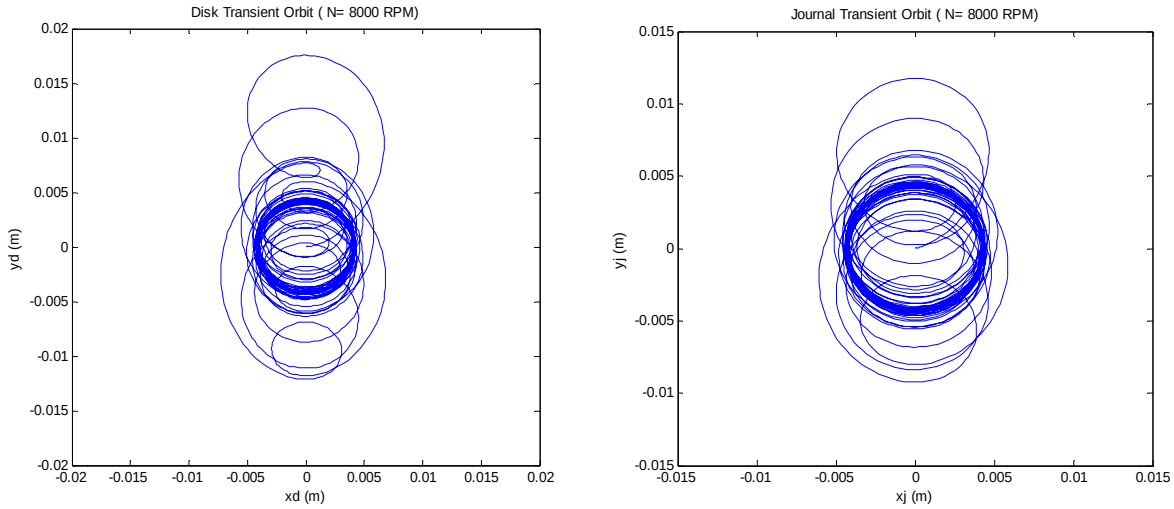

(a) Below threshold of instability (N=8000 RPM)

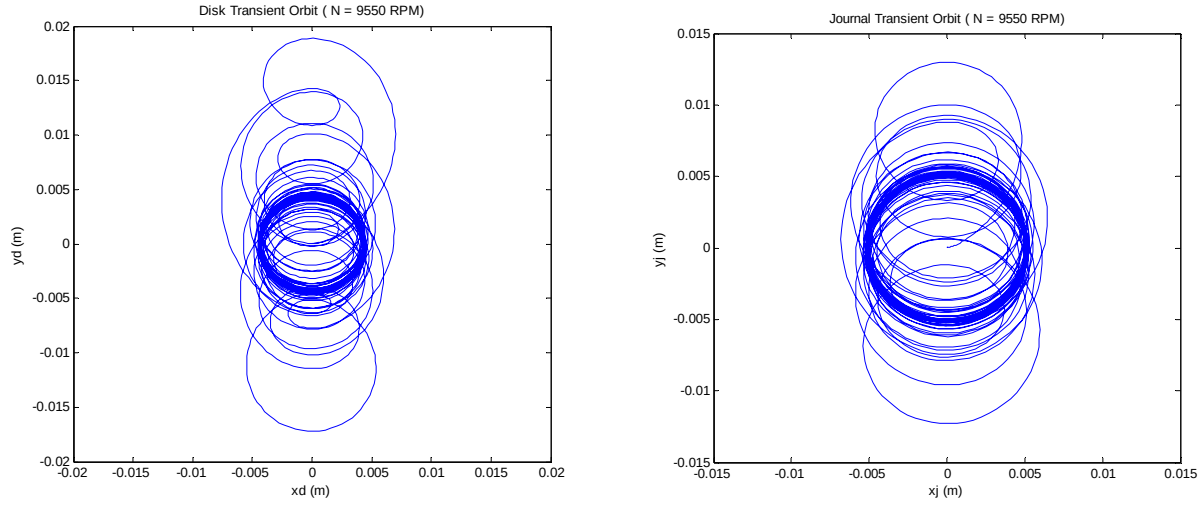

(b) Above threshold of instability (N=9550 RPM)

Figure 2.8 Transient process of unbalanced response for extended Jeffcott rotor system without Morton Effect included

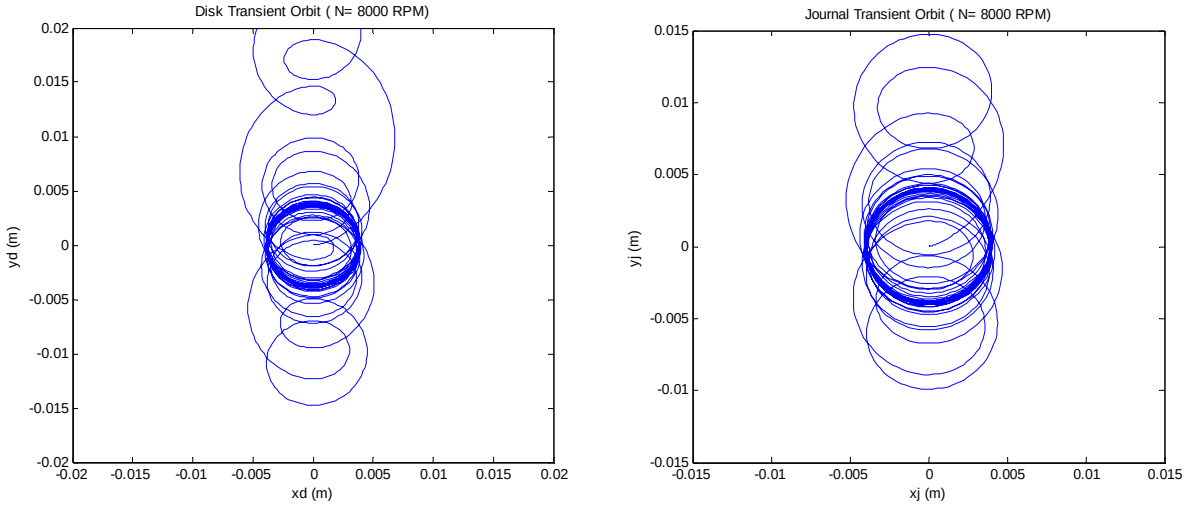

(a) Below threshold of instability (N=8000 RPM)

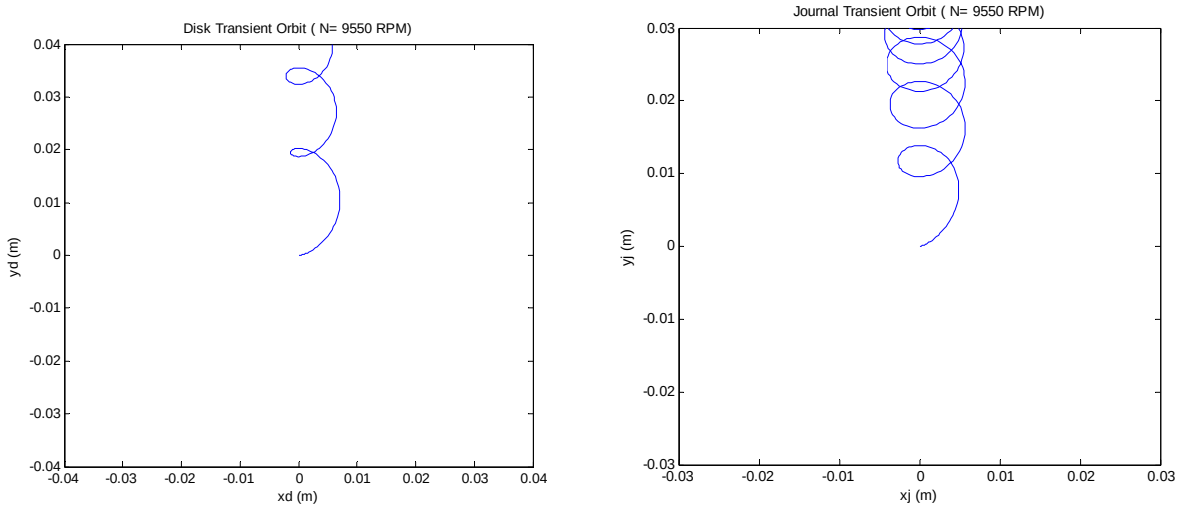

(b) Above threshold of instability (N=9550 RPM)

Figure 2.9 Transient process of unbalanced response for extended Jeffcott rotor system with Morton Effect included

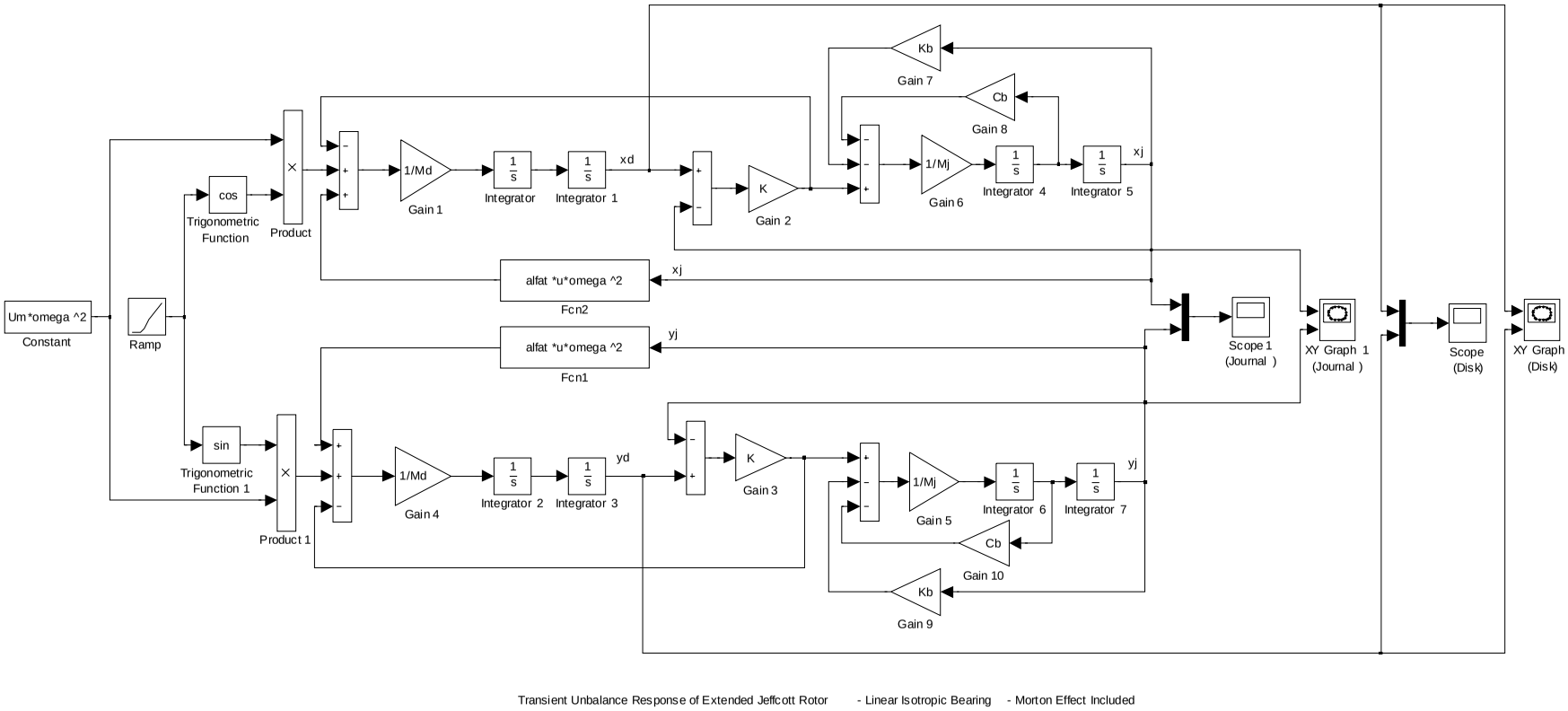

Figure 2.10 SIMULINK model to simulate extended Jeffcott rotor with/without Morton Effect included

2.5 Extended Study on Cases with Thermal Imbalance Misaligned with Displacement

In the previous sections, the rotor models where the thermal imbalance is assumed to coincide with the response displacement direction have been analyzed. Considering that in the various practical rotor systems, especially those supported by the hydrodynamic fluid film bearings, the thermal imbalance may not always in the direction of response displacement, hence it is inspired to discuss the cases where the thermal imbalance misaligns with the displacement direction.

Based on the discussions in the previous analysis and also for the simplicity, the following discussion on the cases where the thermal imbalance no longer aligns with the direction of displacement will be focused on the damped rigid rotor with linear isotropic supports.

2.5.1 Thermal Imbalance Perpendicular to Displacement

First, the special case where the thermal imbalance U_t is in perpendicular direction to that of response displacement (line of centers) will be discussed.

The rotor and bearing model to be used here is as same as shown in Figure 2.2(a). Figure 2.11 displays only the orbit of the journal with both mechanical and thermal imbalances for the model to be discussed.

In the discussion, the magnitude of the thermal imbalance is still assumed to be in the form of Equation (2.2).

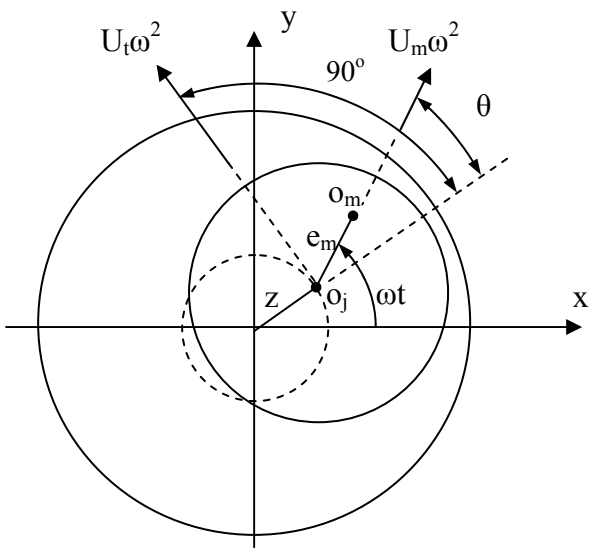

Figure 2.11 Damped rigid rotor with U_t perpendicular to line of centers

The equations of motion are

$$m_d\ddot{x}+c_b\dot{x}+k_bx=U_m\omega^2\cos\omega t+U_t\omega^2\cos(\omega t-\theta+\pi/2)$$
$$m_b\ddot{y}+c_b\dot{y}+k_by=U_m\omega^2\sin\omega t+U_t\omega^2\sin(\omega t-\theta+\pi/2) \quad \textbf{(2.27)}$$

Note

$$U_m=m_de_m$$
$$z=x+iy$$
$$x=z\cos(\omega t-\theta)$$
$$y=z\sin(\omega t-\theta)$$

Use Equation (2.2) for the magnitude of the thermal imbalance and rewrite equation (2.27)

$$m_d\ddot{x}+c_b\dot{x}+k_bx=m_de_m\omega^2\cos\omega t-\alpha_t\omega^2z\sin(\omega t-\theta)$$
$$m_d\ddot{y}+c_b\dot{y}+k_by=m_de_m\omega^2\sin\omega t+\alpha_t\omega^2z\cos(\omega t-\theta) \quad \textbf{(2.28a)}$$

or

$$m_d\ddot{x}+c_b\dot{x}+k_b x+\alpha_t\omega^2 y=m_d e_m\omega^3\cos\omega t$$
$$m_d\ddot{y}+c_b\dot{y}+k_b y-\alpha_t\omega^2 x=m_d e_m\omega^3\sin\omega t \quad \textbf{(2.28b)}$$

Focus on the homogeneous equation for the stability analysis

$$m_d\ddot{x}+c_b\dot{x}+k_b x+\alpha_t\omega^2 y=0$$
$$m_d\ddot{y}+c_b\dot{y}+k_b y-\alpha_t\omega^2 x=0 \quad \textbf{(2.29)}$$

Assume

$$x=\bar{x}_o e^{\lambda t}$$
$$y=\bar{y}_o e^{\lambda t} \quad \textbf{(2.30)}$$

Substitute above into Equation (2.29)

$$\begin{bmatrix} m_d\lambda^2+c_b\lambda+k_b & \alpha_t\omega^2 \\ -\alpha_t\omega^2 & m_d\lambda^2+c_b\lambda+k_b \end{bmatrix}\begin{bmatrix} \bar{x}_o \\ \bar{y}_o \end{bmatrix}=0 \quad \textbf{(2.31)}$$

The characteristic equation is

$$m_d^2\lambda^4+2m_d c_b\lambda^3+(2m_d k_b+c_b^2)\lambda^2+2k_b c_b\lambda+k_b^2+\alpha_t^2\omega^4=0 \quad \textbf{(2.32a)}$$

Rewrite above as

$$a_0\lambda^4+a_1\lambda^3+a_2\lambda^2+a_3\lambda+a_4=0 \quad \textbf{(2.32b)}$$

where

$$a_0=m_d^2$$
$$a_1=2m_d c_b$$
$$a_2=2m_d k_b+c_b^2$$
$$a_3=2k_b c_b$$
$$a_4=k_b^2+\alpha_t^2\omega^4$$

Now, Routh stability rules can be applied. It is obvious that all above coefficients are positive. For stability analysis, only one case is concerned. Using the following array

$$\begin{array}{cccc} \lambda^4 & a_0 & a_2 & a_4 \\ \lambda^3 & a_1 & a_3 & 0 \\ \lambda^2 & \dfrac{a_1a_2-a_0a_3}{a_1} & a_4 & 0 \\ \lambda^1 & \dfrac{(a_1a_2-a_0a_3)a_3-a_1^2a_4}{a_1a_2-a_0a_3} & 0 & 0 \\ \lambda^0 & a_4 & 0 & 0 \end{array} \qquad \textbf{(2.33)}$$

Look at the signs of the first three terms and the last one in the first column after λ's

$$a_0=m_d^2>0$$
$$a_1=2m_dc_b>0$$
$$\frac{a_1a_2-a_0a_3}{a_1}=\frac{2m_dc_b(2m_dk_b+c_b^2)-m_d^2(2k_bc_b)}{2m_dc_b}=\frac{2m_dc_b(m_dk_b+c_b^2)}{2m_dc_b}>0$$
$$a_4=k_b^2+\alpha_t^2\omega^4>0$$

Hence, the stability will be determined by the sign of $\dfrac{(a_1a_2-a_0a_3)a_3-a_1^2a_4}{a_1a_2-a_0a_3}$. Because its denominator has been proved to be positive, just look at the numerator

$$(a_1a_2-a_0a_3)a_3-a_1^2a_4=2m_dc_b(m_dk_b+c_b^2)(2k_bc_b)-(2m_dc_b)^2(k_b^2+\alpha_t^2\omega^4)=4m_dc_b^2(k_bc_b^2-m_d\alpha_t^2\omega^4)$$

It is obvious that the system will be stable if

$$k_bc_b^2-m_d\alpha_t^2\omega^4>0 \qquad \textbf{(2.34a)}$$

Now, the threshold for stability can be found

$$\omega<\omega_{thr}=\sqrt{\frac{c_b\omega_n}{\alpha_t}} \qquad \textbf{(2.34b)}$$

The ratio of the threshold speed defined in Equation (2.34b) over the undamped natural frequency $\omega_n = \sqrt{\frac{k_b}{m_d}}$ can be written as

$$\frac{\omega_{thr}}{\omega_n} = \sqrt{\frac{2\zeta}{A_t}} \tag{2.35}$$

From Equation (2.34), it can be seen that:

(1) The threshold speed of instability for the current model has a different form than in the case where the thermal imbalance aligns with the line of centers. The support damping will play a role in determining the threshold of instability when the thermal imbalance does not align with the center line. Comparably, in the rotor model where the thermal imbalance is in the response displacement direction (line of centers), the support stiffness exclusively determines the threshold speed, with the equivalent thermal coefficient.

(2) The occurrence of the Morton Effect induced instability in this kind of rotor configurations seems to be a result of that it actually introduces a cross-coupled stiffness in the equations of motion, which might be negative to result in an unstable operation of the system.

(3) It seems that the system in this configuration would be unstable if no damping exists. Damping plays an important role in maintaining the stability of this kind of rotor systems.

2.5.2 Thermal Imbalance with Arbitrary Phase Difference from Displacement

In order to acquire a perspective picture on the influence of both the magnitude and the direction of the thermal imbalance, it is necessary to discuss the case where the thermal imbalance has an arbitrary phase difference from the response displacement.

Still use the rotor-bearing model as shown in Figure 2.2(a). Assume that the phase difference of the thermal imbalance from the direction of response displacement is ψ (Figure 2.12). The magnitude of the thermal imbalance still takes the form of Equation (2.2).

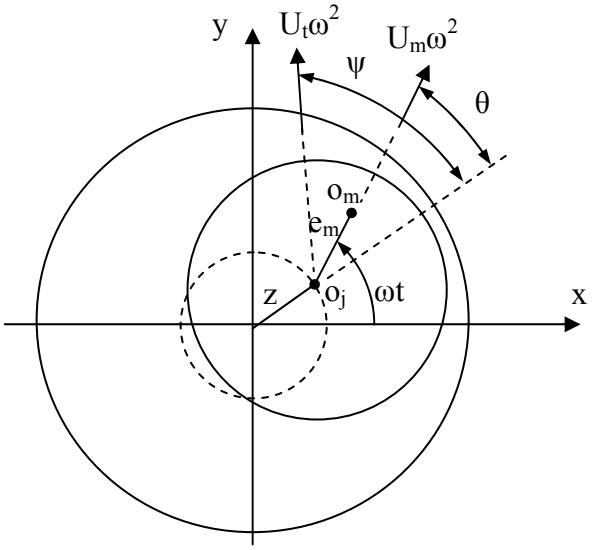

Figure 2.12 Rigid rotor where U_t has arbitrary phase difference from line of centers

By splitting the thermal imbalance into two components: one aligns with line of centers and the other is perpendicular, the equations of motion can be written as

$$\begin{aligned} m_d\ddot{x}+c_b\dot{x}+k_b x &= U_m\omega^2\cos\omega t+(U_t\omega^2\cos\psi)\cos(\omega t-\theta)+(U_t\omega^2\sin\psi)\cos(\omega t-\theta+\pi/2) \\ m_d\ddot{y}+c_b\dot{y}+k_b y &= U_m\omega^2\sin\omega t+(U_t\omega^2\cos\psi)\sin(\omega t-\theta)+(U_t\omega^2\sin\psi)\sin(\omega t-\theta+\pi/2) \end{aligned} \quad \textbf{(2.36)}$$

Note

$$U_m=m_d e_m$$
$$z=x+iy$$
$$x=z\cos(\omega t-\theta)$$
$$y=z\sin(\omega t-\theta)$$

and substitute in Equation (2.2) for the magnitude of the thermal imbalance

Then

$$\begin{aligned} m_d\ddot{x}+c_b\dot{x}+k_b x &= m_d e_m\omega^2\cos\omega t+(\alpha_t\omega^2\cos\psi)z\cos(\omega t-\theta)-(\alpha_t\omega^2\sin\psi)z\sin(\omega t-\theta) \\ m_d\ddot{y}+c_b\dot{y}+k_b y &= m_d e_m\omega^2\sin\omega t+(\alpha_t\omega^2\cos\psi)z\sin(\omega t-\theta)+(\alpha_t\omega^2\sin\psi)z\cos(\omega t-\theta) \end{aligned} \quad \textbf{(2.37a)}$$

Or

$$\begin{aligned} m_d\ddot{x}+c_b\dot{x}+(k_b-\alpha_t\omega^2\cos\psi)x+(\alpha_t\omega^2\sin\psi)y &= m_d e_m\omega^2\cos\omega t \\ m_d\ddot{y}+c_b\dot{y}-(\alpha_t\omega^2\sin\psi)x+(k_b-\alpha_t\omega^2\cos\psi)y &= m_d e_m\omega^2\sin\omega t \end{aligned} \quad \textbf{(2.37b)}$$

For the stability analysis, the homogeneous equation is

$$\begin{aligned} m_d\ddot{x}+c_b\dot{x}+(k_b-\alpha_t\omega^2\cos\psi)x+(\alpha_t\omega^2\sin\psi)y &= 0 \\ m_d\ddot{y}+c_b\dot{y}-(\alpha_t\omega^2\sin\psi)x+(k_b-\alpha_t\omega^2\cos\psi)y &= 0 \end{aligned} \quad \textbf{(2.38)}$$

Assume

$$\begin{aligned} x &= \bar{x}_o e^{\lambda t} \\ y &= \bar{y}_o e^{\lambda t} \end{aligned} \quad \textbf{(2.39)}$$

Substitute above into Equation (2.38)

$$\begin{bmatrix} m_d\lambda^2+c_b\lambda+(k_b-\alpha_t\omega^2\cos\psi) & \alpha_t\omega^2\sin\psi \\ -\alpha_t\omega^2\sin\psi & m_d\lambda^2+c_b\lambda+(k_b-\alpha_t\omega^2\cos\psi) \end{bmatrix}\begin{bmatrix} \bar{x}_o \\ \bar{y}_o \end{bmatrix}=0 \quad \textbf{(2.40)}$$

The characteristic equation is

$$[m_d\lambda^2+c_b\lambda+(k_b-\alpha_t\omega^2\cos\psi)]^2+(\alpha_t\omega^2\sin\psi)^2=0 \quad \textbf{(2.41)}$$

Rewrite above in the standard form

$$a_0\lambda^4+a_1\lambda^3+a_2\lambda^2+a_3\lambda+a_4=0 \quad \textbf{(2.42)}$$

where

$$a_0=m_d^2$$
$$a_1=2m_dc_b$$
$$a_2=c_b^2+2m_d(k_b-\alpha_t\omega^2\cos\psi)$$
$$a_3=2c_b(k_b-\alpha_t\omega^2\cos\psi)$$
$$a_4=(k_b-\alpha_t\omega^2\cos\psi)^2+(\alpha_t\omega^2\sin\psi)^2$$

If applying Routh's stability rules, two possibilities must be considered:

Case 1: Not all coefficients are positive

Since the coefficients a_0, a_1, a_4 are positive, the system would be unstable if $a_2<0$ or $a_3<0$. For the stability, it requires

$$c_b^2+2m_d(k_b-\alpha_t\omega^2\cos\psi)>0 \qquad \textbf{(2.43a)}$$

or

$$\omega^2<\frac{c_b^2}{2m_d\alpha_t\cos\psi}+\frac{k_b}{\alpha_t\cos\psi} \qquad \textbf{(2.43b)}$$

and

$$2c_b(k_b-\alpha_t\omega^2\cos\psi)>0 \qquad \textbf{(2.44a)}$$

or

$$\omega^2<\frac{k_b}{\alpha_t\cos\psi} \qquad \textbf{(2.44b)}$$

Comparing above two conditions, it is evident that the instability threshold will be

$$\omega_{thr1}=\sqrt{\frac{k_b}{\alpha_t\cos\psi}} \qquad \textbf{(2.45)}$$

This is called the first threshold speed of instability. If the angle $\psi=0^o$, the result coincides with the conclusions of the case where the thermal imbalance aligns with the line of centers as discussed in Section 2.2. As for the case where the thermal imbalance is perpendicular to center line, $\omega_{thr1} \to \infty$. The threshold of instability under this condition will be determined by another one which is to be discussed in Case 2.

Case 2: All coefficients are positive

If all coefficients are positive, there is still a possibility that instability occurs. Use the standard fourth-order characteristic as shown in Equation (2.32) and the corresponding coefficients arrays shown in Equation (2.33).

Since all coefficients are assumed to be positive, just need to look at the signs of the third and fourth terms in the first column after $\lambda's$ in Equation (2.33).

$$\frac{a_1a_2-a_0a_3}{a_1}=\frac{2m_dc_b[c_b^2+2m_d(k_b-\alpha_t\omega^2\cos\psi)]-m_d^2[2c_b(k_b-\alpha_t\omega^2\cos\psi)]}{2m_dc_b}$$
$$=\frac{m_dc_b^3+m_dc_b[c_b^2+2m_d(k_b-\alpha_t\omega^2\cos\psi)]}{2m_dc_b}=\frac{m_dc_b^3+m_dc_ba_2}{2m_dc_b}>0$$

So, actually the fourth term in Equation (2.33) determines the stability threshold. As indicated before, only the numerator is concerned with this discussion

$$(a_1a_2-a_0a_3)a_3-a_1^2a_4=[2m_dc_b^3+2m_d^2c_b(k_b-\alpha_t\omega^2\cos\psi)]2c_b(k_b-\alpha_t\omega^2\cos\psi)$$
$$-(2m_dc_b)^2[(k_b-\alpha_t\omega^2\cos\psi)^2+(\alpha_t\omega^2\sin\psi)^2]$$
$$=4m_dc_b^2(k_bc_b^2-c_b^2\alpha_t\cos\psi\omega^2-m_d\alpha_t^2\sin^2\psi\omega^4)$$

The system would be unstable, if

$$(a_1a_2-a_0a_3)a_3-a_1^2a_4=4m_dc_b^2(k_bc_b^2-c_b^2\alpha_t\cos\psi\omega^2-m_d\alpha_t^2\sin^2\psi\omega^4)<0 \qquad \textbf{(2.46a)}$$

or

$$m_d\alpha_t^2\sin^2\psi\omega^4+c_b^2\alpha_t\cos\psi\omega^2-k_bc_b^2>0 \quad \textbf{(2.46b)}$$

If $\psi=0^o$, then the system will be unstable when

$$\omega>\sqrt{\frac{k_b}{\alpha_t}} \quad \textbf{(2.46c)}$$

This agrees with Equations (2.6b) and (2.14b).

If $\psi\neq0$, the system will be unstable when

$$\omega^2<-\sqrt{\left(\frac{c_b^2\cos\psi}{2m_d\alpha_t\sin^2\psi}\right)^2+\left(\frac{c_b\omega_n}{\alpha_t\sin\psi}\right)^2}-\frac{c_b^2\cos\psi}{2m_d\alpha_t\sin^2\psi} \quad \textbf{(2.46d)}$$

or

$$\omega^2>\sqrt{\left(\frac{c_b^2\cos\psi}{2m_d\alpha_t\sin^2\psi}\right)^2+\left(\frac{c_b\omega_n}{\alpha_t\sin\psi}\right)^2}-\frac{c_b^2\cos\psi}{2m_d\alpha_t\sin^2\psi} \quad \textbf{(2.46e)}$$

By dropping out the trivial solution, the system instability threshold can be obtained

$$\omega_{thr2}=\sqrt{\frac{c_b\omega_n}{\alpha_t}\left\{\sqrt{\left(\frac{c_b\cos\psi}{2m_d\omega_n\sin^2\psi}\right)^2+\frac{1}{\sin^2\psi}}-\frac{c_b\cos\psi}{2m_d\omega_n\sin^2\psi}\right\}} \quad \textbf{(2.47)}$$

To distinguish this new threshold with the one defined in Equation (2.45), it is denoted as the second threshold speed of instability. Comparing to previous discussion, if the angle $\psi= \pm90^o$, the Equation (2.47) agrees with the conclusions shown in Equation (2.34b) for the case where the thermal imbalance is perpendicular to the line of centers as discussed in Section 2.5.1.

The threshold speed ratios corresponding to Equations (2.45) and (2.47) can be expressed as

$$\frac{\omega_{thr1}}{\omega_n} = \frac{1}{\sqrt{A_t \cos\psi}} \tag{2.48a}$$

$$\frac{\omega_{thr2}}{\omega_n} = \sqrt{\frac{2\zeta}{A_t}\left\{\sqrt{\frac{\zeta^2\cos^2\psi}{\sin^4\psi} + \frac{1}{\sin^2\psi}} - \frac{\zeta\cos\psi}{\sin^2\psi}\right\}} \tag{2.48b}$$

Figure 2.13 shows a schematic diagram of the stability map of the damped rigid rotor system in polar coordinates for A_t=0.1 and ζ=0.2, based on the above discussion. The polar magnitude represents the ratios of operating speed over the undamped natural frequency and the polar angle is the phase difference of the thermal imbalance measured from the direction of displacement.

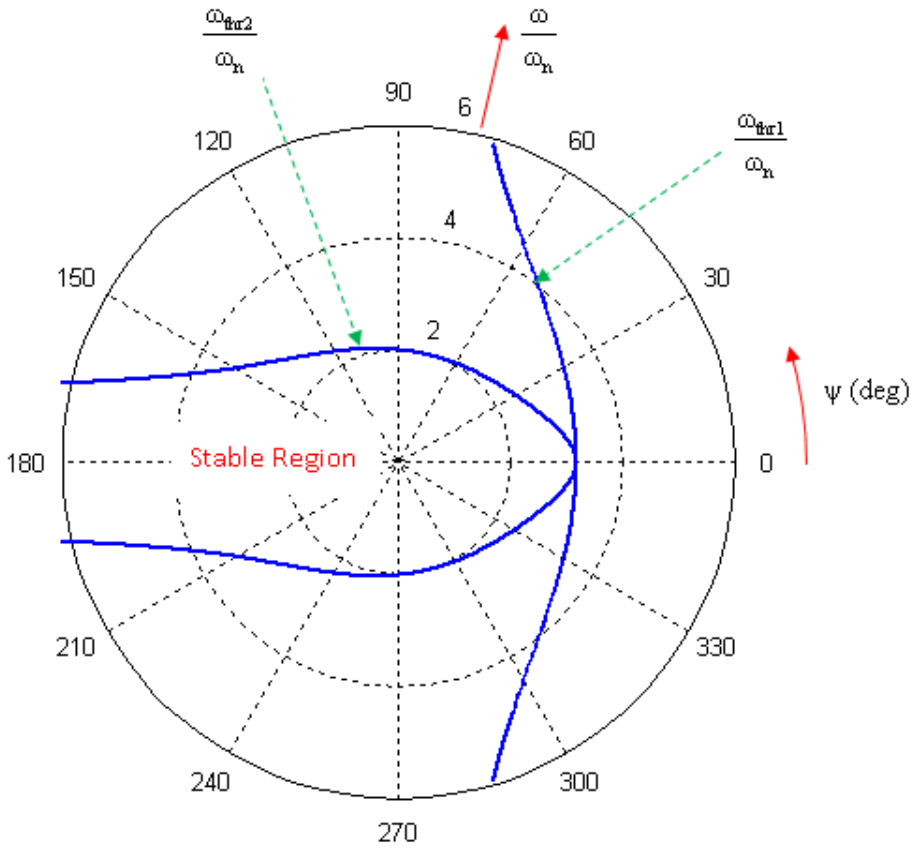

Figure 2.13 Stability map of damped rigid rotor system (A_t=0.1 and ζ=0.2)

This figure actually shows the influence of the orientation of the thermal imbalance on the stability of the rotor system. Obviously, the speed limits for stable operations of the system will be bounded by the above two threshold speeds. There is a narrow safe region around $\psi=180^{o}$, which is indicated by both of the expression and the curves of the ω_{thr2}.

2.6 Root Tack

One of the possible interesting questions after the threshold speeds of instability are studied is the influence on the corresponding frequencies under the Morton Effect. Still consider the damped rigid system as discussed in Section 2.5 and rewrite Equation (2.42) in dimensionless form

$$A_0\Lambda^4+A_1\Lambda^3+A_2\Lambda^2+A_3\Lambda+A_4=0 \qquad \textbf{(2.49)}$$

where

$$A_0=\frac{a_0\omega_n^4}{k_b^2}=1$$

$$A_1=\frac{a_1\omega_n^3}{k_b^2}=4\zeta$$

$$A_2=\frac{a_2\omega_n^2}{k_b^2}=4\zeta^2+2(1-A_t\Omega^2\cos\psi)$$

$$A_3=\frac{a_3\omega_n}{k_b^2}=4\zeta(1-A_t\Omega^2\cos\psi)$$

$$A_4=\frac{a_4}{k_b^2}=(1-A_t\Omega^2\cos\psi)^2+(A_t\Omega^2\sin\psi)^2$$

$$\Lambda=\frac{\lambda}{\omega_n};\qquad \omega_n=\sqrt{\frac{k_b}{m_d}};\qquad \zeta=\frac{c_b}{2\sqrt{k_b m_d}};\qquad \Omega=\frac{\omega}{\omega_n};\qquad A_t=\frac{\alpha_t}{m_d}$$

The dimensionless characteristic roots Λ for the case where $A_t=0.1$ and $\zeta=0.2$ is solved and shown in Figure 2.14.

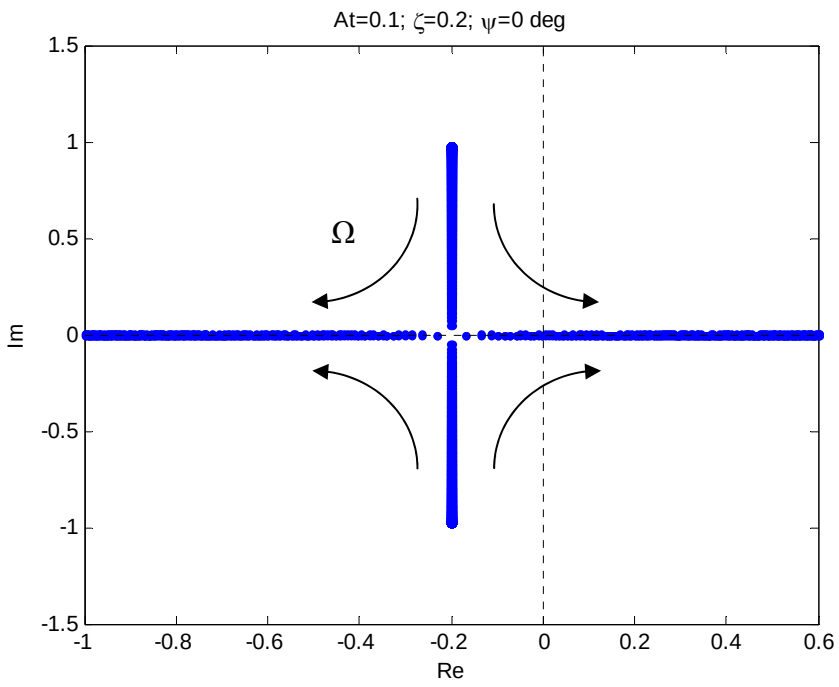

(a) $\Psi=0^{o}$

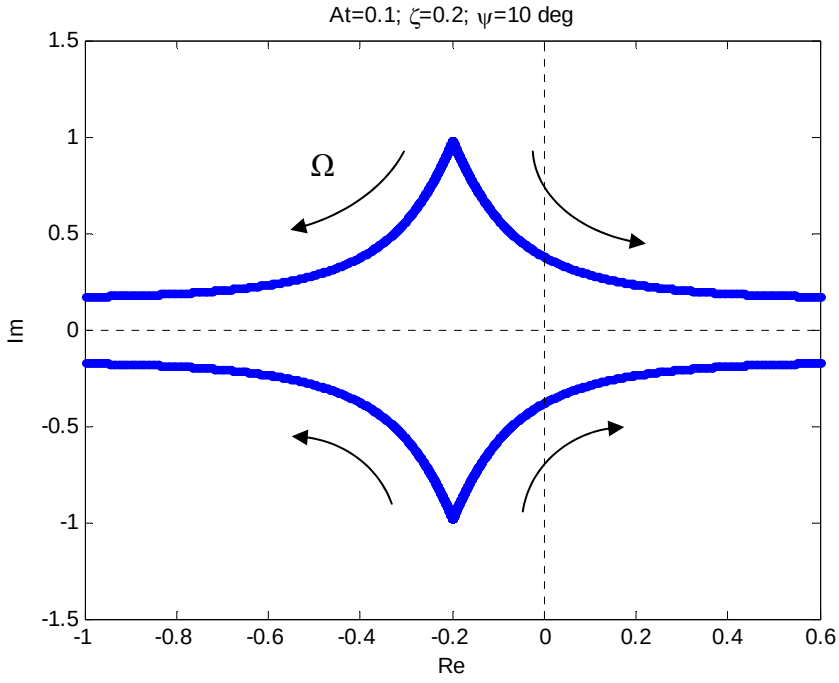

(b) $\Psi=10^{o}$

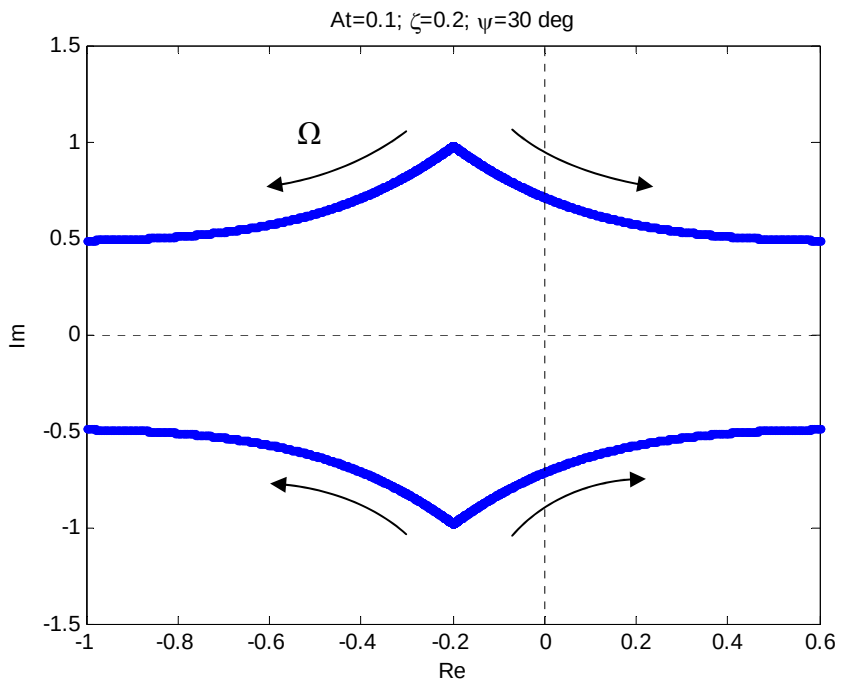
At=0.1; ζ=0.2; ψ=30 deg
Ω
Im
Re
1.5
1
0.5
0
-0.5
-1
-1.5
-1
-0.8
-0.6
-0.4
-0.2
0
0.2
0.4
0.6

(c) Ψ=30^{o}

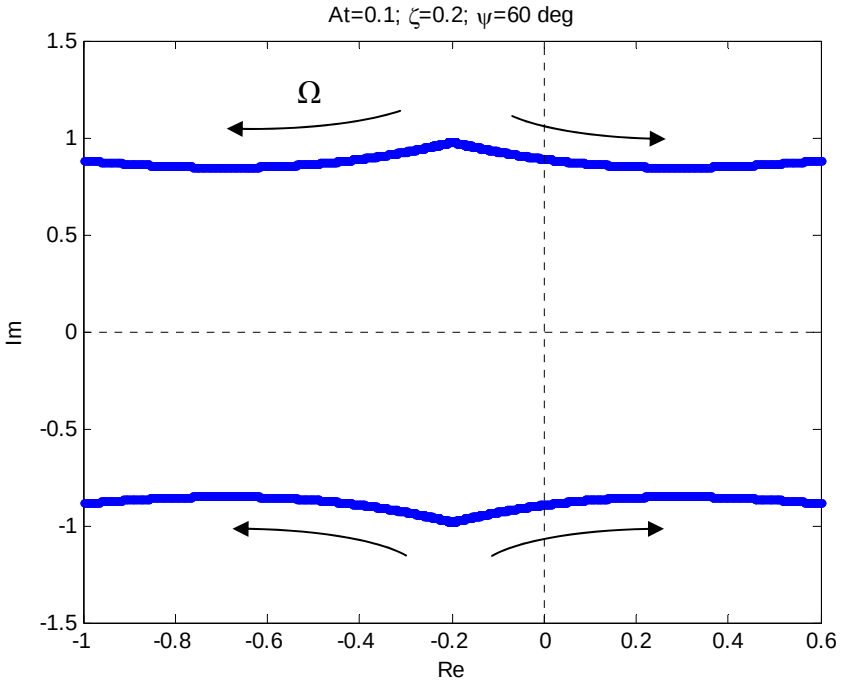
At=0.1; ζ=0.2; ψ=60 deg
Ω
Im
Re
1.5
1
0.5
0
-0.5
-1
-1.5
-1
-0.8
-0.6
-0.4
-0.2
0
0.2
0.4
0.6

(d) Ψ=60^{o}

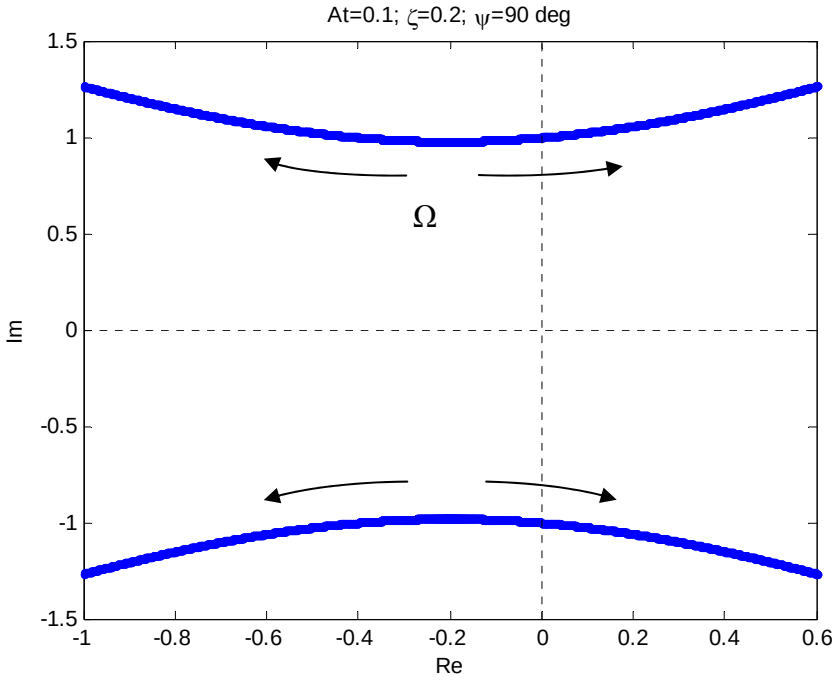

(e) $\Psi=90^{o}$

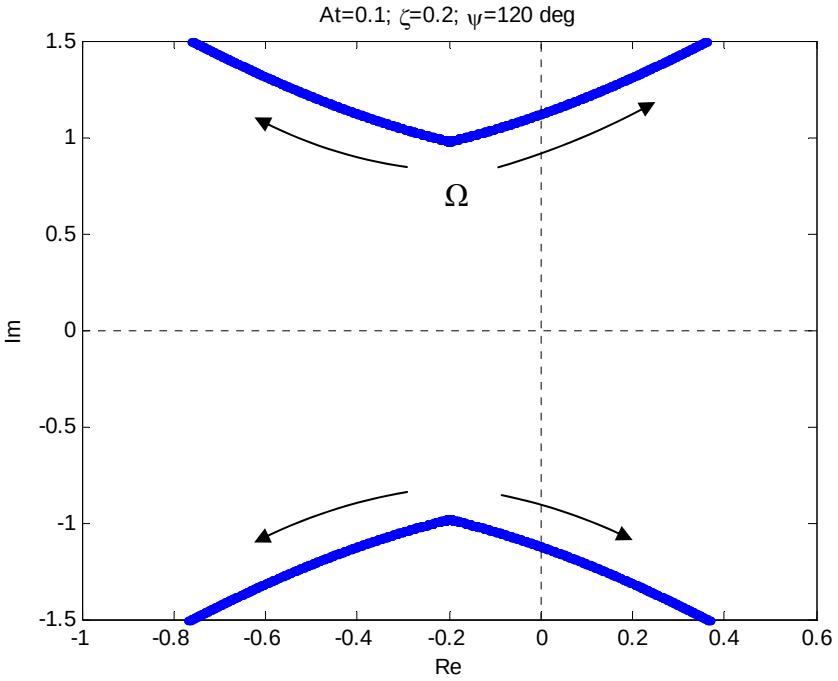

(f) $\Psi=120^{o}$

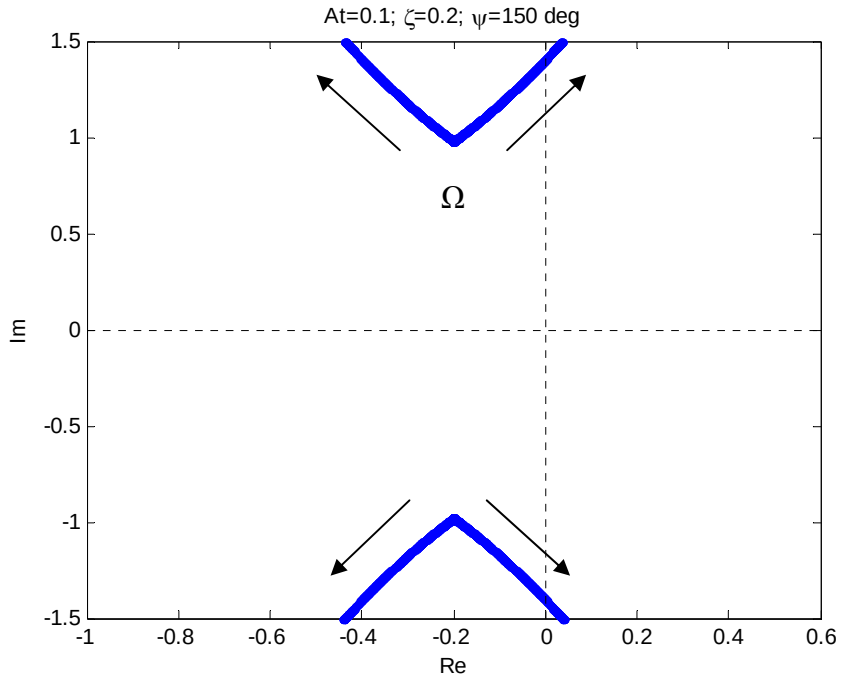

(g) Ψ=150^{o}

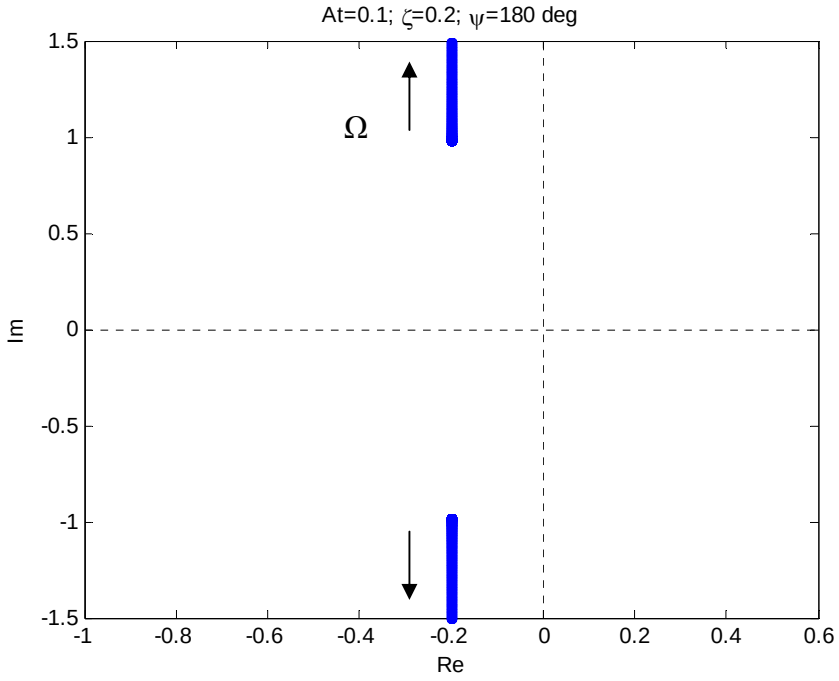

(h) Ψ=180^{o}

Figure 2.14 Root track of damped rigid rotor system (A_t=0.1 and ζ=0.2)

Figure 2.14 shows the root track of the system where the horizontal-axis represents the real part of the dimensionless characteristic roots and the vertical axis represents the imaginary parts, with the rotation speed as parameter. This is similar but not exactly same to the concept of root locus in control theory.

Figure 2.14 shows that the Morton Effect has an impact on the characteristic roots of the system and makes them the functions of the rotation speed. For the non-Morton Effect system, dimensionless characteristic roots are determined only by the damping ratio. However the situation in the Morton Effect involved system is quite different. When the thermal imbalance aligns with the response displacement ($\Psi=0^o$), the system damping ratios (real parts of charateristic roots) is independent of the rotation speed when the system in the oscillatory stable region, but the frequencies (imaginary parts) will decrease with the increase of speed (Figure 4.14(a)). Then the system will become the exponential stable. Once above the threshold speed as defined in Equation (2.48a), the system will become unstable. This is consistent with the discussions in Section 2.3 (see Figure 2.3 and 2.4).

With the thermal imbalance and the response displacement are not in same line ($\Psi=0^o$ or $\Psi=180^o$), both the system damping ratios and the frequencies are dependent on the rotation speed (Figure 2.14 (a) ~ (h)). For smaller phase angles, the frequencies decrease with the increase of the speed and their maginutudes are less than the damped natural frequency of the system (Figure 2.14 (a) ~ (d)). But for the larger phase angles, the frequency increase with the increase of the speed and their maginutude are large than the damped natural frequency (Figure 2.14 (e) ~ (h)).

Once the thermal imbalance are in the oposite direction than the response displacement ($\Psi=180^o$), the system will always stable with the reduced frequencies (Figure 2.14 (h)). There are

no any roots located in the right-hand side of the complex plane. This agrees with the conclusions obtained in Section 2.5 (see Figure 2.13).

It has been proved that when the phase angle $\Psi=0 \sim -180^{o}$, the system shows same root track plots as in Figure 2.14.

2.7 Summary

In this chapter, the mechanism of the Morton Effect induced thermal instability in the mid-span rotor systems are studied using simplified rotor and bearing models. A number of conclusions and equations have been obtained. The results are summarized as follows:

(1) The viscous thermal effect on the rotor systems has been represented by its equivalent thermal induced imbalance. Based on the observations from relevant references and reasonable deductions, a linear expression for the thermal imbalance has been made. A new term called the equivalent coefficient of thermal effect is introduced to represent the thermal effects due to structure and working conditions.

(2) It has been proved that there exists a threshold of instability due to the Morton Effect in the mid-span rotors. Based on the assumptions of linear isotopic bearing supports, this threshold speed takes simple forms of formulas as shown as in Equations (2.6b), (2.14b), and (2.25) for the system with the thermal imbalance acting in the same direction of response displacement, or in Equation (2.34b) for the system with the thermal imbalance acting perpendicular to the direction of response displacement. These equations also show the factors affecting the values of threshold of the Morton Effect induced instability.

(3) A stability map for the damped rigid mid-span rotors with the thermal imbalance having arbitrary phase difference has been obtained. The stable operating regions of the system

are bounded by two curves of threshold of instability, which is shown in Equations. (2.45) and (2.47). The Morton Effect induced instability thresholds are affected by both of the magnitude and the relative phase of the thermal imbalance.

(4) The mechanism of the Morton Effect induced thermal instability of mid-span rotors supported by linear isotropic bearings can be explained through the fact that the Morton Effect introduces either negative stiffness or negative cross-coupled stiffness.

(5) The root track of the damped rigid rotor system where the rotation speed as parameter has been obtained. The results are consistent with the derived analytical solutions of the threshold speed of instability. The Morton Effect has an impact on the characteristic roots of the system and makes them the functions of the rotation speed. The results show that when the thermal imbalance and the response displacement are in the same line (in same or opposite directions), the imaginary parts (frequencies) will dependent on the rotation speed. If they are not in the same line, both the real parts and imaginary parts are dependent on the rotation speed. The relative magnitudes of the frequencies than the system damped natural frequency will depend on the relative phase angles of the thermal imbalance.

3 STEADY-STATE RESPONSE OF MID-SPAN ROTOR SYSTEMS UNDER INFLUENCE OF MORTON EFFECT

3.1 Background

Although the stability analysis is the major concern in the current study, the influence of the Morton Effect on the steady-state response of the system is still of a great interest. Nicholas, Gunter and Allaire [36-37] have made an important investigation on the effect of the residual shaft bow on the unbalance response and balancing of a single mass flexible rotor. The further discussions on so called 'warped rotor" can be referenced to Rao [38] and Meagher et al [39]. Some of the important discoveries made in these publications include the phenomena of the phase jump and the self-balancing speed etc. However, though there are some kinds of similarities, the steady-state response performance of the current system considering the Morton Effect may differ from the referenced warped rotor models due to the following factors:

(1) The residual shaft bow is basically a static bending effect. However, the Morton Effect induced shaft bending is dynamic and changes with the response.

(2) Due to the above reason, the term in the equations of motion describing the residual shaft bow plays only as an additional excitation. However, the term describing the Morton Effect is a function of the rotor response.

3.2 Damped Rigid Rotor

First, the damped rigid rotor with an aligned thermal imbalance as shown in Figure 2.2 is calculated. From Equation (2.8), the steady-state response can be derived by assuming

$$z=z_o e^{i(\omega t-\theta)} \tag{3.1}$$

The magnitude and phase lag are,

$$z_o=\frac{m_d e_m \omega^2}{\sqrt{\left[k_b-\left(m_d+\alpha_t\right)\omega^2\right]^2+\left(c_b\omega\right)^2}}$$

$$\theta=\tan^{-1}\frac{c_b\omega}{k_b-\left(m_d+\alpha_t\right)\omega^2} \tag{3.2}$$

By defining

$$\omega_n=\sqrt{\frac{k_b}{m_d}};\qquad \zeta=\frac{c_b}{2\sqrt{k_b m_d}};\qquad \Omega=\frac{\omega}{\omega_n};\qquad A_t=\frac{\alpha_t}{m_d}$$

The dimensionless form expressions can be obtained

$$\frac{z_o}{e_m}=\frac{\Omega^2}{\sqrt{\left(1-\Omega^2-A_t\Omega^2\right)^2+\left(2\zeta\Omega\right)^2}}$$

$$\theta=\tan^{-1}\frac{2\zeta\Omega}{1-\Omega^2-A_t\Omega^2} \tag{3.3}$$

Figure 3.1 shows the steady-state response diagrams using the above equations, which include amplitude versus speed and phase lag versus speed both in dimensionless forms where the damping ratio ζ=0.1 and the thermal imbalance mass ratio A_t=0.5.

From above equations and the steady-state response diagrams, it can be seen that

(1) Under the influence of the Morton Effect, the finite values of steady-state response of the system will be present within the stable operating speed region. The thermal imbalance would not naturally initiate a diverging response pattern such as resulting from a positive feedback system in nature.

(2) The influence of the Morton Effect on the magnitude of the imbalance response varies in different operating speed regions: it will raise the response level below the peak response speed and reduce it above the peak response speed; it also reduces the peak response speed and the amplitude as well, compared to the non-Morton Effect case. It is as if the entire response level is shifted by the Morton Effect. When the rotor operates above the critical speed, the disk will not simply be auto-centered as in the non-Morton Effect case. Its amplitude will be decreased, which is less than the eccentric distance of mechanical imbalance.

(3) The Morton Effect increases the phase lags of the disk. It is more interesting to note that the Morton Effect changes the phase value at the critical speed $\Omega = 1$ $(\omega = \omega_n)$ and the phase lag is no longer to be 90 degree. At the critical speed , the phase lag will be

$$\theta\big|_{\Omega=1} = \tan^{-1}\frac{2\zeta}{-A_t} \qquad \textbf{(3.4)}$$

The negative value of tangent function implies the phase angle will be above 90 degree. The 90 degree phase lag will occur at $\Omega = \frac{1}{\sqrt{1+A_t}}$, which precedes the critical speed.

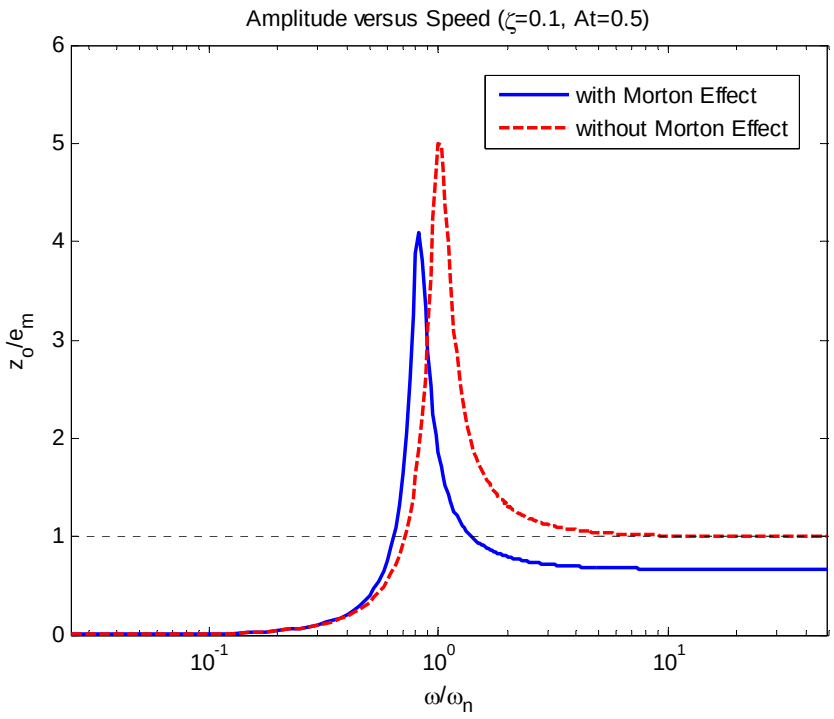

(a) Amplitude

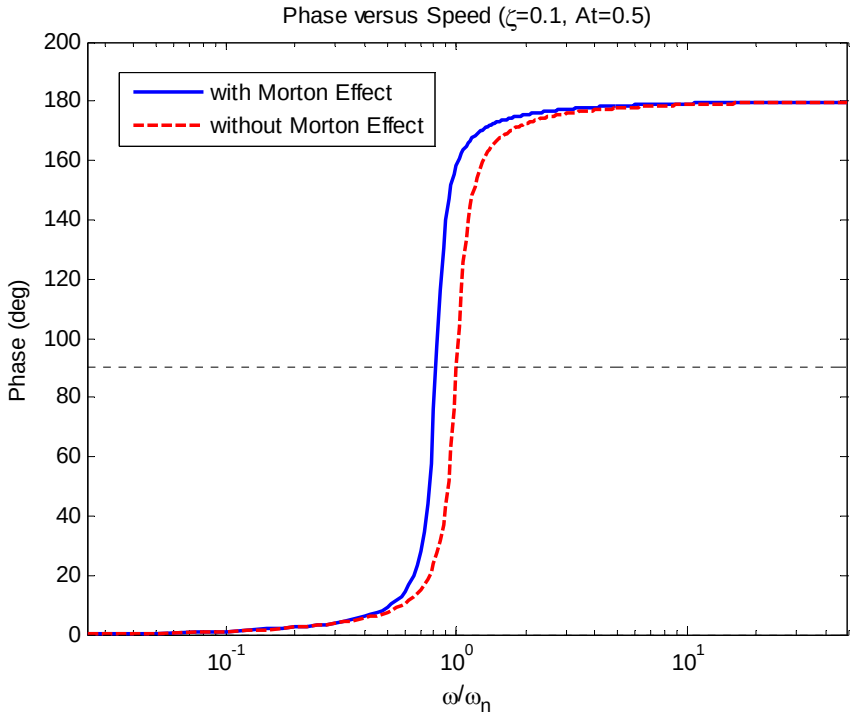

(b) Phase lag

Figure 3.1 Steady-state response diagrams of damped rigid rotor

Figure 3.2 shows the schematic diagrams of the disk response levels and phase lags with the comparison to the non-Morton Effect case.

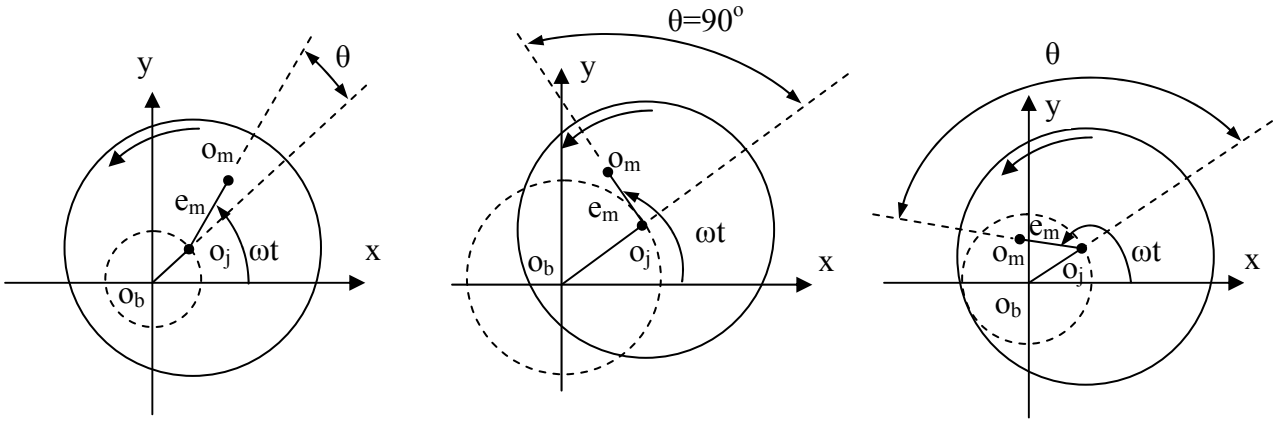

Below critical speed At critical speed Above critical speed

(a) Without Morton Effect

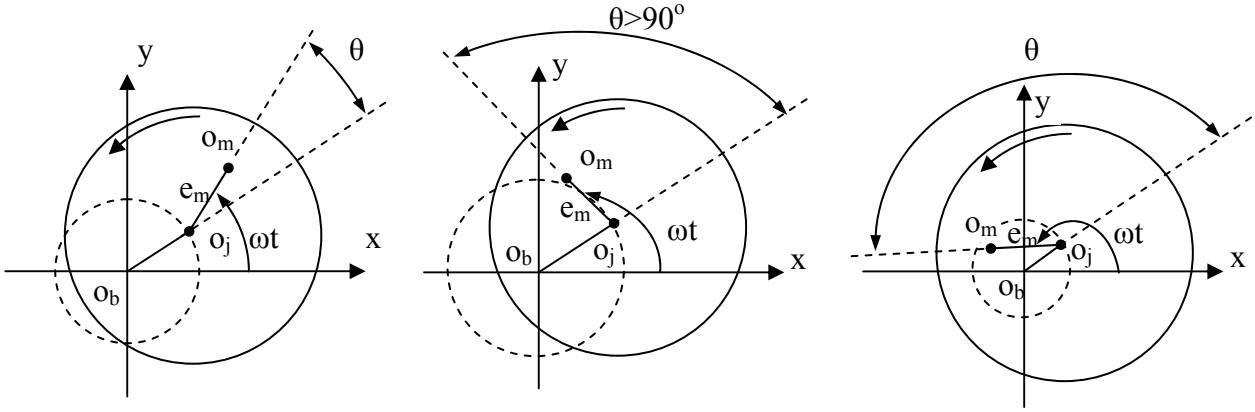

Below critical speed At critical speed Above critical speed

(b) With Morton Effect

Figure 3.2 Disk response levels and phase lags in different operating speed regions

3.3 Extended Jeffcott Rotor

Next, look at the steady-state response of the extended Jeffcott rotor with an aligned thermal imbalance as shown in Figure 2.6.

Assume

$$\begin{aligned} z_d &= z_{do} e^{i(\omega t-\theta_d)} = \bar{z}_{do} e^{i\omega t} \\ z_j &= z_{jo} e^{i(\omega t-\theta_j)} = \bar{z}_{jo} e^{i\omega t} \end{aligned} \tag{3.5}$$

where $\bar{z}_{do}$ and $\bar{z}_{jo}$ are the complex amplitudes (including phase difference) of the disk and the journal, respectively.

Substitute above into the equations of motion (Equation (2.17))

$$\begin{bmatrix} k-m_d\omega^2 & -(k+\alpha_t\omega^2) \\ -k & k+k_b-m_j\omega^2+ic_b\omega \end{bmatrix} \begin{bmatrix} \bar{z}_{do} \\ \bar{z}_{jo} \end{bmatrix} = \begin{bmatrix} m_d e_m \omega^2 \\ 0 \end{bmatrix} \tag{3.6}$$

Solve for $\bar{z}_{do}$ and $\bar{z}_{jo}$

$$\bar{z}_{do} = \frac{\begin{vmatrix} m_d e_m \omega^2 & -(k+\alpha_t\omega^2) \\ 0 & k+k_b-m_j\omega^2+ic_b\omega \end{vmatrix}}{\begin{vmatrix} k-m_d\omega^2 & -(k+\alpha_t\omega^2) \\ -k & k+k_b-m_j\omega^2+ic_b\omega \end{vmatrix}} = \frac{(k+k_b-m_j\omega^2+ic_b\omega)m_d e_m\omega^2}{(k+k_b-m_j\omega^2+ic_b\omega)(k-m_d\omega^2)-k(k+\alpha_t\omega^2)}$$

$$\bar{z}_{jo} = \frac{\begin{vmatrix} k-m_d\omega^2 & m_d e_m \omega^2) \\ -k & 0 \end{vmatrix}}{\begin{vmatrix} k-m_d\omega^2 & -(k+\alpha_t\omega^2) \\ -k & k+k_b-m_j\omega^2+ic_b\omega \end{vmatrix}} = \frac{km_d e_m\omega^2}{(k+k_b-m_j\omega^2+ic_b\omega)(k-m_d\omega^2)-k(k+\alpha_t\omega^2)} \tag{3.7}$$

The amplitudes and phase lags can be obtained

$$\frac{z_{do}}{e_m}=\frac{m_d\omega^2\sqrt{(k+k_b-m_j\omega^2)^2+(c_b\omega)^2}}{\sqrt{[kk_b-(m_dk+m_dk_b+m_jk+\alpha_tk)\omega^2+m_dm_j\omega^4]^2+(kc_b\omega-m_dc_b\omega^3)^2}}$$

$$\theta_d=\tan^{-1}\frac{kc_b\omega-m_dc_b\omega^3}{kk_b-(m_dk+m_dk_b+m_jk+\alpha_tk)\omega^2+m_dm_j\omega^4}-\tan^{-1}\frac{c_b\omega}{k+k_b-m_j\omega^2} \quad \textbf{(3.8)}$$

$$\frac{z_{jo}}{e_m}=\frac{m_d\omega^2k}{\sqrt{[kk_b-(m_dk+m_dk_b+m_jk+\alpha_tk)\omega^2+m_dm_j\omega^4]^2+(kc_b\omega-m_dc_b\omega^3)^2}}$$

$$\theta_j=\tan^{-1}\frac{kc_b\omega-m_dc_b\omega^3}{kk_b-(m_dk+m_dk_b+m_jk+\alpha_tk)\omega^2+m_dm_j\omega^4}$$

The steady state response of the illustrative extended Jeffcott rotor, whose parameters values are same as that listed in Table 2.2 except the thermal imbalance mass ratio A_t, is calculated and shown in Figure 3.3. The value of A_t in this calculation is increased to 0.5, for the apparent illustration of the curves.

It is interesting to notice that the steady state responses at both the disk and journal locations of this two mass system shows a agreeable pattern with the single mass rigid rotor system as showed in Figure. 3.1. If the Morton Effect is included, the amplitude level is higher before the first peak speed, lower between the first and second peak speeds, and higher again above the second peak speed, than the corresponding levels of the non-Morton Effect rotors.

The agreeable pattern can also be observed in the phase lag diagram. Around the first peak speed, the Morton Effect increases the values of the phase lags of both the disk and the journal. Then a shift occurs between the two peak speeds. After that, the phase lags of the disk and the journal when the Morton Effect is involved become lower than that of the non-Morton Effect rotors.

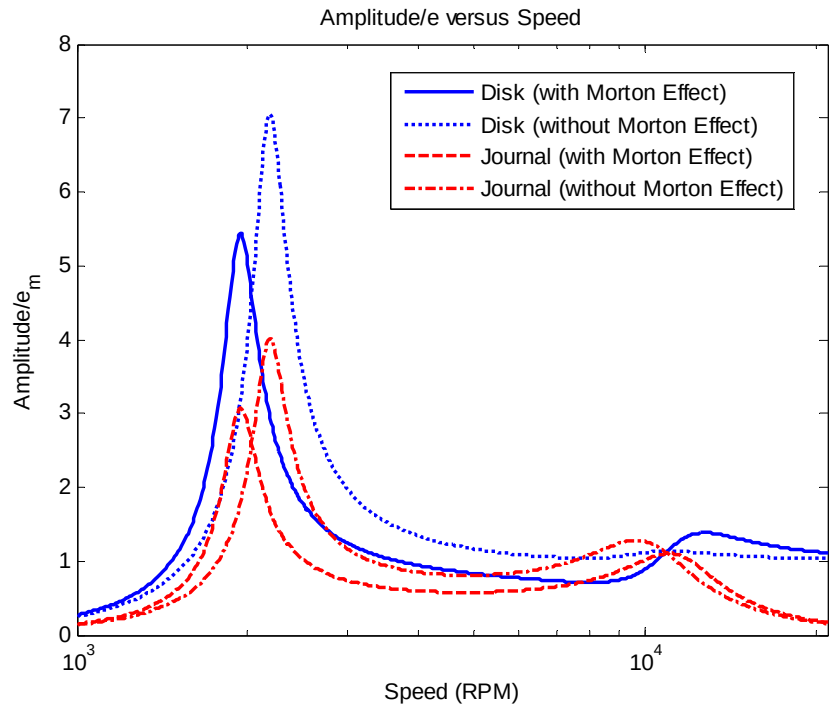

(a) Amplitude

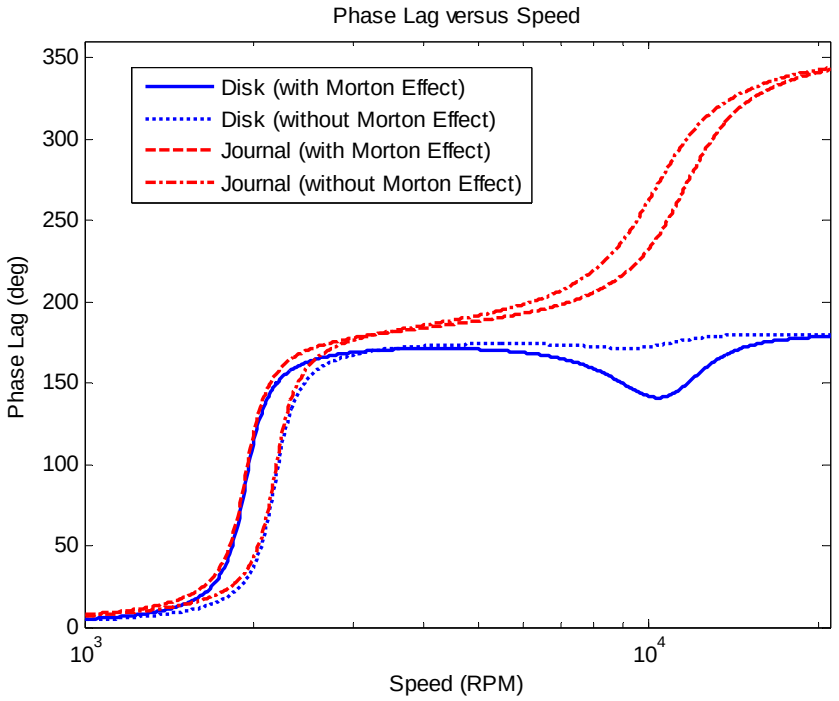

(b) Phase lag

Figure 3.3 Steady-state response diagrams of extended Jeffcott rotor (A_t=0.5)

3.4 Further Discussions

In the preceding two sections, the steady-state responses performance of rigid and elastic rotors where the thermal imbalance is in the direction of the displacement has been discussed. However, for a complete and perspective observation, the cases where the thermal imbalance misaligns with the displacement must be examined. Still consider a rigid rotor supported on the linear isotropic supports where the thermal imbalance has an arbitrary phase difference from the response displacement, as shown in Figure 2.12 of Section 2.5.2. For the analysis of steady-state response, this model is equivalent to the classic Jeffcott rotor if excluding the Morton Effect.

The equations of motion of the system has been derived and shown in Equation (2.37b). Using the same method as in Section 3.2, the steady-state responses can be solved and written as

$$\frac{z_o}{e_m}=\frac{\Omega^2}{\sqrt{\left(1-\Omega^2-A_t\Omega^2\cos\psi\right)^2+\left(2\zeta\Omega-A_t\Omega^2\sin\psi\right)^2}}$$

$$\theta=\tan^{-1}\frac{2\zeta\Omega-A_t\Omega^2\sin\psi}{1-\Omega^2-A_t\Omega^2\cos\psi} \qquad \textbf{(3.9)}$$

where $\omega_n=\sqrt{\frac{k_b}{m_d}}$; $\zeta=\frac{c_b}{2\sqrt{k_b m_d}}$; $\Omega=\frac{\omega}{\omega_n}$; $A_t=\frac{\alpha_t}{m_d}$; ψ is the phase angle of the thermal imbalance.

As discussed in Section 3.2, the above equations show that under the influence of the Morton Effect, the finite values of steady-state response of the system will be present within the stable operating speed regions. The thermal imbalance would not naturally initiate a diverging response pattern such as resulting from a positive feedback system. In addition, it is obvious that

there is not a self-balancing speed which makes the total response be zero as in a warped rotor [36-38].

Next, consider the steady-state responses in several typical cases assuming the damping ratio ζ=0.2:

Case 1: Thermal imbalance along the direction of displacement ($\psi=0^o$)

The model in this case is same as shown in Figure 2.2 and discussed in Section 3.2. Figure 3.4 shows the steady-state response diagrams with the thermal imbalance mass ratio At as a parameter. The results show that the influence of the Morton Effect on the response magnitude varies in different operating speed regions: it raises the response level below the peak response speed and reduce it above the peak response speed; it also reduces the peak response speed and the amplitude as well. It is just as that the response amplitude curves are shifted leftward and downward by the Morton Effect. When the rotor operates above the critical speed, the disk will not simply be auto-centered as in the non-Morton Effect case.

As for the phase diagram, the Morton Effect increases the phase lags of the disk and it looks like the phase lag curves are shifted leftward. Another important feature is that the phase lag at the critical speed is no longer to be 90^o as in the non-Morton Effect case.

Case 2: Thermal imbalance opposite to the direction of displacement ($\psi=180^o$)

However, if the thermal imbalance is opposite to the direction of displacement, the entire picture of the steady-state response is also opposite to Case 1, as shown in Figure 3.5. The amplitude curves are shifted upward and rightward by the Morton Effect while the phase lag curves are shifted rightward.

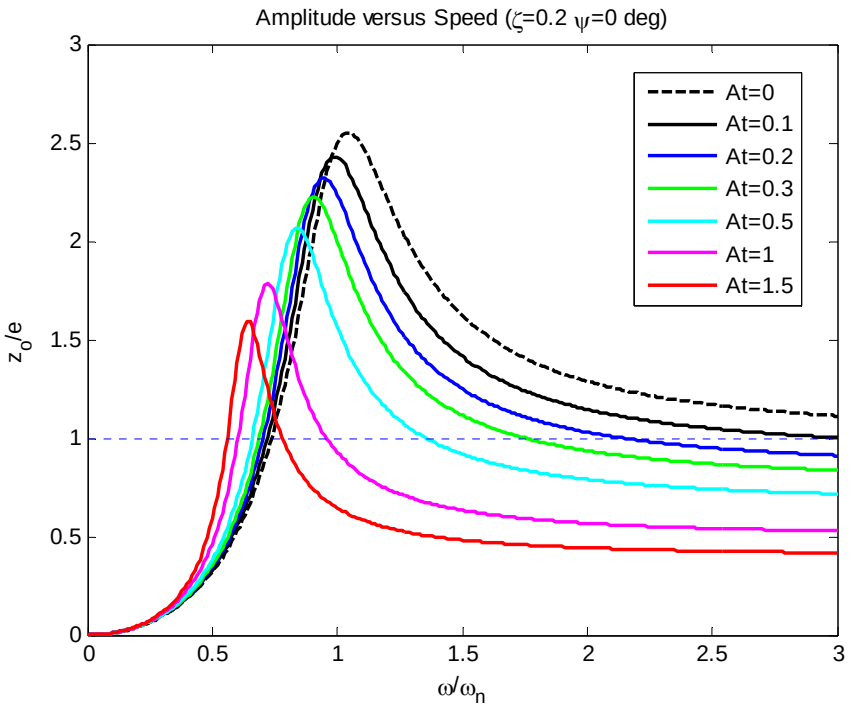

(a) Amplitude

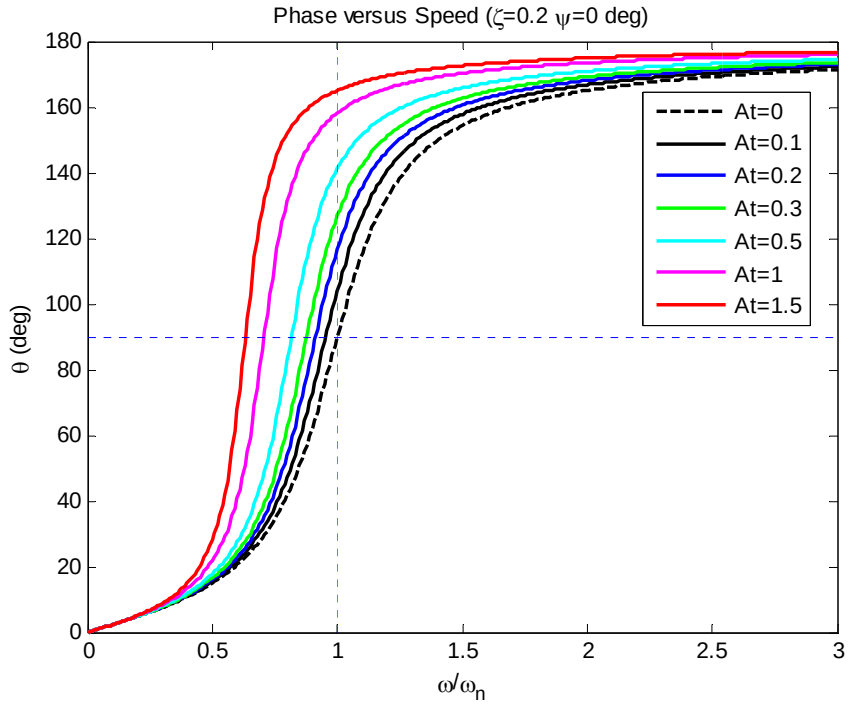

(b) Phase

Figure 3.4 Steady-state response ($\psi=0^o$)

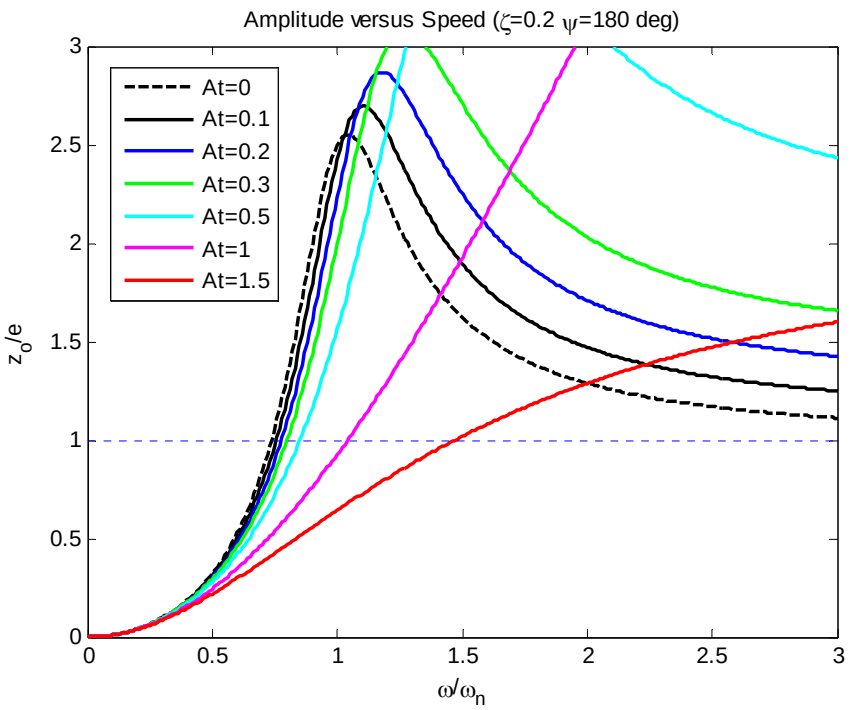

(a) Amplitude

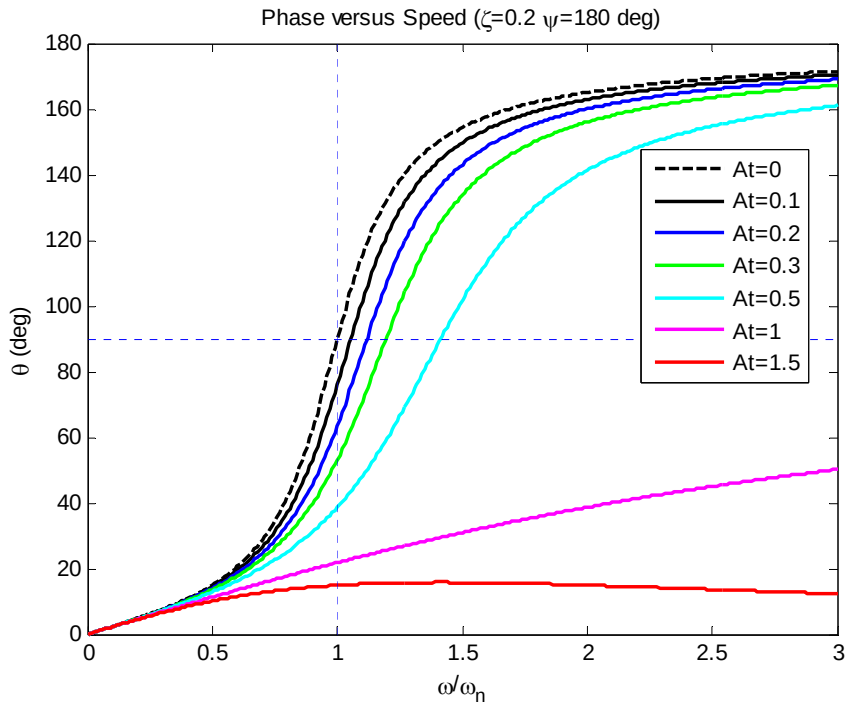

(b) Phase

Figure 3.5 Steady-state response ($\psi=180^{o}$)

Case 3: Thermal imbalance with "perpendicular lead" to the direction of displacement ($\psi=90^o$)

Figure 3.6 shows the steady-state response diagrams for the case where the thermal imbalance has "perpendicular lead" to the direction of displacement. The influence of the Morton Effect on the response amplitude is mixed. The small values of the thermal imbalance ratio may increase the amplitude levels and the large values of it decrease them. The phase lag diagram shows that for the small values of At, the phase angles at the critical speed equal 90^o as in the non-Morton Effect case. However, for the large values of A_t, the phase actually changes from the lag positions to the lead positions. In the latter cases, the phase angles at the critical speed equal -90^o instead.

Case 4: Thermal imbalance with "perpendicular lag" to the direction of displacement ($\psi=270^o$)

Last, consider the case where the thermal imbalance has "perpendicular lag" to the direction of displacement (Figure 3.7). In this case, the response amplitudes seem to be always below the non-Morton Effect. The feature of phase lags is that it always equals 90^o at the critical speed no matter if any Morton Effect is included.

From the above cases it has been observed that once the Morton Effect involved, the phase lags may not always equal 90^o at the critical speed. This is quite different than the non-Morton Effect case.

The steady-state response of the system at the critical speed ($\Omega=1$) can be derived from Equation (3.9)

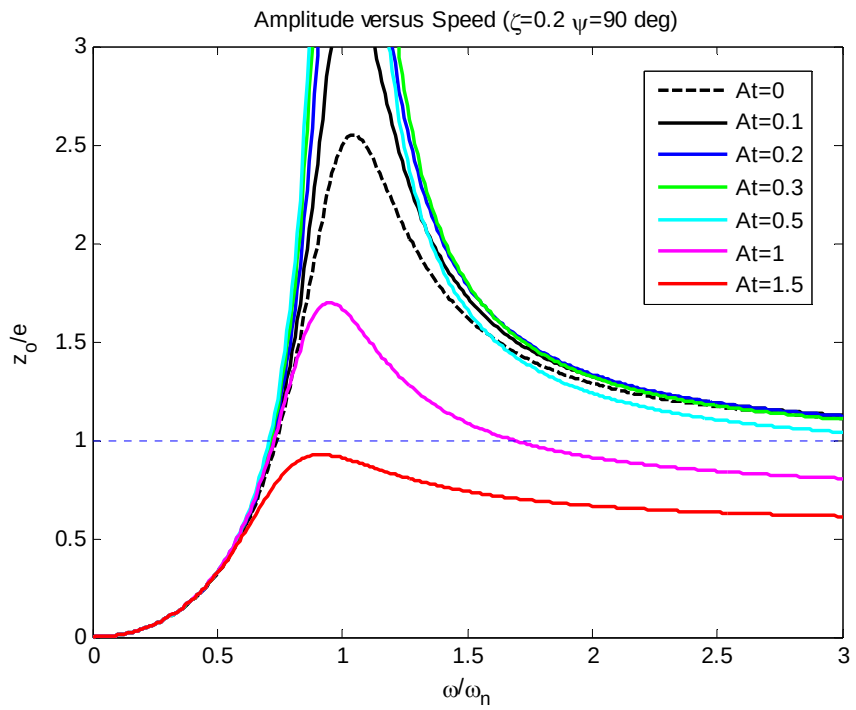

(a) Amplitude

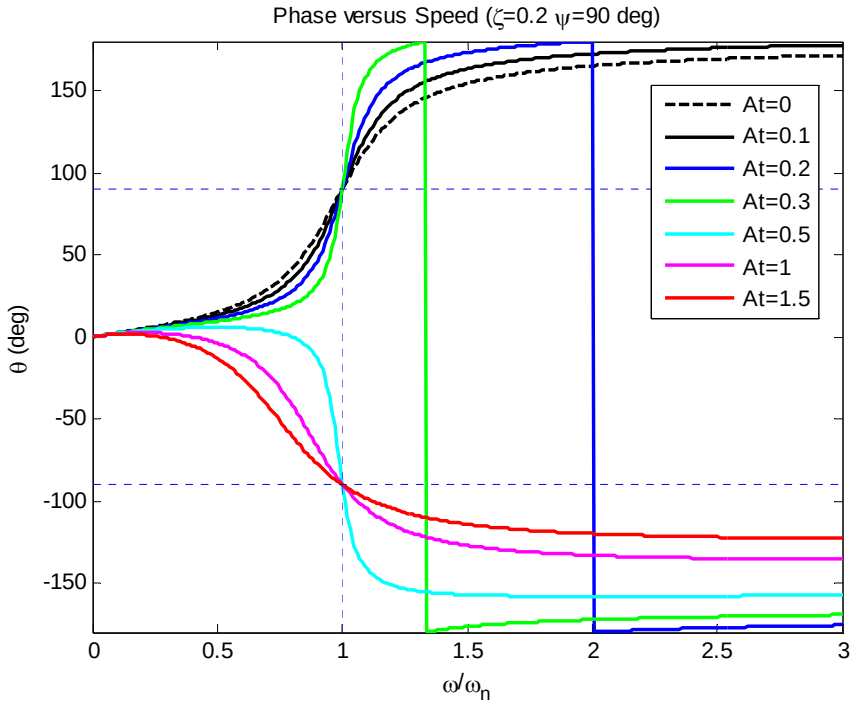

(b) Phase

Figure 3.6 Steady-state response ($\psi=90^{o}$)

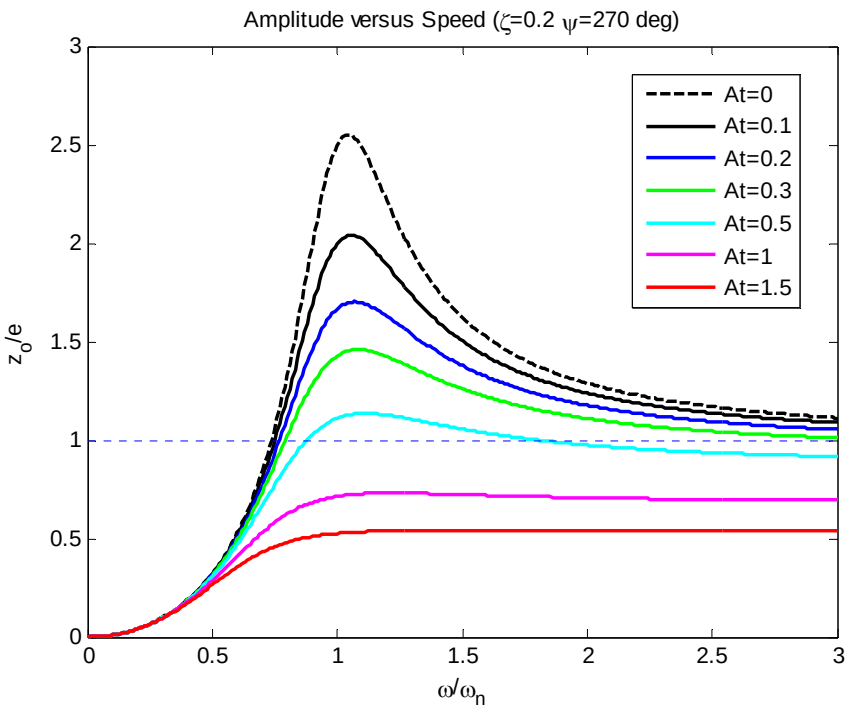

(a) Amplitude

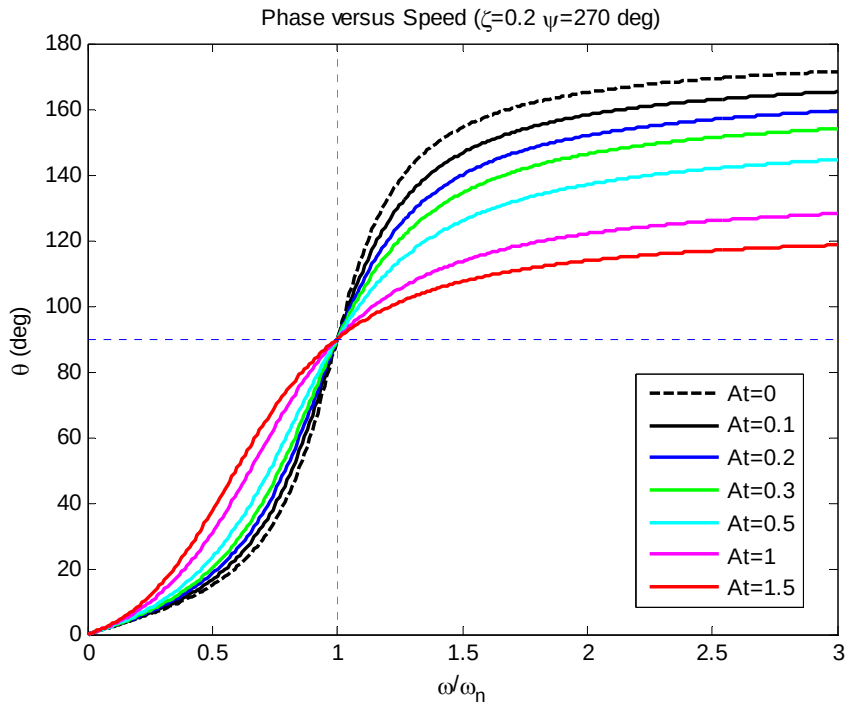

(b) Phase

Figure 3.7 Steady-state response (ψ=270°)

$$\left.\frac{z_o}{e_m}\right|_{\Omega=1} = \frac{1}{\sqrt{\left(A_t\cos\psi\right)^2+\left(2\zeta-A_t\sin\psi\right)^2}}$$

$$\left.\theta\right|_{\Omega=1} = \tan^{-1}\frac{2\zeta-A_t\sin\psi}{-A_t\cos\psi} \qquad \textbf{(3.10)}$$

To examine this feature, the phase lag curves at the critical speed for the different thermal imbalance locations are calculated and shown in Figure 3.8. In the most regions, the phase lags are not equal to 90^o under the influence of the Morton Effect. However, all phase lags pass through 90^o when the thermal imbalance has "perpendicular lag" to the direction of displacement ($\psi=270^o$). For the case when the thermal imbalance has "perpendicular lead" to the direction of displacement ($\psi=90^o$). The phase angle at the critical speed may jump from 90^o to -90^o with the increase of the thermal imbalance mass ratio.

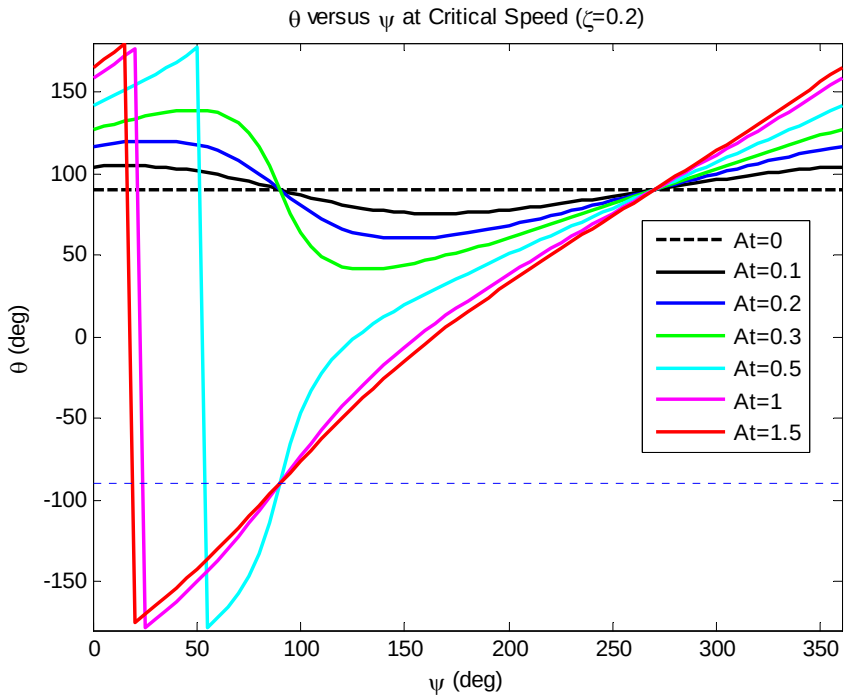

Figure 3.8 Phase at critical speed (Ω=1)

3.5 Summary

In this chapter, the steady-state response performance of several rotor models with the Morton Effect involved as described in Chapter 2 has been calculated and analyzed. The major conclusions are summarized as below:

(1) Under the influence of the Morton Effect, the finite values of steady-state response of the system will be present within the stable operating speed region. The thermal imbalance would not naturally initiate a diverging response pattern such as resulting from a positive feedback system in nature. This phenomenon can also be explained by the derived conclusion that the Morton Effect introduces an additional stiffness.

(2) The Morton Effect has a comprehensive impact on both the amplitude and phase lag of the steady-state unbalance response. It may shift the curves of the response amplitude and phase lag in a manner dependent on the relative magnitude and direction of the thermal imbalance.

(3) One feature of steady-state response of rotor systems under the influence of the Morton Effect is that the phase lag of the disk at the critical speed may not equal 90 degrees except when the thermal imbalance has “perpendicular lag” to the direction of displacement.

4 MORTON EFFECT ANALYSIS OF MID-SPAN ROTOR – HYDRODYNAMIC BEARING SYSTEMS

4.1 System and Assumptions

Using an assumption of isotropic linear bearings, the mechanism of the Morton Effect induced instability has been discussed in Chapter 2. In this chapter, a more realistic system – the rotor supported by the hydrodynamic journal bearings will be discussed. When turning to the rotors supported by the hydrodynamic journal bearings, several differences arise. First, the models to depict the thermal bending of the shaft and the temperature distribution across the journal surface must be developed. This is a basis to calculate the equivalent thermal imbalance, which may be in nonlinear form. As a matter of fact, the magnitude and phase of the thermal imbalance may change with the dynamic position of the journal on its orbit, which is normally not centered at the bearing center as assumed in Chapter 2. Second, the dynamic characteristics of the bearing are no longer linear and isotropic [34-35]. These differences would make the analytical solutions very difficult or impossible.

Although some efforts have been made to establish the thermal bending models for the overhung rotors [17-23], the calculation of the thermal bending and its equivalent thermal imbalance of mid-span rotors are still to be investigated. Hence, the calculation of the thermal imbalance will be the first concern in this chapter. Once that is completed, the stability analysis

of the target system, mid-span rotors with the hydrodynamic journal bearings, will be discussed. For this purpose, some assumptions for Chapter 4 have been made:

(1) The system to be discussed is a symmetrical elastic rotor (extended Jeffcott rotor) supported by two hydrodynamic plain (cylindrical) journal bearings.

(2) The thermal bending deflections are assumed to be small. Hence, it is assumed to be uncoupled with any other deformations.

(3) Although the deflection of the journal within the bearings are considered in calculating the thermal bending of the rotor, the journal deflection effect on the bearing static and dynamic characteristics are neglected, for the simplicity of modeling the system. In addition, the temperature distribution in axial direction in the bearings is assumed to be uniform for the same reason.

(4) The linear stiffness and damping based on the static equilibrium of the bearings are employed. The bearing stiffness and damping are no longer uniform over the entire operating speed range.

(5) The whirling motion of the rotor (journal) is still synchronous. Due to the non-isotropic characteristics of the hydrodynamic bearings, the whirling orbit of the journal will no longer be circular. Instead, the whirling orbit for a typical rotor system with fluid film bearings will be elliptic. The stability analysis and derived results are to be used to predict instabilities when the system is subjected to the forced unbalance excitations.

4.2 Thermal Bending Model

Compared to the normal rotor dynamic systems, the predominant feature of the system with the Morton Effect involved is the inclusion of the thermal bending. Just based on this viewpoint,

the specific discussion on the thermal bending will be conducted first. The conclusions to be obtained in this section will not only be used in the following analysis on the symmetrical elastic rotor systems, but also be applicable in the general rotor-hydrodynamic bearing systems. The latter will be discussed in Chapter 5.

4.2.1 Basic Equations of Thermal Bending

In Timoshenko's classic text [32], the basic equation to account for the pure thermal bending has been discussed.

Under the temperature difference ΔT , the material with the original length L will experience a thermal deformation ΔL . For the one-dimensional problem, this can be represented as

$$\Delta L=\alpha L\Delta T \qquad \textbf{(4.1)}$$

where α is the coefficient of thermal expansion

Figure 4.1 shows a schematic diagram of a uniform beam experiencing thermal effect in simple supports. Assume the initial temperature of beam is T_o, then the temperatures on the top and the bottom are changed to be T_1 and T_2 (uniform in axial direction), respectively. If $T_2 > T_1$, the top and bottom lengths will change and the latter will become relatively larger. Assume the temperature change is linear. From geometrical relationship

$$(r+h)d\theta-rd\theta=\alpha(T_2-T_o)dx-\alpha(T_1-T_o)dx \qquad \textbf{(4.2a)}$$

or

$$hd\theta=\alpha(T_2-T_1)dx \qquad \textbf{(4.2b)}$$

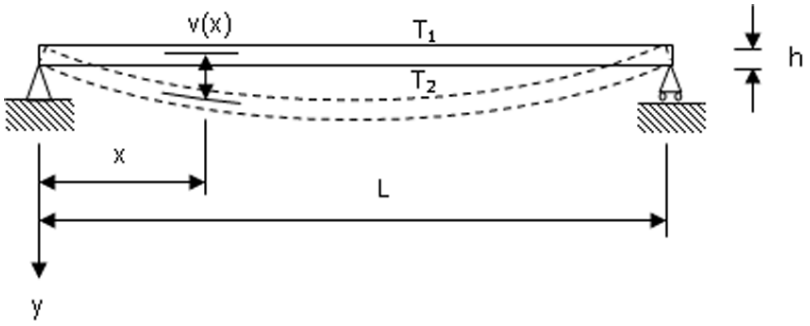

(a) Beam experiencing temperature difference

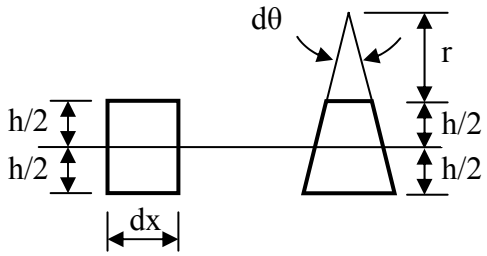

(b) Geometrical relationship

Figure 4.1 Thermal bending beam in simple supports (T_2>T_1)

According to the bending theory, the curvature κ is related to bending angle θ and deflection v

$$\kappa=\frac{1}{\rho}=\frac{d\theta}{dx}=\frac{d^2v}{dx^2} \tag{4.3}$$

and

$$\frac{d^2v}{dx^2}=-\frac{M}{EI} \tag{4.4}$$

where M is the bending moment and EI are the constants of the material and structure.

Then the basic equation for the pure thermal bending due to the temperature difference $\Delta T=(T_2-T_1)$ can be obtained

$$\frac{d^2v}{dx^2}=-\frac{\alpha(T_2-T_1)}{h}=-\frac{\alpha\Delta T}{h} \tag{4.5}$$

The minus sign was added to make above formula in accordance with the practice of bending theory. The rules for the signs of each quantity can be found in reference [32].

Depending on the types of the beam supports (simple beam, cantilever, or fixed ends beam), the bending angles and deflections can be derived for each situation.

From the observation of different rotor systems, it is reasonable to use the simple beam model to simulate the mid-span rotors (see Section 4.2.2), while the cantilever beam seems to be an ideal model for the overhung rotors. As a matter of fact, the most published references on overhung systems employed the cantilever models.

For the simple beam model, the bending angle and deflection can be calculated

$$\begin{aligned} v&=\frac{\alpha(T_2-T_1)x(L-x)}{2h} \\ \theta&=\frac{\alpha(T_2-T_1)(\frac{L}{2}-x)}{h} \end{aligned} \tag{4.6}$$

It can be seen that the simple beam experiencing the thermal effect as discussed above is equivalent to a beam under pure bending with the equivalent thermal moment

$$M_{eq}=\frac{\alpha\Delta TEI}{h} \tag{4.7}$$

4.2.2 Thermal Bending Model for Mid-Span Rotor Systems

When the initial efforts in the current study were conducted, it was uncertain as how to properly model the mid-span rotor systems using basic bending theories. However, if comparing the following two schematic diagrams as shown in Figure 4.2, where T_2 and T_1 (T_2>T_1) are used to represent the temperatures at the hot and cold spots of the journal in the rotor models, it is obvious that using the simple beam undergoing thermal induced bending will be a reasonable model of the mid-span rotor systems. The mid-span rotor-model looks like an interrupted simple beam model.

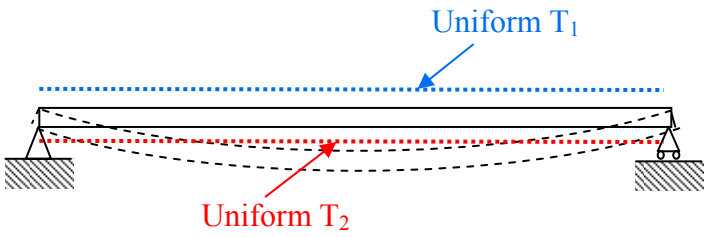

(a) Simple beam

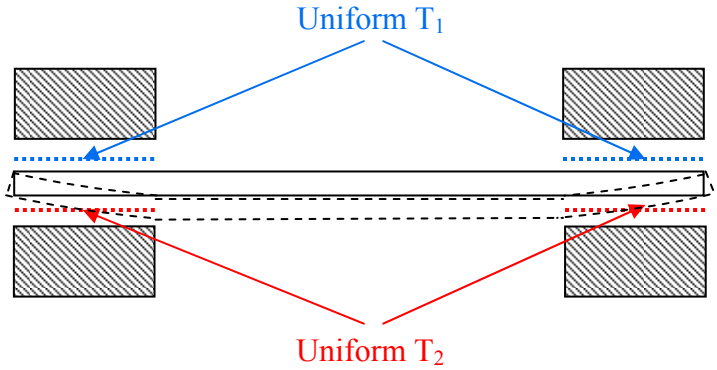

(b) Mid-span rotor supported by two bearings

Figure 4.2 Thermal bending model for mid-span rotor systems

To derive the reaction forces and then deflections of the suggested thermal bending rotor model, the concept of the equivalent systems can be used to simplify the solution (Figure 4.3). The subscripts a and b in Figure 4.3 are used to represent the two bearings on the left-hand and right-hand sides, respectively. For example, L_a and L_b are the respective lengths of the two bearings while L is the total length of the rotor from the left-hand side end of the bearing on the left to the right-hand side end of the bearing on the right. As in the uniform pure thermal bending model, the thermal effect on bending of the beam can be expressed in terms of equivalent thermal moments.

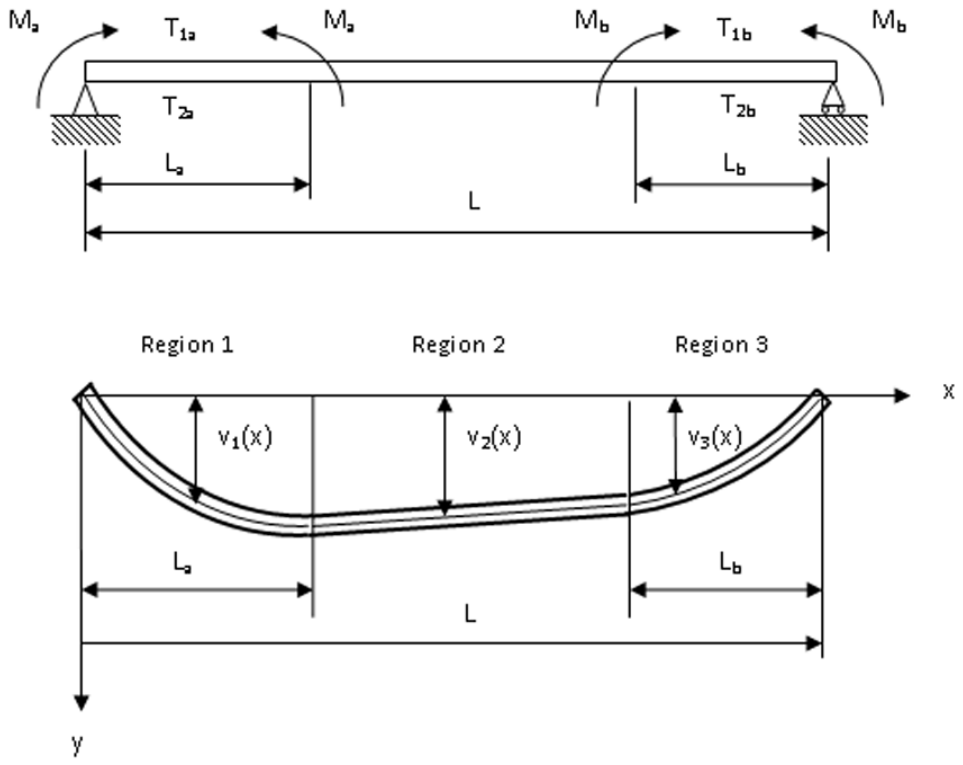

Figure 4.3 Equivalent thermal bending models

In doing so, the deflection equations for the thermal bending model of rotor can be expressed as

$$EIv''=-M=\begin{cases} -M_a=-\dfrac{\alpha\Delta T_a EI_a}{h_a} & 0\le x\le L_a \\ 0 & L_a<x<L-L_a \\ -M_b=-\dfrac{\alpha\Delta T_b EI_b}{h_b} & L-L_b\le x\le L \end{cases} \quad \textbf{(4.8a)}$$

Assume that the journal has the uniform cross sections in each bearing region

$$v''=\begin{cases} -\dfrac{\alpha\Delta T_a}{h_a} & 0\le x\le L_a \\ 0 & L_a<x<L-L_a \\ -\dfrac{\alpha\Delta T_b}{h_b} & L-L_b\le x\le L \end{cases} \quad \textbf{(4.8b)}$$

The corresponding boundary conditions are

$$\begin{aligned} &x=0, \quad v=0 \\ &x=L, \quad v=0 \end{aligned} \quad \textbf{(4.9)}$$

In Region 1 ($0\le x\le L_a$)

$$\begin{aligned} \theta_1=v_1'&=-\frac{\alpha\Delta T_a}{h_a}x+C_1 \\ v_1&=-\frac{\alpha\Delta T_a}{h_a}\frac{x^2}{2}+C_1x+C_2 \end{aligned} \quad \textbf{(4.10a)}$$

Applying the first boundary condition: $x=0$, $v_1=0$, then $C_2=0$

$$\theta_1 = -\frac{\alpha \Delta T_a}{h_a} x + C_1$$
$$v_1 = -\frac{\alpha \Delta T_a}{2h_a} x^2 + C_1 x \qquad \textbf{(4.10b)}$$

In Region 2 ($L_a < x < L - L_a$)

$$\theta_2 = v_2' = C_3$$
$$v_2 = C_3 x + C_4 \qquad \textbf{(4.11)}$$

In Region 3 ($L - L_b \le x \le L$)

$$\theta_3 = v_3' = -\frac{\alpha \Delta T_b}{h_b} x + C_5$$
$$v_3 = -\frac{\alpha \Delta T_b}{h_b} \frac{x^2}{2} + C_5 x + C_6 \qquad \textbf{(4.12a)}$$

Applying the second boundary condition: $x=L$, $v_3=0$, then $C_6 = \frac{\alpha \Delta T_b}{2h_b} L^2 - C_5 L$

$$\theta_3 = -\frac{\alpha \Delta T_b}{h_b} x + C_5$$
$$v_3 = -\frac{\alpha \Delta T_b}{2h_b} (L^2 - x^2) - C_5 (L - x) \qquad \textbf{(4.12b)}$$

Then, the continuous conditions at $x=L_a$ and $x=L-L_b$ are employed to find out four constant constants C_1, C_3, C_4, and C_5

$$x = L_a, \quad v_1 = v_2$$
$$x = L_a, \quad \theta_1 = \theta_2$$
$$x = L - L_b, \quad v_2 = v_3$$
$$x = L - L_b, \quad \theta_2 = \theta_3 \qquad \textbf{(4.13)}$$

The equations about the constants to be determined are

$$\begin{bmatrix} 1 & -1 & 0 & 0 \\ L_a & -L_a & -1 & 0 \\ 0 & 1 & 0 & -1 \\ 0 & L-L_b & 1 & L_b \end{bmatrix} \begin{bmatrix} C_1 \\ C_2 \\ C_3 \\ C_4 \end{bmatrix} = \begin{bmatrix} \dfrac{\alpha\Delta T_a L_a}{h_a} \\ \dfrac{\alpha\Delta T_a L_a^2}{2h_a} \\ -\dfrac{\alpha\Delta T_b (L-L_a)}{h_b} \\ \dfrac{\alpha\Delta T_b (2LL_b - L_b^2)}{2h_b} \end{bmatrix} \tag{4.14}$$

The solutions are

$$\begin{aligned} C_1 &= \frac{\alpha\Delta T_a (2LL_a - L_a^2)}{2h_a L} + \frac{\alpha\Delta T_b L_b^2}{2h_b L} \\ C_3 &= -\frac{\alpha\Delta T_a L_a^2}{2h_a L} + \frac{\alpha\Delta T_b L_b^2}{2h_b L} \\ C_4 &= \frac{\alpha\Delta T_a L_a^2}{2h_a L} \\ C_5 &= -\frac{\alpha\Delta T_a L_a^2}{2h_a L} + \frac{\alpha\Delta T_b [L^2 + (L-L_b)^2]}{2h_a L} \end{aligned} \tag{4.15}$$

The deflection v_2 is the major concern in the following analysis on Morton Effect. It can be written as follows

$$v_2(x) = \left(\frac{\alpha\Delta T_b L_b^2}{2h_b L} - \frac{\alpha\Delta T_a L_a^2}{2h_a L} \right) x + \frac{\alpha\Delta T_a L_a^2}{2h_a} \tag{4.16}$$

which is applicable in the general cases of mid-span rotors, not limited to the symmetrical one.

It is interesting to note that the suggested thermal bending model can also partially explain the phenomenon in the practice that the mid-span rotors are less liable to be influenced by the Morton Effect induced instability than the overhung configurations. While the similar thermal

induced equivalent moments are developed inside the bearings for both rotor configurations, the free end on one side in the overhung rotor models will generate relatively larger deflections and also relatively larger resultant thermal imbalances. Comparing the mid-span rotor model as shown in Figure 4.2 to the overhung model (see Figure 1.1), it can be seen that a smaller effective rotor deflection is a result of the restraining effect between two supports in the mid-span rotors.

4.3 Bearing and Thermal Imbalance Calculations

Next, consider the calculations of thermal imbalance. This involves the analysis of two hydrodynamic journal bearings. Assume they are plain cylindrical bearings and are identical.

4.3.1 Hydrodynamic Plain Journal Bearing

1) Fluid film thickness

Figure 4.4 shows the schematic diagram of the hydrodynamic plain journal bearing.

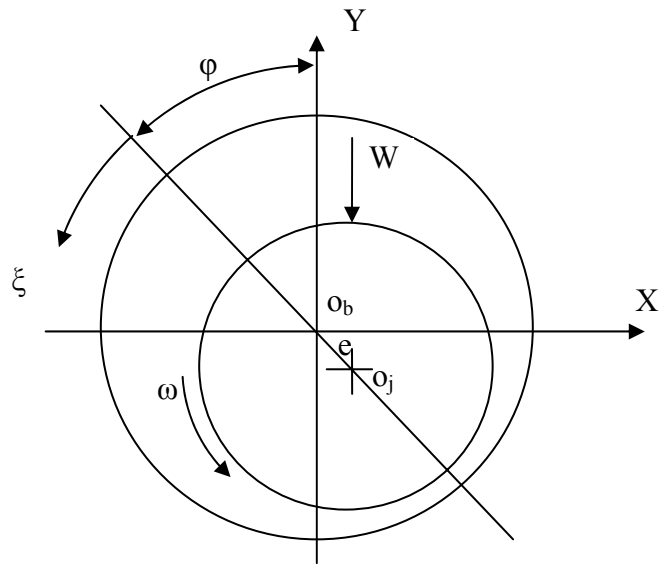

Figure 4.4 Schematic diagram of hydrodynamic plain journal bearing

The fluid film thickness expression is

$$h=C_b(1+\varepsilon\cos\xi) \tag{4.17}$$

Where the eccentricity ratio $\varepsilon=\frac{e}{C_b}$

2) Static equilibrium

The static equilibrium position of rotor will be determined by the two bearings. The short bearing theory is used to calculate the static equilibrium of bearing. The load capacity and attitude angle can be calculated using following formulas [34, 40]

$$W=\frac{\mu\omega DB}{2\psi_b^2}\times\left(\frac{B}{D}\right)^2\frac{\varepsilon_o}{(1-\varepsilon_o^2)^2}\sqrt{\pi^2(1-\varepsilon_o^2)+16\varepsilon_o^2} \tag{4.18a}$$

$$\varphi_o=\tan^{-1}\frac{\pi\sqrt{1-\varepsilon_o^2}}{4\varepsilon_o} \tag{4.18b}$$

where ε_o represents the static eccentricity ratio and ψ_b is the relative clearance, $\psi_b=\frac{C_b}{D/2}$.

3) Stiffness and damping coefficients of bearing

As before, the stiffness and damping coefficients of bearing can be calculated using short bearing theory. Define the dimensionless stiffness and damping coefficients as follows

$$k_{ij}=K_{ij}\frac{\mu\omega B}{\psi_b^3}$$
$$c_{ij}=C_{ij}\frac{\mu B}{\psi_b^3} \qquad (i, j= x,y) \tag{4.19}$$

The stiffness and damping coefficients can be obtained from [40]

$$k_{xx}=\frac{W}{C_b}4[2\pi^2+(16-\pi^2)\varepsilon_o^2]Q(\varepsilon_o)$$

$$k_{xy}=-\frac{W}{C_b}\frac{\pi[-\pi^2+2\pi^2\varepsilon_o^2+(16-\pi^2)\varepsilon_o^4]Q(\varepsilon_o)}{\varepsilon_o(1-\varepsilon_o^2)^{1/2}}$$

$$k_{yx}=-\frac{W}{C_b}\frac{\pi[\pi^2+(32+\pi^2)\varepsilon_o^2+2(16-\pi^2)\varepsilon_o^4]Q(\varepsilon_o)}{\varepsilon_o(1-\varepsilon_o^2)^{1/2}}$$

$$k_{yy}=\frac{W}{C_b}\frac{4[\pi^2+(32+\pi^2)\varepsilon_o^2+2(16-\pi^2)\varepsilon_o^4]Q(\varepsilon_o)}{(1-\varepsilon_o^2)}$$

$$c_{xx}=\frac{W}{C_b\omega}\frac{2\pi(1-\varepsilon_o^2)^{1/2}[\pi^2+2(\pi^2-8)\varepsilon_o^2]Q(\varepsilon_o)}{\varepsilon_o}$$

$$c_{xy}=-\frac{W}{C_b\omega}8[\pi^2+2(\pi^2-8)\varepsilon_o^2]Q(\varepsilon_o)$$

$$c_{yx}=c_{xy}$$

$$c_{yy}=\frac{W}{C_b\omega}\frac{2\pi[\pi^2+2(24-\pi^2)\varepsilon_o^2+\pi^2\varepsilon_o^4]Q(\varepsilon_o)}{\varepsilon_o(1-\varepsilon_o^2)^{1/2}}$$

$$\text{where } Q(\varepsilon_o)=\frac{1}{[\pi^2+(16-\pi^2)\varepsilon_o^2]^{3/2}} \qquad \textbf{(4.20)}$$

4.3.2 Calculations of Temperature

A simplified model is employed to calculate the temperature distribution in the hydrodynamic plain journal bearings [34]. An assumption of long bearing is considered here.

Apply the energy conservation law to the control volume shown in Figure 4.5.

Energy generation rate = energy out flux rate + energy accumulation rate

or

$$\dot{E}_{visc}=(\dot{E}_{lub}\Big|_{x+dx}-\dot{E}_{lub}\Big|_{x})+\dot{E}_J+\dot{E}_B \qquad \textbf{(4.21)}$$

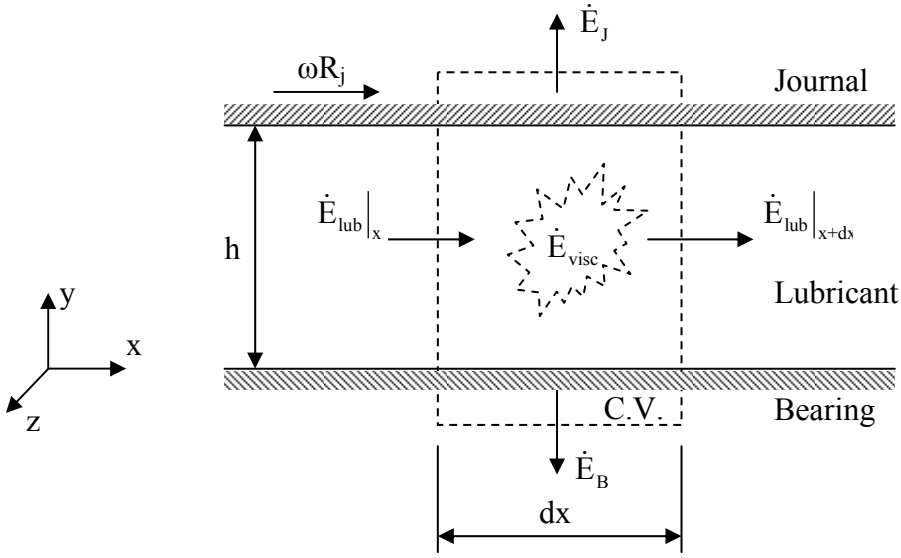

Figure 4.5 Control volume in hydrodynamic plain journal bearing

where $\dot{E}_{visc}$ - energy generation rate by viscous friction

$\dot{E}_{lub}\big|_{x+dx} - \dot{E}_{lub}\big|_x$ - net energy out flux by the flow of lubricant

$\dot{E}_J$ - energy out flux through journal by heat transfer

$\dot{E}_B$ - energy out flux through bearing housing by heat transfer

for steady-state conditions, the energy accumulation rate is zero.

For Newtonian fluid, the shear stress

$$\tau=\mu\frac{du}{dy}\approx\mu\frac{\omega R_j}{h}=\frac{\mu\omega D}{2h} \quad \text{(linear velocity profile approximation)} \qquad \textbf{(4.22)}$$

Hence

$$\dot{E}_{visc}=(\text{force})(\text{velocity})=(\tau dxB)(\omega R_j)=\frac{\mu\omega^2 D^2}{4h}Bdx \qquad \textbf{(4.23a)}$$

For the energy out flux by the flow of lubricant

$$\dot{E}_{lub}\Big|_{x+dx} = (\text{mass flow rate})(\text{specific heat capacity})(\text{temeprature})$$
$$= (\rho_l \frac{\omega R_j}{2} hB)(c_l)\left(T + \frac{dT}{dx}dx\right) \quad \textbf{(4.23b)}$$

$$\dot{E}_{lub}\Big|_{x+dx} = (\rho_l \frac{\omega R_j}{2} hB)(c_l)(T) \quad \textbf{(4.23c)}$$

$$(\dot{E}_{lub}\Big|_{x+dx} - \dot{E}_{lub}\Big|_{x}) = \frac{\rho_l c_l \omega D h}{4}\frac{dT}{dx}Bdx \quad \textbf{(4.23d)}$$

By assuming the fraction factor of energy out flux through the journal is f, then

$$\dot{E}_J = (\text{heat transfer coeffcient})(\text{surface area})(\text{temparature difference})$$
$$= f(H)(Bdx)(T - T_{amb}) \quad \textbf{(4.24a)}$$

$$\dot{E}_B = (1-f)(H)(Bdx)(T - T_{amb}) \quad \textbf{(4.24b)}$$

$$\dot{E}_J + \dot{E}_B = H(T - T_{amb})Bdx \quad \textbf{(4.24c)}$$

Substitute above into Equation (4.21)

$$\frac{\mu\omega^2 D^2}{4h}Bdx = \frac{\rho_l c_l \omega D h}{4}\frac{dT}{dx}Bdx + H(T - T_{amb})Bdx \quad \textbf{(4.25a)}$$

Let

$$\tilde{T} = T - T_{amb}$$

$$x = \frac{D}{2}\xi$$

Hence

$$\frac{d\tilde{T}}{d\xi} + \frac{2H}{\rho_l c_l \omega h}\tilde{T} - \frac{\mu\omega D^2}{2\rho_l c_l h^2} = 0 \quad \textbf{(4.25b)}$$

where ξ is the circumferential angle coordinate of the film measured from the maximum bearing clearance; $\tilde{T}$ is the temperature difference relative to ambient temperature; ρ_l, c_l and μ are the density, specific heat capacity and dynamic viscosity of the lubricant; D and h are the diameter and fluid film thickness of the bearing; H is the coefficient of heat transfer through the journal and bearing surfaces; ω is the rotation speed of the rotor.

Equation (4.25b) gives the temperature distribution in the bearing. Consider the case where there is no heat transfer through journal and bearing surfaces (adiabatic) for the conservative consideration. Then the closed form expression of temperature distribution can be obtained

$$\begin{aligned}\tilde{T}&=\int \frac{\mu\omega D^2}{2\rho_l C_l h^2}d\xi+C=\frac{\mu\omega D^2}{2\rho_l c_l C_b^2}\int \frac{1}{(1+\varepsilon\cos\xi)^2}d\xi+C\\&=\frac{\mu\omega D^2}{2\rho_l c_l C_b^2}\frac{1}{(1-\varepsilon^2)^{3/2}}\left[2\tan^{-1}\left(\sqrt{\frac{1-\varepsilon}{1+\varepsilon}}\tan\frac{\xi}{2}\right)-\varepsilon\sqrt{1-\varepsilon^2}\,\frac{\sin\xi}{1+\varepsilon\cos\xi}\right]+C\end{aligned} \quad \textbf{(4.26)}$$

It can be observed the highest temperature will occur at the minimum fluid film thickness (hot spot) and the lowest temperature at the maximum film thicknesses (cold spot), respectively, for the hydrodynamic plain journal bearings. The temperature difference between the hot and cold spots can be calculated using Equation (4.26)

$$\Delta T=T_{hot}-T_{cold}=\tilde{T}_{hot}-\tilde{T}_{cold}=\tilde{T}(\pi)-\tilde{T}(0)=\frac{\mu\omega D^2}{2\rho_l c_l C_b^2}\left[\frac{\pi}{(1-\varepsilon^2)^{3/2}}\right] \quad \textbf{(4.27a)}$$

The dimensionless temperature difference can be defined as

$$\frac{2\rho_l c_l C_b^2}{\mu\omega D^2}\Delta T=\frac{\pi}{(1-\varepsilon^2)^{3/2}} \quad \textbf{(4.27b)}$$

Figure 4.6 shows the curve of dimensionless temperature difference between the hot and cold spots over the entire range of eccentricity ratio using Equation (4.27b). It shows that within

the relatively broader range of small eccentricity ratio, the relationship between the temperature difference and the eccentricity ratio which is corresponding to the response displacement can be roughly considered to be linear. This agrees with the Morton's observations from his early experiment: "A linear relationship between differential temperature and orbit size was identified during these experiments." [10, 11, 24, 25]. This has also partially proved that the linear assumptions of the thermal imbalance made in Part 1 is reasonable.

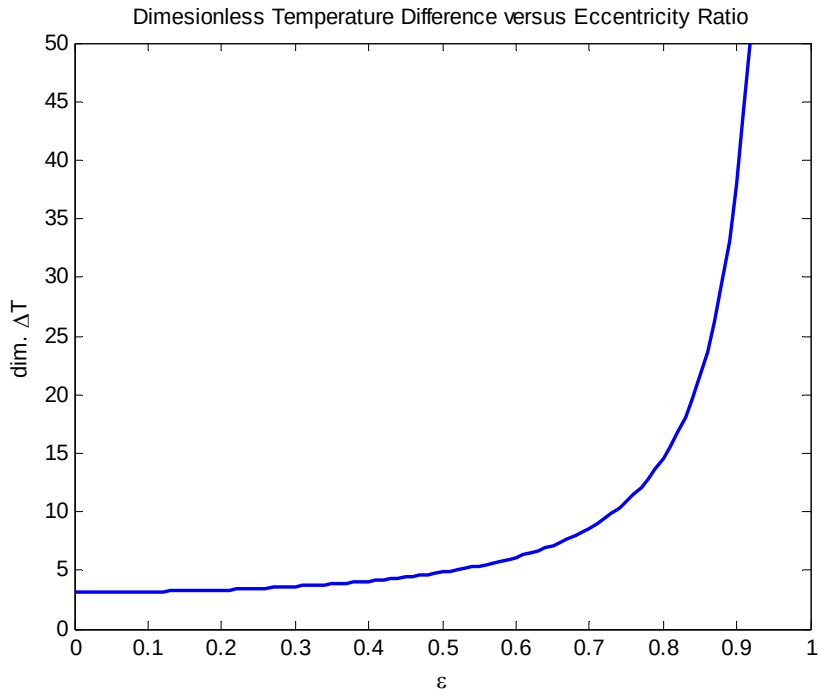

Figure 4.6 Dimensionless temperature difference versus eccentricity ratio

Through appropriate simplifications, Equation (4.25b) can be used to calculate the effective dynamic viscosity μ, which is dependent on the temperature [21, 34, 35]. Assume that the viscosity equals lubricant supply viscosity μ_o for the concentric operating where the oil film thickness equals the bearing clearance C_b . Equation (4.25b) can be written as

$$\frac{d\tilde{T}}{d\xi}+\tilde{A}\tilde{T}-\tilde{B}=0 \quad \textbf{(4.28)}$$

where $\tilde{A}=\frac{2H}{\rho_l c_l \omega C_b}$ $\tilde{B}=\frac{\mu_o \omega D^2}{2\rho_l c_l C_b^2}$

The temperature can be solved

$$\tilde{T}(\xi)=\frac{\tilde{B}}{\tilde{A}}+\left(\tilde{T}_o-\frac{\tilde{B}}{\tilde{A}}\right)e^{-\tilde{A}\xi} \quad \textbf{(4.29)}$$

where $\tilde{T}_o=\tilde{T}(\xi=0)=T_o-T_{amb}$. T_o is the lubricant supply temperature.

The average temperature difference is

$$\Delta T_{avg}=\tilde{T}(\pi)-\tilde{T}(0)=\left(\frac{\tilde{B}}{\tilde{A}}-\tilde{T}_o\right)(1-e^{-\tilde{A}\pi}) \quad \textbf{(4.30)}$$

The effective viscosity can be calculated using the exponential Reynolds formulation

$$\mu=\mu_o e^{-\beta\Delta T_{avg}} \quad \textbf{(4.31)}$$

where β is the thermoviscosity coefficient.

For the case where the heat transfer through solid surfaces is neglected, the average temperature difference can also be derived

$$\Delta T_{avg}=\tilde{T}(\pi)-\tilde{T}(0)=\tilde{B}\pi \quad \textbf{(4.32)}$$

The corresponding effective viscosity of the lubricant is

$$\mu=\mu_o e^{-\beta\tilde{B}\pi} \quad \textbf{(4.33)}$$

4.3.3 Thermal Imbalance

1) Hot and cold spots

Figure 4.7 is the schematic diagram of the journal orbit in the bearing which is used to calculate the locations of hot spot and cold spot.

Let H and C represent the hot spot and cold spot at t moment. Also define

O_b – the center of the bearing

O_{jo} – the center of the journal at static equilibrium

O_j – the dynamic center of the journal at t moment

θ_{jo} – the angle between $\overline{O_{jo}O_b}$ and the positive x-axis, which is related to static attitude angle by $\theta_{jo}=\frac{3\pi}{2}+\varphi_o$

λ – the phase angle of the hot spot H

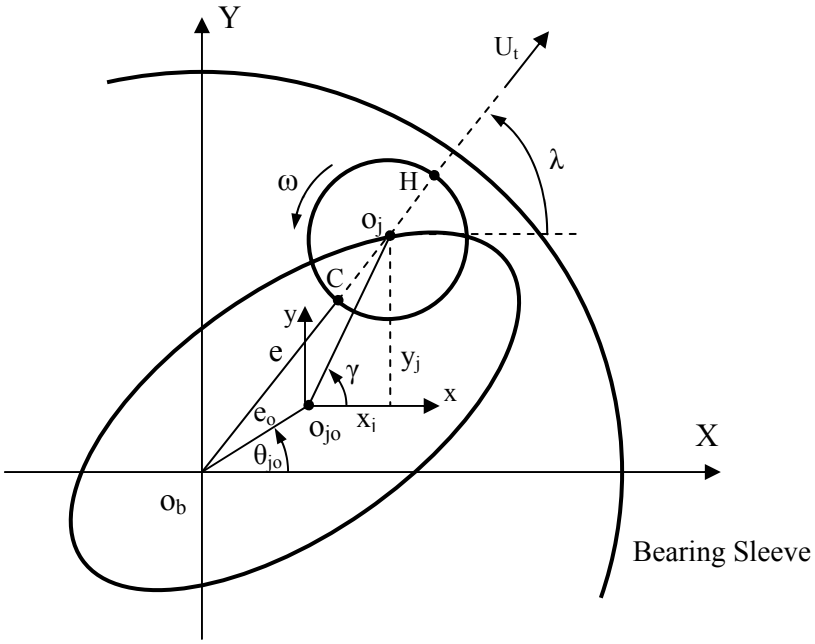

Figure 4.7 Journal orbit and locations of hot and cold spots

As discussed before, the direction of thermal imbalance will be from cold spot to hot spot. Hence, the location of hot spot must be identified first (the location of cold spot has just 180^o phase difference). Due to the hot spot correspondent with the minimum fluid film thickness, from the Figure 4.7, it can be found that the points O_b, O_j, H should be in the same line at any time instant. This leads to

$$\lambda=\tan^{-1}\left(\frac{y_j+e_o\sin(\theta_{jo})}{x_j+e_o\cos(\theta_{jo})}\right)=\tan^{-1}\left(\frac{\frac{y_j}{C_b}-\varepsilon_o\cos(\varphi_o)}{\frac{x_j}{C_b}+\varepsilon_o\sin(\varphi_o)}\right) \tag{4.34}$$

The dynamic eccentricity ratio of the journal will be needed to calculate the magnitude of the thermal imbalance, as shown in Equation (4.25b) and (4.27b)

$$\varepsilon=\frac{e}{C_b}=\frac{\sqrt{[x_j+e_o\cos(\theta_{jo})]^2+[y_j+e_o\sin(\theta_{jo})]^2}}{C_b}=\sqrt{[\frac{x_j}{C_b}+\varepsilon_o\sin(\varphi_o)]^2+[\frac{y_j}{C_b}-\varepsilon_o\cos(\varphi_o)]^2} \tag{4.35}$$

2) Thermal induced imbalance

The temperature difference between the hot spot and cold spot can be obtained by

$$\Delta T=T_{hot}-T_{cold} \tag{4.36}$$

If two bearings are identical and the rotor is symmetrical, the thermal induced deflection at the location of disk can be reduced using

$$\begin{aligned}&\Delta T_a=\Delta T_b=\Delta T\\&L_a=L_b=B\\&h_a=h_b=D\end{aligned} \tag{4.37}$$

Substitute above into Equation (4.16) to obtain the deflection

$$v_d = \frac{\alpha \Delta T B^2}{2D} \tag{4.38}$$

The equivalent thermal induced imbalance can be calculated

$$2U_t = 2m_d v_d = \frac{\alpha \Delta T B^2 m_d}{D} \tag{4.39}$$

For the case there is no heat transfer through both the journal and bearing surfaces, substitute Equation (4.27b) to Equation (3.39), the half-value thermal imbalance will be

$$\begin{aligned} U_t &= \left(\frac{\alpha B^2 m_d}{2D}\right)\left(\frac{\mu \omega D^2}{2\rho_l c_l C_b^2}\right)\left\{\frac{\pi}{\left[1-\left(\frac{x_j}{C_b}+\varepsilon_o \sin\varphi_o\right)^2-\left(\frac{y_j}{C_b}-\varepsilon_o \cos\varphi_o\right)^2\right]^{3/2}}\right\} \\ &= \frac{\alpha \mu \omega B^2 D m_d}{4\rho_l c_l C_b^2}\frac{\pi}{\left[1-\left(\frac{x_j}{C_b}+\varepsilon_o \sin\varphi_o\right)^2-\left(\frac{y_j}{C_b}-\varepsilon_o \cos\varphi_o\right)^2\right]^{3/2}} \\ &= U_{to}\frac{\pi}{\left[1-\left(\frac{x_j}{C_b}+\varepsilon_o \sin\varphi_o\right)^2-\left(\frac{y_j}{C_b}-\varepsilon_o \cos\varphi_o\right)^2\right]^{3/2}} \end{aligned} \tag{4.40}$$

where $U_{to} = \frac{\alpha \mu \omega B^2 D m_d}{4\rho_l c_l C_b^2} = \frac{\alpha \mu \omega D m_d}{\rho_l c_l \psi_b^2}\left(\frac{B}{D}\right)^2$ is defined as the characteristic thermal imbalance, which consists of parameters of structure, materials, and working conditions.

Equation (4.40) shows that the thermal imbalance will grow nonlinearly in nature with the increase of displacement under the certain design conditions (U_{to} is constant). However, as indicated in Figure 4.6, it can also be considered to be approximately linear within the relatively broader range of small eccentricity ratio and response displacements.

It can also be seen from the expressions of U_t and U_{to} that for the fixed value of displacement, the thermal imbalance is proportional to the thermal expansion coefficient of the journal, dynamic viscosity of the lubricant, squared ratio of bearing length to diameter, bearing diameter, disk mass, and the operating speed. In addition, it is inversely proportional to the density and specific heat of the lubricant, and the squared relative clearance of bearing. This quantitative influence can be used to analyze the Morton Effect and the corresponding corrective actions to reduce its effect on the system stabilities.

4.3.4 Some Discussions

One of the possible interesting questions, after the equations and conclusions in Chapter 2 were obtained, is what values or levels of the equivalent coefficient of thermal effect α_t could be expected for a typical rotor system. Now consider an illustrative extended Jeffcott rotor as shown in Figure 2.6(a), but supported by two hydrodynamic plain journal bearings. The parameter values of the system are listed in Table 4.1, where the natural frequency of the rotor with the rigid supports, $\omega_n = \sqrt{k/m_d}$, is used as the reference.

By using Equation (4.27b), (4.33) and (4.40), the values of the thermal imbalance for the case where the heat transfer through the solid surfaces is neglected can be calculated. Figure 4.8 shows the thermal imbalance ratio U_t/U_m over the entire range of the bearing eccentricity ratio and the operating speeds from 1000 RPM to 10000 RPM. The mechanical imbalance is calculated using the definition of the centrifugal force equal to 10% of the total rotor weight at its maximum continuous operating speed [21-22].

$$2U_m = \frac{0.1W_{rotor}}{\omega_{MCOS}^2} \tag{4.41}$$

where the value of ω_{MCOS} is assumed to be 1047.20 rad/s (10000 RPM) in this case for the purpose of calculating U_m.

Table 4.1 Parameter values of illustrative rotor-hydrodynamic bearing system

Parameter	Value	Unit
Disk Mass $2m_d$	50	kg
Journal Mass m_j	5	kg
Stiffness of Shaft $2k$	13.72E6	N/m
Journal C.T. E. α	1.10E-5	$1/C^o$
Bearing Diameter D	50	mm
Bearing Length B	30	mm
Bearing Relative Clearance ψ	2.5E-3	
Lubricant Supply Viscosity μ_o	1.96E-2	$N\text{-}s/m^2$
Lubricant Density ρ_l	850	kg/m^3
Lubricant Specific Heat Capacity c_l	2000	$J/kg\text{-}C^o$
Thermoviscosity Coefficient β	0.029	$1/C^o$
Mechanical Imbalance $2U_m$	5.36E-5	kg-m
Natural Frequency $\omega_n = \sqrt{k/m_d}$	523.83	rad/s

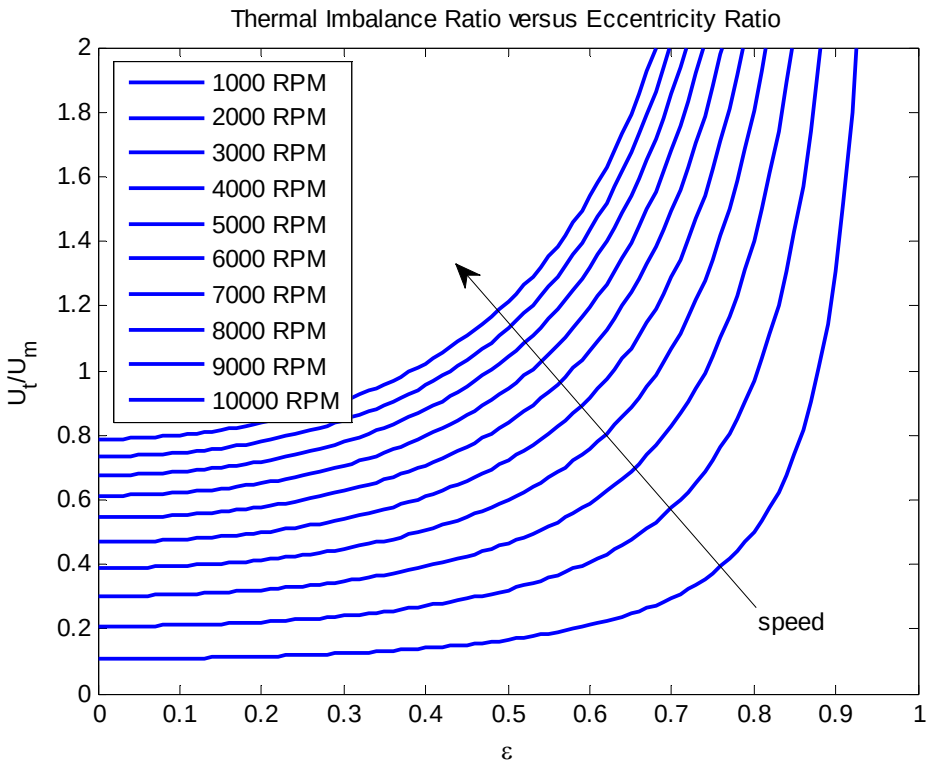

Figure 4.8 Thermal imbalances of illustrative rotor-bearing system

It can be seen that with the increase of the eccentricity ratio (corresponding to response displacement) and the operating speed, the thermal imbalance ratio rises and the thermal imbalance values gradually approach the magnitude of the mechanical imbalance. The large magnitude of thermal imbalance can be considered a signal of the possible occurrence of the Morton Effect induced thermal instability. Considering that the heat transfer through the solid surfaces has been neglected in this illustrative calculation, the actual thermal imbalance should be lower than what the curves show. However, it is still helpful to prove many conclusions obtained in Chapter 2. Due to the nonlinear expression for the thermal imbalance, no uniform value of the equivalent coefficient of thermal effect α_t could be obtained. However, the approximate magnitude value levels of the coefficient α_t can be evaluated using the slope of

thermal imbalance over eccentricity as shown in Equation (3.42a), which is correspondent to the definition of the coefficient α_t

$$\alpha_t \sim \frac{\partial U_t}{C_b \partial \varepsilon} = \frac{U_{to}}{C_b} \frac{3\pi\varepsilon}{(1-\varepsilon^2)^{5/2}} \tag{4.42a}$$

As in Chapter 2, use the thermal imbalance mass ratio to represent the relative level of the coefficient α_t

$$A_t = \frac{\alpha_t}{m_d} \sim \frac{\frac{\partial U_t}{C_b \partial \varepsilon}}{m_d} \tag{4.42b}$$

The results are shown in Figure 4.9. These results give a rough idea about the possible magnitude of the equivalent coefficient of thermal effect α_t for a typical hydrodynamic bearing supported mid-span rotor.

For an illustrative example, consider a hypothetical system where the rotor is supported by two linear isotropic bearings whose stiffness is $k_b = 5 \times 10^6$ N/m but the Morton Effect is produced by the above hydrodynamic plain journal bearings. The threshold speed ratio of instability defined by Equation (2.25), for the evaluated values of A_t indicated by Figure 4.9, are calculated and shown in Figure 4.10. It can be seen that the threshold speed ratio of instability decreases with the increase of the thermal imbalance mass ratios. Considering that the rotor with the hydrodynamic plain journal bearings might encounter the instability due to the oil film self-induced vibration around two times natural frequency, it should be paid a particular attention once the Morton Effect induced instability threshold falls below $2 \times \omega_n$.

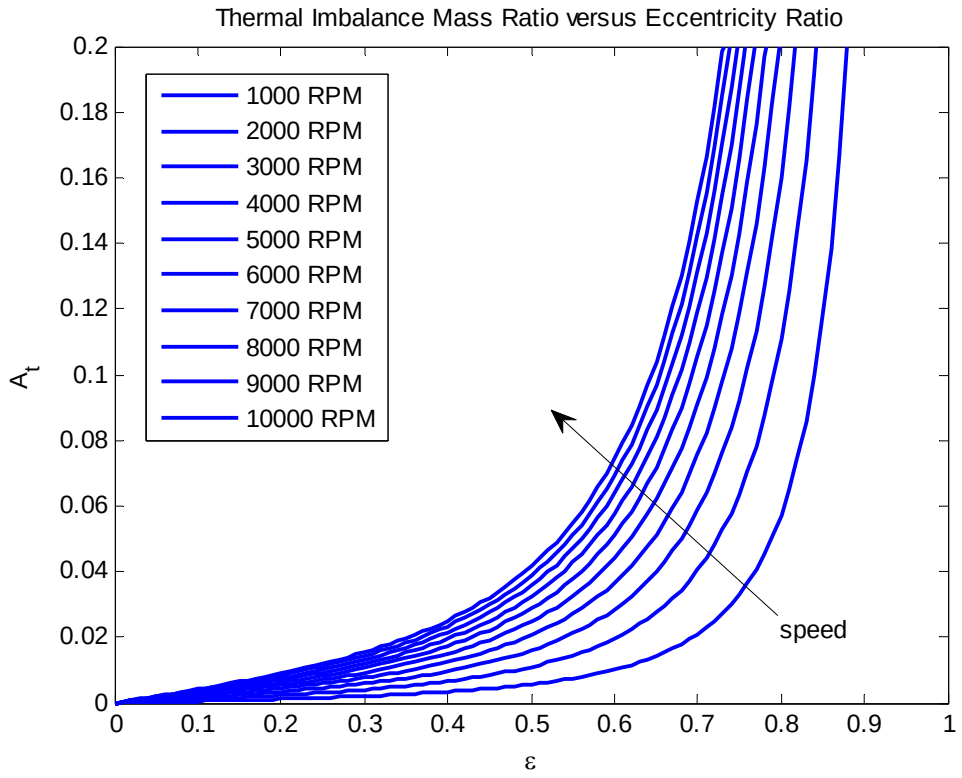

Figure 4.9 Slope of thermal imbalances of illustrative rotor-bearing system

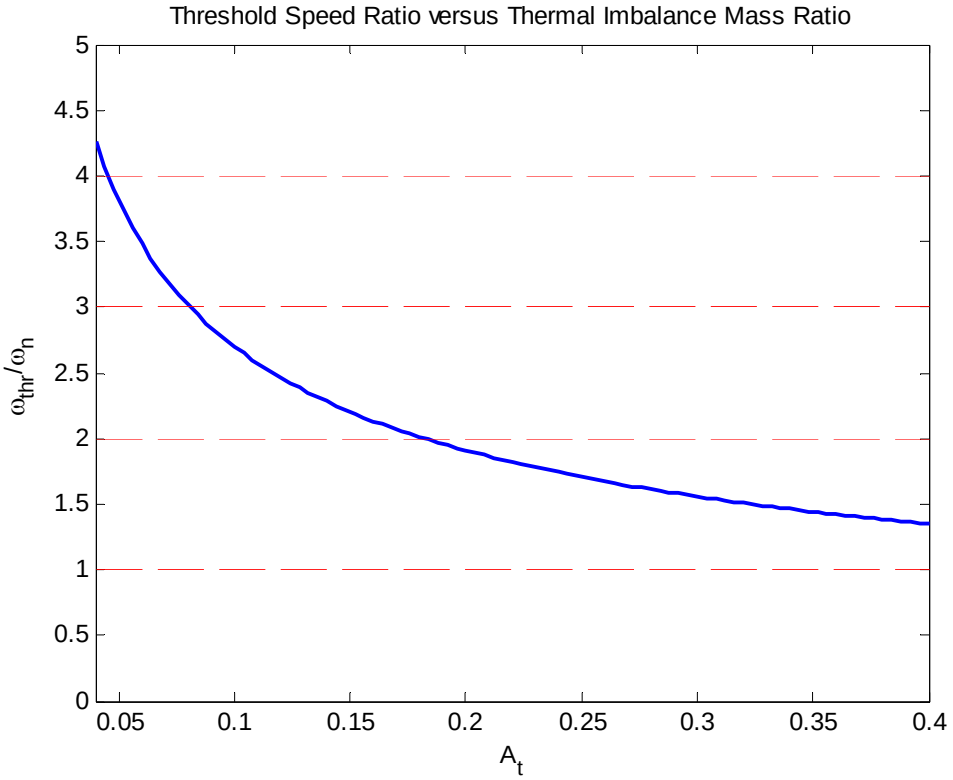

Figure 4.10 Threshold speed for illustrative calculation

4.4 Models and Equations of Rotor-Bearing Systems Incorporating Morton Effect

In this section, a simplified model and equations to describe the symmetrical elastic rotor (extended Jeffcott rotor) supported by two identical hydrodynamic plain journal bearings will be discussed. Figure 4.11 shows the schematic diagram of the system and the orbits of the journal and the disk in a coordinate system oriented at the static equilibrium of the journal center.

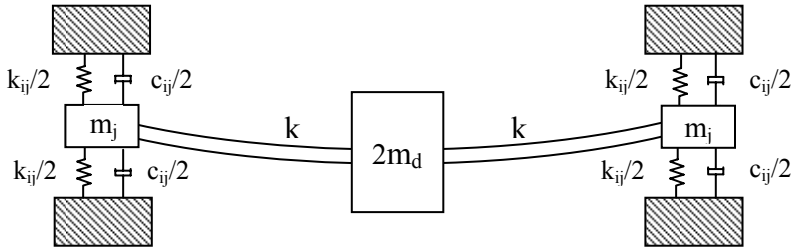

(a) Rotor and bearing model

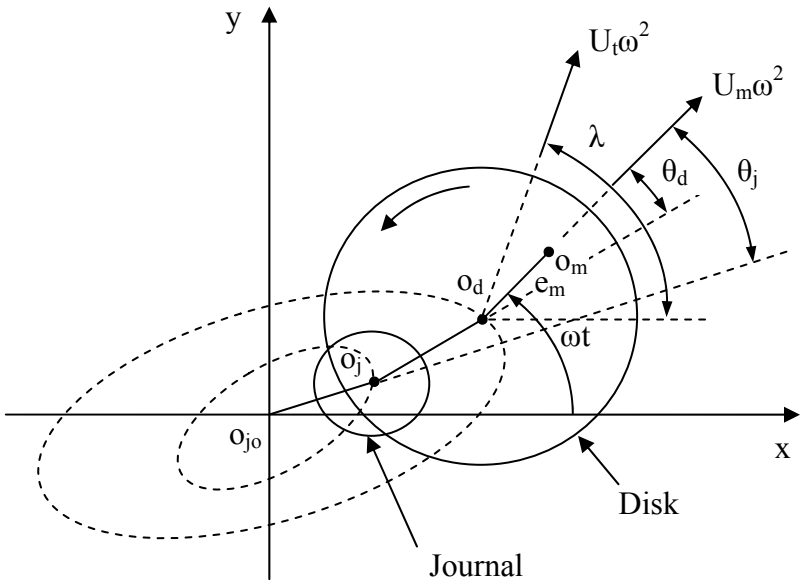

(b) Orbits of journal and disk

Figure 4.11 Schematic of Jeffcott rotor - hydrodynamic plain journal bearing system

4.4.1 Equations of Motion

The equations of motion of the system shown in Figure 4.11 can be expressed as

$$\begin{aligned}
&m_d\ddot{x}_d+k(x_d-x_j)=U_m\omega^2\cos\omega t+U_t\omega^2\cos\lambda\\
&m_d\ddot{y}_d+k(y_d-y_j)=U_m\omega^2\sin\omega t+U_t\omega^2\sin\lambda\\
&m_j\ddot{x}_j+c_{xx}\dot{x}_j+c_{xy}\dot{y}_j+k_{xx}x_j+k_{xy}y_j-k(x_d-x_j)=0\\
&m_j\ddot{y}_j+c_{yx}\dot{x}_j+c_{yy}\dot{y}_j+k_{yx}x_j+k_{yy}y_j-k(y_d-y_j)=0
\end{aligned} \qquad \textbf{(4.43)}$$

where U_m is the mechanical imbalance and U_t the thermal imbalance; λ is the phase angle of hot spot, which also serves as the phase angle of the thermal imbalance in this model (the direction of thermal imbalance has been defined to be from the cold spot to the hot spot for mid-span rotor systems).

From Figure 4.7 and discussion in Section 4.3.3

$$\begin{aligned}
\cos\lambda&=\frac{x_j+e_o\cos(\theta_{jo})}{\sqrt{[x_j+e_o\cos(\theta_{jo})]^2+[y_j+e_o\sin(\theta_{jo})]^2}}\\
&=\frac{\frac{x_j}{C_b}+\varepsilon_o\sin(\varphi_o)}{\sqrt{[\frac{x_j}{C_b}+\varepsilon_o\sin(\varphi_o)]^2+[\frac{y_j}{C_b}-\varepsilon_o\cos(\varphi_o)]^2}}
\end{aligned} \qquad \textbf{(4.44)}$$

$$\begin{aligned}
\sin\lambda&=\frac{y_j+e_o\sin(\theta_{jo})}{\sqrt{[x_j+e_o\cos(\theta_{jo})]^2+[y_j+e_o\sin(\theta_{jo})]^2}}\\
&=\frac{\frac{y_j}{C_b}-\varepsilon_o\cos(\varphi_o)}{\sqrt{[\frac{x_j}{C_b}+\varepsilon_o\sin(\varphi_o)]^2+[\frac{y_j}{C_b}-\varepsilon_o\cos(\varphi_o)]^2}}
\end{aligned}$$

The equations of motion of the system can be written as

$$m_d\ddot{x}_d+k(x_d-x_j)-U_t\omega^2\frac{\frac{x_j}{C_b}+\varepsilon_o\sin\varphi_o}{\left[(\frac{x_j}{C_b}+\varepsilon_o\sin\varphi_o)^2+(\frac{y_j}{C_b}-\varepsilon_o\cos\varphi_o)^2\right]^{1/2}}=U_m\omega^2\cos\omega t$$

$$m_d\ddot{y}_d+k(y_d-y_j)-U_t\omega^2\frac{\frac{y_j}{C_b}-\varepsilon_o\cos\varphi_o}{\left[(\frac{x_j}{C_b}+\varepsilon_o\sin\varphi_o)^2+(\frac{y_j}{C_b}-\varepsilon_o\cos\varphi_o)^2\right]^{1/2}}=U_m\omega^2\sin\omega t \qquad \textbf{(4.45)}$$

$$m_j\ddot{x}_j+c_{xx}\dot{x}_j+c_{xy}\dot{y}_j+k_{xx}x_j+k_{xy}y_j-k(x_d-x_j)=0$$

$$m_j\ddot{y}_j+c_{yx}\dot{x}_j+c_{yy}\dot{y}_j+k_{yx}x_j+k_{yy}y_j-k(y_d-y_j)=0$$

Consider the case where there is no heat transfer through the journal and bearing surfaces (adiabatic). By substituting Equations (4.40) to Equation (4.45), the the system equations will become

$$m_d\ddot{x}_d+k(x_d-x_j)-U_{to}\omega^2\frac{\pi}{\left[1-(\frac{x_j}{C_b}+\varepsilon_o\sin\varphi_o)^2-(\frac{y_j}{C_b}-\varepsilon_o\cos\varphi_o)^2\right]^{3/2}}\frac{\frac{x_j}{C_b}+\varepsilon_o\sin\varphi_o}{\left[(\frac{x_j}{C_b}+\varepsilon_o\sin\varphi_o)^2+(\frac{y_j}{C_b}-\varepsilon_o\cos\varphi_o)^2\right]^{1/2}}=U_m\omega^2\cos\omega t$$

$$m_d\ddot{y}_d+k(y_d-y_j)-U_{to}\omega^2\frac{\pi}{\left[1-(\frac{x_j}{C_b}+\varepsilon_o\sin\varphi_o)^2-(\frac{y_j}{C_b}-\varepsilon_o\cos\varphi_o)^2\right]^{3/2}}\frac{\frac{y_j}{C_b}-\varepsilon_o\cos\varphi_o}{\left[(\frac{x_j}{C_b}+\varepsilon_o\sin\varphi_o)^2+(\frac{y_j}{C_b}-\varepsilon_o\cos\varphi_o)^2\right]^{1/2}}=U_m\omega^2\sin\omega t$$

$$m_j\ddot{x}_j+c_{xx}\dot{x}_j+c_{xy}\dot{y}_j+k_{xx}x_j+k_{xy}y_j-k(x_d-x_j)=0$$

$$m_j\ddot{y}_j+c_{yx}\dot{x}_j+c_{yy}\dot{y}_j+k_{yx}x_j+k_{yy}y_j-k(y_d-y_j)=0$$

(4.46)

where $U_{to}=\dfrac{\alpha\mu\omega Dm_d}{\rho_l c_l \psi_b^2}\left(\dfrac{B}{D}\right)^2$

4.4.2 Stability Analysis

The equations of motion as shown in Equation (4.45) or (4.46) are basically nonlinear. The local stability of the system around its equilibriums can be analyzed through calculating the eigenvalues of its corresponding Jacobian matrix at the equilibriums [41-42].

Still consider the case where there is no heat transfer through the journal and bearing surfaces (adiabatic) and define

$$\begin{bmatrix} x_1 \\ x_2 \\ x_3 \\ x_3 \\ x_3 \\ x_3 \\ x_3 \\ x_3 \end{bmatrix} = \begin{bmatrix} x_d \\ \dot{x}_d \\ y_d \\ \dot{y}_d \\ x_j \\ \dot{x}_j \\ y_j \\ \dot{y}_j \end{bmatrix} \tag{4.47}$$

Write the equations of motion shown in Equation (4.46) in the space state

$$\begin{bmatrix} \dot{x}_1 \\ \dot{x}_2 \\ \vdots \\ \vdots \\ \vdots \\ \vdots \\ \vdots \\ \dot{x}_8 \end{bmatrix} = \begin{bmatrix} f_1(x_1, x_2, \cdots\cdots, x_8) \\ f_2(x_1, x_2, \cdots\cdots, x_8) \\ \vdots \\ \vdots \\ \vdots \\ \vdots \\ \vdots \\ f_8(x_1, x_2, \cdots\cdots, x_8) \end{bmatrix} \tag{4.48}$$

The Jacobian Matrix takes the form

$$J = \begin{bmatrix} \frac{\partial f_1}{\partial x_1} & \frac{\partial f_1}{\partial x_2} & \cdots & \cdots & \cdots & \frac{\partial f_1}{\partial x_8} \\ \frac{\partial f_2}{\partial x_1} & \frac{\partial f_2}{\partial x_2} & \cdots & \cdots & \cdots & \frac{\partial f_2}{\partial x_8} \\ \vdots & & & & & \vdots \\ \vdots & & & & & \vdots \\ \vdots & & & & & \vdots \\ \frac{\partial f_8}{\partial x_1} & \frac{\partial f_8}{\partial x_2} & \cdots & \cdots & \cdots & \frac{\partial f_8}{\partial x_8} \end{bmatrix} \quad \textbf{(4.49)}$$

Substitute Equation (4.46) into Equations (4.48) and (4.49), the Jacobian matrix of the system considering for the case where there is no heat transfer through the journal and bearing surfaces (adiabatic) can be obtained

$$J = \begin{bmatrix} 0 & 1 & 0 & 0 & 0 & 0 & 0 & 0 \\ -\frac{k}{m_d} & 0 & 0 & 0 & J_{25} & 0 & J_{27} & 0 \\ 0 & 0 & 0 & 1 & 0 & 0 & 0 & 0 \\ 0 & 0 & -\frac{k}{m_d} & 0 & J_{45} & 0 & J_{47} & 0 \\ 0 & 0 & 0 & 0 & 0 & 1 & 0 & 0 \\ \frac{k}{m_j} & 0 & 0 & 0 & -\frac{k+k_{xx}}{m_j} & -\frac{c_{xx}}{m_j} & -\frac{k_{xy}}{m_j} & -\frac{c_{xy}}{m_j} \\ 0 & 0 & 0 & 0 & 0 & 0 & 0 & 1 \\ 0 & 0 & \frac{k}{m_j} & 0 & -\frac{k_{yx}}{m_j} & -\frac{c_{yx}}{m_j} & -\frac{k+k_{yy}}{m_j} & -\frac{c_{yy}}{m_j} \end{bmatrix} \quad \textbf{(4.50)}$$

where

$$J_{25}=\frac{\partial f_2}{\partial x_5}=\frac{k}{m_d}+\frac{U_{to}\omega^2\pi}{m_d C_b}\left\{\frac{3(\frac{x_j}{C_b}+\varepsilon_o\sin\varphi_o)^2}{\left[1-(\frac{x_j}{C_b}+\varepsilon_o\sin\varphi_o)^2-(\frac{y_j}{C_b}-\varepsilon_o\cos\varphi_o)^2\right]^{5/2}\left[(\frac{x_j}{C_b}+\varepsilon_o\sin\varphi_o)^2+(\frac{y_j}{C_b}-\varepsilon_o\cos\varphi_o)^2\right]^{1/2}}\right.$$
$$\left.+\frac{(\frac{y_j}{C_b}-\varepsilon_o\cos\varphi_o)^2}{\left[1-(\frac{x_j}{C_b}+\varepsilon_o\sin\varphi_o)^2-(\frac{y_j}{C_b}-\varepsilon_o\cos\varphi_o)^2\right]^{3/2}\left[(\frac{x_j}{C_b}+\varepsilon_o\sin\varphi_o)^2+(\frac{y_j}{C_b}-\varepsilon_o\cos\varphi_o)^2\right]^{3/2}}\right\}$$

$$J_{27}=\frac{\partial f_2}{\partial x_7}=\frac{U_{to}\omega^2\pi}{m_d C_b}\left\{\frac{3(\frac{x_j}{C_b}+\varepsilon_o\sin\varphi_o)(\frac{y_j}{C_b}-\varepsilon_o\cos\varphi_o)}{\left[1-(\frac{x_j}{C_b}+\varepsilon_o\sin\varphi_o)^2-(\frac{y_j}{C_b}-\varepsilon_o\cos\varphi_o)^2\right]^{5/2}\left[(\frac{x_j}{C_b}+\varepsilon_o\sin\varphi_o)^2+(\frac{y_j}{C_b}-\varepsilon_o\cos\varphi_o)^2\right]^{1/2}}\right.$$
$$\left.+\frac{(\frac{x_j}{C_b}+\varepsilon_o\sin\varphi_o)(\frac{y_j}{C_b}-\varepsilon_o\cos\varphi_o)}{\left[1-(\frac{x_j}{C_b}+\varepsilon_o\sin\varphi_o)^2-(\frac{y_j}{C_b}-\varepsilon_o\cos\varphi_o)^2\right]^{3/2}\left[(\frac{x_j}{C_b}+\varepsilon_o\sin\varphi_o)^2+(\frac{y_j}{C_b}-\varepsilon_o\cos\varphi_o)^2\right]^{3/2}}\right\}$$

$$J_{45}=\frac{\partial f_4}{\partial x_5}=J_{27}$$

$$J_{47}=\frac{\partial f_4}{\partial x_7}=\frac{k}{m_d}+\frac{U_{to}\omega^2\pi}{m_d C_b}\left\{\frac{3(\frac{y_j}{C_b}-\varepsilon_o\cos\varphi_o)^2}{\left[1-(\frac{x_j}{C_b}+\varepsilon_o\sin\varphi_o)^2-(\frac{y_j}{C_b}-\varepsilon_o\cos\varphi_o)^2\right]^{5/2}\left[(\frac{x_j}{C_b}+\varepsilon_o\sin\varphi_o)^2+(\frac{y_j}{C_b}-\varepsilon_o\cos\varphi_o)^2\right]^{1/2}}\right.$$
$$\left.+\frac{(\frac{x_j}{C_b}+\varepsilon_o\sin\varphi_o)^2}{\left[1-(\frac{x_j}{C_b}+\varepsilon_o\sin\varphi_o)^2-(\frac{y_j}{C_b}-\varepsilon_o\cos\varphi_o)^2\right]^{3/2}\left[(\frac{x_j}{C_b}+\varepsilon_o\sin\varphi_o)^2+(\frac{y_j}{C_b}-\varepsilon_o\cos\varphi_o)^2\right]^{3/2}}\right\}$$

At the equilibrium position ($x_j=y_j=0$), the above four elements become as

$$J_{25}\ (x_j=0,\ y_j=0) = \frac{k}{m_d} + \frac{U_{to}\omega^2\pi}{m_d C_b}\left[\frac{3(\varepsilon_o \sin\varphi_o)^2}{(1-\varepsilon_o^2)^{5/2}\varepsilon_o} + \frac{(\varepsilon_o \cos\varphi_o)^2}{(1-\varepsilon_o^2)^{3/2}\varepsilon_o^3}\right]$$

$$J_{27}\ (x_j=0,\ y_j=0) = \frac{U_{to}\omega^2\pi}{m_d C_b}\left[\frac{-3\varepsilon_o^2 \sin\varphi_o \cos\varphi_o}{(1-\varepsilon_o^2)^{5/2}\varepsilon_o} + \frac{\varepsilon_o^2 \sin\varphi_o \cos\varphi_o}{(1-\varepsilon_o^2)^{3/2}\varepsilon_o^3}\right] \quad \textbf{(4.51)}$$

$$J_{45}\ (x_j=0,\ y_j=0) = J_{27}\ (x_j=0,\ y_j=0)$$

$$J_{47}\ (x_j=0,\ y_j=0) = \frac{k}{m_d} + \frac{U_{to}\omega^2\pi}{m_d C_b}\left[\frac{3(\varepsilon_o \cos\varphi_o)^2}{(1-\varepsilon_o^2)^{5/2}\varepsilon_o} + \frac{(\varepsilon_o \sin\varphi_o)^2}{(1-\varepsilon_o^2)^{3/2}\varepsilon_o^3}\right]$$

4.5 Simulation Results and Discussions

Use the system damping u_s to describe the system characteristics of stability, which is defined as the minimum value of negative real parts of all eigenvalues of Jacobian matrix as shown in Equation (4.50). In addition, the threshold speed of instability is defined as the point where the value of the system damping equals zero when it changes from the positive values to negative ones. This threshold speed may be due to the different factors in the system: the oil film self induced, the Morton Effect induced, or the both.

Consider a system whose parameter values are same as listed in Table 4.1 except for the bearing length. Two comparative cases have been calculated for the discussion. In Case1, the bearing length still takes the value of 30 mm (B/D=0.6), which represents a typical case in a standard rotor experiment. In Case 2, the bearing length is increased to 35 mm (B/D=0.7). The results of stability analysis are shown in Table 4.2 and Figure 4.12.

It can be seen that in Case 1, the value of threshold speed of instability is decreased by 190 RPM if the Morton Effect is included in the calculation. Comparatively, the Morton Effect

becomes more apparent In Case 2, with the increase of the bearing length. The threshold speed drop due to the Morton Effect is increased to be 360 RPM.

Table 4.2 Threshold speeds of instability for two comparative cases

Case No.	Bearing Length	$\frac{B}{D}$	Threshold Speed of Instability (RPM)		
			without Morton Effect	with Morton Effect	difference
1	30	0.6	7240	7050	-190
2	35	0.7	7320	6960	-360

The results of above calculations show that the inclusion of the Morton Effect may lead to an unstable operation of the system. Considering the existence of the traditional oil film self-induced vibration, the Morton Effect may make a further negative impact on the instabilities of the rotor system under some working conditions.

Figure 4.13, 14, and 15 show the curves of the bearing eccentricity ratios, temperature differences, and thermal imbalances, respectively, over the entire speed range of the operation for the two calculated cases. It is interesting to note that the temperature differences in Case 2 actually are slightly lower than that of Case 1. This is because the bearing eccentricity ratios in Case 2 are relatively smaller than in Case 1, due to the increase of the bearing length. However, the thermal imbalances in Case 2 are apparently larger than that of Case1. This relationship can be explained by Equation (4.39)

The transient responses to the unbalanced excitation of the same system starting at the equilibrium have been simulated using the MATHWORKS MATLAB-SIMULINK. This calculation is based on the Equation (4.46). The results of Case 1 are shown in Figure 4.16,

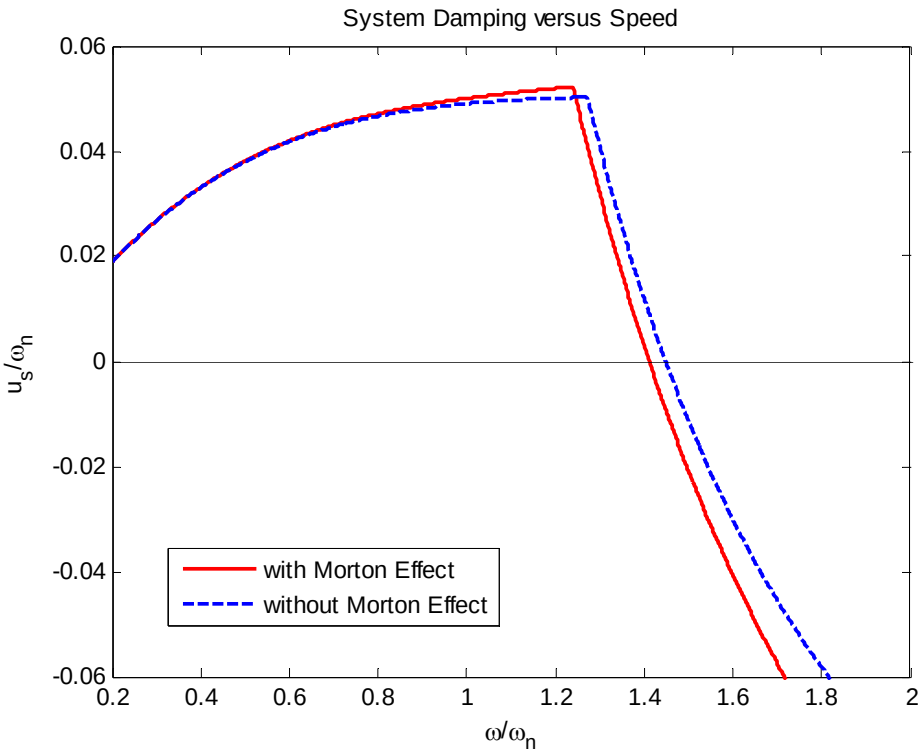

(a) Case 1

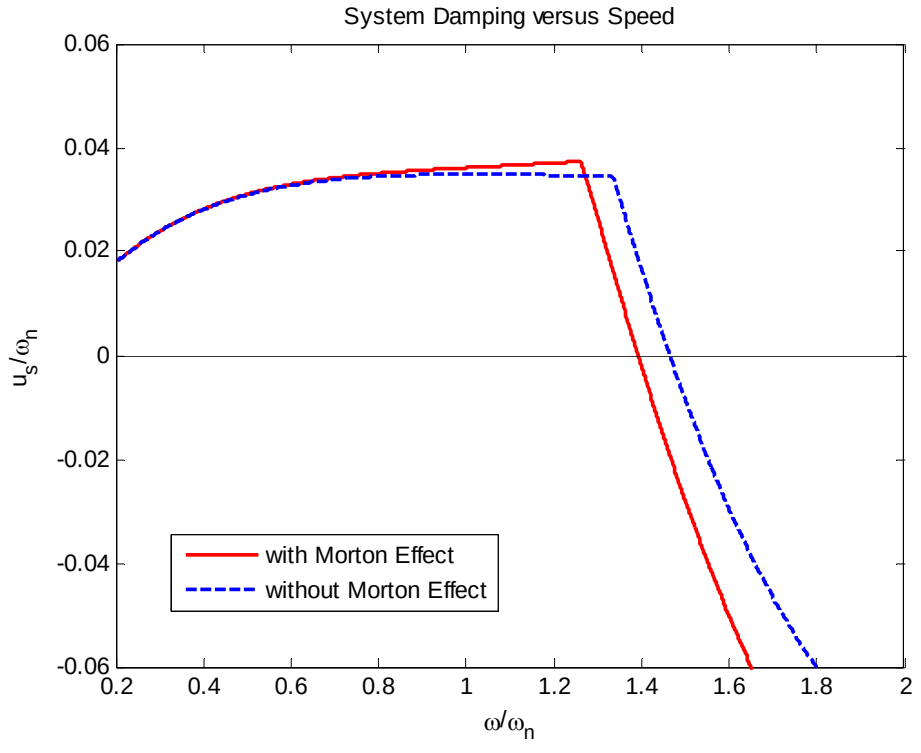

(b) Case 2

Figure 4.12 System damping versus speed of two comparative cases

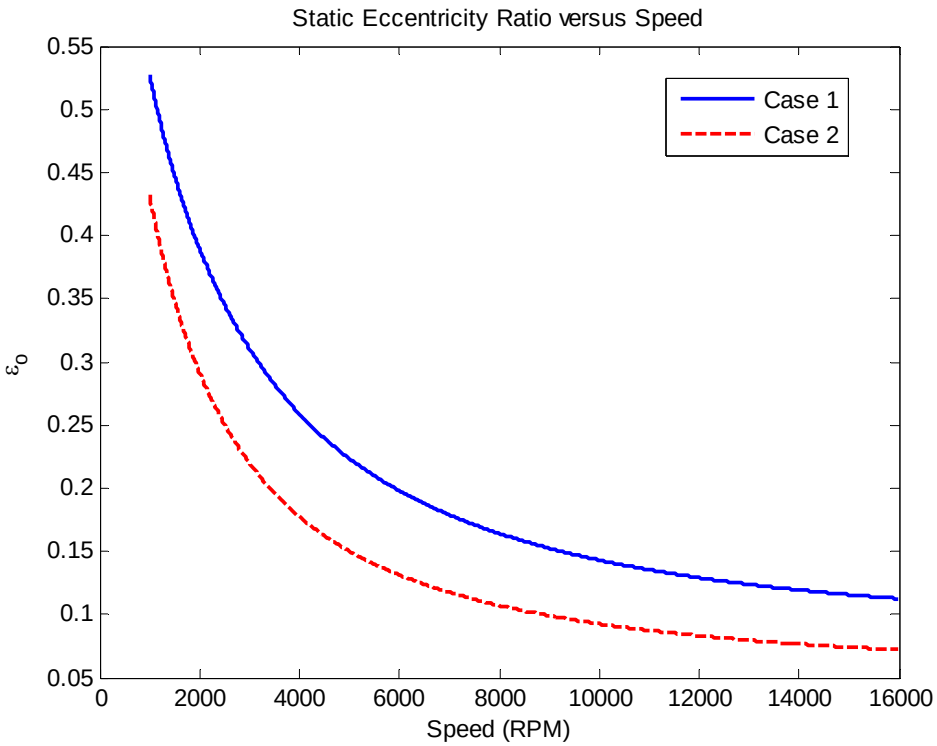

Figure 4.13 Static eccentricity ratio of the bearing versus speed

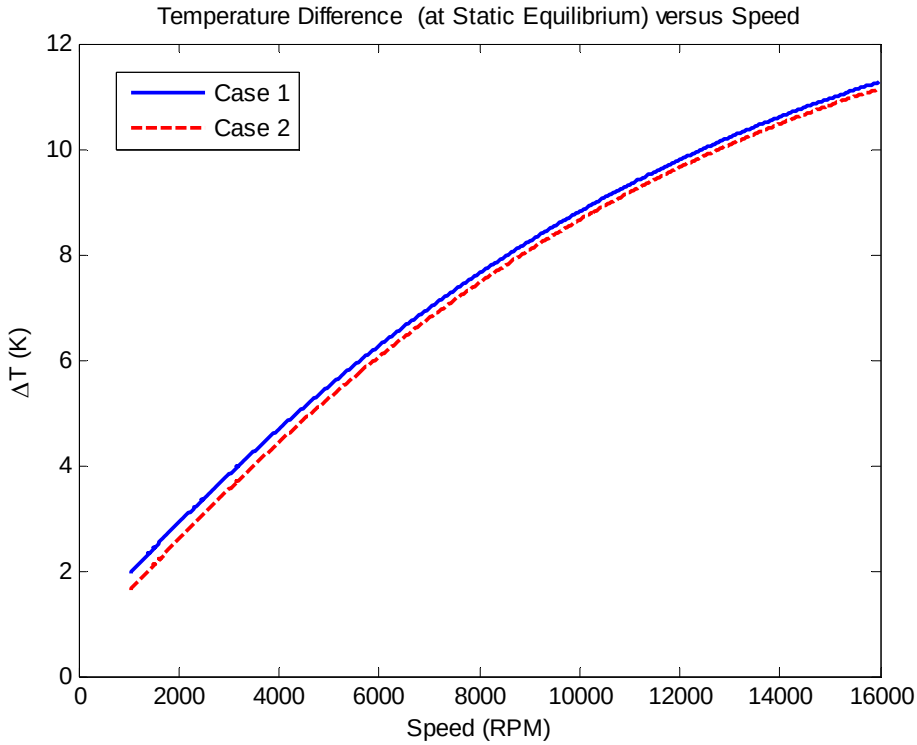

Figure 4.14 Temperature difference versus speed

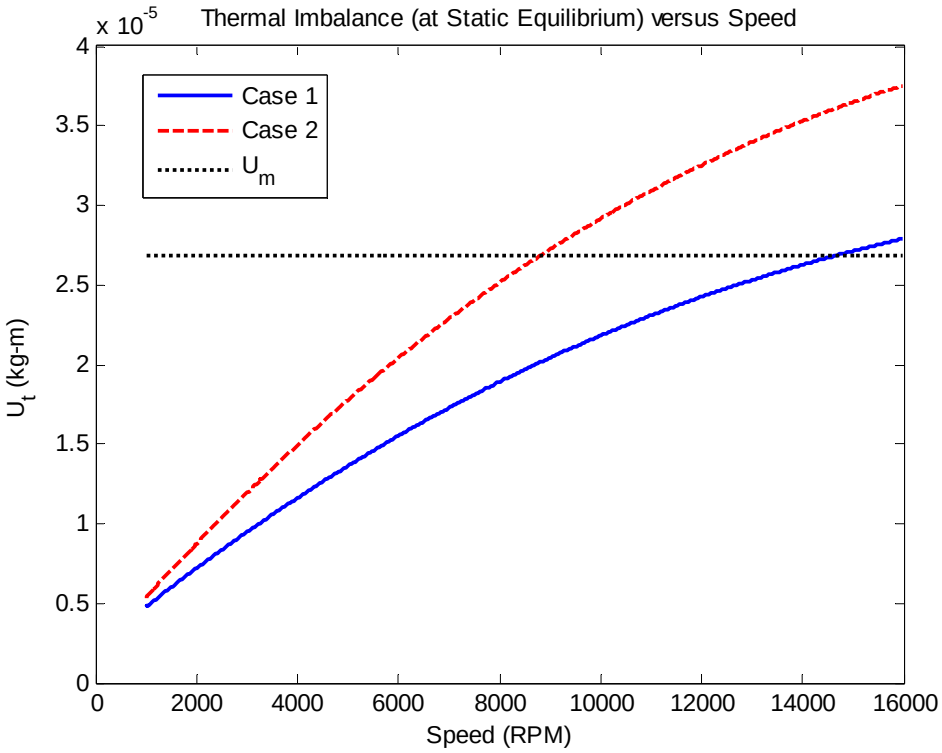

Figure 4.15 Thermal imbalance versus speed

where the rotor is running at 4000 RPM. Figure 4.16 includes the transient responses at the locations of the journal and the disk before and after the Morton Effect is included in the simulations. It can be seen that the inclusion of the Morton Effect also has an impact on the unbalance response the system. While the orbits at the journal and the disk of the non-Morton Effect system are the elliptical as expected, the Morton Effect truly changes the shapes of the orbits. Although it looks like the locations of two orbits were shifted for the Morton Effect included system, the truth is that due to the changing values of the phase difference between the mechanical imbalance and the thermal imbalance over cycles of the whirling motion in this particular system, one side of the orbits is decreased in magnitude while the other side is increased. It is true for both locations at the journal and the disk.

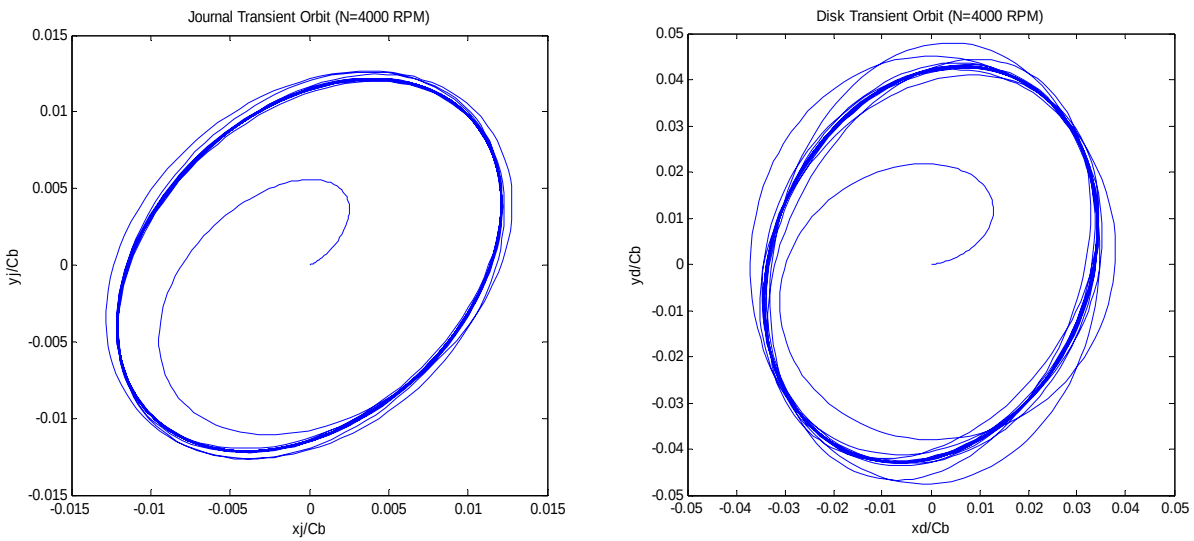

(a) Without Morton Effect

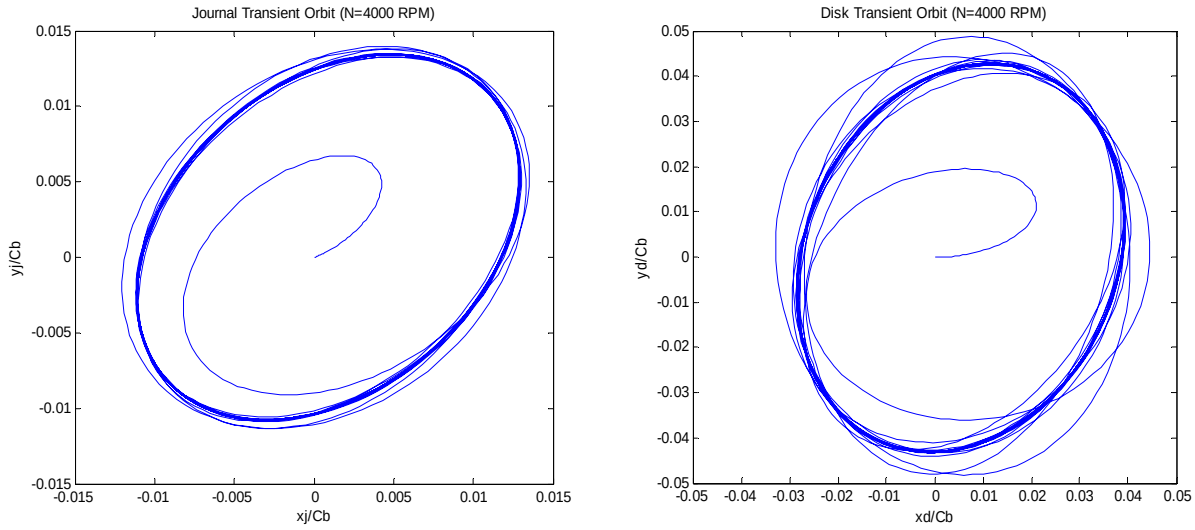

(b) With Morton Effect

Figure 4.16 Transient responses at journal and disk (Case 1)

Figure 4.17 is the SIMULINK model for the simulations of the mid-span rotor-hydrodynamic plain journal bearing systems.

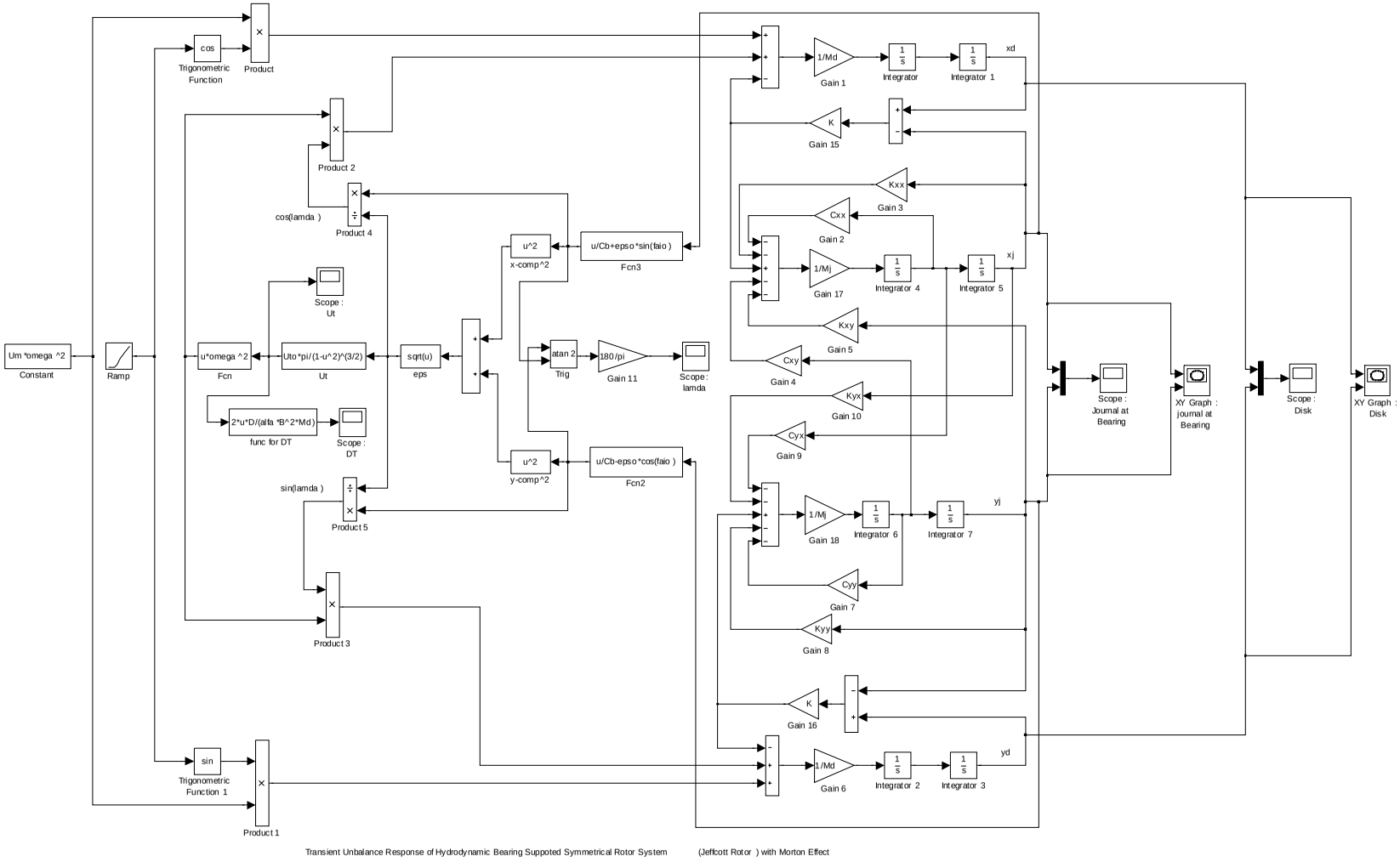

Figure 4.17 SIMULINK model for mid-span rotor - hydrodynamic bearing system

4.6 Summary

A systematic study on the symmetrical mid-span rotor supported on hydrodynamic plain journal bearings has been conducted. The major conclusions can be summarized as follows:

(1) A new thermal bending model of mid-span rotors has been presented. The formulas of deflections are obtained, which is the basis to calculate the equivalent thermal imbalance. The suggested thermal bending model can also partially explain that the mid-span rotors are less liable to be influenced by the Morton Effect induced instability because of the restraining effect between two supports, than the overhung configurations.

(2) Using an established equation to calculate the temperature distribution and temperature differences of hydrodynamic plain journal bearing, the new expressions of differential temperatures for the case where heat transfer through the bearing and journal surfaces is neglected have been derived for the analytical discussion. Figure 4.6 shows that for an eccentricity ratio less than 0.5, the relationship between the temperature difference and the eccentricity distance which is corresponding to the response displacement can be roughly considered to be linear.

(3) Based on the suggested thermal bending model and differential temperature formulas, the equivalent thermal imbalance can be calculated. Especially, for the case where heat transfer through solid surfaces is neglected, the closed form of thermal imbalance has been obtained.

(4) Using the obtained formulas of the thermal imbalance, initial calculation has been conducted to understand the magnitude levels of the thermal imbalance for a typical rotor model, which can be used to evaluate the equivalent coefficient of thermal effect. These initial results are promising and illustrative. They have also proved many important conclusions obtained in Chapter 2. It shows that the thermal imbalance induced by the Morton Effect may increase to the

level of the mechanical imbalance and then its influence on the system stability should be included.

(5) The model for the dynamics of a symmetrical elastic rotor–hydrodynamic plain journal bearing system has been established. The local stability around the equilibriums is conducted through calculating the characteristic roots of the system's Jacobian matrix. The simulation of the system transient response to unbalance excitation is also performed to exhibit the influence of the Morton Effect. The results show that the Morton Effect may make a further negative impact on the instabilities of the rotor system under some working conditions, considering the existence of the oil film self-induced vibration due to the dynamic characteristics of fluid film bearings. In addition, the Morton Effect also has an impact on the unbalance response of the system. The simulation results show that the Morton Effect changes the shapes of the whirling orbits and makes them no longer the standard elliptical orbits around the static equilibriums.

5 PREDICTIVE SOLUTIONS OF MORTON EFFECT INDUCED INSTABILITY FOR ROTOR – HYDRODYNAMIC BEARING SYSTEMS

5.1 System and Methodology

Considering that in the current practice the Morton Effect has not been included in the standard rotor dynamics calculations and software, it is necessary and practical to apply the predictive solutions to either predict or analyze the Morton Effect induced instability in the general rotor-hydrodynamic bearing systems. This method was originally presented and applied to overhung rotors in references [19-22]. In this chapter, the effort will be made to apply the predictive solutions to mid-span rotors. The Morton Effect predictive software covering both overhung and mid-span rotors supported by various hydrodynamic journal bearings will then be presented.

For the mid-span rotor systems to be discussed using predictive solutions, the assumptions have been made:

(1) The system consists of an elastic mid-span rotor and two hydrodynamics journal bearings. The rotor may be symmetrical or not. The available bearing types include plain (cylindrical) journal bearing or tilting pad journal bearing. Two bearings may be different in size.

(2) The thermal bending deflections are assumed to be small. Hence, it is assumed to be uncoupled with any other deformations.

(3) The whirling motion of the rotor is synchronous. The stability analysis and derived results are for the purpose of predicting instability when the system is subjected to the forced unbalance excitations.

The basic concept of the predictive solutions can be expressed as follows: In real machines satisfactory performance is established by using specified vibration, or unbalance threshold levels that are given in standards published by various organizations. One method of specifying such levels is to restrict the maximum allowable centrifugal force that acts on the machine. This restriction then limits the allowable imbalance for each speed value. Such a criterion determines whether the rotor will be "stable" or "unstable" during operation, i.e. if the total mechanical and thermal unbalance level exceeds the threshold level given by the allowable imbalance then the rotor will be "unstable."

The entire procedure of predictive solutions for the Morton Effect induced instability basically consists of the following steps:

(1) Determine the initial mechanical imbalance of the rotor

(2) Solve for the static equilibrium position and steady-state orbit of the journal

(3) Choose a number of dynamic positions of the journal for average thermal calculations

(4) Determine the hot and cold spot locations on the journal

(5) Compute the temperature gradient across the journal surface

(6) Compute the average temperature difference, thermal bend and thermal imbalance

(7) Calculate the total imbalance resulting from the mechanical and thermal imbalances

(8) Compare the total imbalance to the stability threshold

Figure 5.1 shows the flowchart of the entire procedure for the predictive solutions.

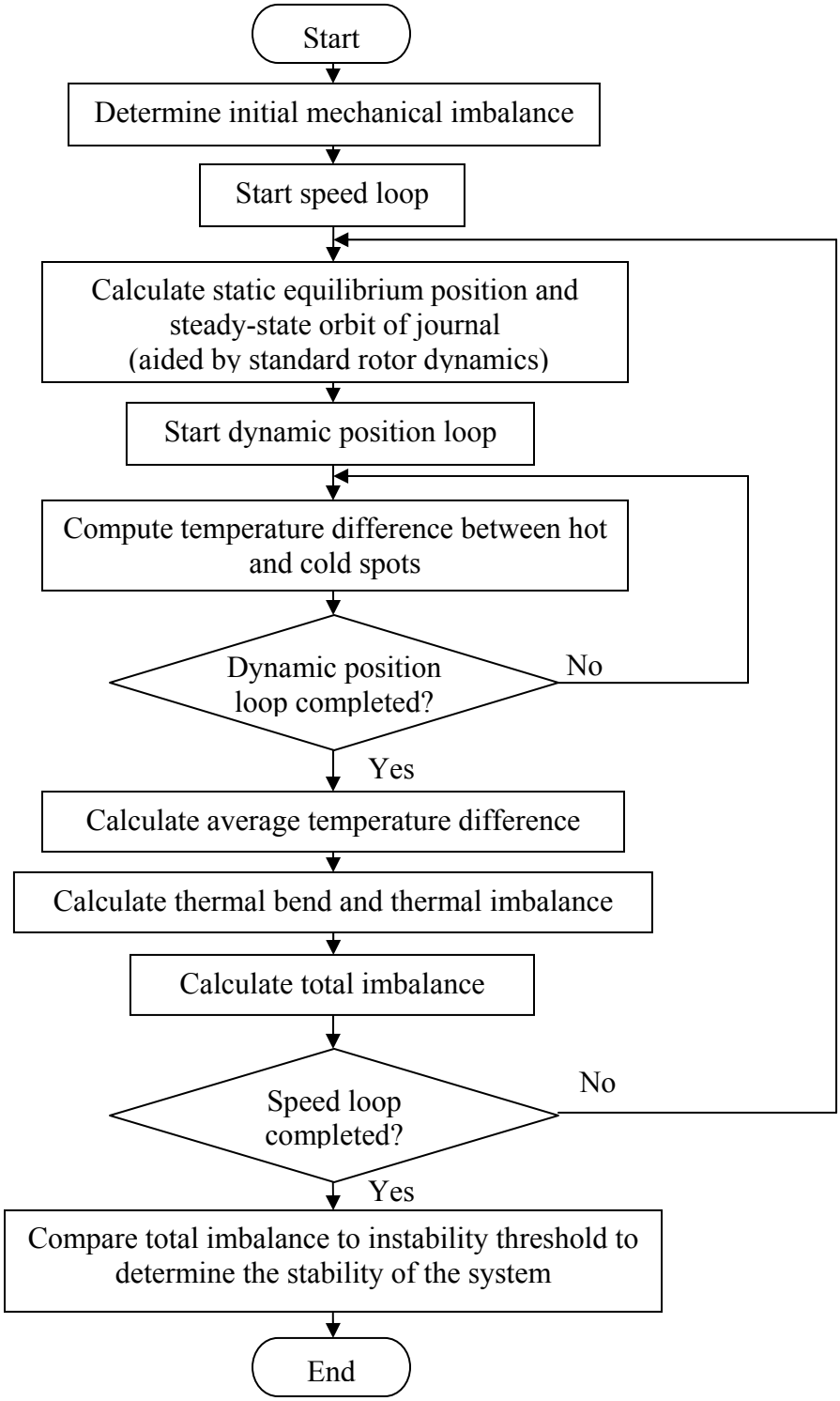

Figure 5.1 Flowchart of predictive solutions

5.2 Models and Equations

The models and equations to predict the Morton Effect induced instability in rotor-bearing systems will be presented in this section, with an emphasis on mid-span configurations. The detail discussions on overhung rotors can be found in references [19-23]. Please note that for a better reference, most of major equations to be used in predictive solutions will be displayed in the following paragraphs, where some of them may be in similar or modified forms as in the previous chapters. The theoretical details may not be repeated, if they have been discussed in the previous chapters. In addition, considering the following calculations are for general rotor models, the mass and imbalance values such as m_d, U_m, U_t, U etc. all refer to their respective total values (compared to the previous chapters where they represent half values for symmetrical rotors). All equations to be shown here are exclusively for the application of predictive solutions presented in this chapter:

1) Initial mechanical imbalance

A nominal initial mechanical imbalance U_m, has been defined as the imbalance created from a centrifugal force equal to 10% of the total static rotor weight W_{rotor}. This ratio selection is based on the experimental observation representing the most typical situation in reality. U_m will be calculated for the rotor running at its maximum continuous operating speed, ω_{MCOS}, which can be mathematically defined as:

$$U_m = \frac{0.1 W_{rotor}}{\omega_{MCOS}^2} \tag{5.1}$$

This imbalance will be assumed to act on the rotor at an initial phase angle of zero degree with respect to a coordinate system and will be located at the center-of-gravity of the overhung mass or mid-span mass.

2) Static equilibrium position and steady-state orbit

One of the essential calculations is to compute the static equilibrium position and steady-state orbit of the journal at bearing locations. First, the fluid film thickness expressions of the bearing must be known. For the plain journal bearing, Cameron [34] gives the following expression (Figure 4.4)

$$h=C_b(1+\varepsilon\cos\xi) \tag{5.2}$$

where ξ is the circumferential angle coordinate measured from the maximum fluid film thickness and the eccentricity ratio $\varepsilon=\frac{e}{C_b}$

The fluid film thickness expression for the tilting pad journal bearings has been derived by Balbahadur and Kirk [19-21]:

$$h=(R_p-R_j)+e\cos(\theta_c-\theta)-(R_p-R_b)\cos(\theta-\theta_p)-\delta(R_p+t_p)\sin(\theta-\theta_p) \tag{5.3}$$

where R_p = pad radius of curvature, R_j=radius of journal, R_j=radius of bearing, θ_c = angle to line joining journal center to bearing center, δ = tilt angle, and t_p = pad thickness.

To solve for the static equilibrium position, the narrow bearing assumption has been used for the fixed geometry journal bearing case. Such an assumption enabled the use of an analytical solution for the static eccentricity ratio and the static attitude angle as described in Section 4.3.1.

$$W=\frac{\mu\omega DB}{2\psi_b^2}\times\left(\frac{B}{D}\right)^2\frac{\varepsilon_o}{(1-\varepsilon_o^2)^2}\sqrt{\pi^2(1-\varepsilon_o^2)+16\varepsilon_o^2} \tag{5.4a}$$

$$\varphi_o=\tan^{-1}\frac{\pi\sqrt{1-\varepsilon_o^2}}{4\varepsilon_o} \tag{5.4b}$$

where ε_o represents the static eccentricity ratio and ψ_b is the relative clearance, $\psi_b = \frac{C_b}{D/2}$.

However, due to the complexity of the tilting pad bearings, it is necessary to numerically compute the static equilibrium position for this type bearing. The solutions by Balbahadur and Kirk [19-21] using finite element method is adopted for the tilting pad bearing calculations. It involves the balancing of the vertical and horizontal forces acting on the journal and the equilibrium of the moments acting on the pads. The resulting system of equations is then solved using the Newton-Raphson method.

For the suggested predictive solutions, the synchronous orbit of the journal must be known for an assumed initial mechanical imbalance. The standard rotor dynamics programs, such as DyRoBeS [43] and VT-FAST [44], can be used to compute the steady-state orbits of the journal. Figure 5.2 shows the schematic of the journal orbit, for the discussion of the predictive solutions. In general, the journal will traverse an elliptical path around its static equilibrium position O_{jo}.

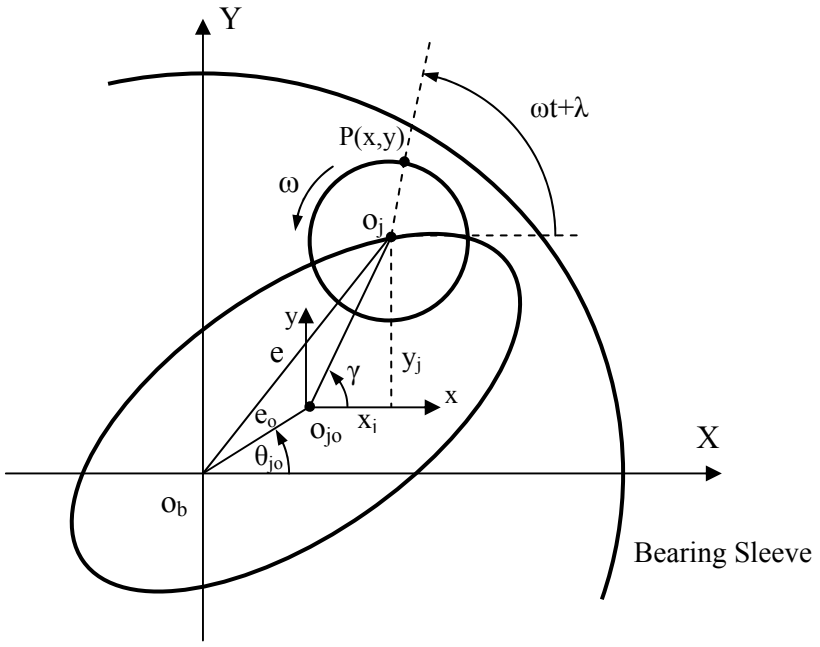

Figure 5.2 Journal orbit

The journal center O_j can be described as

$$\begin{aligned} x_j &= A_x \cos(\omega t + \varphi_x) \\ y_j &= A_y \sin(\omega t + \varphi_y) \end{aligned} \tag{5.5}$$

where A_x, A_y, φ_x, φ_y are the amplitudes and phase angles in x-axis and y-axis, respectively.

Once this orbit is known, the path taken by the general point P(x,y) on the journal surface can be mathematically described as:

$$\begin{aligned} x &= e_o \cos(\theta_{jo}) + A_x \cos(\omega t + \varphi_x) + R_j \cos(\omega t + \lambda) \\ y &= e_o \sin(\theta_{jo}) + A_y \sin(\omega t + \varphi_y) + R_j \sin(\omega t + \lambda) \end{aligned} \tag{5.6}$$

where λ is the initial phase of the point P.

For the plain journal bearing, the geometry in Figure 5.2 can be related to Equation (5.2) by using the following relationship:

$$\xi = \pi - (\omega t + \lambda - \theta_j) \tag{5.7}$$

where

$$\theta_j = \tan^{-1}\left[\frac{e_o \sin(\theta_{jo}) + A_y \sin(\omega t + \varphi_y)}{e_o \cos(\theta_{jo}) + A_x \cos(\omega t + \varphi_x)}\right]$$

$$\theta_{jo} = \frac{3\pi}{2} + \varphi_o$$

3) Dynamic journal positions

In the predictive solutions, a number of dynamic positions evenly distributed alone the steady-state orbit of the journal have been chosen to compute the average temperature gradients

developed across the journal surfaces for a given speed. The case studies on the overhung rotors show that 10 to 20 dynamic positions would give the results with satisfactory accuracy. As matter of fact, the number of 10 dynamic positions has been usually employed [19-23].

4) Hot spot and cold spot

To compute the temperature gradients across the journal surface, the locations of the hot spot and cold spot at each dynamic position must be identified. Use initial angle λ_o to define the location of hot spot. The time-dependent locations of the hot spot and the diametrically-opposite cold spot can now be obtained by using the following equations (Figure 5.2):

$$\begin{aligned} x_H &= e_o\cos(\theta_{jo}) + A_x\cos(\omega t+\varphi_x) + R_j\cos(\omega t+\lambda_o) \\ y_H &= e_o\sin(\theta_{jo}) + A_y\sin(\omega t+\varphi_y) + R_j\sin(\omega t+\lambda_o) \end{aligned} \qquad \textbf{(5.8a)}$$

and

$$\begin{aligned} x_C &= e_o\cos(\theta_{jo}) + A_x\cos(\omega t+\varphi_x) + R_j\cos(\omega t+\lambda_o+\pi) \\ y_C &= e_o\sin(\theta_{jo}) + A_y\sin(\omega t+\varphi_y) + R_j\sin(\omega t+\lambda_o+\pi) \end{aligned} \qquad \textbf{(5.8b)}$$

Several methods have been used to locate the hot and cold spot regions:

(1) Original Method

In this method, the hot spot (H) is defined as the point closest to the bearing sleeve at time t = 0 [19-21]. It is also assumed that $\gamma = \omega t+\lambda$ so that O_{j0}, O_j and H all lie on the same straight line at this instant (see Figure 5.2 and 5.3). Hence at time t = 0:

$$\gamma=\gamma_o=\tan^{-1}\left(\frac{A_y\sin\varphi_y}{A_x\cos\varphi_x}\right)=\lambda_o \qquad \textbf{(5.9)}$$

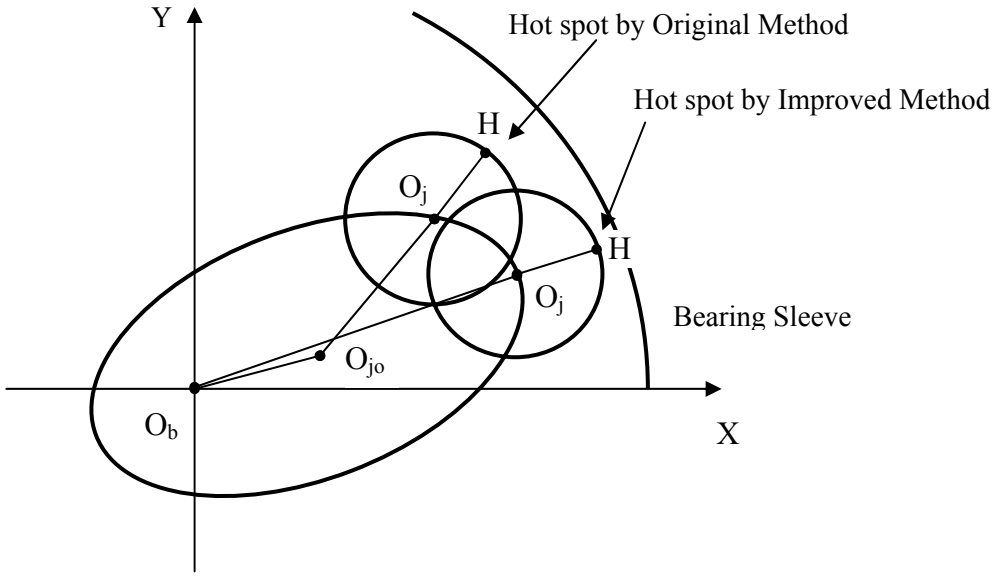

Figure 5.3 Hot spot locations

(2) Improved Method

For plain journal bearing, the hot spot can be defined as the point closest to the bearing at some instant $t=t_m$ [22-23]. Along the steady-state orbit, there exists a point which has the maximum dynamic eccentricity. The time t_m corresponding to this dynamic position can be obtained. In this configuration, the hot spot H is located on the straight line with O_b and O_j (Figure 5.3) at that instant. The following equation can be obtained:

$$\omega t_m+\lambda_o=\tan^{-1}\left(\frac{e_o\sin\theta_{jo}+A_y\sin(\omega t_m+\varphi_y)}{e_o\cos\theta_{jo}+A_x\cos(\omega t+\varphi_x)}\right) \qquad \textbf{(5.10)}$$

The initial angle to define the hot spot, λ_o, can then be determined.

The same principle can also be applied to tilting pad journal bearings where t_m is defined as the time instant with the maximum temperature of hot spot along the entire orbit. The determination of t_m involves the numerical solutions without the explicit expressions.

The application results on overhung rotors show that there is no big difference in computing the average temperature differences using above two methods [22-23]. Usually, Improved Method is the default selection.

(3) New Method

A new method has also been tried to locate the hot spot and cold spot. This method is based on the discussions in Section 4.3.3. The concept is different than the first two methods (see Figure 4.7). For hydrodynamic plain bearings, the hot spot and cold spot at each dynamic position of the journal can be identified using Equation (4.34). Due to the inherent difference of this new method, a new stability threshold may need to be set up (also see Chapter 7).

5) Temperature calculations 3

The calculations of temperature distributions across the journal surface have been discussed in Section 4.3.2. The basic governing equation is

$$\frac{d\tilde{T}}{d\xi}+\frac{2H}{\rho_l c_l \omega h}\tilde{T}-\frac{\mu\omega D^2}{2\rho_l c_l h^2}=0 \qquad \textbf{(5.11)}$$

where ξ is the circumferential angle coordinate of the film measured from the maximum bearing clearance; $\tilde{T}$ is the temperature difference relative to ambient temperature; ρ_l, c_l and μ are the density, specific heat capacity and dynamic viscosity of the lubricant; D and h are the diameter and fluid film thickness of the bearing; H is the coefficient of heat transfer through the journal and bearing surfaces; ω is the rotation speed of the rotor.

In addition, the effective viscosity μ can be calculated using the exponential Reynolds formulation

$$\mu=\mu_o e^{-\beta\Delta T_{avg}} \qquad \textbf{(5.12)}$$

where β is the thermoviscosity coefficient and ΔT_{avg} is the average temperature difference for the calculation of effective viscosity, which can be evaluated using Equation (4.30).

6) Thermal bend and thermal imbalance

The thermal bending model for the general mid-span rotors has been discussed in Section 4.2. However, different than symmetrical systems, the difference between two supporting bearings must be considered. This leads to the necessity of calculating two bearings and the complex thermal bending models for the general mid-span rotor systems (Figure 5.4).

Assume the average temperature gradients between the hot spot and cold spot have been obtained for each of bearings, denoted as ΔT_a and ΔT_b respectively. The equivalent thermal bending moment can be calculated (see Section 4.2.2)

$$\begin{aligned} \frac{M_a}{EI_a} &= \frac{\alpha \Delta T_a}{h_a} \\ \frac{M_b}{EI_b} &= \frac{\alpha \Delta T_b}{h_b} \end{aligned} \tag{5.13}$$

where the directions of the thermal induced moments can be determined using the connecting lines from the cold spot to the hot spot for the mid-span rotors, as discussed in previous chapters.

Use M_{axz}, M_{bxz} , M_{ayz}, M_{byz},to represent the components of equivalent thermal bending moments in x-z and y-z planes, respectively (Figure 5.4). The components of thermal induced deflections at disk mass can be calculated (see Section 4.2.2)

$$\begin{aligned} v_{dx} &= \left(\frac{M_{axz}}{EI_a}\right)\frac{L_a^2}{2L}\left(L-L_d\right)+\left(\frac{M_{bxz}}{EI_b}\right)\frac{L_b^2}{2L}L_d \\ v_{dz} &= \left(\frac{M_{ayz}}{EI_a}\right)\frac{L_a^2}{2L}\left(L-L_d\right)+\left(\frac{M_{byz}}{EI_b}\right)\frac{L_b^2}{2L}L_d \end{aligned} \tag{5.14}$$

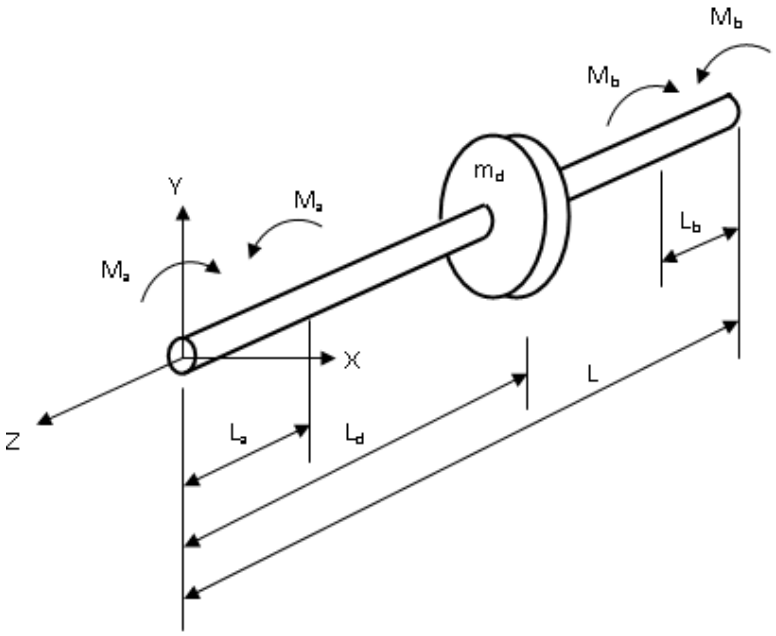

(a) Rotor model

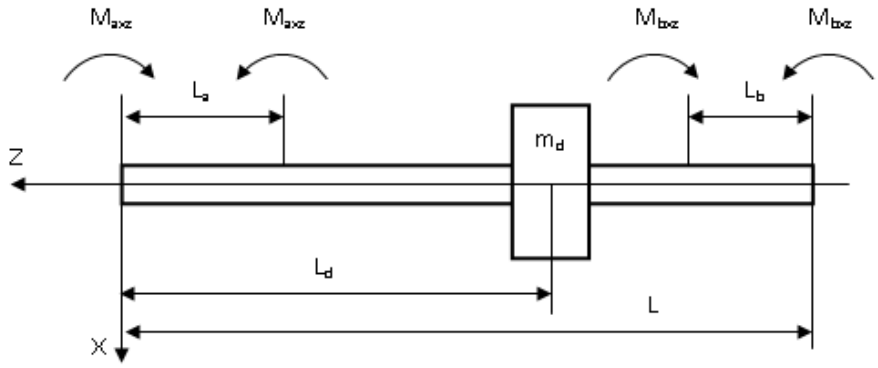

(b) In x-z plane

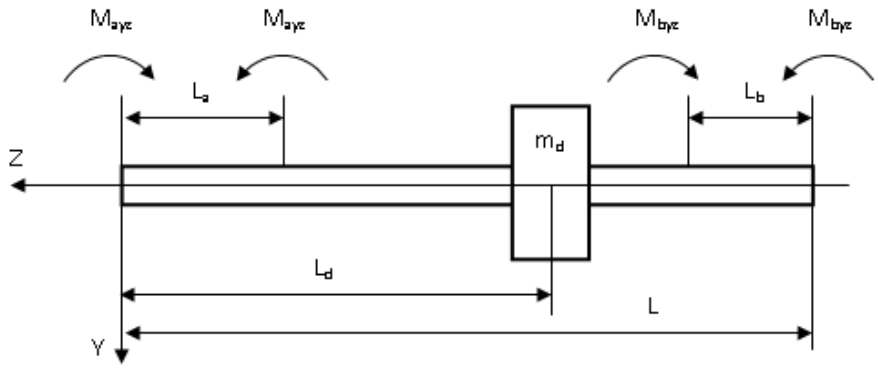

(c) In y-z plane

Figure 5.4 Thermal bend calculations

Then the total thermal induced deflection can be computed (Figure 5.6)

$$v_d = \sqrt{v_{dx}^2 + v_{dy}^2} \tag{5.15a}$$

The phase angle of thermal induced deflection is

$$\theta_d = \tan^{-1} \frac{v_{dy}}{v_{dx}} \tag{5.15b}$$

Then the thermal imbalance can be determined

$$U_t = m_d v_d \tag{5.16}$$

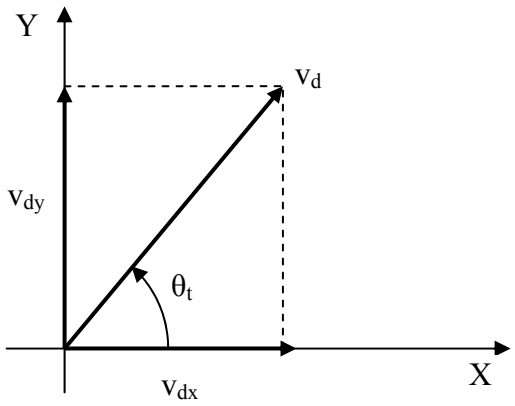

Figure 5.5 Total thermal induced deflection

7) Total imbalance

The mechanical imbalance U_m and the thermal imbalance U_t can be combined to produce the resultant imbalance U. Figure 5.6 shows all vectors in calculating the total imbalance.

$$U = \sqrt{U_t^2 + U_m^2 + 2U_t U_m \cos(\omega t - \theta_t)} \tag{5.17}$$

where the phase difference between the thermal and mechanical imbalances, ϕ, can also be obtained.

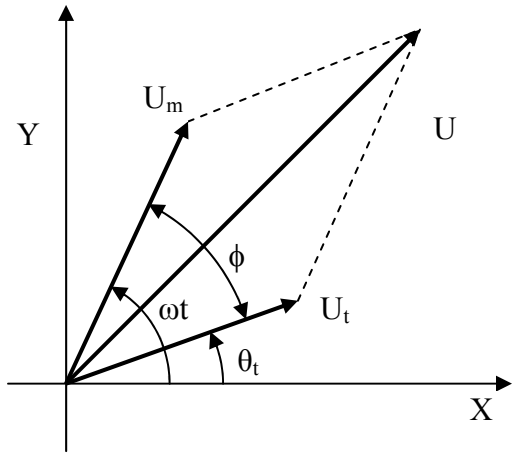

Figure 5.6 Total imbalance

8) Stability threshold

To complete the system analysis, a threshold imbalance must be defined. Following the old API standard, the threshold of the total imbalance is assumed to be 50% larger than the original mechanical imbalance. Hence the threshold imbalance force is equal to 15% of the rotor weight and can be mathematically expressed as

$$U_{thr} = \frac{0.15 W_{rotor}}{\omega^2} \tag{5.18}$$

where ω is the angular journal speed.

The rotor is considered to be unstable whenever U exceeds U_{thr}. As a result, the threshold speed for instability ω_{thr} occurs when $U = U_{thr}$. This instability criterion can be obtained

graphically from the intersection of the U - ω and the U_{thr} - ω curves and it determines the onset of the Morton Effect in the rotor system.

5.3 VT-MAP: Predictive Software for Morton Effect Analysis

Based on the theoretical models discussed before, VT-MAP (Virginia Tech - Morton Analysis Program), a front-end program to predict the Morton Effect induced instability in both overhung and mid-span rotors, has been developed. This program allows users to choose the bearing type, rotor configuration, and all relevant parameters that pertain to the different rotors and bearings.

5.3.1 Design of Software

The purpose of this program is to predict whether a given rotor system, which is supported by specified fluid-film bearings, will exhibit the Morton Effect. The following functions have been considered in developing the software:

(1) The program is capable of predicting the Morton Effect in either overhung rotors or mid-span rotors, which may be supported by the plain (cylindrical) journal bearing(s) or tilting pad journal bearing(s).

(2) User may choose either English or Metric unit system to input parameter values and display the results.

(3) A graphical user's interface (GUI) is adopted to supply a user-friendly interface for the application of the program. As many standard commercial software, the basic procedure of application consists of three steps, PreProcess, Solve and PostProcess. PreProcess is a front-end

interface to prepare input data file. Solve is the core component of the program to solve for the Morton Effect. PostProcess is a front-end interface to display or print analysis results both numerically and graphically.

(4) The concept of "problem directory" is used to manage input and output data files. The principle is one problem takes one specific directory. The users are recommended to build separate problem directories for different problems in order to avoid any confusion of file management. The user may name the different problem folders by their characteristics for the convenience of managing directories.

(5) For the applications using tilting pad journal bearings, the maximum flexibility to input parameter values is allowed. For example, users can choose number of pads and set different parameter values for different pads.

The GUI of the software is written in Microsoft Visual Basic 6.0 and the solver in FORTRAN 95. The theoretical models and initial codes for overhung rotors and tilting pad journal bearings have been referenced from [19-23]. In addition, VT-MAP employs ComponentOne Chart 7.0 to display the graphic results in PostProcess. ComponentOne is a registered trademark of ComponentOne LLC. The users of VT-MAP have been authorized to use the packed components of ComponentOne Chart in the software for the exclusive application of VT-MAP.

5.3.2 VT-MAP Launcher

The most recent version of the software is VT-MAP 4.0. When running the program, right after the logo page (Figure 5.7), VT-MAP 4.0 Launcher will be displayed first (Figure 5.8).

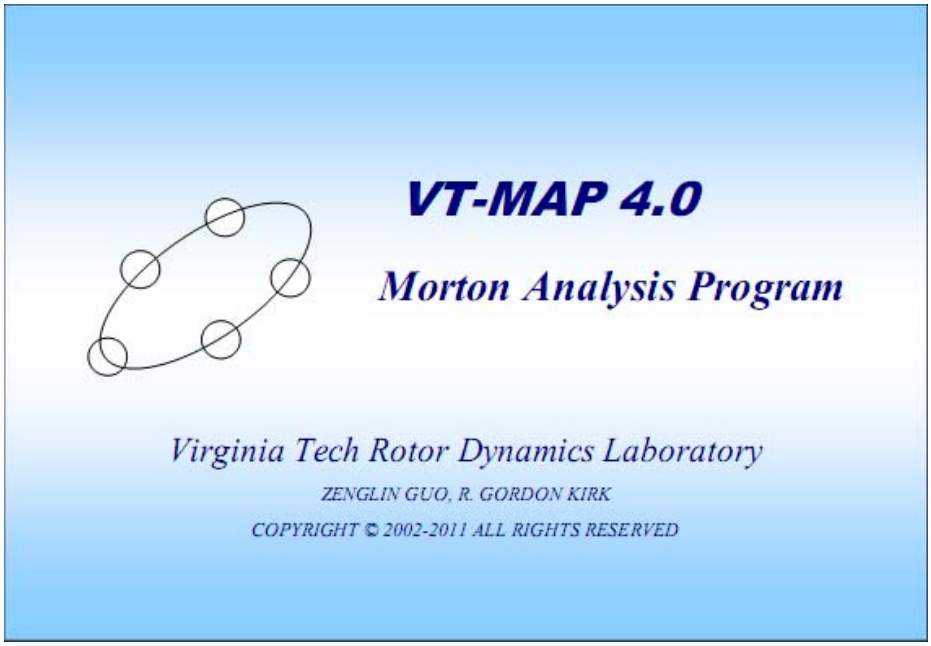

Figure 5.7 VT-MAP 4.0 Logo

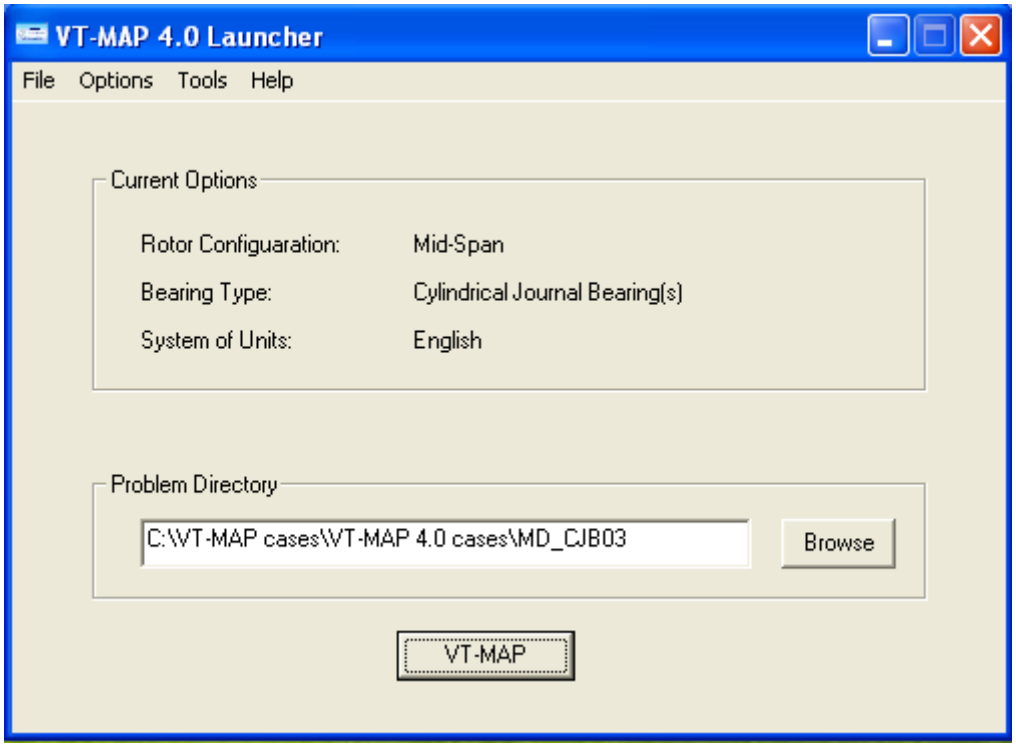

Figure 5.8 VT-MAP 4.0 Launcher

Here users may choose application options and problem directory. Top menus consist of four sub-menus: File, Options, Tools and Help. The windows explorer is also available for users to manage application files.

Application options should be made through Options. The details of all options on the top menus are shown in Figure 5.9(a), (b) and (c). The options include: Overhung and Mid-Span for Rotor Configuration; Tilting Pad Journal Bearing and Cylindrical Journal Bearing for Bearing Type; Metric and English for System of Units. In Options, Save As Default Setting will save the application options as a default setting, if it is checked.

Figure 5.9(d) shows Help menus which connect to three major help documents in html format.

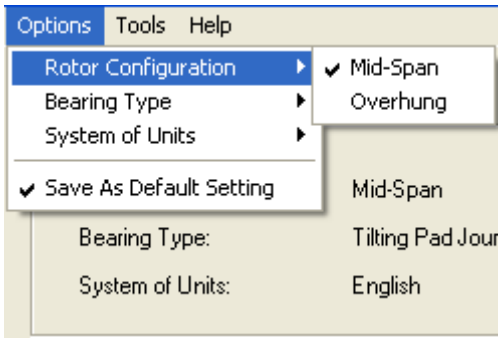

(a) Rotor Configuration

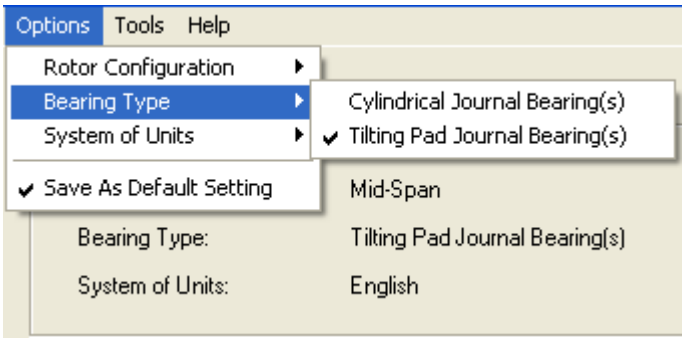

(b) Bearing Type

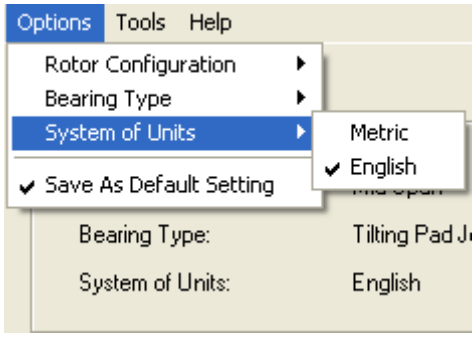

(c) System of Units

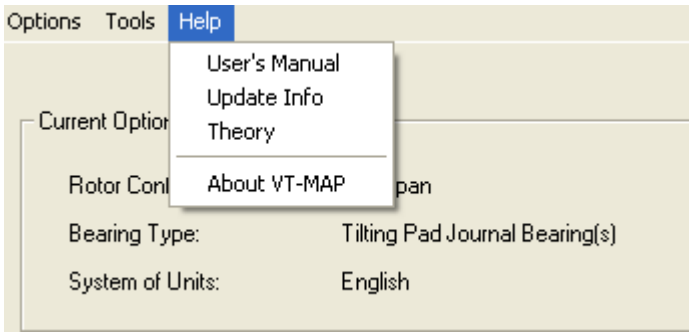

(d) Help

Figure 5.9 Options in VT-MAP 4.0 Launcher

The selected application options are displayed in Current Options on the panel of VT-MAP Launcher (Figure 5.8).

Next step in VT-MAP Launcher is to select the problem directory. As indicated before, it is recommended that a separate problem directory be built for each specific problem. Users may use an existing problem directory by browsing the drives and folders (Figure 5.10) or just build a new one for a new application by typing in the desired path (Figure 5.8).

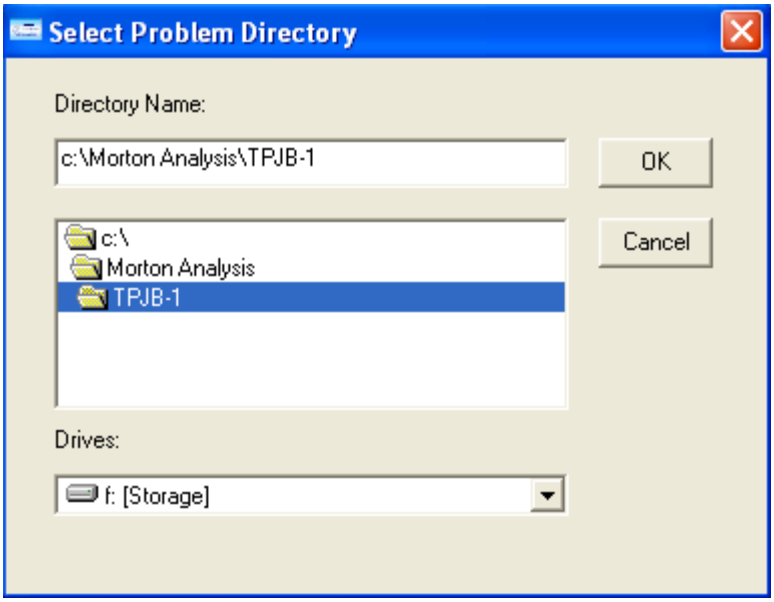

Figure 5.10 Select Problem Directory

5.3.3 VT-MAP GUI

Once finished the Current Options and Problem Directory in VT-MAP Launcher, users may click VT-MAP button to enter the VT-MAP project window (Figure 5.11). The project window consists of three parts: the top line shows the current problem directory and the project type (rotor configuration and bearing type); right below it is the main menu of VT-MAP; the

display window is used to display the input data or output results in numerical or/and graphical format.

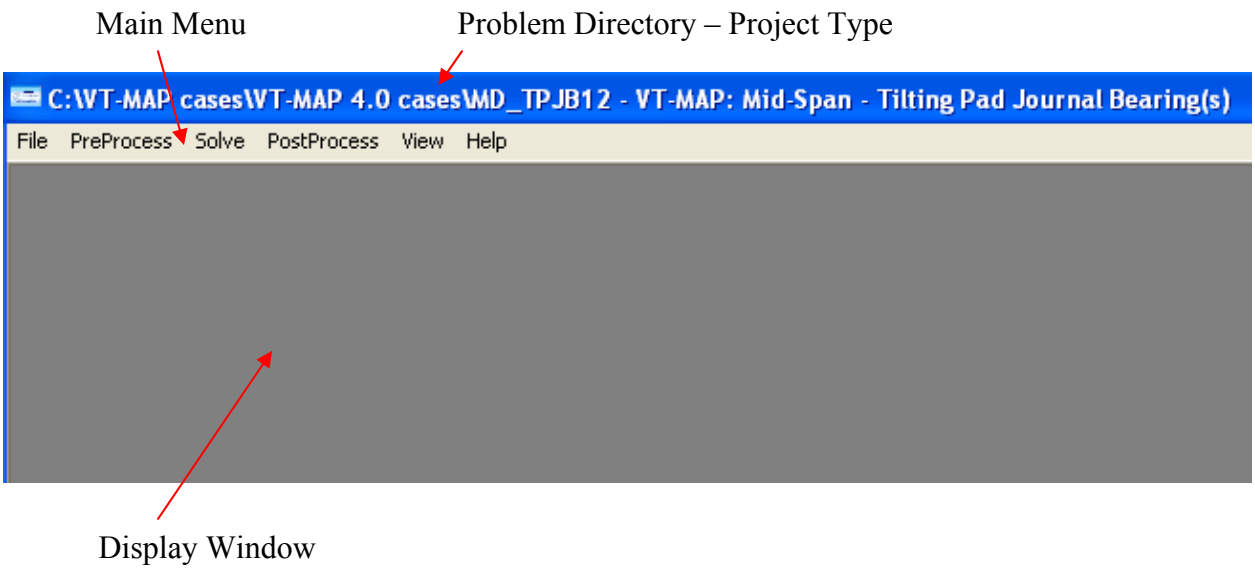

Figure 5.11 VT-MAP GUI

The main menu includes: File, PreProcess, Solve, PostProcess, View and Help

When users run a new problem, a default template of input data file will be automatically built in user's problem directory for further editing. The basic steps to run a project are:

Step 1 Input parameter values by going through Preprocess (also see Section 5.3.4).

Step 2 Run solver by clicking Solve/Solver Monitor

Step 3 View numerical and graphical results by clicking correspondent options in PostProcess. Usually this needs to load the calculation results first by clicking File/Load PostProcess File.

If users want to print any plot from PostProcess, click File/Print Image to print the current plot either to clipboard, or file, or printer. View provides options to control picture size of output plots.

5.3.4 Preparation of Input Data

Preparation of input data file is the first and key step to successfully complete a Morton Effect analysis. This can be done by applying options in PreProcess.

1) Input data file

Figure 5.12 shows an example of input data file. It is for mid-span rotors with tilting pad journal bearing supports. The parameters in this input data file are explained below in the order of appearance for the purpose of illustration:

- Case Description

  Use this feature to type in a short text to describe the current project, which will appear in the titles of all PostProcess plots and also show in the corresponding output data files.

- Rotor Parameters

  NSPD = number of operation speeds

  WROTOR = total weight of rotor

  LR = total length of rotor

  MD = magnitude of an equivalent disk mass

  LD = distance between the left end of the bearing on the LHS and the center-of-gravity of equivalent disk mass

  UNBM = initial zero-phase mechanical unbalance

```
CASE:
"Example COMPRESSOR - case 9L  NDE (MD_TPJB)"

ROTOR PARAMETERS:
NSPD      WROTOR(lbf)        LR(in)        MD(lbm)       LD(in)      UNBM(oz in)
 4             270           20.02         182.35        10.01         0.15

BEARING 1 (LHS)
Pad Parameters:
NPADS1
 5

L1(in)    PADANGLE1(deg)  THETAP1(deg)     TP1(in)       r-CP1(mils)   M1          OFFSET1
 2.375         56            18            0.5           5.25          0.34          0.5
 2.375         56            90            0.5           5.25          0.34          0.5
 2.375         56            162           0.5           5.25          0.34          0.5
 2.375         56            234           0.5           5.25          0.34          0.5
 2.375         56            306           0.5           5.25          0.34          0.5

Bearing parameters:
R1(in)     W1-LOAD(lbf)   ALPHA1(/deg F)
 2.5           0             6.67E-06

Lubricant Parameters:
P01(psi)       T01(deg F)    TAMB1(deg F)  MU01(reyn)  RHOL1(lbm/in^3) CAPL1(Btu/lbm/F)
 15            122           78            0.00000294    0.031         0.478

Speeds and Responses
N(RPM) XAMP1(mil 0-p) XPH1(deg MP) YAMP1(mil 0-p) YPH1(deg MP) G1-LOAD(lbf) G1-ANG(deg) T1-OP(F) MU1-OP(reyn)
5000   0.014456       13.5090      0.014197       20.030       317          270         156.49   2.1226E-06
6000   0.015256       -5.0047      0.015530        0.457       317          270         163.76   1.9817E-06
7000   0.015425      -18.3840      0.015781      -13.891       317          270         171.02   1.8503E-06
8000   0.014885      -30.0540      0.015350      -26.578       317          270         178.27   1.7278E-06

BEARING 2 (RHS)
Pad Parameters:
NPADS2
 5

L2(in)    PADANGLE2(deg)  THETAP2(deg)     TP2(in)       r-CP2(mils)   M2          OFFSET2
 2.375         56            18            0.5           5.25          0.34          0.5
 2.375         56            90            0.5           5.25          0.34          0.5
 2.375         56            162           0.5           5.25          0.34          0.5
 2.375         56            234           0.5           5.25          0.34          0.5
 2.375         56            306           0.5           5.25          0.34          0.5

Bearing parameters:
R2(in)     W2-LOAD(lbf)   ALPHA2(/deg F)
 2.5           0             6.67E-06

Lubricant Parameters:
P02(psi)       T02(deg F)    TAMB2(deg F)  MU02(reyn)  RHOL2(lbm/in^3) CAPL2(Btu/lbm/F)
 15            122           78            0.00000294    0.031         0.478

Speeds and Responses
N(RPM) XAMP1(mil 0-p) XPH1(deg MP) YAMP1(mil 0-p) YPH1(deg MP) G1-LOAD(lbf) G1-ANG(deg) T1-OP(F) MU1-OP(reyn)
5000   0.014456       13.5090      0.014197       20.030       317          270         156.49   2.1226E-06
6000   0.015256       -5.0047      0.015530        0.457       317          270         163.76   1.9817E-06
7000   0.015425      -18.3840      0.015781      -13.891       317          270         171.02   1.8503E-06
8000   0.014885      -30.0540      0.015350      -26.578       317          270         178.27   1.7278E-06

STIFFNESS & DAMPING COEFFICIENT PARAMETERS:
SDFLAG(0 => do not calculate K,C coeff., 1 => calculate K,C coeff.)
 1

PREFERENCES:
MTDFLAG        NTAVG         HTCFLAG       TRAMP         TRPHASE      RDFLAG         CFLAG
 2             10            1             1             1             1             1

SYSTEM OF UNITS (1 => Metric, 2 => English):
 2
```

Figure 5.12 Input data file

- Bearing 1 (LHS) – Pad Parameters

  NPADS1 = number of pads of titling pad journal bearing

  L1 = axial length of i^{th} pad

  PADANGLE1 = angular dimension of i^{th} pad

  THETAP1 = angular location of the pivot of i^{th} pad

  TP1 = pad thickness at the pivot location of i^{th} pad

  r-CP1 = radial (or diametrical) pad (or bearing) clearance of i^{th} pad

  M1 = preload factor of i^{th} pad

  OFFSET1 = angular distance between the leading edge of the pad and the pivot divided by PADANGLE1

- Bearing 1 (LHS) – Bearing Parameters

  R1 = journal radius

  W1-LOAD = gravity load on bearing

  ALPHA1 = linear coefficient of thermal expansion for the journal

- Bearing 1 (LHS) – Lubricant Parameters

  P01 = lubricant supply pressure

  T01 = lubricant supply temperature

  TAMB1 = ambient shaft temperature without lubricant heating effects

  MU01 = lubricant supply viscosity at supply temperature

  RHOL1 = lubricant density

  CAPL1 = lubricant specific heat capacity

- Bearing 1 (LHS) – Speed and Responses

  N = rotor speed in RPM

XAMP1 = x-amplitude (zero-to-peak or peak-to-peak) of the response for each rotor speed at the mid-span of the bearing to an initial mechanical imbalance

XPH1 = x-phase (for each rotor speed) of the response at the mid-span of the bearing to an initial mechanical imbalance. MP: VT-MAP format; FT: VT-FAST format; TD: Test Data (Field Data) format; SK: Analytical Single Keyphasor format

YAMP1 = y-amplitude (zero-to-peak or peak-to-peak) of the response for each rotor speed at the mid-span of the bearing to an initial mechanical imbalance

YPH1 = y-phase (for each rotor speed) of the response at the mid-span of the bearing to an initial mechanical imbalance. MP: VT-MAP format; FT: VT-FAST format; TD: Test Data (Field Data) format; SK: Analytical Single Keyphasor format

G1-LOAD = gear load on bearing

G1-ANG = gear load angle measuring from the east (positive X-axis), CCW.

T1-OP = operating temperature of bearing at specified speed

MU1-OP = lubricant operating viscosity at specified speed

Following the parameters of the bearing 1 on the LHS are similar descriptions for the bearing 2 on the RHS.

- Stiffness & Damping Coefficients Parameters

  SDFLAG = flag to determine if calculate stiffness and damping coefficients

- Preferences

MTDFLAG = method to locate hot spot: 1 = Original Method; 2 = Improved Method; 3 = New Method

NTAVG = number of dynamic positions for average temperature difference calculations (default value is 10)

HTCFLAG = if heat transfer through journal and bearing housing is included: 1 = Yes; 2 = No

TRAMP = flag to indicate amplitude format: 1 = zero-to-peak; 2 = peak-to-peak

TRPHASE = flag to indicate phase angle format: 1 = VT-MAP format (indicated as MP); 2 = VT-FAST format (indicated as FT); 3 = Test Data (Field Data) format (indicated as TD); 4 = Analytical Single Keyphasor (indicated as SK)

RDFLAG = flag to indicate some data format (radial or diametrical): 1 = radial parameters (use R1, R2 and r-CP1, r-CP2 or r-CB1, r-CB2); 2 = diametrical parameters (use D1, D2 and d-CP1, d-CP2 or d-CB1, d-CB2)

CFLAG = flag to indicate tilting pad bearing clearance format: 1 = pad clearance (use r-CP1 r-CP2 or d-CP1, d-CP2); 2 = bearing clearance (use r-CB1, r-CB2 or d-CB1, d-CB2)

- System of Units

  This flag indicates the unit system used in the current project: 1 = Metric; 2 = English

2) PreProcess

All of parameter values can be edited through PreProcess. Figure 5.13 shows the submenus of PreProcess.

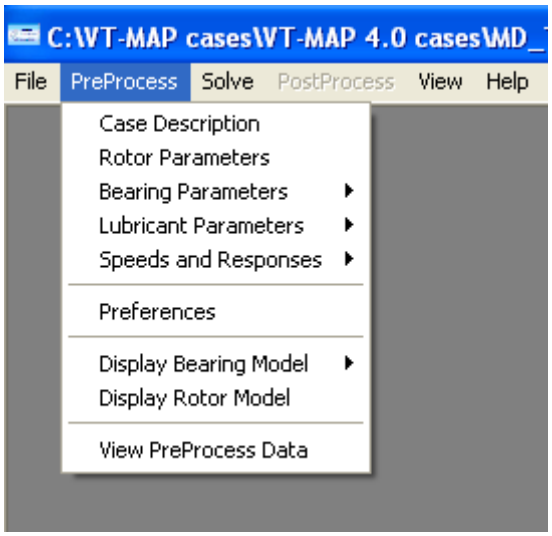

Figure 5.13 PreProcess

Still using the mid-span rotor with titling pad journal bearings as shown in Figure 5.12, each part of submenus of PreProcess is displayed as follows:

- Case Description

  Figure 5.14 shows the panel to input the short text description of the project.

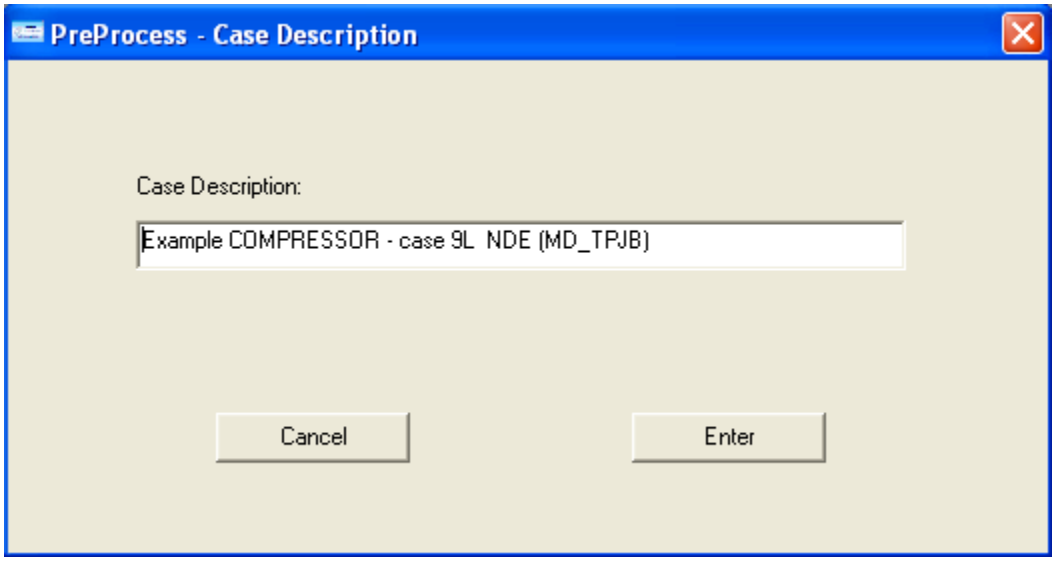

Figure 5.14 Case Description

- Rotor Parameters

  Use this panel (Figure 5.15) to input the parameter values of the rotor.

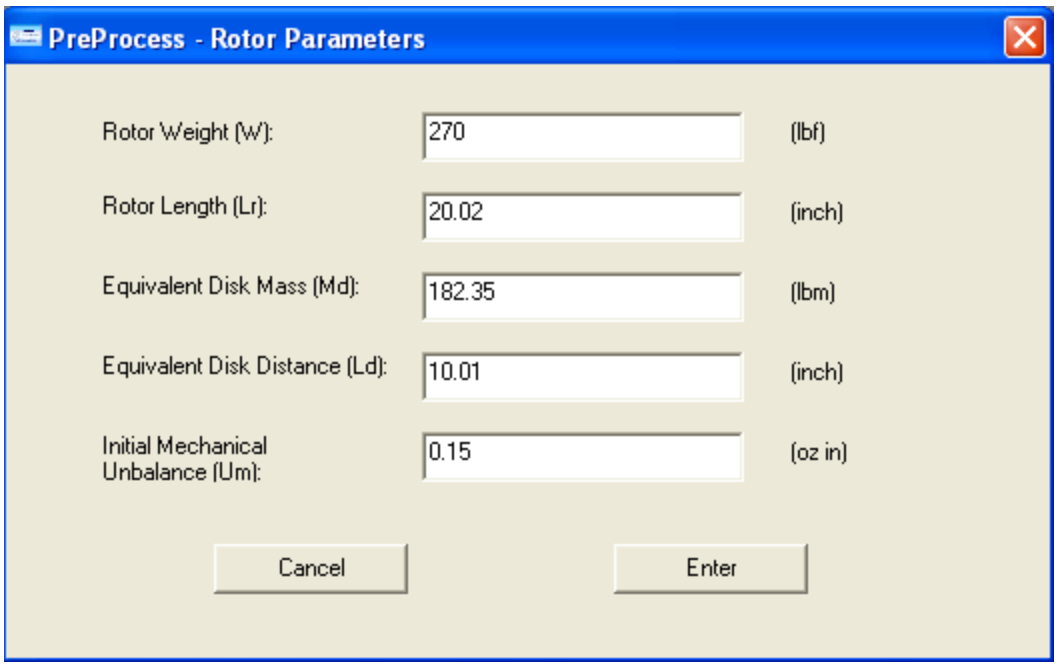

Figure 5.15 Rotor Parameters

- Bearing Parameters (Bearing 1 on LHS)

If choose to enter parameter values of Bearing 1 on LHS (Figure 5.16a), then the first panel is for the input of bearing parameter values, the choice of number of pads and pad value configurations (Figure 5.16b).

In single-value bearing configurations, the parameter values of each pad are same to that of others. A following panel as showed in Figure 5.16c is then opened for users to input values of these parameters. If using multiple-value bearing configurations, all of parameters of each pad can be different from that of other pads (Figure 5.16d). This feature provides users with more flexibility to configure the tilting pad journal bearing design.

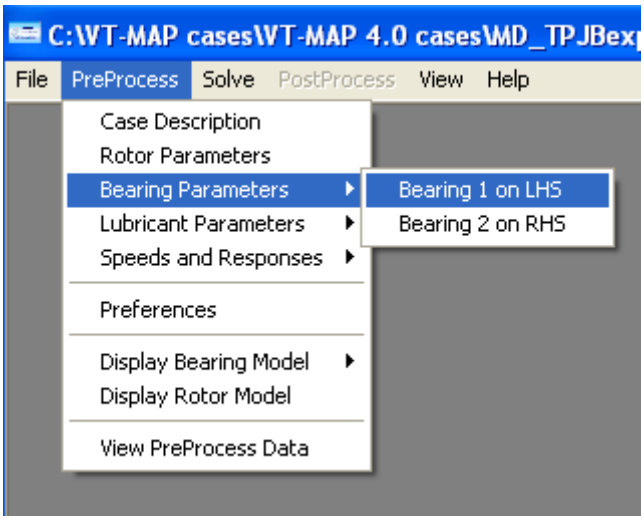

(a) Bearing 1 on LHS

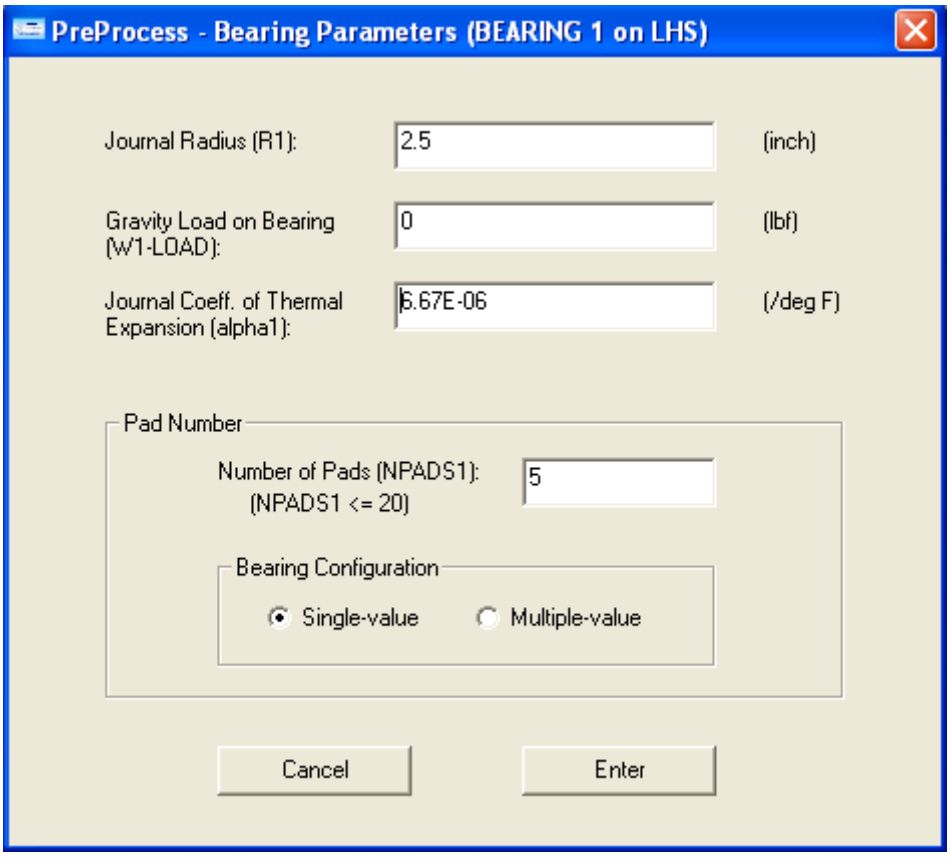

(b) Bearing parameters and pad number

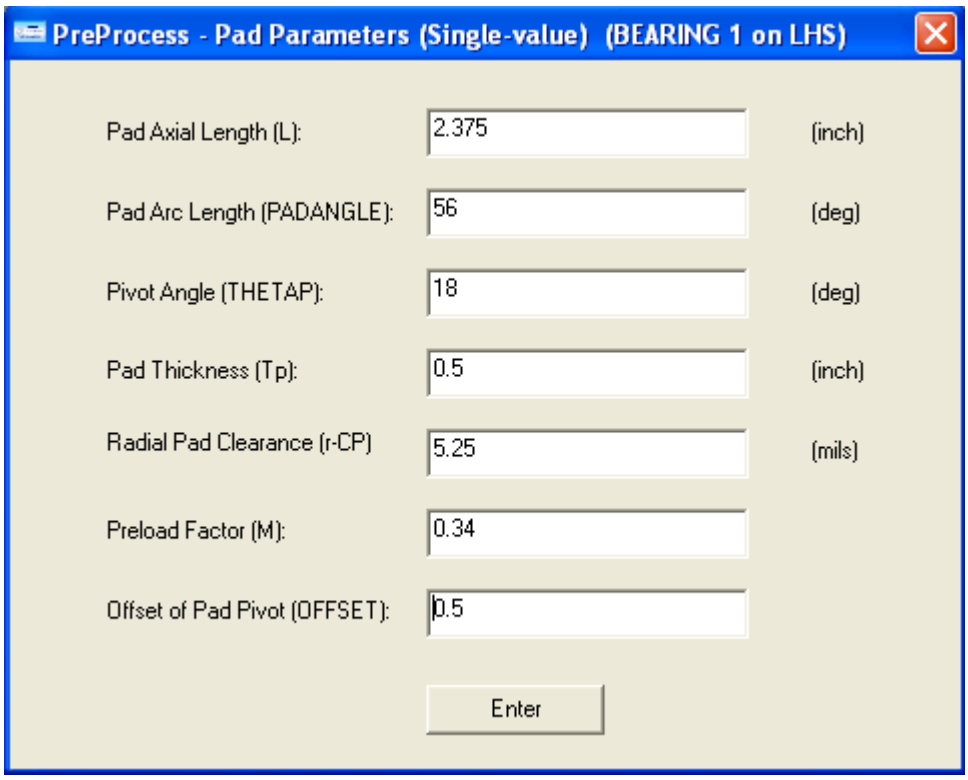

(c) Pad parameters in single-value configurations

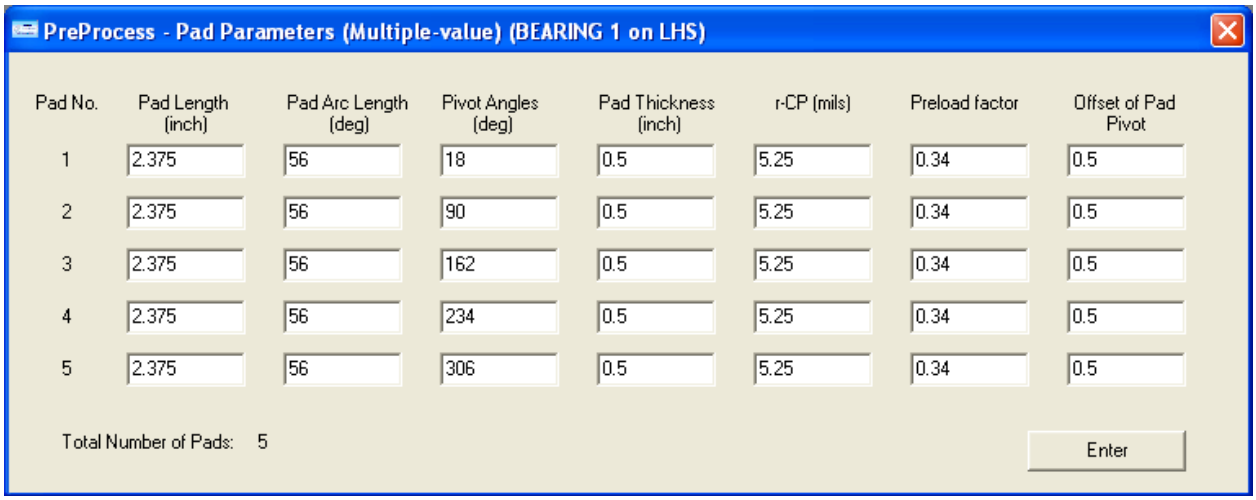

(d) Pad parameters in multiple-value configurations

Figure 5.16 Bearing Parameters

- Lubricant Parameters (Bearing 1 on LHS)

This panel allows users to input all parameter values of the lubricant for each bearing (Figure 5.17).

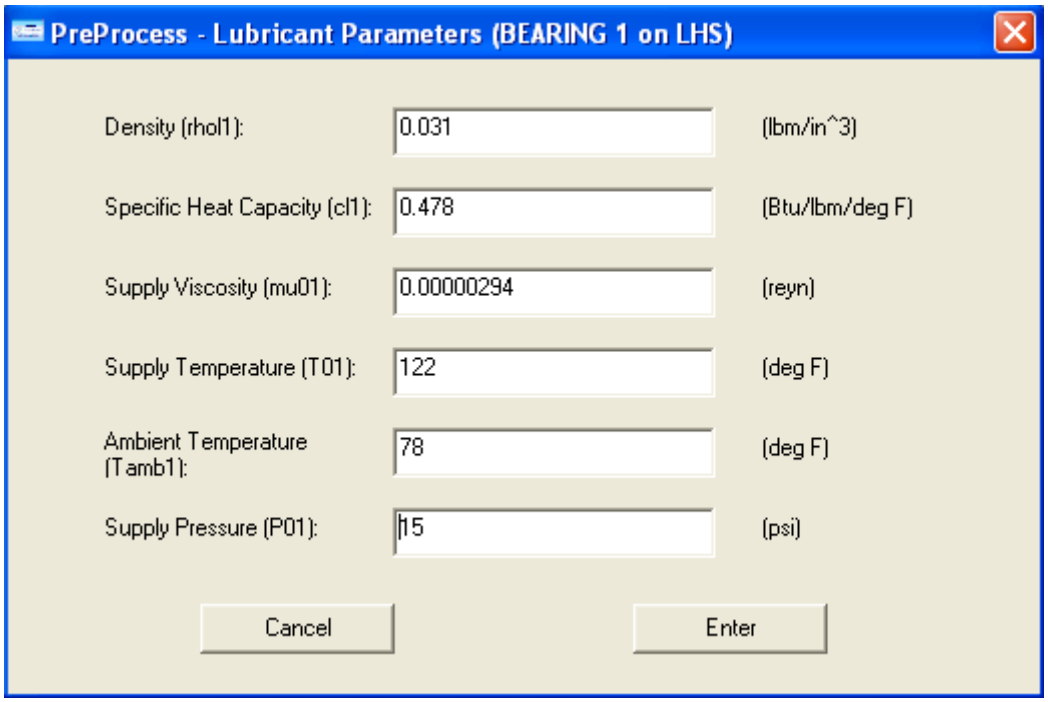

Figure 5.17 Lubricant Parameters

- Speeds and Responses (Bearing 1 on LHS)

Users may input synchronous response data obtained from the standard rotor dynamics calculations or other sources such as DyRoBeS or VT-FAST (Figure 5.18). There are two options to complete the input: use a script file or edit data in table.

(1) Use script file Figure 5.19 shows all steps to input speeds and responses by using a script file. First, open a script file template (Figure 5.19a). Then copy and paste the response data into the file and save it. Finally import the response data in the saved script file to VT-MAP input data (Figure 5.19b). Users also have options to input operating temperatures and lubricant

viscosities with script file or let VT-MAP generate approximate values of these parameters (Figure 5.19c). It is recommended to input operating temperatures and viscosities from the same source as responses data.

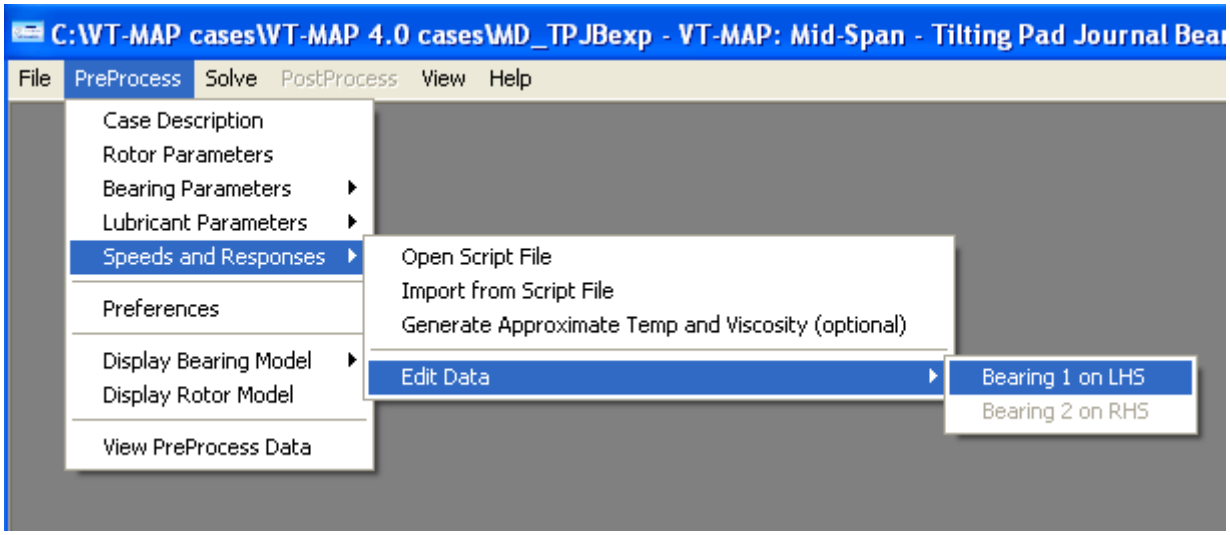

Figure 5.18 Speeds and Responses

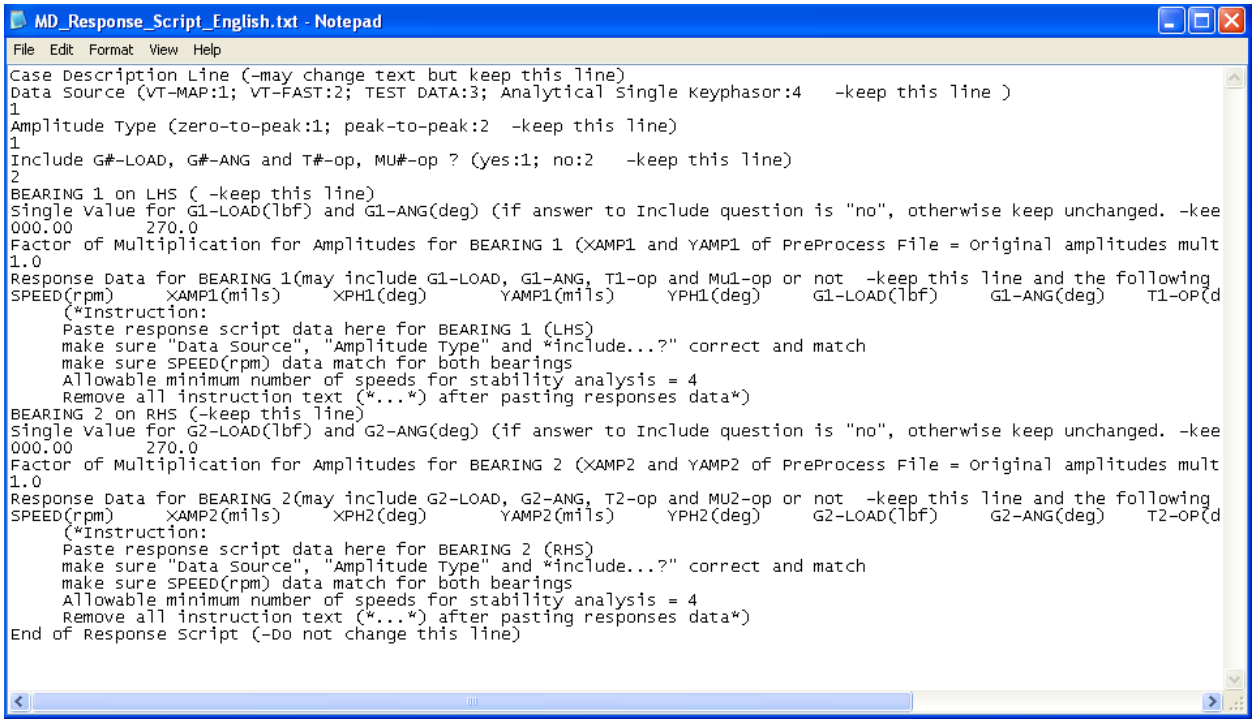

(a) Open script file

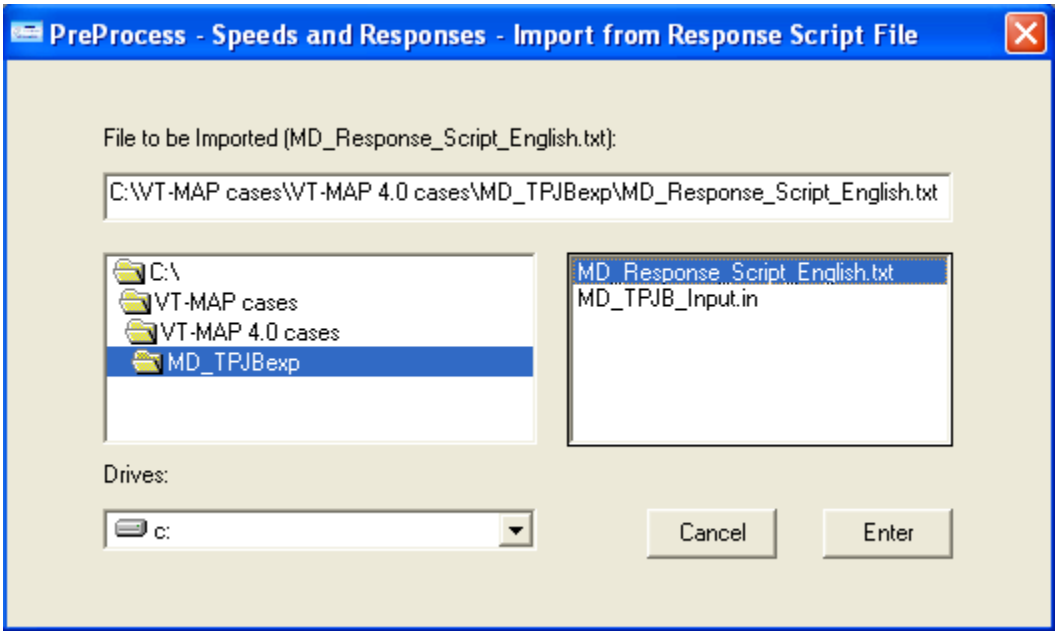

(b) Import from script file

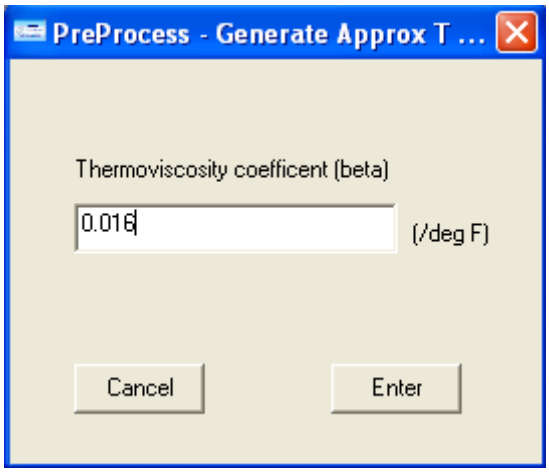

(c) Generate approximate operation temperature and viscosity

Figure 5.19 Script file to input speed and response data

(2) Edit data in table Users can also input all parameter values of speed and response in table form (Figure 5.20). First, input the number of speeds (Figure 5.20a). Then a new panel will be opened to allow users to input all parameter values in table form (Figure 5.20b)

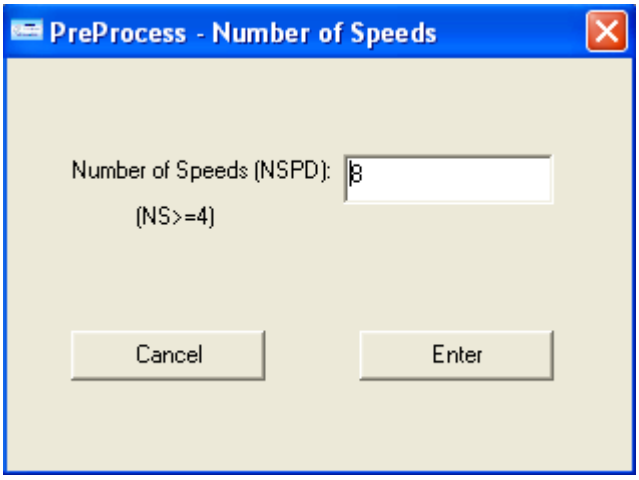

(a) Number of speeds

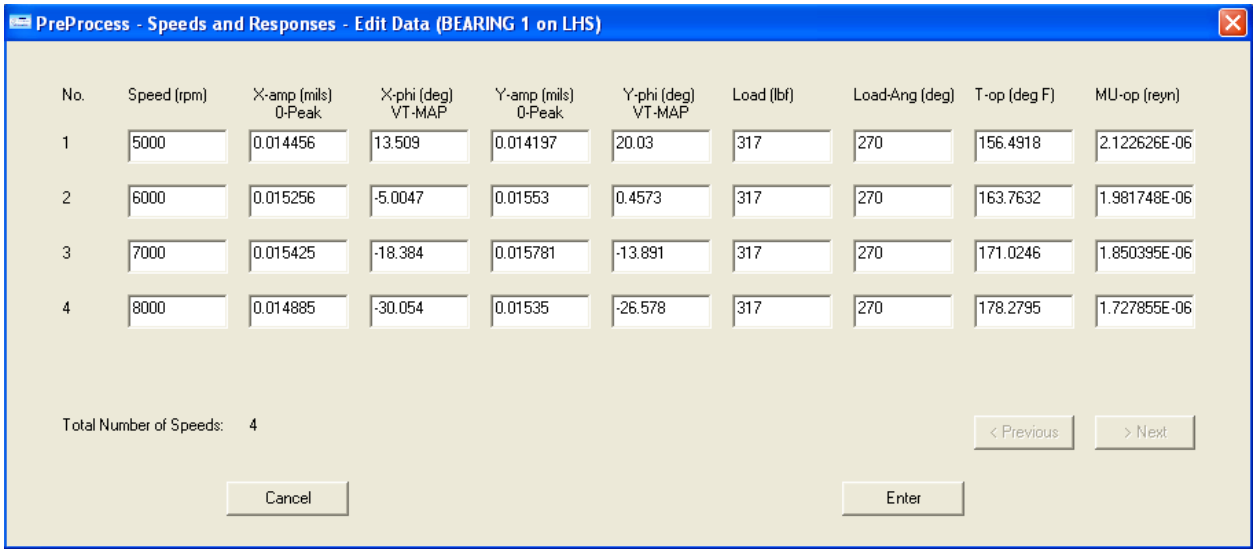

(b) Table of speed and response

Figure 5.20 Table to input speed and response data

- Preferences

In Preferences, users are allowed to choose options for the solver and format to display some of input data, as discussed in Section 5.3.4. Click corresponding options to complete the

preferences, while default values have been indicated and Reset button can be used to restore all default settings (Figure 5.21).

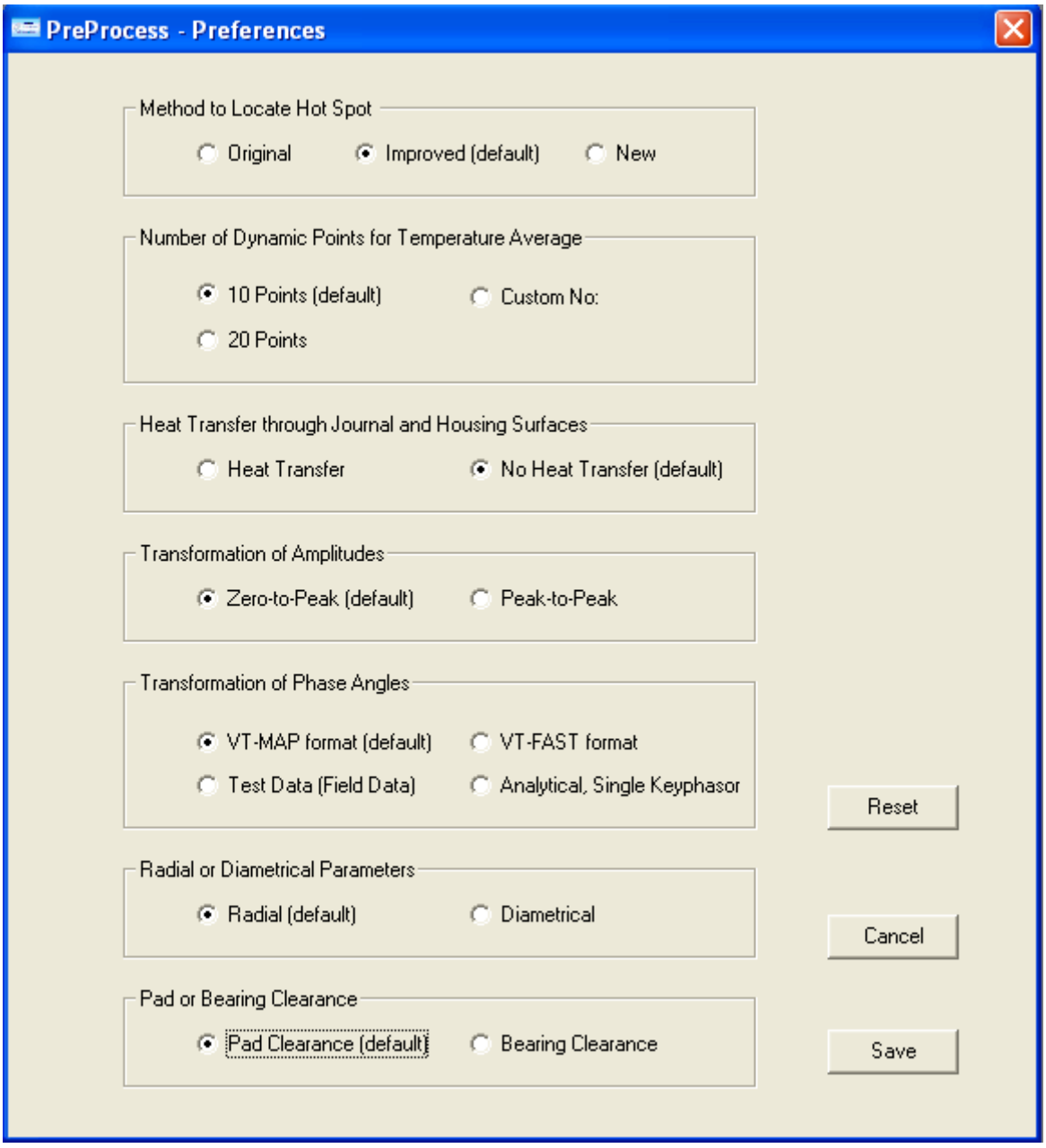

Figure 5.21 Preferences

- Display Rotor Model and Bearing Model (Bearing 1 on LHS)

This feature allows users to visually display the rotor model and bearing model in a scaled 2-D plot (Figure 5.22).

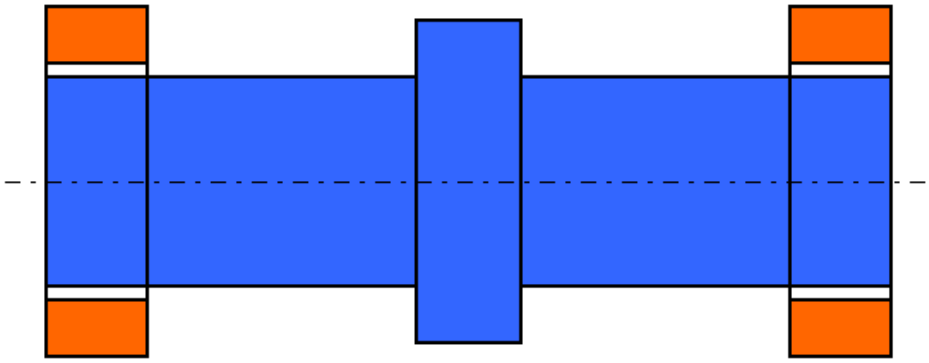

(a) Rotor model

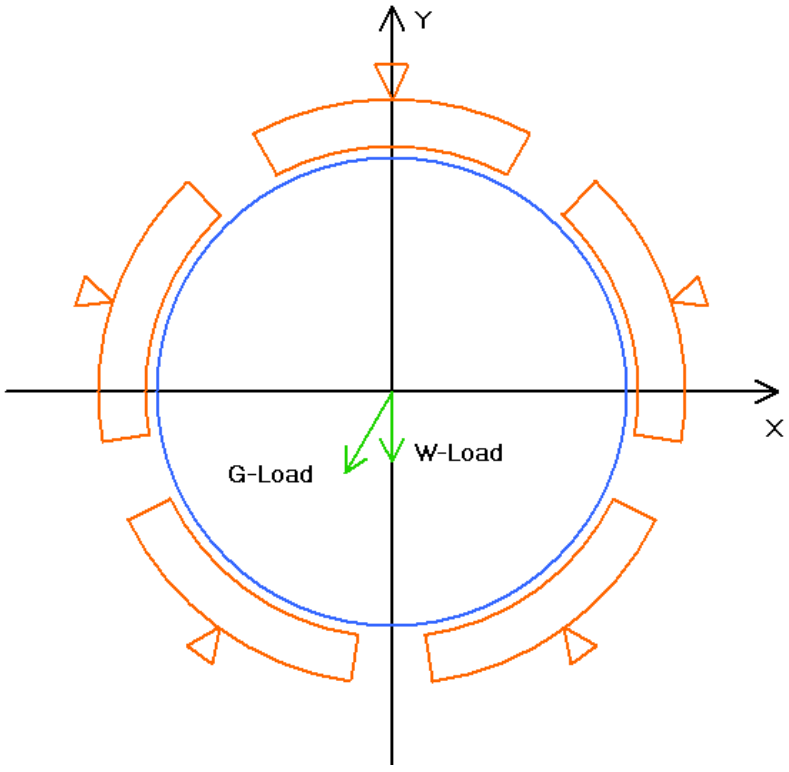

(b) Bearing model

Figure 5.22 Display rotor and bearing models

- View PreProcess Data

This panel allows users to review all parameter values in input data file in the window of MS Notepad as shown in Figure 5.12.

5.3.5 Analysis of Result

VT-MAP PostProcess provides a front-end interface to display the Morton Effect analysis results either in numerical or graphical form (Figure 5.23). Results Data displays the numerical results; T-P-h Plot displays the three-dimensional distributions of bearing temperature, pressure and film thickness; Orbit Plot shows the journal orbit at specified speed; Stability Plot displays final stability analysis curves; Unbalance Analysis shows detailed information for stability analysis.

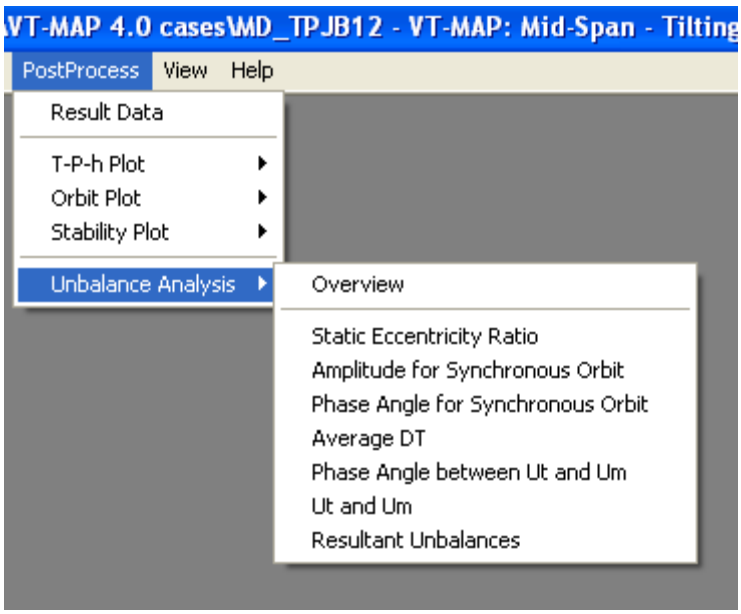

Figure 5.23 PostProcess

- T-P-h Plot

It displays the three dimensional distribution of temperature, pressure and fluid film thickness in the bearing at specified speed (Figure 5.24). Users are allowed to display pictures at any operation speed by selecting desired speed values in Speed Index for Display in the tool menu shown on the right hand side.

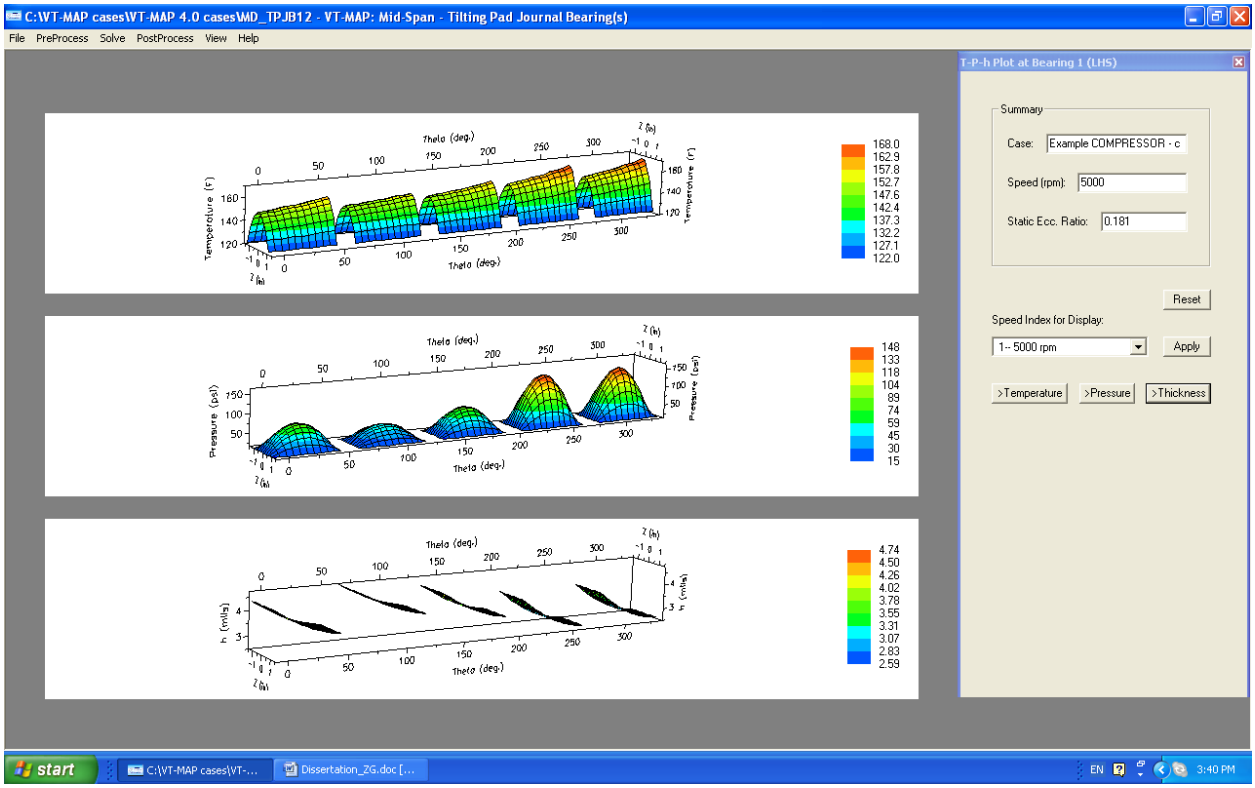

Figure 5.24 T-P-h Plot

- Orbit Plot

It displays the journal orbit plot at specified speed (Figure 5.25). The circle symbol in the plot represents the cold spot while the cross symbol represents the hot spot on the journal surface. The number label connected with the hot spot represents the temperature difference at

that position. The average temperature difference DT is showed in the title area, which is based on the average of temperature differences of all dynamic positions. The number label with * represents the temperature difference at the first point of calculation when time t=0.

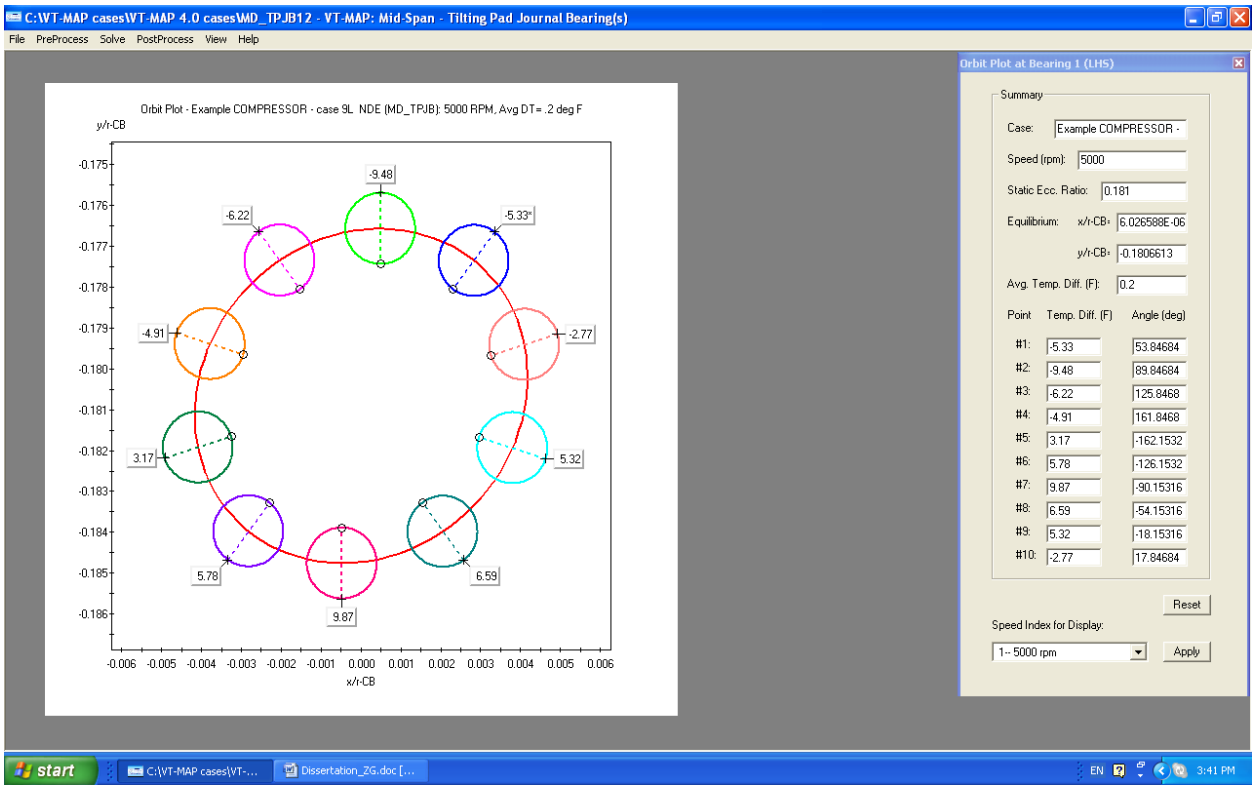

Figure 5.25 Orbit Plot

- Stability Plot

For stability analysis, there are two kinds of methods in VT-MAP, which can be used to determine the influence of the Morton Effect on the stability of the system: Old API (0.1g) – recommended and New API (4W/N). The former method has been explained in Section 5.2 and is recommended for most of applications. If using Old API (0.1g) method, the stability plot is as shown in Figure 5.26. This window display the unbalance curves and tell whether and when

there will exhibit the Morton Effect induced instability in the given rotor system. There may be two kinds of threshold speed: destabilizing threshold that represents rotor system going from non- Morton Effect zone to Morton Effect zone, which is displayed in red color; stabilizing threshold that represents rotor system going from Morton-Effect zone to non- Morton Effect zone, which is displayed in green color. The unbalance curve (in blue) is obtained by using Not-a-Knot cubic spline interpolation to fit the discrete results of calculation. Users may also choose different values of threshold factors or apply band-value threshold factors for comprehensive analysis of the Morton Effect.

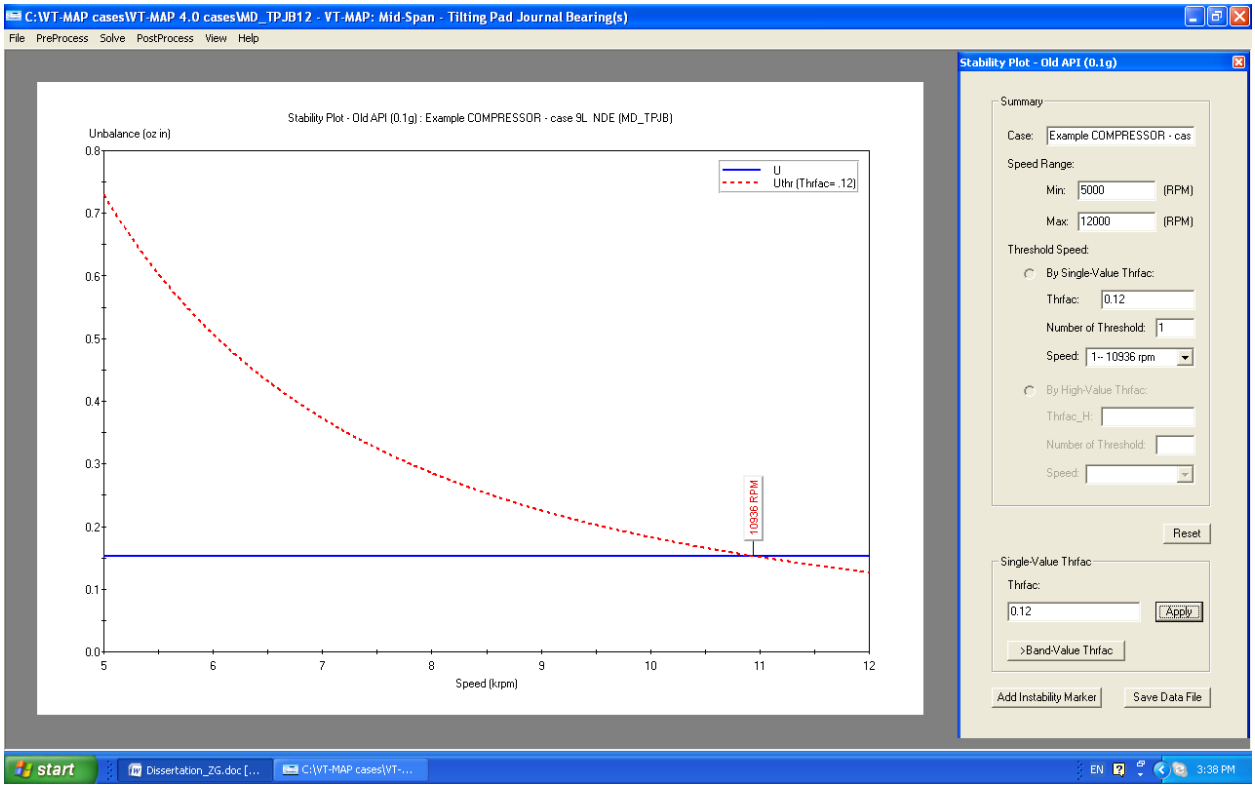

Figure 5.26 Stability Plot

- Unbalance Analysis

This feature provides users more detailed information on how the final stability analysis results are obtained (Figure 5.27).

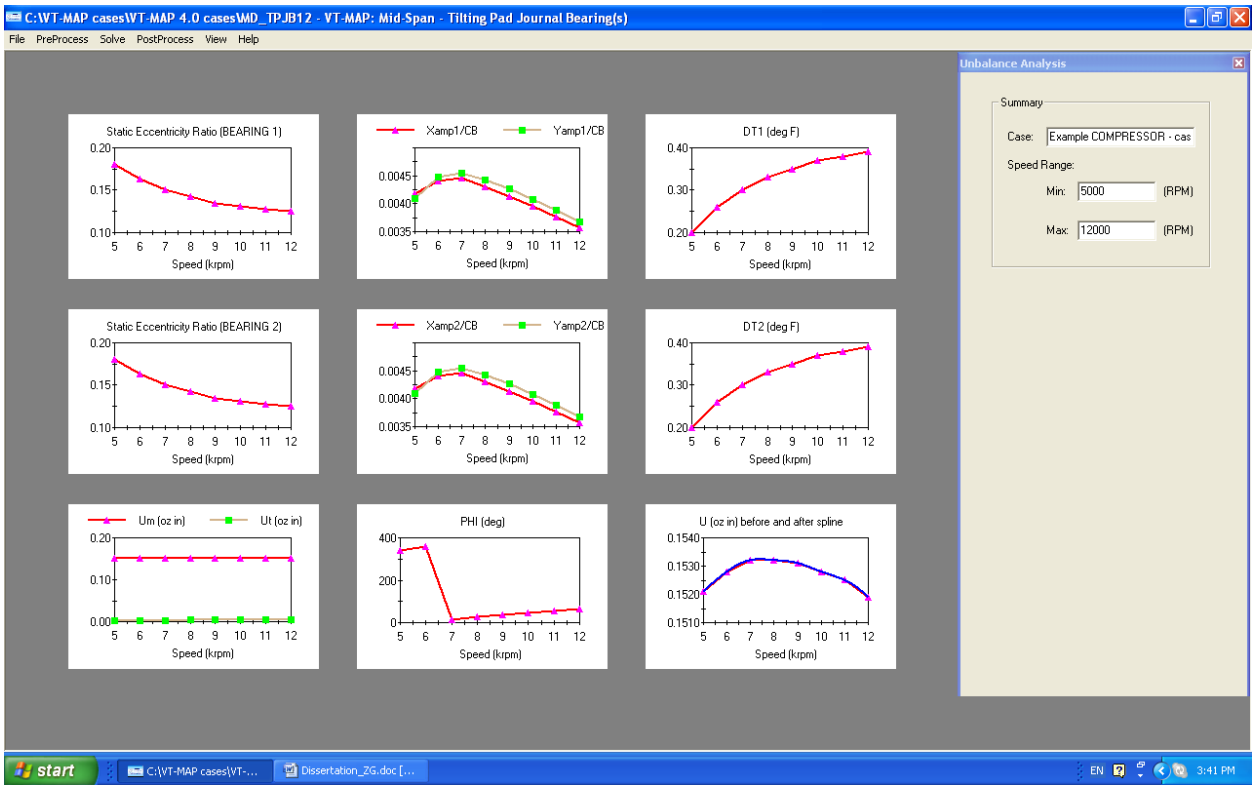

Figure 5.27 Unbalance Analysis

5.4 Case Studies

A number of overhung rotor systems have been analyzed using the predictive solutions. Several cases including Keogh and Morton rotor, Faulkner, Strong and Kirk rotor, de Jongh and Morton rotor, de Jongh and van der Hoeven rotor were discussed in [19-21]. Two other cases about a pipeline compressor rotor and a tilting pad journal bearing supported rotor were analyzed in [22-23]. As a reference, the latter two cases are attached in Appendices.

Contrast to the successive predictive studies of different cases involving the Morton Effect induced instabilities in overhung rotors, there is apparently short of practical instability case reports from industries to date. In this section, the classic rotor model presented by Keogh and Morton [11] will be first employed to show the influence and comparison of the Morton Effect on both overhung and mid-span configurations. Then, a practical mid-span rotor supported by the tilting pad journal bearings will be discussed.

5.4.1 Keogh and Morton Rotor

Keogh and Morton conducted a theoretical analysis on a symmetric rotor, as illustrated in Figure 5.28. Table 5.1 provides the data necessary for simulating the Keogh and Morton rotor.

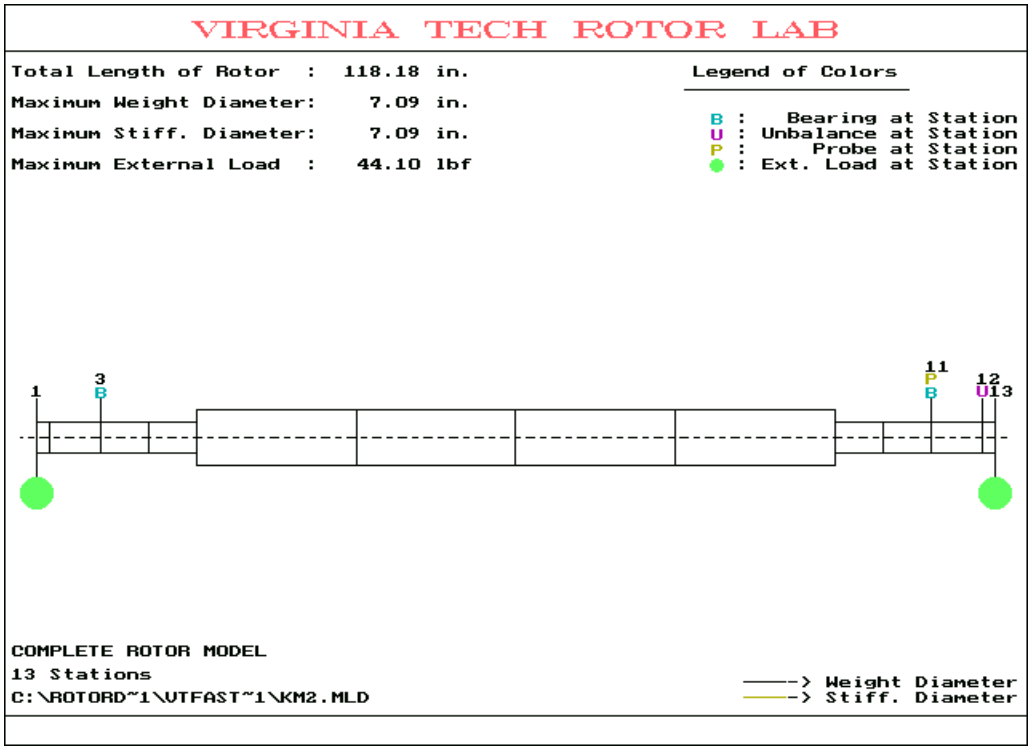

Figure 5.28 VT-FAST model of Keogh and Morton symmetrical rotor

Table 5.1 Data for Keogh and Morton symmetrical rotor

Parameter	SI Units	EG Unit
Bearing length, L	0.035 m	1.38 in
Radius of journal, R_j	0.050 m	1.97 in
Radial clearance, C_b	100 μm	3.94 mils
Bearing load, W	2500 N	562 lb_f
Heat transfer coefficient, H	50 $W/m^2/^oC$	2.43E-5 $hp/in^2/^oF$
Journal C.T.E., α	1.10E-05 $/^oC$	6.11E-06 $/^oF$
Rotor weight, W_{rotor}	5000 N	1124 lb_f
Overhung mass, M_d	32.3 kg	71.3 lb_m
Overhang distance, L_d	0.16 m	6.4 in
Max. cont. op. speed, ω_{MCOS}	1047 rad/s	10000 RPM
Initial mech. imbalance, U_m	4.54E-4 kg-m	0.63 oz-in
Lubricant supply temp, T_0	45.0 ^oC	113 ^oF
Lubricant supply viscosity, μ_0	0.0095 Pa-s	1.38 μreyn
Lubricant density, ρ_l	850 kg/m^3	0.031 lb_m/in^3
Lubricant sp. heat capacity, c_l	2000 J/kg/K	0.478 $Btu/lb_m/^oF$
Thermoviscosity coeff., β	0.029 $/^oC$	0.016 $/^oF$

The rotor consists of a shaft with a step variation in diameter and it is supported by two identical plain journal bearings. On either shaft end, there is a disk with constant mass at an overhung position. This rotor model was originally used to analyze the Morton Effect occurred in its overhung ends. Keogh and Morton examined the stability of this rotor by calculating the

eigenvalues of the rotor system and determining the corresponding growth factors. The positive growth factor would indicate a theoretical instability. Their growth factor plot revealed that the critical speed range, in which rotor thermal bending can occur, is between 1023 rad/s (9769 RPM) and 1086 rad/s (10371 RPM).

VT-MAP and VT-FAST have been used to predict a synchronous thermal instability range which is from 1051 rad/s (10038 RPM) to 1202 rad/s (11482 RPM). This predicted instability range overlaps the Keogh and Morton calculated instability range.

For the Keogh and Morton rotor, an unbalance response analysis reveals that the rotor has a critical speed (4th critical) near 10500 RPM. This lateral critical speed creates large amplitude orbits in this region. Figure 5.29 shows the orbit plots and temperature calculations at 4775 RPM, 5730 RPM, 10505 RPM and 11460 RPM. The large average temperature is associated with large amplitude orbits.

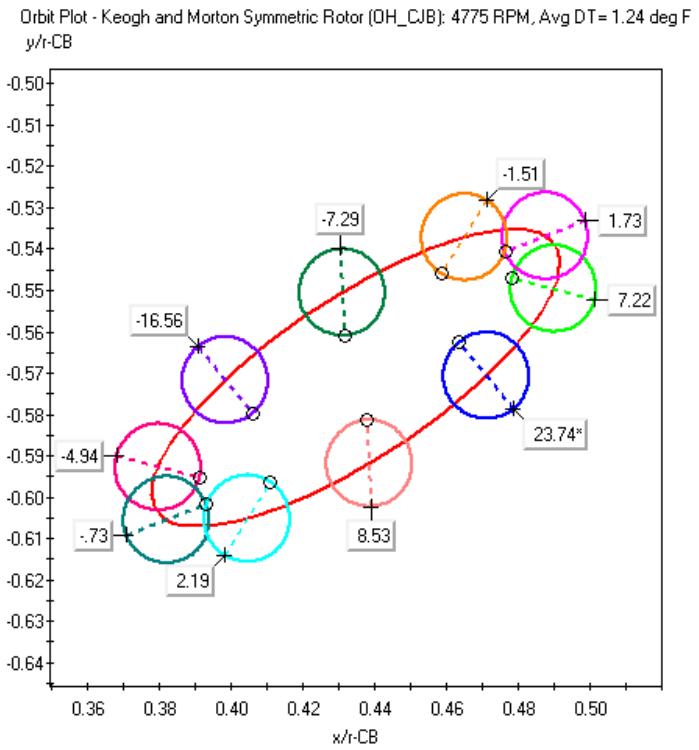

(a) 4775 RPM

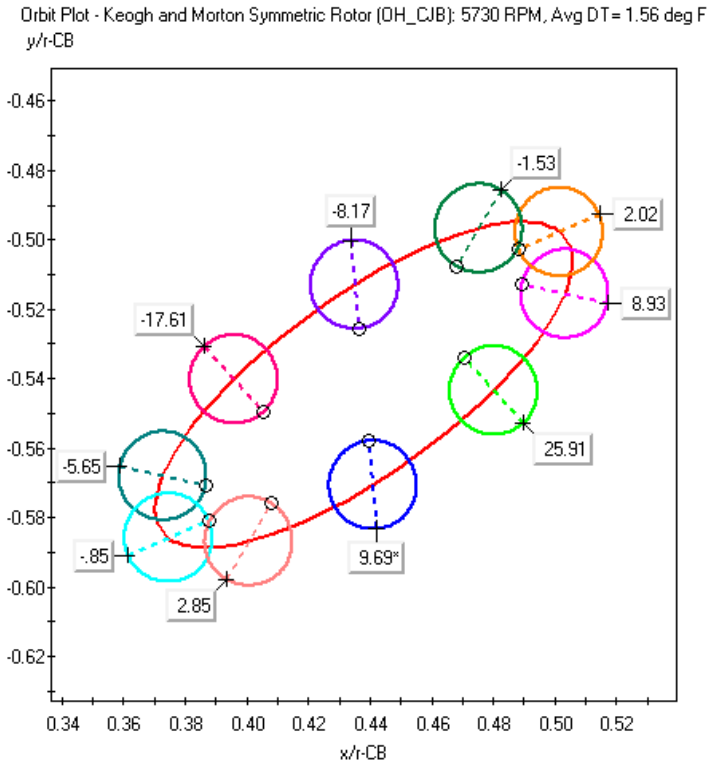

(b) 5730 RPM

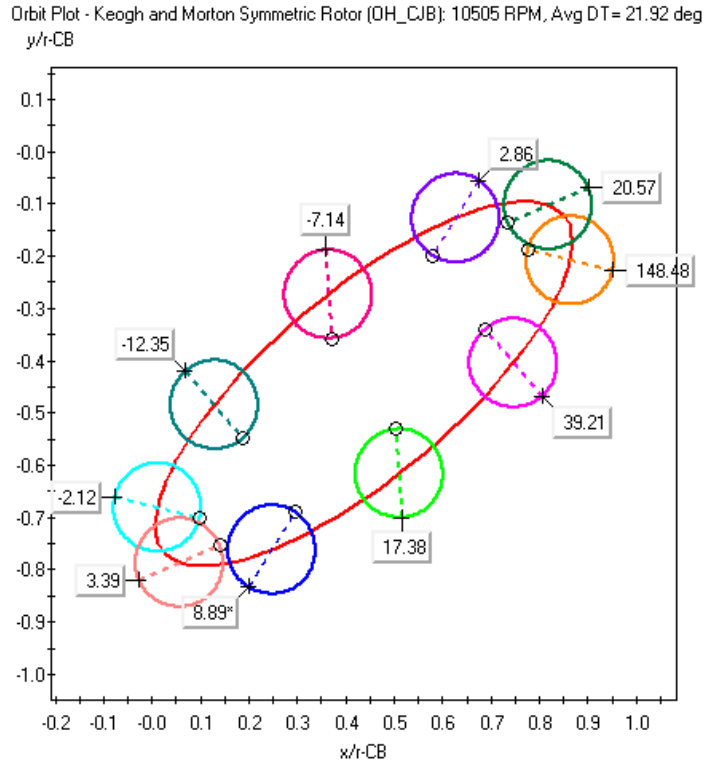

(c) 10505 RPM

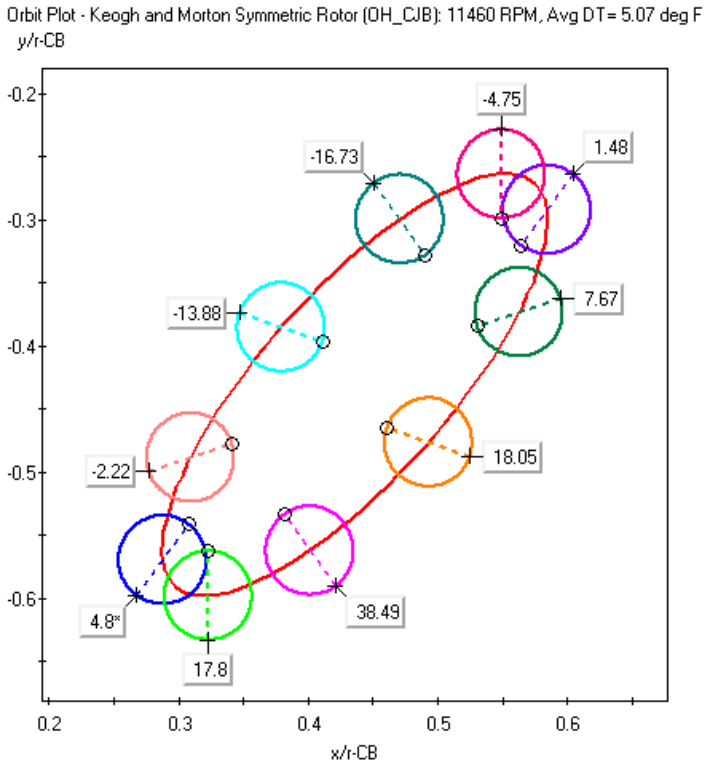

(d) 11460 RPM

Figure 5.29 Orbit plots of Keogh and Morton symmetrical rotor

Figure 5.30 is the stability plot of the Keogh and Morton rotor generated by VT-MAP. The resultant unbalance curve is obtained by employing the Not-a-Knot spline method to fit the results on the calculated speeds. The instability thresholds are obtained from the intersection of the resultant unbalance and threshold unbalance curves.

Figure 5.30 shows that there is an instability threshold at speed 10038 RPM, which falls between the lower and upper speed limits indicated by Keogh and Morton. In addition, the stability plot indicates another range of instability above 12300 RPM. The green speed marker at 11482 RPM indicates the onset of a transition back to stable region from unstable operation.

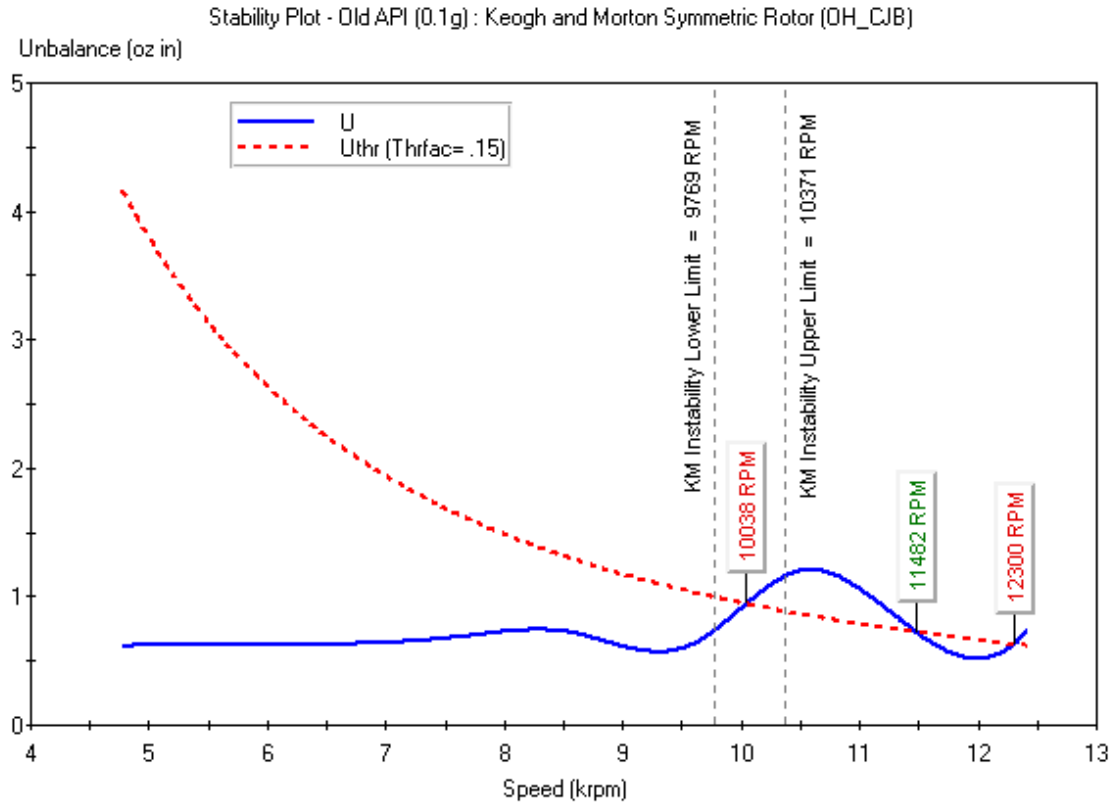

Figure 5.30 VT-MAP stability plot for Keogh and Morton symmetrical rotor

Next, consider the influence of the Morton Effect on the mid-span portions of the same rotor. Because the thermal bending deflections have been assumed to be small and uncoupled with other deformations in the derivations of mid-span rotor models as discussed in Chapter 4, the Morton Effect for the mid-span portions of the Keogh and Morton symmetrical rotor can be calculated using the same data as the above calculations. The thermal bending deflections at the central point of the mid-span rotor can be calculated for comparison with that on the center of gravity of the overhung mass. This comparison can be carried out in VT-MAP through assuming the virtual central-hung mass with the same values as in the overhung rotor calculations.

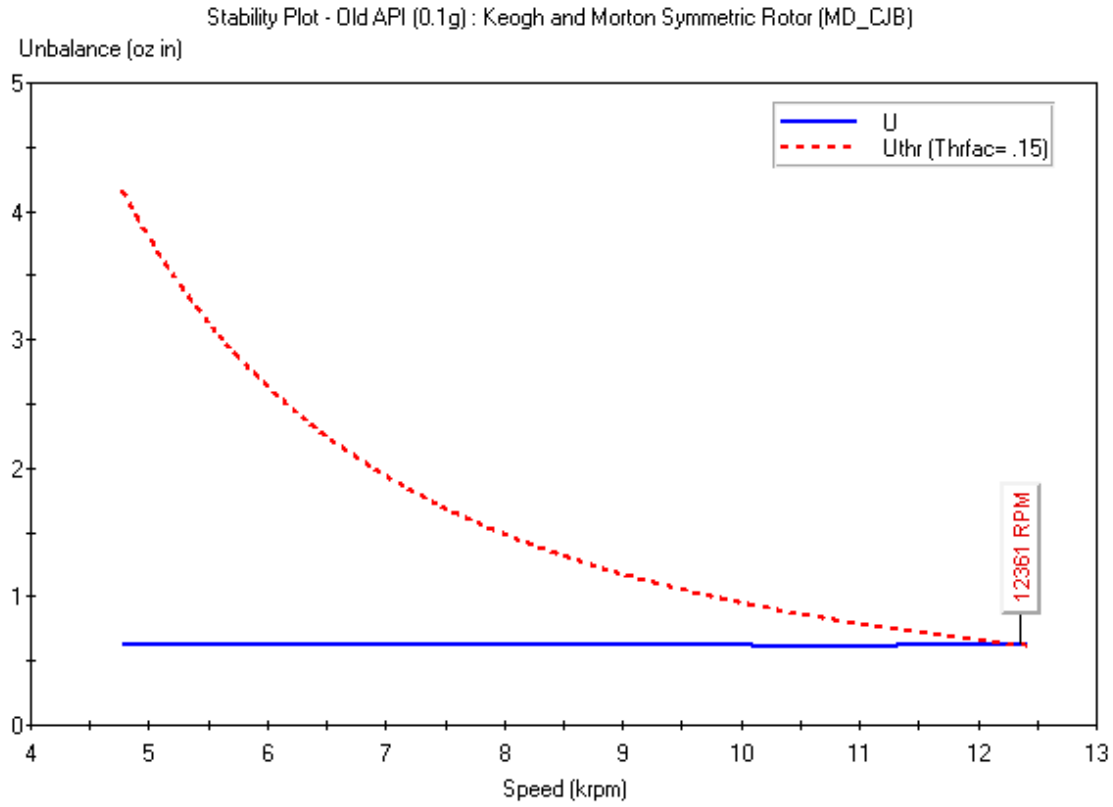

Figure 5.31 VT-MAP stability plot for mid-span Keogh and Morton rotor

Figure 5.31 shows the stability map for mid-span calculations of the Keogh and Morton rotor. It can be seen that the thermal bending does not generate the lower threshold of instability as it did in the overhung case. This is mainly due to the much smaller values of thermal bending deflections and the corresponding thermal imbalance generated in the mid-span rotor calculations for this rotor model.

This phenomenon can be further explained using the figures of mechanical and thermal imbalances, and the phase angle between them. Figure 5.32 and 5.33 show the detailed results for the overhung rotor and mid-span rotor calculations, respectively.

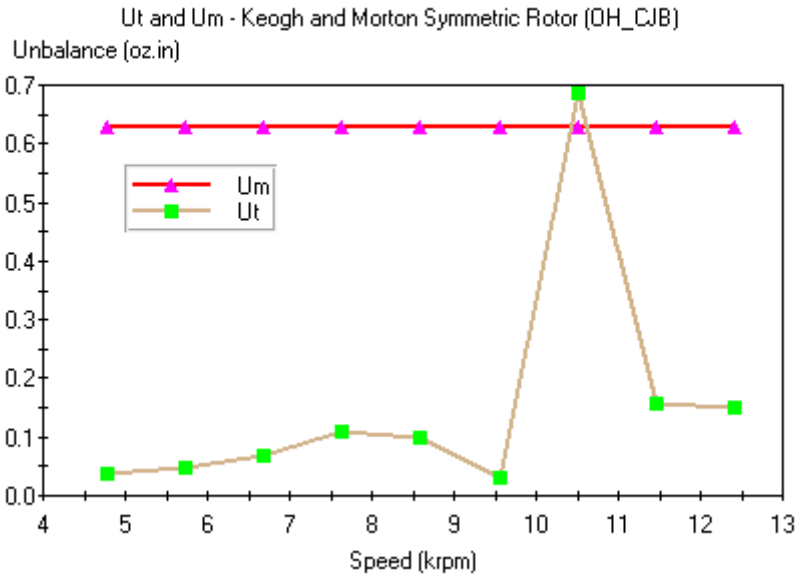

(a) Mechanical and thermal imbalances

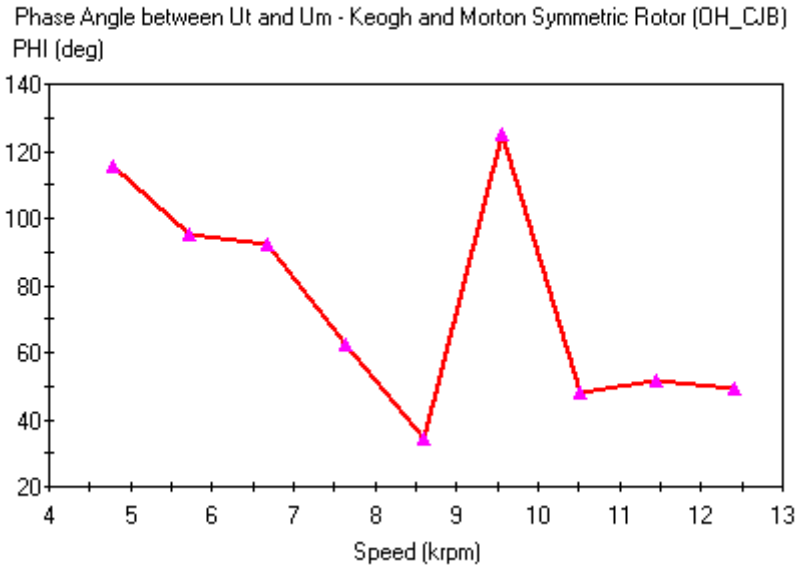

(b) Phase angles between mechanical and thermal imbalances

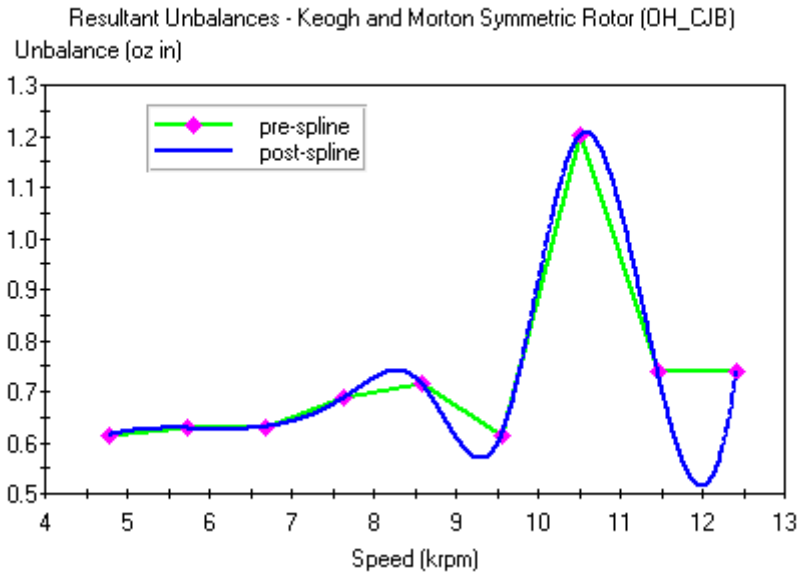

(c) Resultant imbalance

Figure 5.32 Stability analysis for overhung rotor calculations

It can be seen that for the overhung rotor calculations, the relative large values of the thermal bending deflections and the thermal imbalance increase the total levels of the resultant imbalance. The phase angles between the mechanical and thermal imbalances also make contributions to the overall increase of the total imbalance.

However, for the mid-span rotor calculations, the Morton Effect induced thermal bending deflections and the thermal imbalances are much smaller than the overhung case. The phase angles between the mechanical and thermal imbalances further reduce the negative impact by the thermal imbalance. It can be observed that the thermal imbalance does not make negative contributions to the threshold of instability in the stability plot.

This calculation can be used to explain why the mid-span rotors are less liable to be influenced by the Morton Effect induced instability.

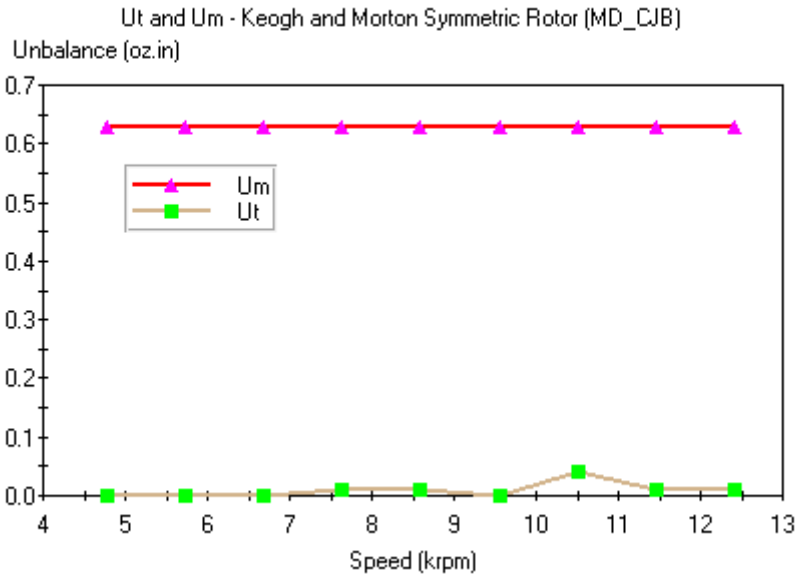

(a) Mechanical and thermal imbalances

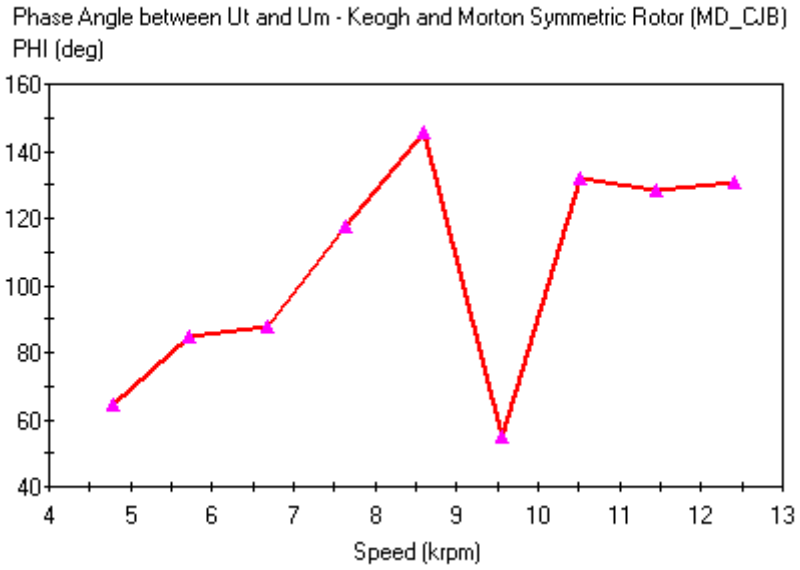

(b) Phase angles between mechanical and thermal imbalances

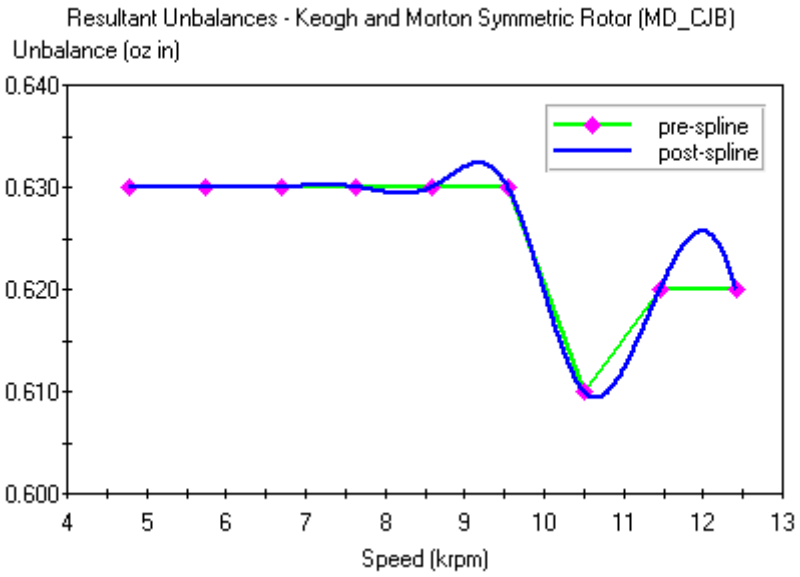

(c) Resultant imbalance

Figure 5.33 Stability analysis for mid-span rotor calculations

Figure 5.31shows that although the Morton Effect reduces the total imbalance above the 4th critical speed, the stability plot still indicates a threshold speed of instability at 12361 RPM. This is because the initial mechanical imbalance is evaluated at the maximum continuous operating speed, ω_{MCOS}=1047 rad/s (10000 RPM), for this rotor model. In fact, the Morton Effect does not induce instability here. This fact should always be included in the understanding of stability analysis results for the speed range which is above the maximum continuous operating speed.

5.4.2 TPJB Supported Mid-Span Rotor

This practical mid-span rotor comes from an example in DyRoBeS [43]. Figure 5.34 shows the rotor model and Table 5.2 the data for the calculation. The rotor is supported by two 4-pad tilting pad journal bearings.

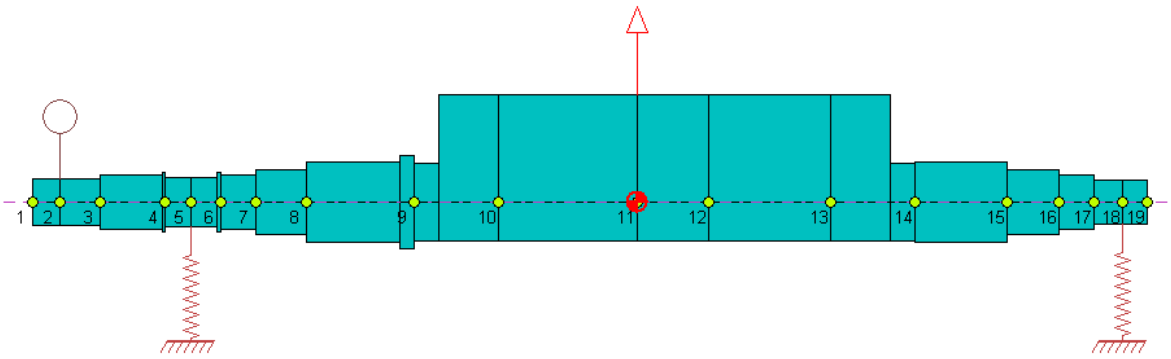

Figure 5.34 DyRoBeS model of TPJB supported mid-span rotor

This rotor experiences the critical speed around 2400 RPM. The calculation covers the speed range from 1000 RPM to 5000 RPM with 41 speeds calculated. Figure 5.35 shows the profiles of temperature, pressure and fluid film thickness for the bearing on the left-hand side at the speed of 2400 RPM. Figure 5.36 is the orbit plot of the same bearing at 2400 RPM.

Figure 5.37 shows the VT-MAP stability plot for this rotor model. It can be seen that the Morton Effect does not induce instability during the entire speed range of the calculation. The onset at 4348 RPM is a result of the calculated mechanical imbalance using a lower design speed (see comment referring to Figure 5.31 on page 158). The influence of the Morton Effect can be further explained by exploring the calculations of the resultant imbalance as shown in Figure 5.38. Figure 5.38(a) indicates that the thermal imbalance is quite smaller than the mechanical imbalance. The phase angle curve in Figure 5.38(b) shows that the thermal imbalance increases the total imbalance below the critical speed and decreases the total imbalance above the critical speed. This can be further proved in the calculation of using 2× orbit size (Figure 5.39 and 5.40).

These results show that for this mid-span rotor, the Morton Effect has the negative impact on the total level of imbalance below the critical speed. But if above the critical, its influence is positive.

Table 5.2 Data for TPJB supported mid-span rotor

Parameter	SI Units	EG Units
Number of pads, N_{pads}	4	4
Axial pad or brg length, L	89.89 mm	3.539 in.
Pad thickness, t_p,	19.05 mm	0.75 in.
Radial pad clearance, C_p	101.6 μm	4 mils
Angular dimension of pad, Δ_p	70 deg	70 deg
Pivot angles of pads, θ_p	45, 135, 225, 315 deg	45, 135, 225, 315 deg
Preload factor, m	0.5	0.5
Frac. ang. position of pivot, f_p	0.5	0.5
Radius of journal, R_j	44.95 mm	1.7695 in.
Radial bearing clearance, C_b	50.8 μm	2 mils
Bearing load, W	4448.2 N	1000 lb_f
Disk mass, M_d	453.6 kg	1000 lb_m
Rotor weight, W_{rotor}	8534.8 N	1918.7 lb_f
Initial mech. imbalance, U_m	6.264 kg-mm	8.7 oz-in.
Lubricant supply pressure, P_0	0.104 MPa	15 psi
Lubricant supply temp, T_0	48.9 ^oC	120 ^oF
Lubricant supply viscosity, μ_0	0.019 Pa-s	2.80 μreyn

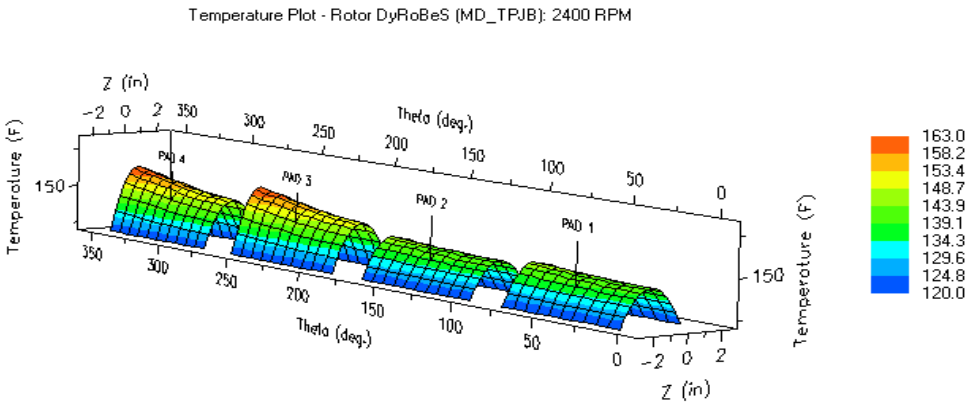

(a) Temperature distribution

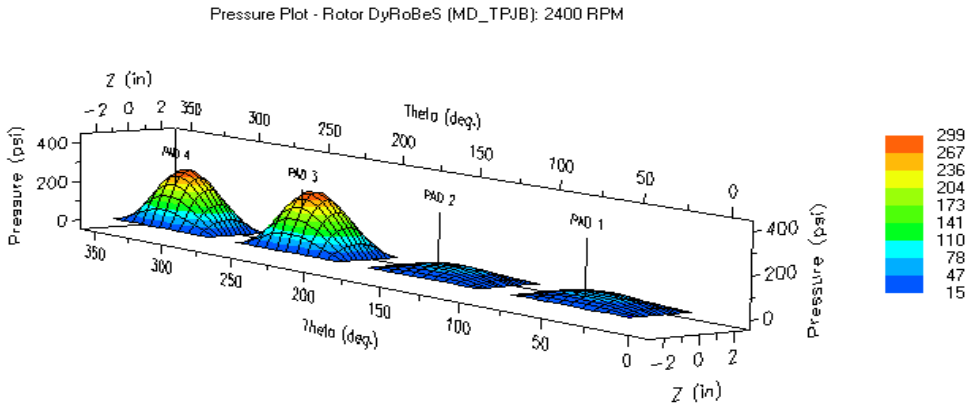

(b) Pressure distribution

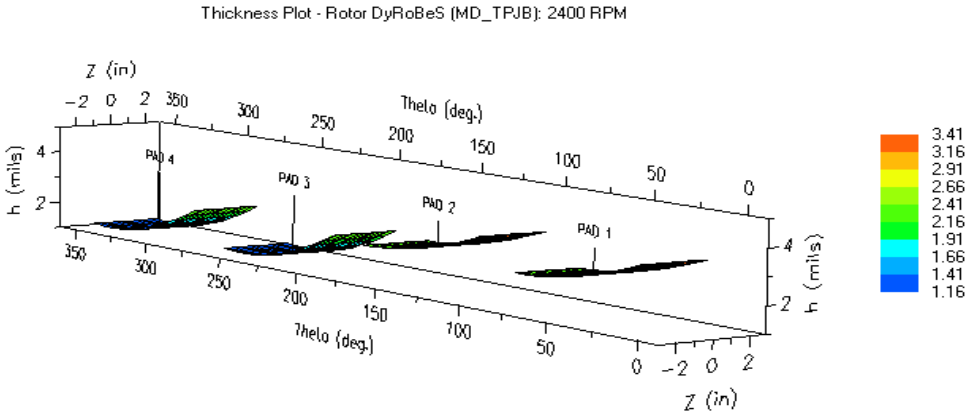

(c) Fluid film thickness

Figure 5.35 T-P-h plots at 2400 RPM for LHS bearing

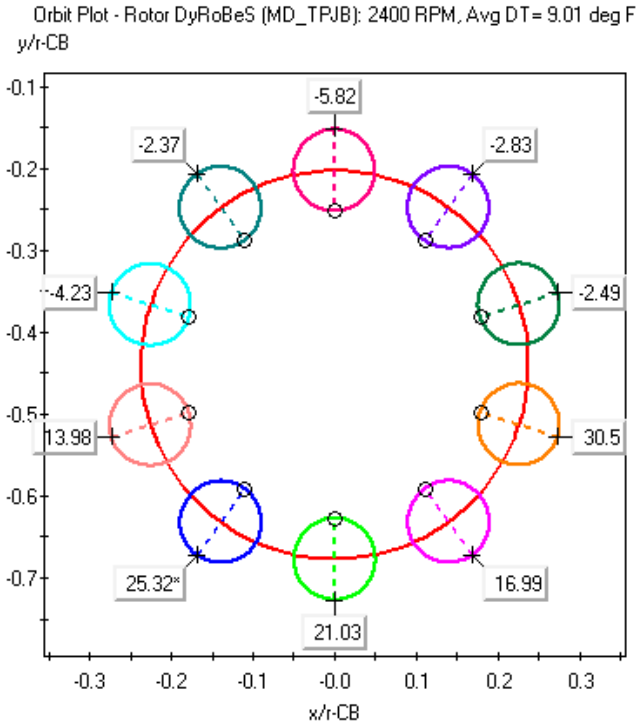

Figure 5.36 Orbit plot at 2400 RPM for LHS bearing

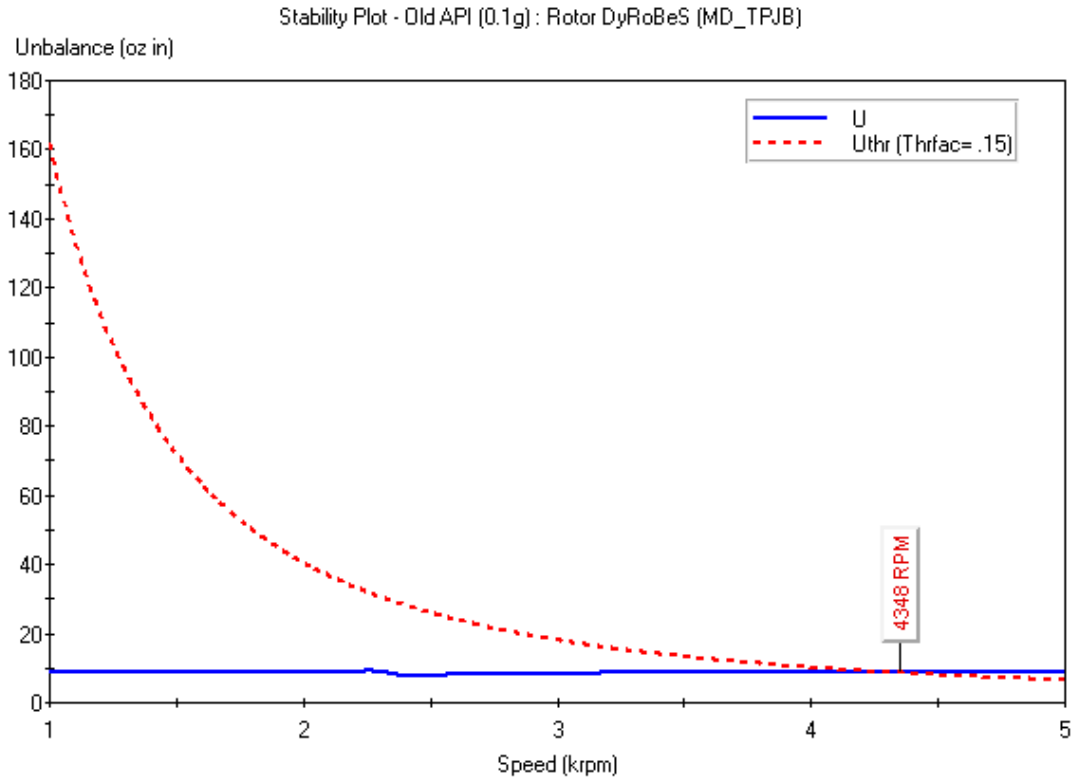

Figure 5.37 VT-MAP stability plot for TPJB supported mid-span rotor

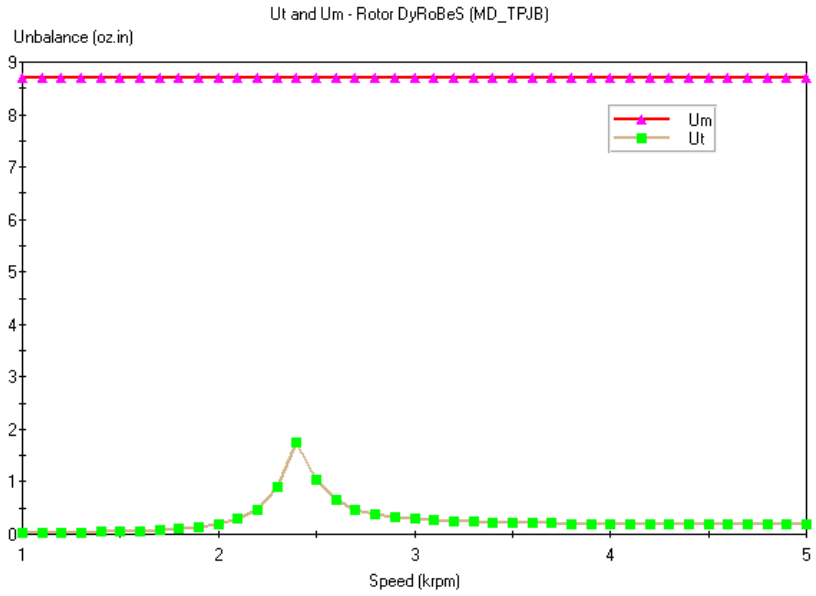

(a) Mechanical and thermal imbalances

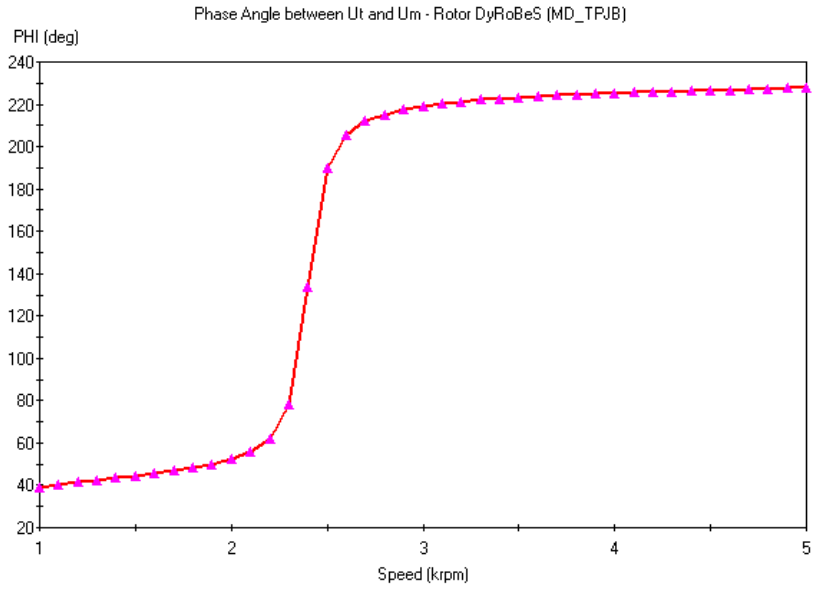

(b) Phase angles between mechanical and thermal imbalances

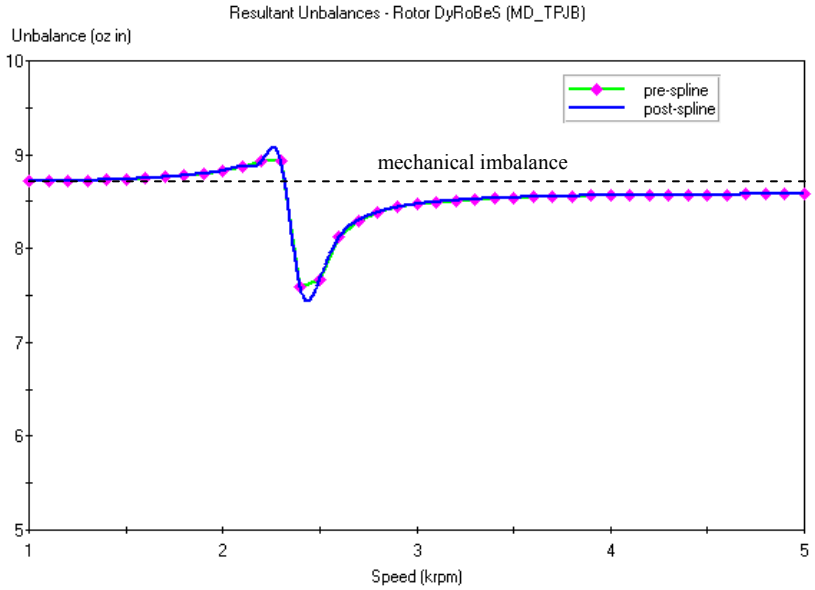

(c) Resultant imbalance

Figure 5.38 Stability analysis for TPJB supported mid-span rotor

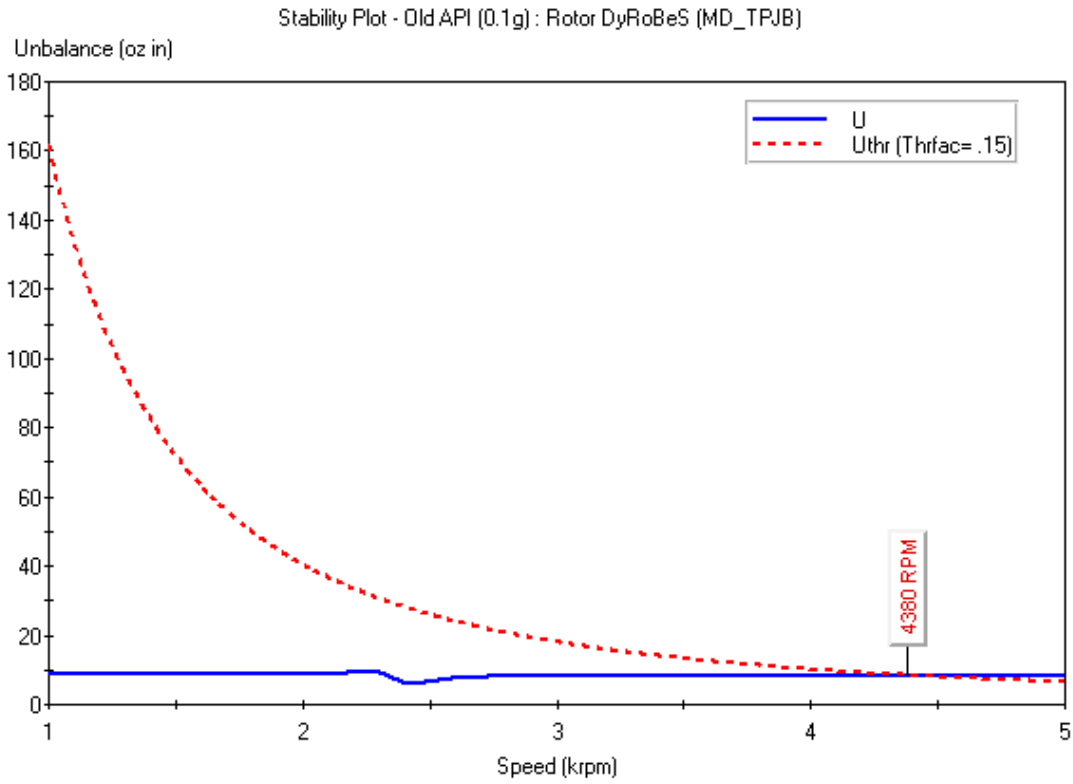

Figure 5.39 VT-MAP stability plot for TPJB supported mid-span rotor (2× orbit size)

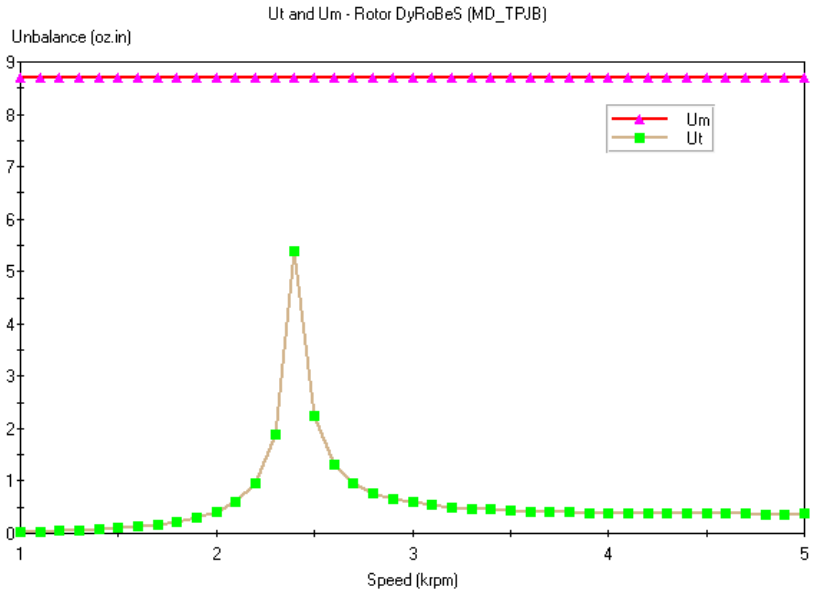

(a) Mechanical and thermal imbalances

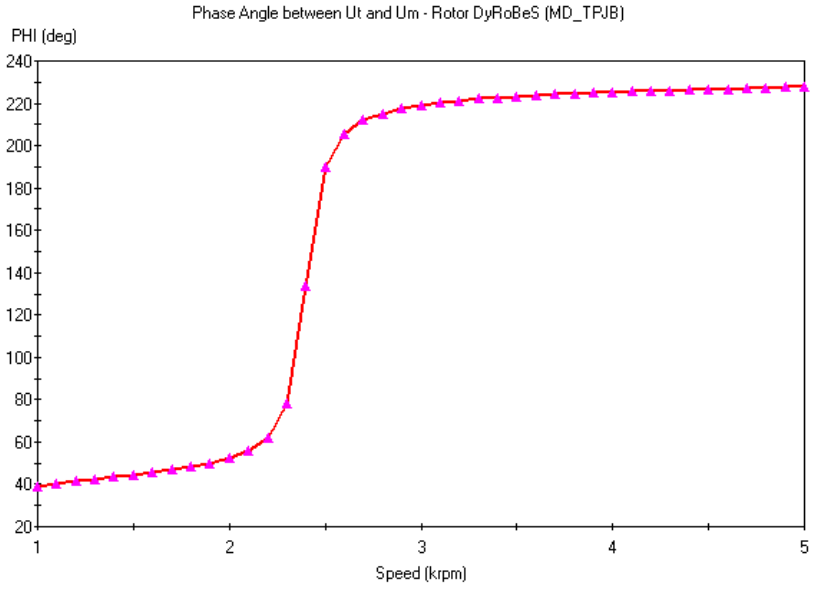

(b) Phase angles between mechanical and thermal imbalances

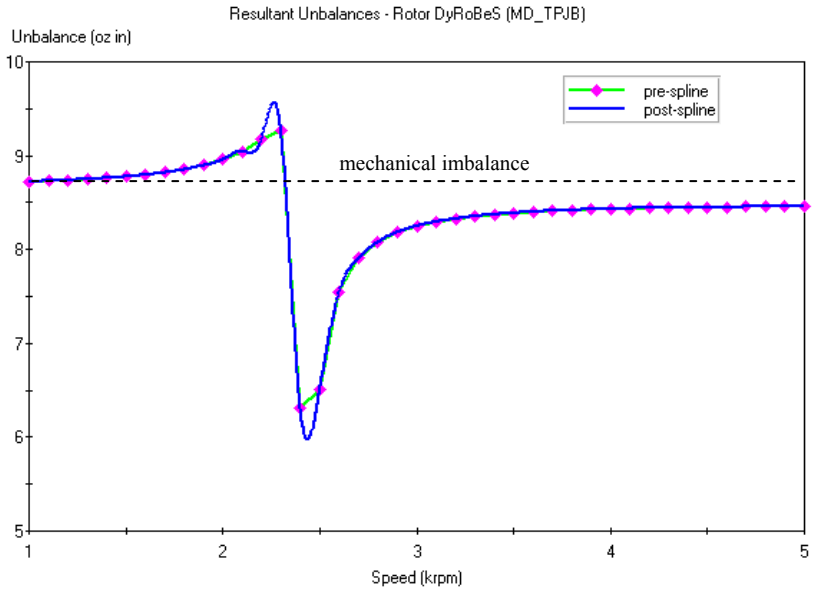

(c) Resultant imbalance

Figure 5.40 Stability analysis for TPJB supported mid-span rotor (2× orbit size)

5.5 Summary

The predictive solutions and corresponding software have been discussed in applying to mid-span rotors. The major conclusions can be summarized as follows:

(1) The concept of predictive solutions is extended to the mid-span rotors. This method can be used to predict the occurrence of the Morton Effect induced instability in general rotor-bearing systems based on the standard rotor dynamics calculations. It utilizes a threshold imbalance criterion for prediction of stability instead of employing traditional frequency-domain feedback analysis. The systematic approach including models and equations for mid-span rotors with various hydrodynamic journal bearings are presented.

(2) For practical applications, VT-MAP, the front-end software to predict the Morton Effect induced instability in both overhung and mid-span rotors supported by either hydrodynamic plain journal bearings or tilting pad journal bearings, is presented. The code adopts the standard interface design as most of popular commercial-quality programs. It provides the maximum flexibility in preparing input data file and reviewing the results of calculation.

(3) The case studies using predictive solutions are also presented. The calculations are conducted using VT-MAP to compare the influence of the Morton Effect on overhung and mid-span configurations for the Keogh and Morton rotor. Then the stability analysis on a practical mid-span rotor supported by the titling pad journal bearings is conducted. The results can be used to explain why the mid-span rotors are less liable to be influenced by the Morton Effect induced instability.

6 CONCLUSIONS

In this dissertation, a systematic study on the Morton Effect induced instability in mid-span rotor systems is presented, which includes the mechanism study of the Morton Effect induced instability, stead-state response performance of the system under the influence of the Morton Effect, models and simulations of mid-span rotor-hydrodynamic journal bearing systems, and the predictive solutions of general mid-span rotor systems. A number of conclusions and equations have been obtained. The results are summarized as follows:

1) Mechanism of Morton Effect Induced Instability

(1) The viscous thermal effect on the rotor systems has been represented by its equivalent thermal induced imbalance. Based on the observations from relevant references and reasonable deductions, a linear expression for the thermal imbalance has been made. A new term called the equivalent coefficient of thermal effect is introduced to represent the thermal effects due to structure and working conditions.

(2) It has been proved that there exists a threshold of instability due to the Morton Effect in the mid-span rotors. Based on the assumptions of linear isotopic bearing supports, this threshold speed takes simple forms of formulas as shown as in Equations (2.6b), (2.14b), and (2.25) for the system with the thermal imbalance acting in the same direction of response displacement, or in Equation (2.34b) for the system with the thermal imbalance acting

perpendicular to the direction of response displacement. These equations also show the factors affecting the values of threshold of the Morton Effect induced instability.

(3) A stability map for the damped rigid mid-span rotors with the thermal imbalance having arbitrary phase difference has been obtained. The stable operating regions of the system are bounded by two curves of threshold of instability, which is shown in Equations. (2.45) and (2.47). The Morton Effect induced instability thresholds are affected by both of the magnitude and the relative phase of the thermal imbalance.

(4) The mechanism of the Morton Effect induced thermal instability of mid-span rotors supported by linear isotropic bearings can be explained through the fact that the Morton Effect introduces either negative stiffness or negative cross-coupled stiffness.

(5) The root track of the damped rigid rotor system where the rotation speed as parameter has been obtained. The results are consistent with the derived analytical solutions of the threshold speed of instability. The Morton Effect has an impact on the characteristic roots of the system and makes them the functions of the rotation speed. The results show that when the thermal imbalance and the response displacement are in the same line (in same or opposite directions), the imaginary parts (frequencies) will dependent on the rotation speed. If they are not in the same line, both the real parts and imaginary parts are dependent on the rotation speed. The relative magnitudes of the frequencies than the system damped natural frequency will depend on the relative phase angles of the thermal imbalance.

2) Steady-State Response Under Morton Effect

(6) Under the influence of the Morton Effect, the finite values of steady-state response of the system will be present within the stable operating speed region. The thermal imbalance would not naturally initiate a diverging response pattern such as resulting from a positive

feedback system in nature. This phenomenon can also be explained by the derived conclusion that the Morton Effect introduces an additional stiffness.

(7) The Morton Effect has a comprehensive impact on both the amplitude and phase lag of the steady-state unbalance response. It may shift the curves of the response amplitude and phase lag in a manner dependent on the relative magnitude and direction of the thermal imbalance.

(8) One feature of steady-state response of rotor systems under the influence of the Morton Effect is that the phase lag of the disk at the critical speed may not equal 90 degrees except when the thermal imbalance has "perpendicular lag" to the direction of displacement.

3) Models and Simulations of Mid-Span Rotor -Hydrodynamic Bearing Systems

(9) A new thermal bending model of mid-span rotors has been presented. The formulas of deflections are obtained, which is the basis to calculate the equivalent thermal imbalance. The suggested thermal bending model can also partially explain that the mid-span rotors are less liable to be influenced by the Morton Effect induced instability because of the restraining effect between the two supports, than the overhung configurations.

(10) Using an established equation to calculate the temperature distribution and temperature differences of hydrodynamic plain journal bearing, the new expressions of differential temperatures for the case where heat transfer through the bearing and journal surfaces is neglected have been derived for the analytical discussion. Figure 4.6 shows that for an eccentricity ratio less than 0.5, the relationship between the temperature difference and the eccentricity distance which is corresponding to the response displacement can be roughly considered to be linear.

(11) Based on the suggested thermal bending model and differential temperature formulas, the equivalent thermal imbalance can be calculated. Especially, for the case where heat transfer through solid surfaces is neglected, the closed form of thermal imbalance has been obtained.

(12) Using the obtained formulas of the thermal imbalance, initial calculation has been conducted to understand the magnitude levels of the thermal imbalance for a typical rotor model, which can be used to evaluate the equivalent coefficient of thermal effect. These initial results are promising and illustrative. They have also proved many important conclusions obtained in Chapter 2. It shows that the thermal imbalance induced by the Morton Effect may increase to the level of the mechanical imbalance and then its influence on the system stability should be included.

(13) The model for the dynamics of a symmetrical elastic rotor–hydrodynamic plain journal bearing system has been established. The local stability around the equilibriums is conducted through calculating the characteristic roots of the system's Jacobian matrix. The simulation of the system transient response to unbalance excitation is also performed to exhibit the influence of the Morton Effect. The results show that the Morton Effect may make a further negative impact on the instabilities of the rotor system under some working conditions, considering the existence of the oil film self-induced vibration due to the dynamic characteristics of fluid film bearings. In addition, the Morton Effect also has an impact on the unbalance response of the system. The simulation results show that the Morton Effect changes the shapes of the whirling orbits and makes them no longer the standard elliptical orbits around the static equilibriums.

4) Predictive Solutions and Software

(14) The concept of predictive solutions is extended to the mid-span rotors. This method can be used to predict the occurrence of the Morton Effect induced instability in general rotor-bearing systems based on the standard rotor dynamics calculations. It utilizes a threshold imbalance criterion for prediction of stability instead of employing traditional frequency-domain feedback analysis. The systematic approach including models and equations for mid-span rotors with various hydrodynamic journal bearings are presented.

(15) For practical applications, VT-MAP, the front-end software to predict the Morton Effect induced instability in both overhung and mid-span rotors supported by either hydrodynamic plain journal bearings or tilting pad journal bearings, is presented. The code adopts the standard interface design as most of popular commercial-quality programs. It provides the maximum flexibility in preparing input data file and reviewing the results of calculation.

(16) The case studies using predictive solutions are also presented. The calculations are conducted using VT-MAP to compare the influence of the Morton Effect on overhung and mid-span configurations for the Keogh and Morton rotor. Then the stability analysis on a practical mid-span rotor supported by the titling pad journal bearings is conducted. The results can be used to explain why the mid-span rotors are less liable to be influenced by the Morton Effect induced instability.

7 SUGGESTED FUTURE RESERACH

The extensive study on the Morton Effect induced instability in the mid-span rotor – hydrodynamic bearing systems has been presented in this dissertation. However, there are still some aspects which are expected to be added in the future research pursuit on this subject.

1) Improved Models in Analytical Study

In the current model, the time delay in the thermal calculations was neglected. The inclusion of the thermal time delay in the future modeling may be used to explain some of the observed phenomenon in the practical rotors, which include the pulse pattern when the Moron Effect induced instability occurred [14-15] and the delayed positions of the hot spot relative to the minimum fluid film thickness [25].

In addition, a more accurate model to calculate the bearing temperature distributions is also expected.

2) Experimental Study

The experimental investigation can be conducted to further prove the relevant conclusions obtained in the theoretical analysis and calculations. For this purpose, a new test rig must be designed and manufactured to exhibit the Morton Effect. The differential temperatures across the journal surface and the instability thresholds under the influence of the Morton Effect are two

major expected measurements. Considering this research involves comprehensive work and time, it is suggested that it should be undertaken as a separate M.S. or Ph.D. project.

3) Predictive Solutions and VT-MAP

In Section 5.2, three methods to locate the hot and cold spots are presented. Among them, Original Method and Improved Method have been successfully applied in overhung rotors and further extended to mid-span rotors. In developing VT-MAP, an alternative option, named New Method, is presented. The concept of New Method is different than the first two methods. For the hydrodynamic plain journal bearings, the hot spot and cold spot at each dynamic position of the journal will be identified using Equation (4.34).

Figure 7.1 shows the comparison of using three different methods in an example calculation for hydrodynamic plain journal bearings. The calculation results show that there is no big difference for the first two methods in predicting average temperature difference and resultant thermal imbalance. In this calculation, the average temperature difference at speed of 8595 RPM is 2.75 ^{o}F and 3.18 ^{o}F, respectively for using Original Method and Improved Method (Figure 7.1a, b). However, if New Method is employed, this average temperature difference will turn to be 26.89 ^{o}F. The reason to cause this difference is that the first two methods track a fixed spot during the entire whirling circle where the last method tracks the maximum temperature differences instead.

It is obvious that due to the inherent difference of this new method relative to the first two methods, a new stability threshold imbalance criterion may need to be set up and calibrated in future.

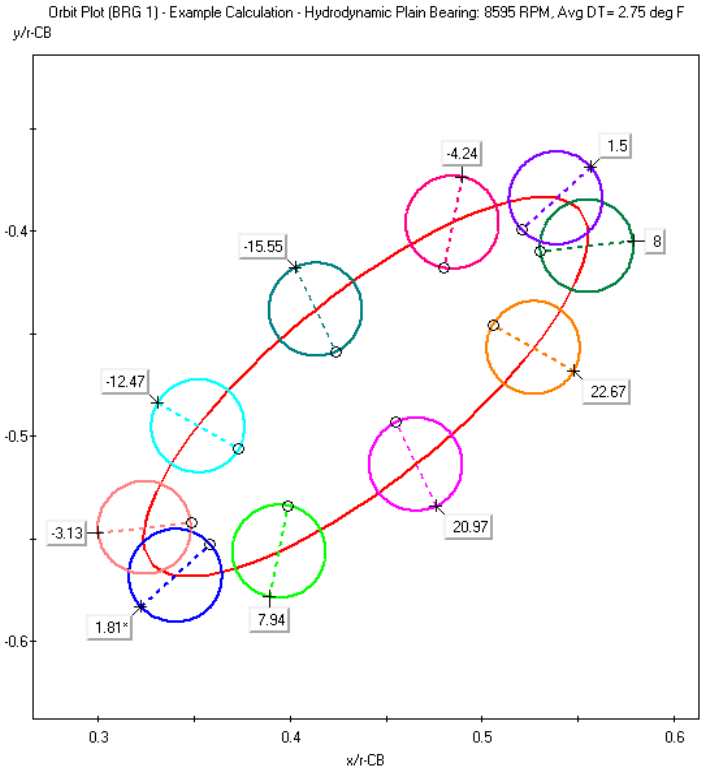

(a) Original Method

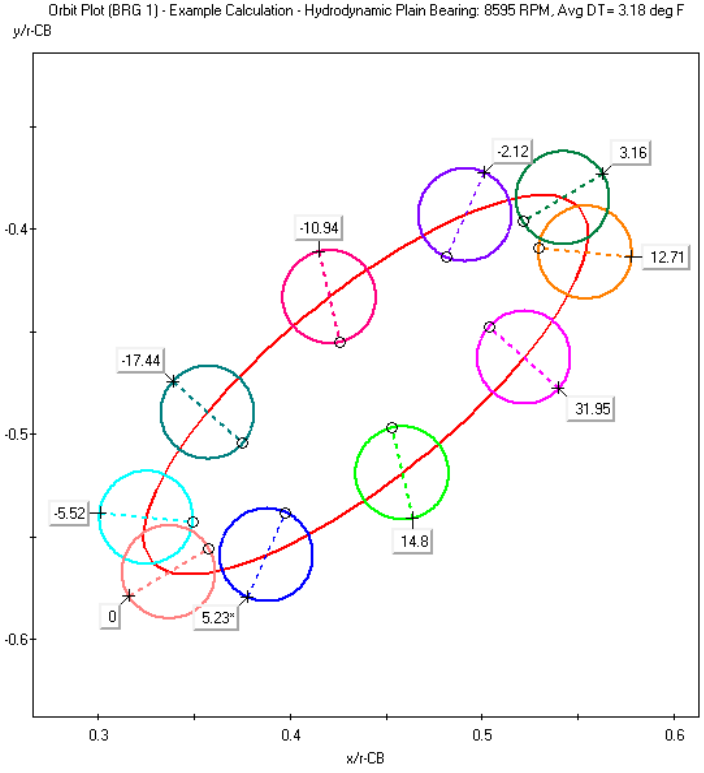

(b) Improved Method

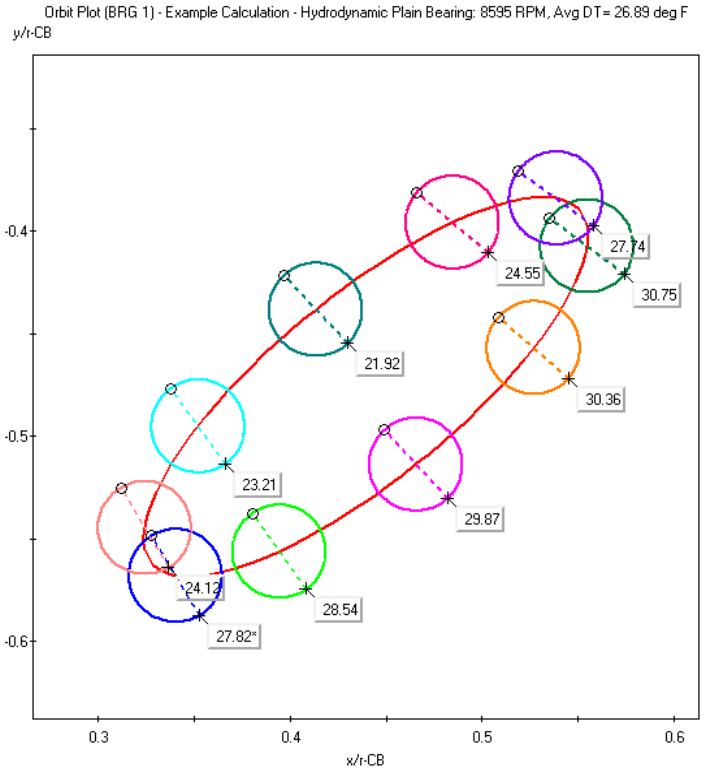

(c) New Method

Figure 7.1 Comparison of three methods to locate hot and cold spots

REFERENCES

1. Jeffcott, H. H., 1919, "The Lateral Vibration of Loaded Shafts in the Neighborhood of a Whirling Speed - The Effect of Want of Balance," Phil. Mag., Vol. 37, pp.304-314.
2. Newkirk, B. L., and Taylor, H. D., 1925, "Shaft Whipping Due to Oil Action in Journal Bearings," General Electric Review, Vol. 28, pp.559-568.
3. Hagg, A. C., 1946, "The Influence of Oil-Film Journal Bearings on the Stability of Rotating Machines," Trans. ASME, Journal of Applied Mechanics, Vol.68, pp.211-220.
4. Poritsky, H., 1953, "Contribution to the Theory of Oil Whip," Trans. ASME, Journal of Applied Mechanics, Vol.75, pp.1153-1161.
5. Pinkus, O., 1956, "Experimental Investigation of Resonant Whip," Trans. ASME, Journal of Applied Mechanics, Vol.78, pp.975-983.
6. Lund, J.W., and Sternlicht, B., 1962, "Rotor Bearing Dynamics with Emphasis on Attenuation," Trans. ASME, Journal of Basic Engineering, Vol. 84, pp.491-502
7. Gunter, E. J., 1966, "Dynamic Stability of Rotor-Bearing Systems," NASA SP-113.
8. De Choudhury, P., 1971, " Dynamic Stability of Flexible Rotor-Bearing Systems," Ph.D. Thesis, University of Virginia, Charlottesville, VA
9. Kirk, R. G., 1972, "Nonlinear Transient Analysis of Multi-Mass Flexible Rotors," Ph. D. Thesis, University of Virginia, Charlottesville, VA.

10. Keogh, P. S. and Morton, P. G., 1993, "Journal Bearing Differential Heating Evaluation with Influence on Rotor Dynamic Behaviour," Proceedings of Royal Society, London, England, Series A, Vol. 441, pp.527-548.

11. Keogh, P. S. and Morton, P. G., 1994, "The dynamic nature of rotor thermal bending due to unsteady lubricant shearing within bearing," Proceedings of Royal Society of London, Series A, Vol. 445, pp. 273-290.

12. de Jongh, F. M. and Morton, P. G., 1994, "The synchronous instability of a compressor rotor due to bearing journal differential heating," ASME paper, 94-GT-35, pp. 1-13.

13. Ettles, C. M., 1992, "The Analysis of Pivoted Pad Journal Bearing Assemblies Considering Thermoelastic Deformation and Heat Transfer Effects", Tribology Transactions, Vol. 35, No.1, pp.156-162.

14. Faulkner, H. B., Strong, W. F., and Kirk, R. G., 1997, "Thermally induced synchronous instability of a radial inflow overhung turbine, part I", DETC97/VIB-4063, Proceedings of 1997 ASME Design Engineering Technical Conferences, September 14-17, Sacramento, California.

15. Faulkner, H. B., Strong, W. F., and Kirk, R. G., 1997, "Thermally induced synchronous instability of a radial inflow overhung turbine, part II", DETC97/VIB-4174, Proceedings of 1997 ASME Design Engineering Technical Conferences, September 14-17, Sacramento, California.

16. Monmousseau, P., Fillon, M., and Frene, J., 1997, "Transient Thermoelastohydrodynamic Study of Tilting-Pad Journal Bearings - Comparison between Experimental Data and Theoretical Results," Journal of Tribology, Vol. 119, pp. 401-407.

17. Larsson, B., 1999a, “Journal Asymmetric Heating - Part I: Nonstationary Bow,” Journal of Tribology, Vol. 121, pp. 157-163.

18. Larsson, B., 1999b, “Journal Asymmetric Heating - Part II: Alteration of Rotor Dynamic Properties,” Journal of Tribology, Vol. 121, pp. 164-168.

19. Balbahadur, A. C. and Kirk, R. G., 2002, “Part I – Theoretical model for a synchronous thermal instability operating in overhung rotors”, Proceedings of 2002 IFTOMM, Sixth International Conference on Rotor Dynamics, September 30-October 4, Sydney, Australia.

20. Balbahadur, A. C. and Kirk, R. G., 2002, “Part II – Case studies for a synchronous thermal instability operating in overhung rotors”, Proceedings of 2002 IFTOMM, Sixth International Conference on Rotor Dynamics, September 30-October 4, Sydney, Australia.

21. Balbahadur, A. C., 2001, “A Thermoelastohydrodynamic Model of the Morton Effect Operating in Overhung Rotors Supported by Plain or Tilting Pad Journal Bearings,” Ph.D. Dissertation, Virginia Polytechnic Institute and State University, Blacksburg, Virginia.

22. Kirk, R. G; Guo, Zenglin; Balbahadur, A. C., 2003, “Synchronous Thermal Instability Prediction for Overhung Rotors,” Proceedings of 32nd Turbomachinery Symposium, Texas A&M University, Houston, Texas, September 8-11.

23. Kirk, R. G.; Guo, Z., 2005, “Morton Effect Analysis — Theory, Program and Case Study”, Proceedings of ISCORMA-3, pp.390-401, Cleveland, Ohio, 19-23 September.

24. Morton, P. G., 2008, “Unstable shaft vibrations arising from thermal effects due to oil shearing between stationary and rotating elements”, Proceedings of IMECH-9th International Conference on Vibrations of Rotating Machinery, September 8-10, Exeter, England.

25. de Jongh, F. M., 2008, “The Synchronous Rotor Instability Phenomenon-Morton Effect”, Turbomachinery Symposium, Texas A & M University, September 8-11, Houston, Texas.
26. Schmied, J., 1987, “Spiral Vibrations of Rotors,” Rotating Machinery Dynamics, Vol. 2, ASME Design Technology Conference, Boston, September.
27. Newkirk, B. L., 1926, “Shaft Rubbing”, Mechanical Engineering,” Vol.48, No.8, pp.830-832.
28. Dimarogonas, A. D., 1973, “Newkirk Effect: Thermally Induced Dynamic Instability of High-Speed Rotors,” ASME paper, 73-GT-26, pp. 2-11.
29. Hesseborn, B., 1978, “Measurements of Temperature Unsymmetries in Bearing Journal Due to a Vibration,” Internal Report ABB Stal.
30. Smith, D. M., 1974, “The Dynamics of Synchronous Whirl in Turbine Rotors,” Proceedings of IUTAM Symposium Lyngby, Denmark, August 12-16, pp.524-545.
31. Inman, D. J., 2007, “Vibrating Engineering”, 3rd edition, Prentice Hall.
32. Timoshenko, S. P., 1972, “Mechanics of Materials,” D. Van Nostrand Company, New York.
33. Popov, E. P., 1976, “Mechanics of Materials,” second edition, Prentice Hall, Inc. Englewood Cliffs, New Jersey.
34. Cameron, A., 1966, “The Principles of Lubrication,” Longmans Green & Co. Ltd., London.
35. Pinkus, O., 1990, “Thermal Aspects of Fluid Film Tribology,” ASME Press, New York.
36. Nicholas, J. C., Gunter, E. J., and Allaire, P.E., 1976, “Effect of Residual Shaft Bow on Unbalance Response and Balancing of a Single Mass Flexible Rotor, Part 1: Unbalance Response”, Trans. ASME, Journal of Engineering for Power, 98(2), pp.171-181.

37. Nicholas, J. C., Gunter, E. J., and Allaire, P.E., 1976, “Effect of Residual Shaft Bow on Unbalance Response and Balancing of a Single Mass Flexible Rotor, Part 2: Balancing”, Trans. ASME, Journal of Engineering for Power, 98(2), pp.182-189.

38. Rao, J. S., 2001, “A Note on Jeffcott Warped Rotor”, Mechanism and Machine Theory, 36, pp.563-575.

39. Meagher, J., Wu, X., and Lencioni, C., 2008, “Response of a Warped Flexible Rotor with a Fluid Bearing”, International Journal of Rotating Machinery, pp.1-9.

40. Vance, J. M., 1988, “Rotordynamics of Turbomachinery”, Wiley-Interscience.

41. Strogatz, S.H., 2001, “Nonlinear Dynamics and Chaos: With Applications to Physics, Biology, Chemistry, and Engineering”, Westview Press.

42. Nayfeh, A. H. and Balachandran, B., 1995, “Applied Nonlinear Dynamics: Analytical, Computational, and Experimental Methods”, Wiley-InterScience, New Jersey.

43. Chen, W. J. and Gunter, E. J., 2005,“Introduction to Dynamics of Rotor-Bearing Systems”, Trafford Publishing.

44. Kirk, R. G., Raju, K.V.S., and Ramesh, K., 1999, “PC-Based Analysis of Turbomachinery Vibration,” The Shock and Vibration Digest, Vol. 31, No. 6, pp. 449-454.

APPENDIX A

VT-MAP ANALYSIS: PIPELINE COMPRESSOR ROTOR

The following case came from a domestic compressor company. An initial running of the pipeline compressor was unstable on the test stand and it was thought it might be a thermal instability. Virginia Tech Rotor Lab was contacted to evaluate the rotor for thermal instability using newly developed predictive software. The VT-FAST rotor model for the compressor is shown in Figure A.1.

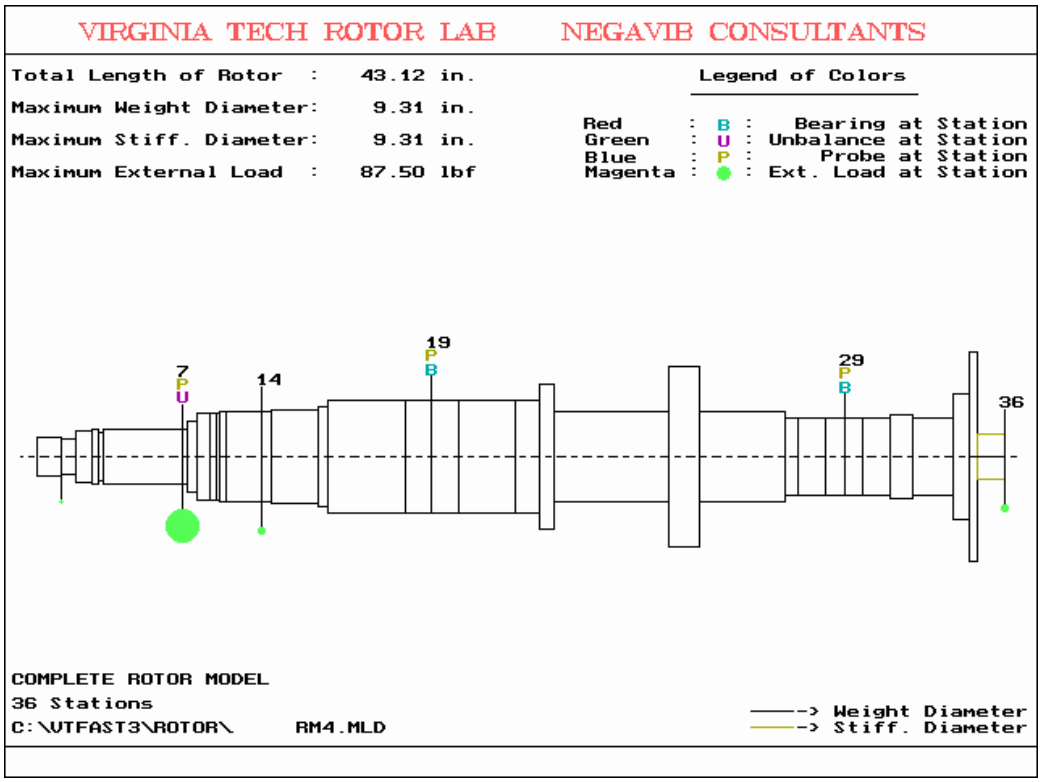

Figure A.1 VT-FAST model of a pipeline compressor rotor

The required data for thermal stability analysis is presented in Table A.1 for the pipeline compressor. The calculated speed range is from 6000 to 11000 RPM.

Table A.1 Data for pipeline compressor rotor, L/D = 0.476

Parameter	SI Units	EG Units
Number of pads, N_{pads}	5	5
Axial pad or brg length, L	0.0604 m	2.38 in.
Pad thickness, t_p,	0.0127 m	0.5 in.
Radial pad clearance, C_p	133.35 μm	5.25 mils
Angular dimension of pad, Δ_p	56 deg	56 deg
Pivot angles of pads, θ_p	18, 90, 162, 234, 306 deg	18, 90, 162, 234, 306 deg
Preload factor, m	0.34	0.34
Frac. ang. position of pivot, f_p	0.5	0.5
Radius of journal, R_j	0.0635 m	2.50 in.
Radial bearing clearance, C_b	88.14 μm	3.47 mils
Bearing load, W	1277 N	287 lb_f
Overhang mass, M_d	77.45 kg	170.4 lb_m
Overhang distance L_d	0.227 m	8.95 in.
Rotor weight, W_{rotor}	1202 N	270 lb_f
Initial mech. imbalance, U_m	0.11 kg-mm	0.15 oz-in.
Lubricant supply pressure, P_0	0.104 MPa	15 psi
Lubricant supply temp, T_0	50 ^oC	122 ^oF
Lubricant supply viscosity, μ_0	20.3 cP	2.94 μreyn
Lubricant density, ρ_l	888 kg/m^3	0.031 lb_m/in^3
Lubricant sp. heat capacity, c_l	1992 J/kg/K	0.478 Btu/lb_m/ ^oF
Thermoviscosity coeff., β	0.031 / ^oC	0.017 /^oF

Figure A.2 shows the temperature, pressure and film thickness distributions at 8000 RPM, obtained from the VT-MAP internal bearing analysis.

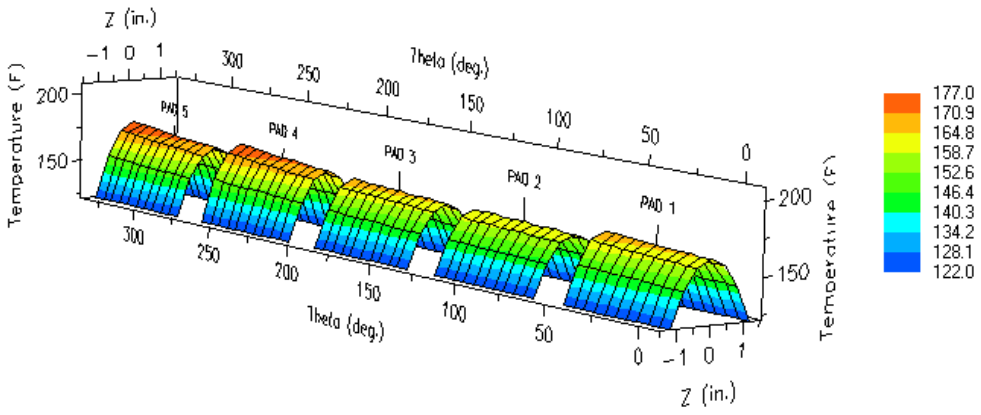

(a) Temperature distribution

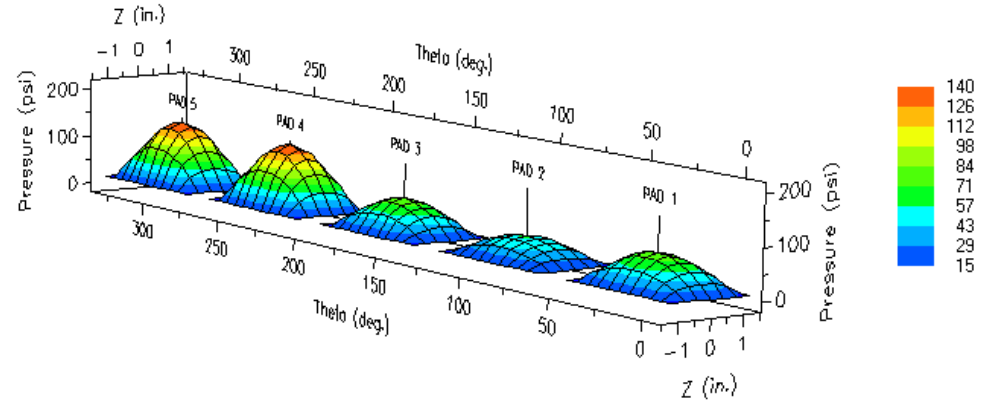

(b) Pressure distribution

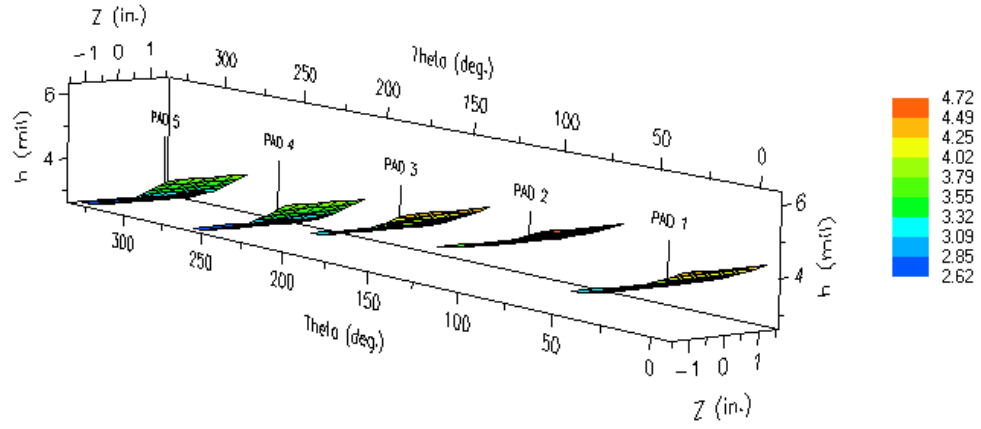

(c) Fluid film thickness

Figure A.2 T-P-h plots at 8000 RPM, L/D=0.476

The stability plot is shown in Figure A.3. It can be seen that thermal instability is predicted to occur at 9895 RPM. From the test stand operation, the instability was reported at a speed of 10,200 RPM.

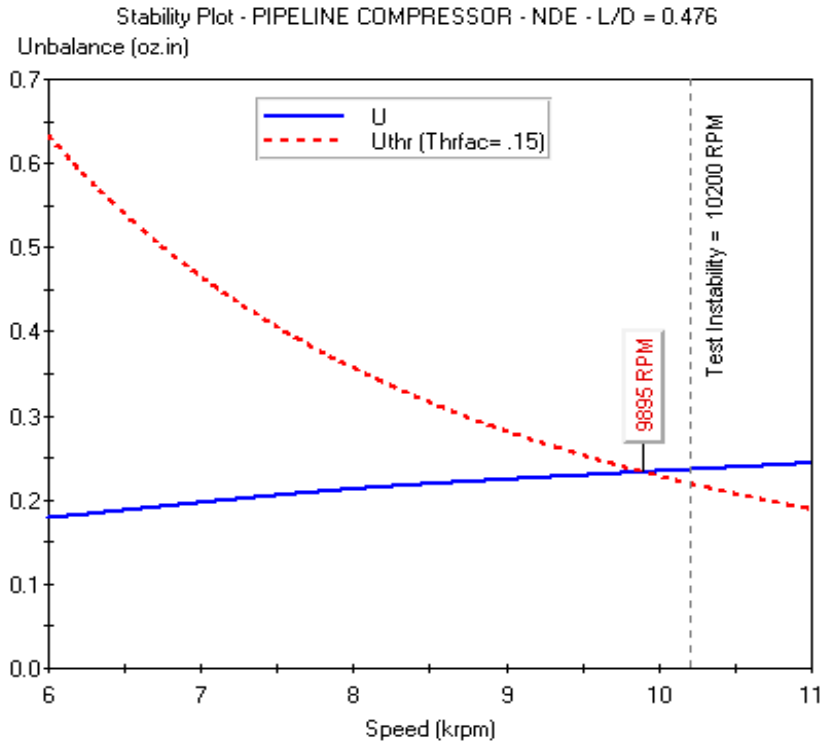

Figure A.3 Stability plot of pipeline compressor, L/D=0.476

Figure A.4 are the orbit plots at 6000 RPM, 8000RPM, and 10000 RPM, respectively. It can be seen that the magnitudes of thermal difference and resultant thermal imbalance increase with the increase of speed. It is also learned from the numerical result that the phase angle between thermal and mechanical imbalances gradually decrease with the increase of speed. This mechanism of combining the increased thermal imbalance and decreased phase angle eventually leads to the thermal instability.

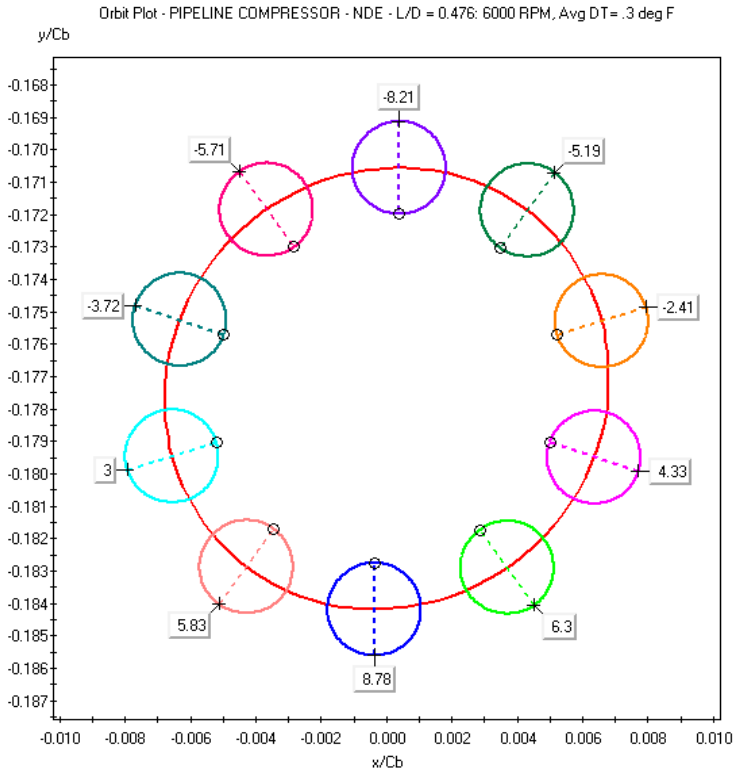

(a) 6000 RPM

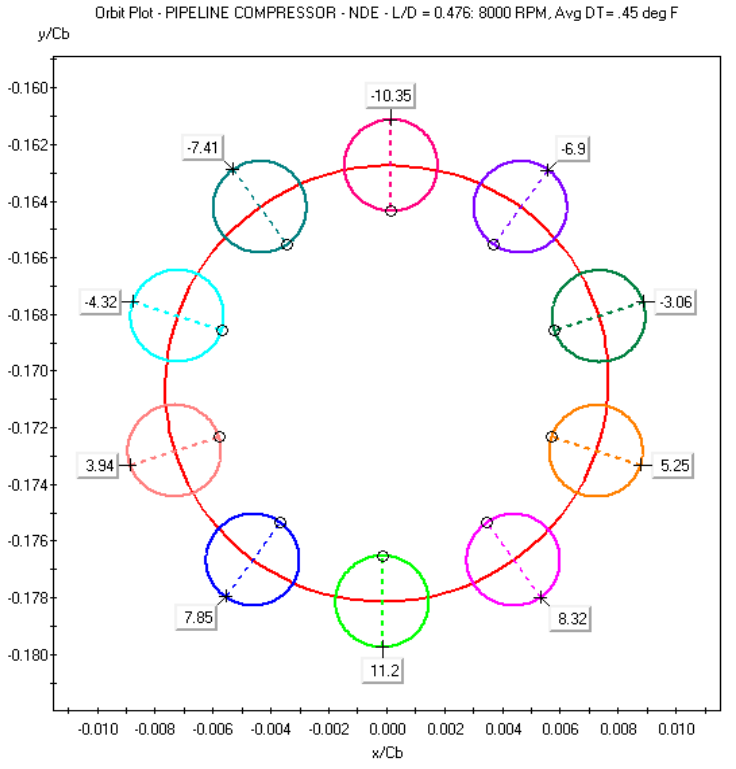

(b) 8000 RPM

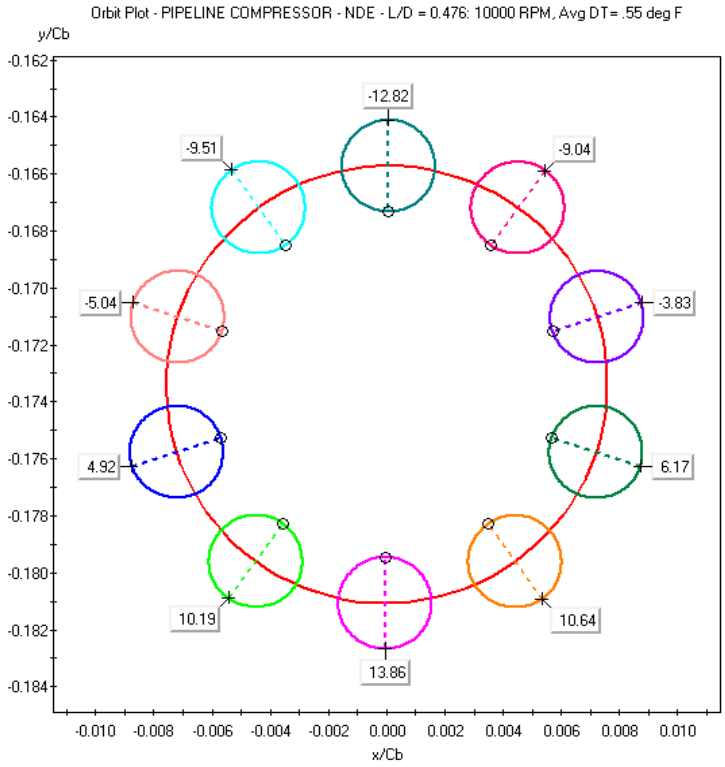

(c) 10000 RPM

Figure A.4 Orbit Plots of Pipeline Compressor, L/D=0.476

The elimination of the thermal instability may be achieved by any procedure that will sufficiently reduce the thermal gradient in the journal area of the rotor shaft. For tilting pad bearings, a modification in pad length may be an acceptable solution. To prove this in the VT-MAP analysis, consider the design as shown in Table A.2, where the L/D has been reduced from 0.476 to 0.25. The resulting stability prediction indicates the threshold has moved up to 10675 RPM (Figure A.5). The compressor on test had the bearing length reduced and the instability was in fact eliminated. Hence, the new analysis is in agreement with the test stand result. However, the threshold speed is still close to the desired operating speed and proper balance will be essential for continued stability.

Table A.2 Data for pipeline compressor rotor, L/D = 0.25

Parameter	SI Units	EG Units
Number of pads, N_{pads}	5	5
Axial pad or brg length, L	0.032 m	1.25 in.
Pad thickness, t_p,	0.030 m	1.20 in.
Radial pad clearance, C_p	177.8 μm	7 mils
Angular dimension of pad, Δ_p	56 deg	56 deg
Pivot angles of pads, θ_p	18, 90, 162, 234, 306 deg	18, 90, 162, 234, 306 deg
Preload factor, m	0.5	0.5
Frac. ang. position of pivot, f_p	0.5	0.5
Radius of journal, R_j	0.0635 m	2.50 in.
Radial bearing clearance, C_b	88.9 μm	3.5 mils
Bearing load, W	1277 N	287 lb_f
Overhang mass, M_d	77.45 kg	170.4 lb_m
Overhang distance, L_d	0.227 m	8.95 in.
Rotor weight, W_{rotor}	1202 N	270 lb_f
Initial mech. imbalance, U_m	0.11 kg-mm	0.15 oz-in.
Lubricant supply pressure, P_0	0.104 MPa	15 psi
Lubricant supply temp, T_0	50 ^oC	122 ^oF
Lubricant supply viscosity, μ_0	0.0203 Pa-s	2.94 μreyn
Lubricant density, ρ_l	888 kg/m^3	0.031 lb_m/in^3
Lubricant sp. heat capacity, c_l	1992 J/kg/K	0.478 Btu/lb_m/ ^oF
Thermoviscosity coeff., β	0.031 / ^oC	0.017 /^oF

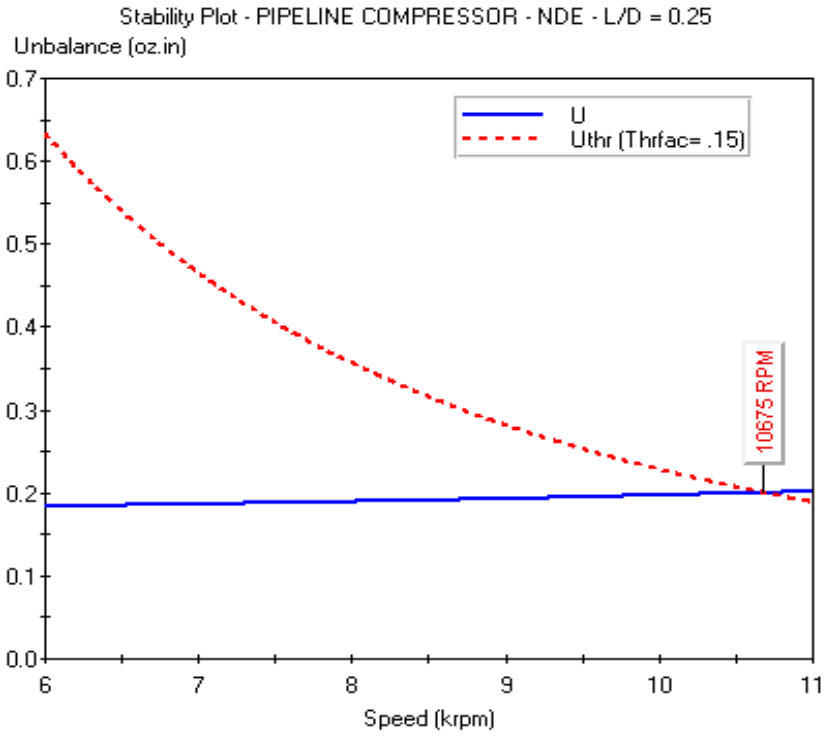

Figure A.5 Stability plot of pipeline compressor, L/D=0.25

APPENDIX B

VT-MAP ANALYSIS: TPJB SUPPORTED OVERHUNG ROTOR

This case came from another domestic company, which is the thermal instability analysis on a tilting pad journal bearing (TPJB) supported rotor with an overhung mass. Figure B.1 is the DyRoBeS rotor model for this analysis. The tilting pad journal bearing has 4 pads and the arc length is 75 degree. The diameter of the bearing is 95.5 mm (3.76 inch). It has a load-between-pad configuration with the load of 4047.9 N (910 lb_f). The speed range considered is from 15000 RPM to 30000 RPM.

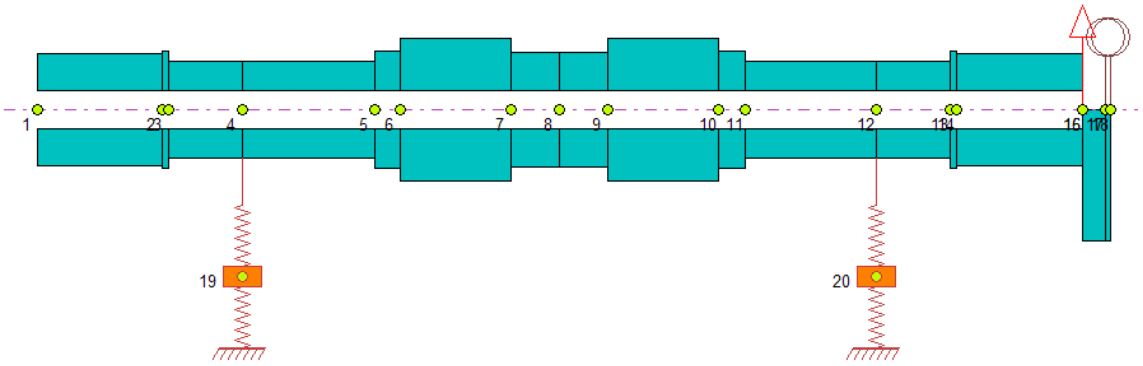

Figure B.1 DyRoBeS model of a tilting pad journal bearing supported rotor

The influence of major bearing parameters such as preload and bearing clearance on the Morton Effect has been studied in this model. Table B.1 shows the case index and the corresponding conditions used for the analysis.

Table B.1 Parameters for analysis of tilting pad journal bearing supported rotor

Case Index	Preload	Bearing Clearance		Pad Clearance	
Case 1.11	50%	0.061 mm	0.0024 in	0.122 mm	0.00480 in
Case 1.12	40%	0.061 mm	0.0024 in	0.102 mm	0.00400 in
Case 1.13	30%	0.061 mm	0.0024 in	0.086 mm	0.00340 in
Case 1.21	50%	0.074 mm	0.0029 in	0.147 mm	0.00580 in
Case 1.22	40%	0.074 mm	0.0029 in	0.122 mm	0.00480 in
Case 1.23	30%	0.074 mm	0.0029 in	0.104 mm	0.00410 in
Case 1.31	50%	0.086 mm	0.0034 in	0.173 mm	0.00680 in
Case 1.32	40%	0.086 mm	0.0034 in	0.144 mm	0.00567 in
Case 1.33	30%	0.086 mm	0.0034 in	0.123 mm	0.00486 in
Case 1.41	50%	0.099 mm	0.0039 in	0.198 mm	0.00780 in
Case 1.42	40%	0.099 mm	0.0039 in	0.165 mm	0.00650 in
Case 1.43	30%	0.099 mm	0.0039 in	0.142 mm	0.00557 in

Figure B.2 shows the stability plots for four specific bearing clearances while in each plot the different preload factors are considered. It can be seen that with the increase of bearing clearance, the thermal instability is improved obviously while the preload factor seems to have no serious impact relatively on the thermal instability, if within the same values of bearing clearance. The further data about the first onset of thermal instability for the cases in Figure B.2(a) are: Case 1.11 (50% preload) is 20340 RPM; Case 1.12 (40% preload) is 20520 RPM and Case 1.13 (30% preload) is 20565 RPM. This indicates that with the decrease of preload factor,

the Morton Effect induced thermal instability can obtain an improvement, though relatively limited.

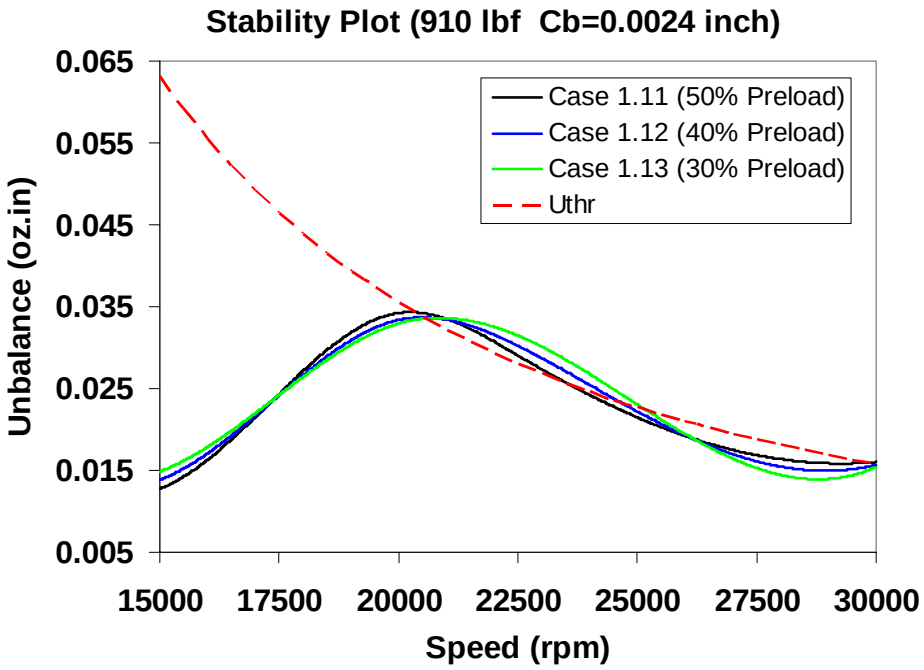

(a) Bearing clearance = 0.061 mm (0.0024 in)

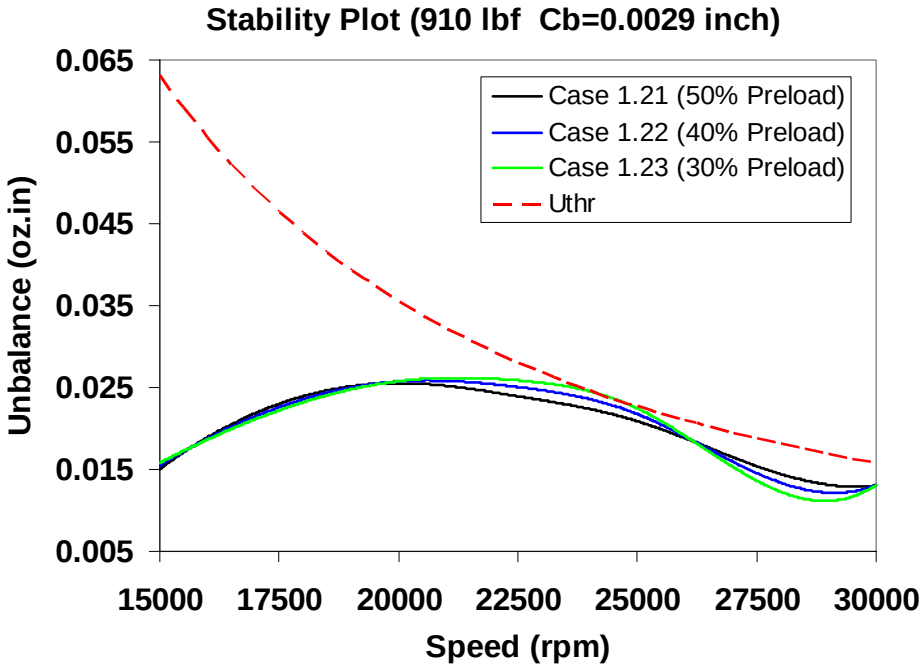

(b) Bearing clearance = 0.074 mm (0.0029 in)

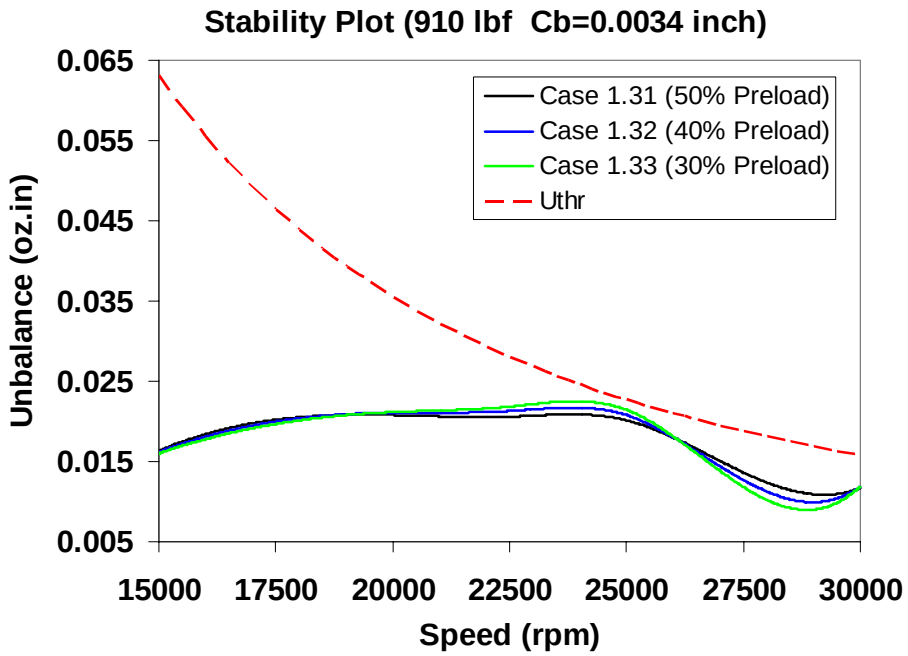

(c) Bearing clearance = 0.086 mm (0.0034 in)

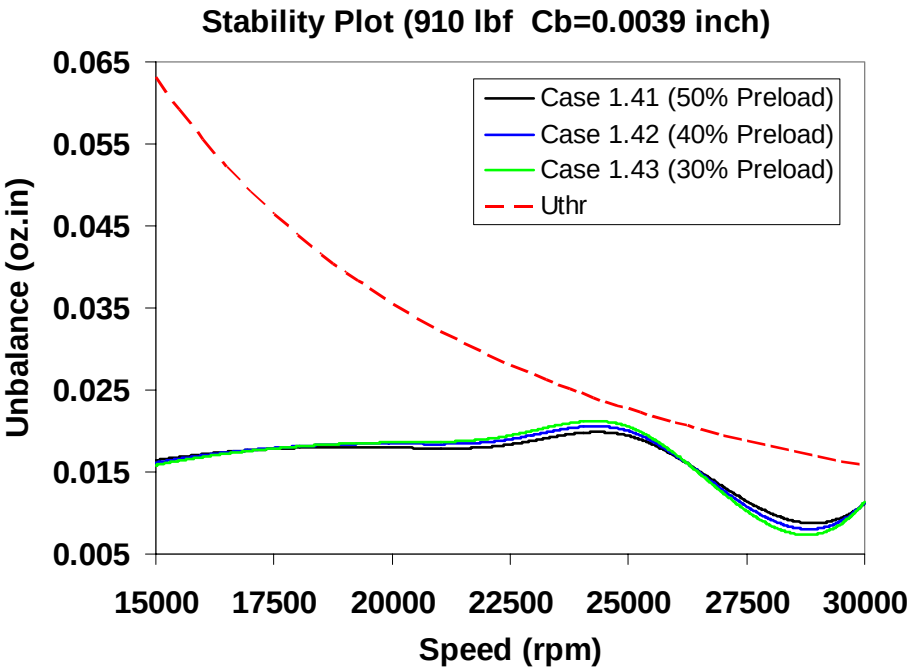

(d) Bearing clearance = 0.099 mm (0.0039 in)

Figure B.2 Stability plots for four specific bearing clearances

Figure B.3 displays the stability plots for three specific preload factors while in each plot the different bearing clearances are considered. The dominant factor is the bearing clearance.

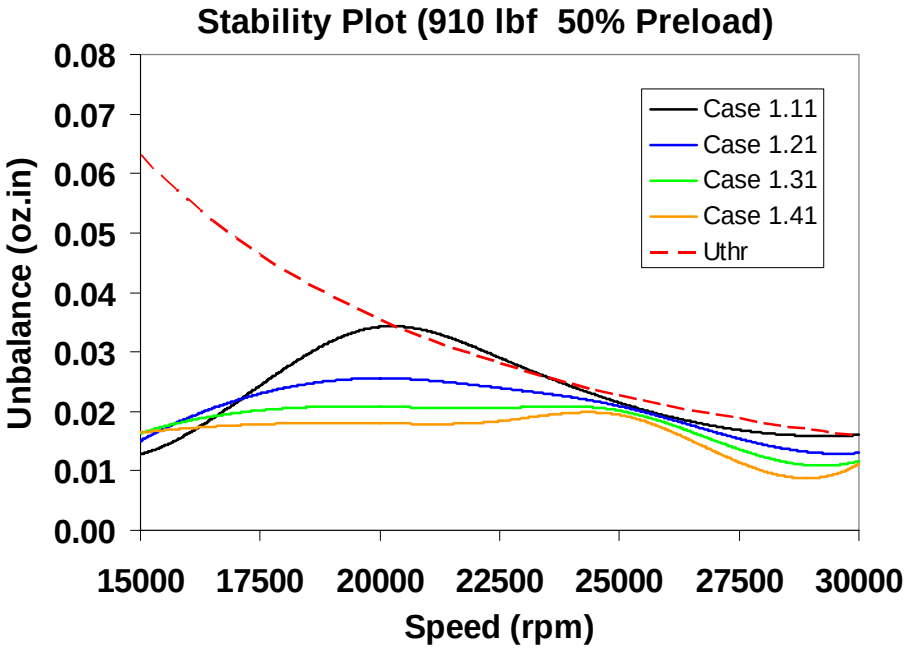

(a) Preload = 50%

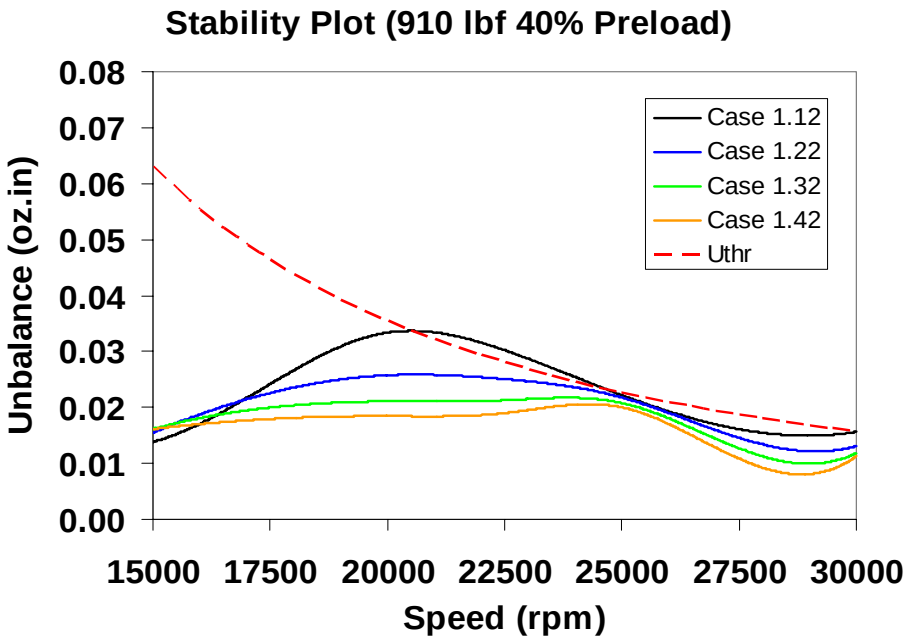

(b) Preload = 40%

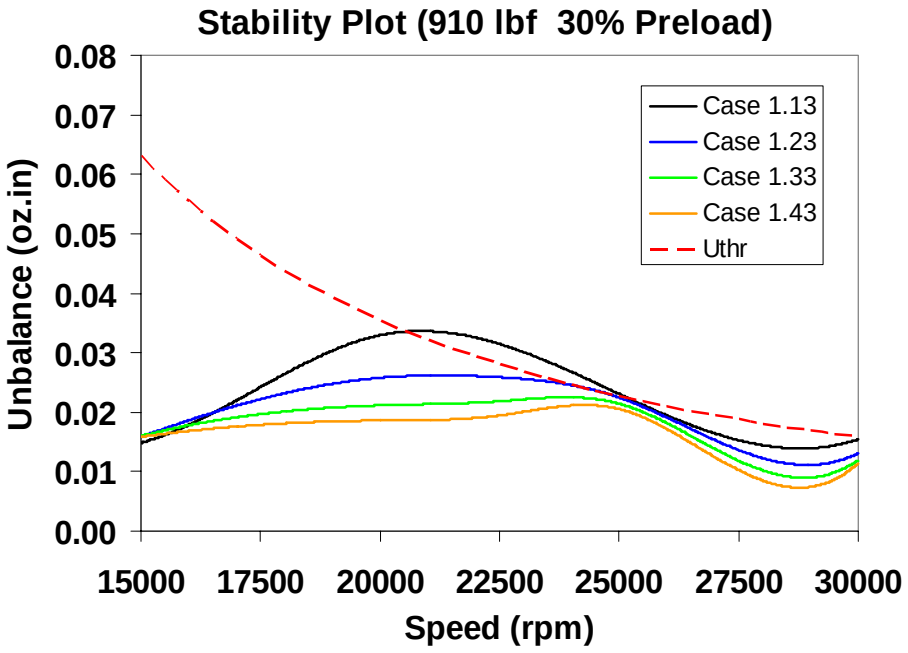

(c) Preload = 30%

Figure B.3 Stability plots for three specific preload factors

The results show that the bearing clearance has the more obvious influence on the thermal instability than the preload factor. In general, large bearing clearance can be used to improve the Morton Effect induced thermal instability. A general recommendation for preload factor for improved thermal stability is not possible. The choice of preload depends on the rotor speed being considered for thermal instability, as shown in Figure B.2(a).